

MEASUREMENT OF DOUBLE-HELICITY ASYMMETRY  
AND SEARCH FOR OPEN CHARM IN SINGLE-MUON  
PRODUCTION IN POLARIZED PROTON-PROTON  
COLLISIONS

BY

MIKHAIL STEPANOV, B.S., M.S.

A dissertation submitted to the Graduate School

in partial fulfillment of the requirements

for the degree

Doctor of Philosophy

Major Subject: Physics

New Mexico State University

Las Cruces, New Mexico

December 2009

“Measurement of Double-helicity Asymmetry and Search for Open Charm in Single-muon Production in Polarized  $p - p$  Collisions,” a dissertation prepared by Mikhail Stepanov in partial fulfillment of the requirements for the degree, Doctor of Philosophy, has been approved and accepted by the following:

---

Linda Lacey  
Dean of the Graduate School

---

Vassilios Papavassiliou  
Chair of the Examining Committee

---

Date

Committee in charge:

Dr. Vassilios Papavassiliou, Chair

Dr. Gary S. Kyle

Dr. Heinrich Nakotte

Dr. Igor Sevostianov

## DEDICATION

To my grandmother, Svetlana Mikhailovna Starostina, and my father, Yuri Mikhailovich Stepanov. They would be very proud of me.

## ACKNOWLEDGMENTS

First of all, I would like to thank my adviser, Vassili Papavassiliou, who mentored me during the long years of my research, encouraging me to work on the project and sharing his extensive knowledge with me. I would also like to thank professors of our NMSU Nuclear and Particle Physics group, Gary Kyle and Stephen Pate, for always supporting me and for lots and lots of scientific discussions, providing constructive criticism and useful advices during my research.

I wish to thank all the PHENIX experiment collaborators — without their successful work it would not be possible to run experiment and make measurements used in my research analysis. My special thanks to muon group collaborators Ming Liu, Melynda Brooks, and Xiaorong Wang for providing helpful details and advices on muon analyses. Special thanks to Sasha Bazilevsky for useful discussions about spin physics and spin measurements. For providing details on the Central-Arm operation and analyses I would also like to give special thanks to Raul Armendariz, Ralf Averbeck, Victor Baublis, Sergey Belikov, Sergey Butsyk, Arthur Durum, Alexei Khanzadeev, Boris Komkov, Dmitri Kotchetkov, Sasha Milov, Vlad Pantuev, Ilia Ravinovich, Victor Riabov, Yuri Riabov, Evgueni Vznuzdaev, Andrey Yanovich. Hugo Pereira notably helped me with the simulation project combined for the PHENIX Muon and Central Arms. I would like to acknowledge internal analysis reviewers Christine Aidala, Tony Frawley, Mike Leitch, and Kensuke Okada.

Last but not least, thanks to my mother, Lidia Stepanova, and my sister, Natalia Stepanova, for their love, support and faith in me, which always motivated me for new achievements. Finally, my dissertation work would not be accomplished without help of my wife, Tatiana. Thank you for your love, patience and for always being beside me always ready to help.

## VITA

- March 28, 1974 Born at Nazarovo, Krasnoyarsk region, Russia
- 1991-1995 B.S., Novosibirsk State University,  
Novosibirsk, Russia
- 1995-1997 M.S., Novosibirsk State University,  
Novosibirsk, Russia
- 1997-2000 Research Fellow, Budker Institute of Nuclear Physics,  
Novosibirsk, Russia
- 2000-2009 Research and Teaching Assistant, Department of Physics,  
New Mexico State University

## PROFESSIONAL AND HONORARY SOCIETIES

American Physical Society

## PUBLICATIONS

M. Stepanov, in *Proceedings of the Third Workshop of the APS Topical Group in Hadron Physics (GHP2009), Denver, Colorado, 2009*, at <http://www.fz-juelich.de/ikp/ghp2009/Proceedings.shtml>.

M. Stepanov, *Joint Fall Meeting of the Texas and Four Corners Sections of APS, El Paso, Texas, Oct., 2008*.

67 publications with the PHENIX collaboration (2003-2009).

M. Yu. Stepanov, *Physica B* **276&278**, 81 (2000).

8 publications with the AMBAL-M collaboration (1998-2000).

## FIELD OF STUDY

Major Field: Nuclear and Particle Physics

Physics of Plasma

ABSTRACT

MEASUREMENT OF DOUBLE-HELICITY ASYMMETRY  
AND SEARCH FOR OPEN CHARM IN SINGLE-MUON  
PRODUCTION IN POLARIZED PROTON-PROTON  
COLLISIONS

BY

MIKHAIL STEPANOV, B.S., M.S.

Doctor of Philosophy

New Mexico State University

Las Cruces, New Mexico, 2009

Dr. Vassilios Papavassiliou, Chair

High-energy experiments at RHIC using longitudinally-polarized proton-proton collisions study, among other things, the gluon contribution to the proton spin. The production of  $c\bar{c}$  pairs in  $p - p$  collisions at RHIC energies is dominated by gluon-gluon processes. Therefore, the production of single muons from charm decay in polarized  $p - p$  collisions is expected to be sensitive to the polarized gluon distribution in the proton.

In this work, I present double-helicity asymmetry,  $A_{LL}$ , measurements for inclusive muons detected in the Muon Arms of the PHENIX detector in longitudinally-polarized  $p-p$  collisions at  $\sqrt{s} = 200$  GeV. The PHENIX 2003 inclusive single-muon  $A_{LL}$  results and  $A_{LL}$  predictions for PHENIX 2006 single-muon data demonstrated that large statistical uncertainties preclude constraining the gluon polarization with the current limited statistics available for the  $A_{LL}$  measurements.

In order to develop discriminants and selection cuts for enriching the charm content of a sample of single-muon events, we investigated correlations between muon tracks in the Muon Arms at forward rapidity and mid-rapidity charged hadron/lepton tracks in the Central Arms of the PHENIX detector, using a multi-stage Monte Carlo simulation which included the PHENIX detector response. Two separate simulation outputs have been produced and compared: for open charm ( $c\bar{c}$ ) events and minimum-bias (i.e. mostly light-quark) events. The azimuthal-angle correlations of the maximum- $p_T$  Central-Arm and Muon-Arm tracks have been studied as a function of Muon-Arm track  $p_T$ . We also studied correlations between the  $p_T$  of the Muon-Arm track and the  $p_T$  of the particles detected in the Central Arms. The simulation results demonstrated that additional correlation studies, including likelihood calculations, for other kinematic quantities are required in order to develop multivariate selection criteria, which can significantly enhance the charm content of a sample of single-muon events.

## CONTENTS

LIST OF TABLES . . . . .	xii
LIST OF FIGURES . . . . .	xxii
1 INTRODUCTION . . . . .	1
2 SPIN PHYSICS CONCEPTS AND PREREQUISITES . . . . .	3
2.1 Proton Spin Structure Model . . . . .	3
2.2 Deep-Inelastic Scattering as a Probe of Nucleon Spin Structure . . . . .	6
2.3 Kinematics of a Proton-Proton Collision . . . . .	20
2.4 Spin-Dependent Parton Densities and Cross Sections in Polarized Proton-Proton Collisions . . . . .	22
2.5 Asymmetries . . . . .	28
2.6 Asymmetry Errors . . . . .	32
2.7 Gluon Polarization Probes at RHIC . . . . .	33
2.7.1 Prompt-Photon Production . . . . .	34
2.7.2 Combination of Compton Process and Drell-Yan Production of Lepton Pair . . . . .	38
2.7.3 Jet and Large- $p_T$ Hadron Production . . . . .	39
2.7.4 $\Delta g$ in Heavy-Flavor Production . . . . .	41
3 RECENT DOUBLE-HELICITY ASYMMETRY AND POLARIZED GLUON DISTRIBUTION MEASUREMENTS . . . . .	44

4	HEAVY-FLAVOR PRODUCTION . . . . .	52
4.1	Theoretical Predictions for Heavy-Flavor Production . . . . .	53
4.2	Experimental Measurements of Heavy-Flavor Production . . . . .	66
4.3	Search for Open Charm with a Combined Analysis of Single-Muon Events in the Central and Muon Arms of the PHENIX Detector . . .	76
5	EXPERIMENTAL SETUP AND DATA ACQUISITION . . . . .	80
5.1	The RHIC Accelerator Complex . . . . .	80
5.2	Luminosity in the Collider and Other Definitions . . . . .	85
5.3	The PHENIX Experiment Overview . . . . .	87
	5.3.1 The PHENIX Detector Subsystem Overview . . . . .	88
	5.3.2 The PHENIX coordinate system . . . . .	95
5.4	The Muon Arms . . . . .	96
	5.4.1 The Muon Tracker . . . . .	98
	5.4.2 The Muon Identifier . . . . .	103
5.5	The Drift Chamber . . . . .	109
6	DOUBLE-HELICITY ASYMMETRY FOR SINGLE-MUON PRO- DUCTION . . . . .	116
6.1	2002-2003 RHIC Run 3 Summary . . . . .	117
6.2	Data Sample and Triggering . . . . .	117
6.3	Event and Muon-Arm Track Selection . . . . .	121
6.4	Beam Polarization . . . . .	123
6.5	Asymmetry Measurement Systematic Errors . . . . .	126

6.6	Data Analysis: Results and Discussion . . . . .	127
6.7	2005-2006 RHIC Run-6 Data . . . . .	133
6.8	Run-6 $A_{LL}^\mu$ Predictions . . . . .	135
7	SEARCH FOR OPEN CHARM . . . . .	139
7.1	Simulation . . . . .	141
7.1.1	Monte Carlo Event Generation . . . . .	143
7.1.2	Detector Simulation and Data Reconstruction Chain . . . . .	144
7.1.3	Multistage Simulation Chain and Ancestry Tracking . . . . .	151
7.1.4	Minimum-bias Modeling . . . . .	155
7.1.5	Charm Modeling . . . . .	156
7.2	Central-Arm Track Selection . . . . .	157
7.3	Simulation Data Analysis: Track Correlation Study . . . . .	158
7.3.1	Simulation Studies of Azimuthal-Angle Correlations . . . . .	159
7.3.2	Simulation Studies of $p_T$ Correlations . . . . .	178
7.4	Single-Muon $p_T$ Spectra . . . . .	197
7.5	Multivariate Likelihood Function . . . . .	199
8	CONCLUSION AND OUTLOOK . . . . .	203
	REFERENCES . . . . .	206

## LIST OF TABLES

1	Quark and gluon parton densities containing spin information . . .	25
2	RHIC experiments . . . . .	83
3	Summary of the PHENIX detector subsystems used in the analysis	89
4	Summary of the MuID performance simulation [110] . . . . .	108
5	PHENIX Run-3 good run list used in the analysis . . . . .	120
6	Muon-Arm track and road cuts . . . . .	122
7	PHENIX Run-3 inclusive single muon $A_{LL}^{\mu}$ values . . . . .	131
8	PYTHIA switches and parameters, default for the analysis . . . . .	144
9	Variable <i>origin</i> from ancestry tracking . . . . .	154
10	Central-Arm (DC/PC1) track cuts . . . . .	158
11	Parameter $p1$ referring to the slope of the linear fit . . . . .	167
12	Slope parameter $p1$ for LO charm simulation . . . . .	177

## LIST OF FIGURES

1	Neutrino-nucleon and antineutrino-nucleon cross-sections measured as a function of energy at the CERN 24 GeV Synchrotron with the use of the heavy-liquid bubble chamber “Gargamelle” [4, 7] . . . . .	7
2	Feynman diagram for deep-inelastic charged-lepton scattering from a nucleon (kinematic quantities are defined in the text) . . . . .	8
3	Deep Inelastic lepton-nucleon Scattering in the parton model . . . . .	10
4	Drawing explaining the process of the absorption of the virtual-photon by quarks with the spin aligned or antialigned with the parent nucleon spin [9] . . . . .	15
5	HERMES double-helicity asymmetry versus transverse momentum of one of the hadron pair participant [6] . . . . .	19
6	Gluon polarization extracted from HERMES semi-inclusive data [6] . . . . .	19
7	Kinematics of a $p - p$ collision . . . . .	20
8	Production of a hadron with large $p_T$ in a $p - p$ collision . . . . .	23
9	Longitudinal polarization analyzing powers for different partonic reactions vs. the partonic center-of-mass system scattering angle [34] . . . . .	30
10	Leading-order Feynman diagrams for the production of a photon in the final state: a) quark-gluon Compton scattering, b) $q\bar{q}$ annihilation . . . . .	35

11	NLO prediction for the prompt-photon production double-helicity asymmetry for different polarized parton density sets [6] . . . . .	36
12	Polarized gluon densities for different NLO sets of polarized parton distribution functions (at $Q^2 = 100 \text{ GeV}^2$ ) [39] . . . . .	37
13	Feynman diagram for combination of Compton Process and Drell-Yan Production of Lepton Pair . . . . .	38
14	Lowest-order Feynman diagrams of gluon-initiated subprocesses for jet production . . . . .	40
15	NLO predicted jet production double-helicity asymmetry as a function of jet transverse momentum, for different polarized parton densities [24] . . . . .	40
16	Feynman diagram for heavy quark pair production via gluon-gluon fusion . . . . .	41
17	An example of heavy quarkonium ( $J/\psi$ ) production via gluon-gluon fusion, with subsequent decay to a lepton pair; the oval between the $c\bar{c}$ pair and the $J/\psi$ represents the formation of the $J/\psi$ from the $c\bar{c}$ pair . . . . .	42
18	PHENIX inclusive- $\pi^0$ $A_{LL}$ [59, 60, 61]. The NLO curves are addressed in the text . . . . .	46
19	STAR inclusive-jet $A_{LL}$ [62]. The NLO curves are addressed in the text . . . . .	46

20	Polarized gluon distribution functions at $Q^2 = 10 \text{ GeV}^2$ from the global analysis by DSSV [64] and from the prior GRSV and DNS models . . . . .	48
21	$\langle \Delta g/g \rangle$ from open-charm and high $p_T$ hadron pair production measured by COMPASS, HERMES, and SMC [69] . . . . .	51
22	Leading-order Feynman diagrams for heavy-flavor production: a) gluon-gluon fusion, b) $q\bar{q}$ annihilation . . . . .	53
23	LO partonic level double-helicity asymmetry for gluon-gluon fusion vs. the center-of-mass scattering angle for different values of $\sqrt{\hat{s}}/2m$ (see text) [71] . . . . .	55
24	Examples of NLO Feynman diagrams for heavy-flavor production (see text) . . . . .	57
25	$(m^2/\alpha_s^2)\hat{\sigma}_{gg}$ and $(m^2/\alpha_s^2)\Delta\hat{\sigma}_{gg}$ in LO and NLO [79] . . . . .	58
26	NLO charm spin asymmetry at $\sqrt{s} = 200 \text{ GeV}$ for PHENIX [79] . . . . .	60
27	FONLL uncertainty bands for $c$ quark and $D$ meson $p_T$ distributions [80] . . . . .	62
28	FONLL uncertainty bands for $b$ quark and $B$ meson $p_T$ distributions [80] . . . . .	63
29	NLO total charm (left-hand side) and bottom (right-hand side) cross sections as functions of $\sqrt{s}$ [81] . . . . .	64

30	Examples of heavy-flavor production diagrams in parton-shower approach [82]: a) pair creation, b) flavor excitation, c) and d) gluon splitting . . . . .	65
31	Total charm (a) and bottom (b) production cross sections for $p - p$ collisions calculated in parton-shower approach using PYTHIA [82]	67
32	Invariant differential cross section of electrons from decays of heavy flavor (a); ratio of the data to the FONLL calculation (b) [85] . . .	71
33	$p_T$ spectrum of “vertex-independent” negative muons compared to theoretical calculations [94] . . . . .	75
34	Production of single muons from charm decay used to access gluons in the proton . . . . .	76
35	Example of single lepton (muon or electron) production in semi-leptonic decays of heavy-flavored mesons from open charm . . . . .	77
36	Schematic view of the RHIC accelerator complex . . . . .	81
37	Helicity . . . . .	87
38	A three-dimensional sectional view drawing of the PHENIX detector with the labeled subsystems [111] . . . . .	90
39	The PHENIX detector performance for the detection of various particle species . . . . .	91
40	Magnetic field produced by the Central Magnet and two Muon Magnets	94
41	The PHENIX coordinate system . . . . .	95

42	A cutaway schematic view of the PHENIX detector with the PHENIX coordinate system axes . . . . .	97
43	The Muon Arm tracking spectrometer (MuTr) [110] . . . . .	98
44	MuTr optical alignment system [115] . . . . .	101
45	Position resolution measured in cosmic-ray test runs for the station 2 [111] . . . . .	103
46	MuID panels in a gap (panels A, C and E shown) around the beam pipe hole (in the center) . . . . .	106
47	Beam-Beam Counter total charge versus number of hits in the MuID [116] . . . . .	109
48	The DC frame structure . . . . .	110
49	DC sector, side view: wire assembly within a sector and inside the anode plane [107] . . . . .	112
50	Schematic view (top view) of stereo wire orientation in the DC sectors	113
51	Bunch filling pattern in two RHIC beams representing the spin states of polarized protons . . . . .	116
52	Fill-by-fill polarizations for 100 GeV Blue and Yellow beams in RHIC Run 3 . . . . .	124
53	The “non-physical” same-sign double-helicity asymmetry for inclusive single muons . . . . .	128
54	The “non-physical” opposite-sign double-helicity asymmetry for inclusive single muons . . . . .	128

55	$p_T$ spectrum for $\mu$ tracks in the PHENIX Muon Arms with maximum transverse momentum in an event (2002-2003 RHIC Run 3) . . . . .	129
56	$A_{LL}^\mu$ for inclusive single muons from PHENIX Run-3 (2002-2003) data, compared with theoretical prediction . . . . .	130
57	$A_{LL}^\mu$ theoretical predictions for single muons from heavy-flavor production [122] using different polarized parton distribution function sets; GRSV01-MAX curve is the same theoretical prediction curve shown in Figure 56 compared with the measurement results . . . . .	132
58	Predicted $p_T$ spectrum for $\mu$ tracks in the PHENIX Muon Arms with maximum transverse momentum in an event for 2005-2006 PHENIX Run-6 data . . . . .	136
59	Predicted inclusive single muon $\Delta A_{LL}^\mu$ for PHENIX Run-6 (2005-2006) data, along with $A_{LL}^\mu$ theoretical predictions . . . . .	137
60	Tracks in the PHENIX Muon and Central Arms involved in the track correlation studies . . . . .	140
61	Multistage simulation chain and ancestry tracking . . . . .	142
62	PISA configuration file <code>pisa.kumac</code> for the current analysis simulation	147
63	The second part of the <code>pisa.kumac</code> file for the current analysis simulation . . . . .	148
64	PISA kinematic filter file <code>event.par</code> for the current analysis simulation	149
65	Minimum-bias simulation single-muon $p_T$ spectrum compared to single-muon $p_T$ spectrum from the PHENIX Run-6 $p - p$ data . . . . .	156

66	Azimuthal angle between maximum- $p_T$ Muon-Arm track and maximum- $p_T$ Central-Arm track for $c\bar{c}$ events . . . . .	161
67	Azimuthal angle between maximum- $p_T$ Muon-Arm track and maximum- $p_T$ Central-Arm track for minimum-bias events . . . . .	161
68	Ratio of two distributions — open-charm $\Delta\phi$ distribution over minimum-bias $\Delta\phi$ distribution . . . . .	162
69	Azimuthal angle between maximum- $p_T$ Muon-Arm and Central-Arm tracks for $0.0 < p_T^{\mu(max)} \leq 1.0$ GeV/ $c$ ( $c\bar{c}$ events) . . . . .	163
70	Azimuthal angle between maximum- $p_T$ Muon-Arm and Central-Arm tracks for $1.0 < p_T^{\mu(max)} \leq 2.0$ GeV/ $c$ ( $c\bar{c}$ events) . . . . .	163
71	Azimuthal angle between maximum- $p_T$ Muon-Arm and Central-Arm tracks for $2.0 < p_T^{\mu(max)} \leq 3.0$ GeV/ $c$ ( $c\bar{c}$ events) . . . . .	164
72	Azimuthal angle between maximum- $p_T$ Muon-Arm and Central-Arm tracks for $3.0$ GeV/ $c < p_T^{\mu(max)}$ ( $c\bar{c}$ events) . . . . .	164
73	Azimuthal angle between maximum- $p_T$ Muon-Arm and Central-Arm tracks for $0.0 < p_T^{\mu(max)} \leq 1.0$ GeV/ $c$ (minimum-bias events) . . . . .	165
74	Azimuthal angle between maximum- $p_T$ Muon-Arm and Central-Arm tracks for $1.0 < p_T^{\mu(max)} \leq 2.0$ GeV/ $c$ (minimum-bias events) . . . . .	165
75	Azimuthal angle between maximum- $p_T$ Muon-Arm and Central-Arm tracks for $2.0 < p_T^{\mu(max)} \leq 3.0$ GeV/ $c$ (minimum-bias events) . . . . .	166
76	Azimuthal angle between maximum- $p_T$ Muon-Arm and Central-Arm tracks for $3.0$ GeV/ $c < p_T^{\mu(max)}$ (minimum-bias events) . . . . .	166

77	Open-charm $\Delta\phi$ distribution over minimum-bias $\Delta\phi$ distribution ratio for $0.0 < p_T^{\mu(max)} \leq 1.0$ GeV/ $c$ . . . . .	168
78	Open-charm $\Delta\phi$ distribution over minimum-bias $\Delta\phi$ distribution ratio for $1.0 < p_T^{\mu(max)} \leq 2.0$ GeV/ $c$ . . . . .	168
79	Open-charm $\Delta\phi$ distribution over minimum-bias $\Delta\phi$ distribution ratio for $2.0 < p_T^{\mu(max)} \leq 3.0$ GeV/ $c$ . . . . .	169
80	Open-charm $\Delta\phi$ distribution over minimum-bias $\Delta\phi$ distribution ratio for $3.0$ GeV/ $c < p_T^{\mu(max)}$ . . . . .	169
81	Azimuthal angle between maximum- $p_T$ Muon-Arm track and maximum- $p_T$ Central-Arm track for LO charm production . . . . .	171
82	Azimuthal angle between maximum- $p_T$ Muon-Arm track and maximum- $p_T$ Central-Arm track for minimum-bias events (no origin cuts) . . .	171
83	Ratio of two distributions — LO charm $\Delta\phi$ distribution over minimum-bias $\Delta\phi$ distribution . . . . .	172
84	Azimuthal angle between maximum- $p_T$ Muon-Arm and Central-Arm tracks for $0.0 < p_T^{\mu(max)} \leq 1.0$ GeV/ $c$ (LO $c\bar{c}$ production) . . . . .	173
85	Azimuthal angle between maximum- $p_T$ Muon-Arm and Central-Arm tracks for $1.0 < p_T^{\mu(max)} \leq 2.0$ GeV/ $c$ (LO $c\bar{c}$ production) . . . . .	173
86	Azimuthal angle between maximum- $p_T$ Muon-Arm and Central-Arm tracks for $2.0 < p_T^{\mu(max)} \leq 3.0$ GeV/ $c$ (LO $c\bar{c}$ production) . . . . .	174
87	Azimuthal angle between maximum- $p_T$ Muon-Arm and Central-Arm tracks for $3.0$ GeV/ $c < p_T^{\mu(max)}$ (LO $c\bar{c}$ production) . . . . .	174

88	LO charm production $\Delta\phi$ distribution over minimum-bias $\Delta\phi$ distribution ratio for $0.0 < p_T^{\mu(max)} \leq 1.0$ GeV/ $c$ . . . . .	175
89	LO charm production $\Delta\phi$ distribution over minimum-bias $\Delta\phi$ distribution ratio for $1.0 < p_T^{\mu(max)} \leq 2.0$ GeV/ $c$ . . . . .	175
90	LO charm production $\Delta\phi$ distribution over minimum-bias $\Delta\phi$ distribution ratio for $2.0 < p_T^{\mu(max)} \leq 3.0$ GeV/ $c$ . . . . .	176
91	LO charm production $\Delta\phi$ distribution over minimum-bias $\Delta\phi$ distribution ratio for $3.0$ GeV/ $c < p_T^{\mu(max)}$ . . . . .	176
92	$c\bar{c}$ and minimum-bias 2-dimensional histograms — maximum Muon-Arm track $p_T$ against maximum Central-Arm track $p_T$ . . . . .	180
93	Two-dimensional cut tables for Figure 92 — upper table for $c\bar{c}$ events, lower table for minimum-bias events . . . . .	181
94	Maximum Muon-Arm track $p_T$ against the sum of the transverse momenta of 3 Central-Arm tracks with the largest $p_T$ values . . . . .	183
95	Two-dimensional cut tables for Figure 94 — upper table for $c\bar{c}$ events, lower table for minimum-bias events . . . . .	184
96	Maximum Muon-Arm track $p_T$ against the sum of the transverse momenta of 4 Central-Arm tracks with the largest $p_T$ values . . . . .	185
97	Two-dimensional cut tables for Figure 96 — upper table for $c\bar{c}$ events, lower table for minimum-bias events . . . . .	186
98	Maximum Muon-Arm track $p_T$ against the sum of the transverse momenta of 5 Central-Arm tracks with the largest $p_T$ values . . . . .	187

99	Two-dimensional cut tables for Figure 98 — upper table for $c\bar{c}$ events, lower table for minimum-bias events . . . . .	188
100	Maximum Central-Arm track $p_T$ vs. the sum of the $p_T$ of 3 Central- Arm tracks with the largest $p_T$ values for all $p_T^{\mu(max)}$ . . . . .	189
101	Two-dimensional cut tables for Figure 100 — upper table for $c\bar{c}$ events, lower table for minimum-bias events . . . . .	190
102	Maximum Central-Arm track $p_T$ vs. the sum of the $p_T$ of 3 Central- Arm tracks with the largest $p_T$ values for $0.0 < p_T^{\mu(max)} < 1.0$ GeV/ $c$	191
103	Two-dimensional cut tables for Figure 102 — upper table for $c\bar{c}$ events, lower table for minimum-bias events . . . . .	192
104	Maximum Central-Arm track $p_T$ vs. the sum of the $p_T$ of 3 Central- Arm tracks with the largest $p_T$ values for $1.0 \leq p_T^{\mu(max)} < 2.0$ GeV/ $c$	193
105	Two-dimensional cut tables for Figure 104 — upper table for $c\bar{c}$ events, lower table for minimum-bias events . . . . .	194
106	Maximum Central-Arm track $p_T$ vs. the sum of the $p_T$ of 3 Central- Arm tracks with the largest $p_T$ values for $2.0$ GeV/ $c \leq p_T^{\mu(max)}$ . . .	195
107	Two-dimensional cut tables for Figure 106 — upper table for $c\bar{c}$ events, lower table for minimum-bias events . . . . .	196
108	Single-muon $p_T$ spectra in the Muon Arms for the minimum-bias (squares), the open-charm (circles), and the bottom (triangles) sim- ulation samples . . . . .	198

## 1 INTRODUCTION

Spin is one of the most intriguing objects in physics. It is one of the most nonintuitive physics concepts. It starts to surprise our mind from the idea that elementary point-like particle such as an electron has intrinsic characteristic such as perpetual angular momentum called spin. It continues to impress our intuition in our understanding of the proton spin.

Since the 1960s, Deep-Inelastic Scattering (DIS) experiments have produced data, which allowed to make significant progress in understanding of the structure of the proton. We know that the proton consists of quarks, antiquarks, and gluons. We also know that the proton structure is dynamic, rather than static, and that the proton constituents appear in constant motion inside the proton. In the 1980s and 1990s, polarized DIS experiments with polarized leptons scattered from polarized target nucleons contradicted expectation that mainly the proton's three valence quarks contributed to the proton spin. The polarized DIS experiments have demonstrated that on average only about 30% of the proton spin is carried by the quarks and antiquarks in the proton. This is known as "spin deficit" or "spin crisis".

Where is the remaining proton spin? It appears that the proton spin receives substantial contributions from the gluons and orbital angular momentum of the proton constituents. The gluon polarization can be significant. This means that the gluons in the proton can be predominantly spinning in the same direction.

The DIS experiments have shown that the proton spin structure is much more interesting than one had expected. Furthermore, spin represents a very powerful tool in physics investigations. The ultimate physics objective of this dissertation research is to contribute to the evaluation of the gluon polarization in the proton. At the Relativistic Heavy Ion Collider (RHIC) at Brookhaven National Laboratory high-energy experiments with polarized proton-proton collisions are capable to proceed with an exciting project — to measure the direction of the gluon spin in the proton for the first time.

## 2 SPIN PHYSICS CONCEPTS AND PREREQUISITES

This chapter begins with a description of the models of the proton and of the proton spin structure. Then it is discussed how the nucleon structure and the nucleon spin structure can be probed by Deep-Inelastic Scattering (DIS) and what information the DIS experiments gave about the proton spin structure. This is followed by an overview of more sophisticated complimentary information about the proton spin structure, which is obtained in the polarized proton-proton collisions at Relativistic Heavy Ion Collider (RHIC). And lastly, more important for the ultimate goal of the dissertation, it is discussed how the gluon polarization in the proton ( $\Delta g$ ) is accessed in the polarized proton-proton collisions.

### 2.1 Proton Spin Structure Model

When the Quark Model was first suggested in 1964 [1, 2], it comprised three types of quarks, up ( $u$ ), down ( $d$ ), and strange ( $s$ ), of charges  $\frac{2}{3}$ ,  $-\frac{1}{3}$ , and  $-\frac{1}{3}$ , respectively, and of spin  $\frac{1}{2}$  each [3]. In this simple Quark Model, the proton structure consisted of three quarks:  $u$ ,  $u$ , and  $d$ . The Quark-Parton Model of the proton (see [4, 5] for reviews) proposed later contained, in addition to the three commonly called valence quarks ( $u$ ,  $u$ ,  $d$ ), a background of quark-antiquark pairs, often called the sea, and neutral gluons, which are quanta of the strong interaction field binding the quarks. In 1970s, after the Quark-Parton Model of the proton structure was developed, it was understood that the static Quark Model, in which the valence

quarks gave all the properties of the proton, should be replaced with the dynamical model taking in account how much of the proton's momentum is carried by the constituents of a particular type. The fraction of the momentum of the proton is given by a variable  $x$  (Bjorken- $x$ ), defined later in Chapter 2.2. Soon afterwards, the proton models were developed introducing the sea quarks playing significant role at small Bjorken- $x$ , and with the valence quarks dominating at large Bjorken- $x$ .

After it was demonstrated that the proton was not an elementary particle, a new challenging task arose to explain the proton spin structure in terms of the proton's constituents. In the simple Quark Model, a proton non-relativistic wave function can be written as [6]

$$|p \uparrow\rangle = \frac{1}{\sqrt{6}}(2|u \uparrow u \uparrow d \downarrow\rangle - |u \uparrow u \downarrow d \uparrow\rangle - |u \downarrow u \uparrow d \uparrow\rangle), \quad (1)$$

where the permutations were omitted for brevity. In this simple model, the spin of the proton is determined entirely by the valence up and down quarks. The  $u$  and  $d$  quarks components of the proton spin can be defined as

$$\Delta u = u^\uparrow - u^\downarrow, \quad (2)$$

$$\Delta d = d^\uparrow - d^\downarrow, \quad (3)$$

where  $u^\uparrow(d^\uparrow)$  and  $u^\downarrow(d^\downarrow)$  are the numbers of up (down) quarks polarized along the direction of the proton polarization, respectively aligned and antialigned with the proton spin. Thus in the simple Quark Model the proton spin is

$$J_z^p = \frac{1}{2}\Delta\Sigma \equiv \frac{1}{2}(\Delta u + \Delta d + \Delta s) = \frac{1}{2}, \quad (4)$$

where  $\Delta\Sigma$  stands for the fraction of the proton spin having origin from quarks, and all of the spin is carried by the quarks.

In the more complicated Quark-Parton Model, if one considers a proton moving in the  $z$ -direction and polarized in the helicity (defined in Chapter 5.2) eigenstate  $\lambda = 1/2$ , the proton spin composition can be written as

$$J_z^p = \frac{1}{2}\Delta\Sigma + \Delta G + L_z^q + L_z^g = \frac{1}{2}, \quad (5)$$

where, in addition to  $\Delta\Sigma$ , there are non-zero contributions from  $\Delta G$ , the intrinsic spin having origin from gluons, and  $L_z$ , the orbital angular momenta of quarks and gluons. Equation 5 is the sum rule for the spin of the proton. By definition the amount of the spin of the proton carried by the partons of a particular type is given by the integral of the corresponding polarized parton density (or polarized distribution function), defined in Chapter 2.2, over the entire Bjorken- $x$  range. Thus, integrating the polarized quark densities for flavors  $i = u, d, s, \dots$  over  $x$  gives the fraction of the proton spin carried by quarks,

$$\Delta\Sigma = \int_0^1 dx \sum_i (\Delta q_i(x) + \Delta \bar{q}_i(x)). \quad (6)$$

The gluon polarization in the proton is the integral of the polarized gluon density,

$$\Delta G = \int_0^1 dx \Delta g(x). \quad (7)$$

Because the proton structure is determined by the strong interaction, the contributions from the different sources to the proton spin can in principle be calculated from Quantum Chromodynamics (QCD), the current theory of strong interaction,

though this is not possible at present. But fortunately the proton spin formation can be studied directly in experiments. As discussed in Chapter 2.2,  $\Delta\Sigma$  can be measured from polarized Deep-Inelastic Scattering. In a longitudinally-polarized proton,  $\Delta G$  affects spin-dependent scattering processes, and thus can be accessed through the measurement of various experimental spin asymmetries.

## 2.2 Deep-Inelastic Scattering as a Probe of Nucleon Spin Structure

In the 1960's, new indications of quarks became apparent in experiments on deep-inelastic lepton-nucleon scattering, which have led to a dynamical understanding of the quark substructure of the nucleon. These experiments demonstrated that the complex process of lepto-production of copious hadrons in the lepton-nucleon scattering could be plainly interpreted as quasi-elastic scattering of the lepton by a point-like constituent particle (parton), later on associated with the quark. One of the most impressive demonstrations of the composite entity of the nucleon was the total cross-section, as a function of energy, of neutrino-nucleon scattering, such as:  $\nu_\mu + N \rightarrow \mu^- + \text{hadrons}$ . The process yield appeared very complicated, but if one measured the total cross-section of the process, the outcome of this was very simple — the cross-section, presented in Figure 1, demonstrated nearly linear increase with the neutrino energy  $E_\nu$  for both neutrinos and anti-neutrinos [4, 7]. This was precisely the same outcome one would anticipate, if the complex process of hadron production was substituted by the elastic scattering of the neutrino by a single point-like particle, or parton.

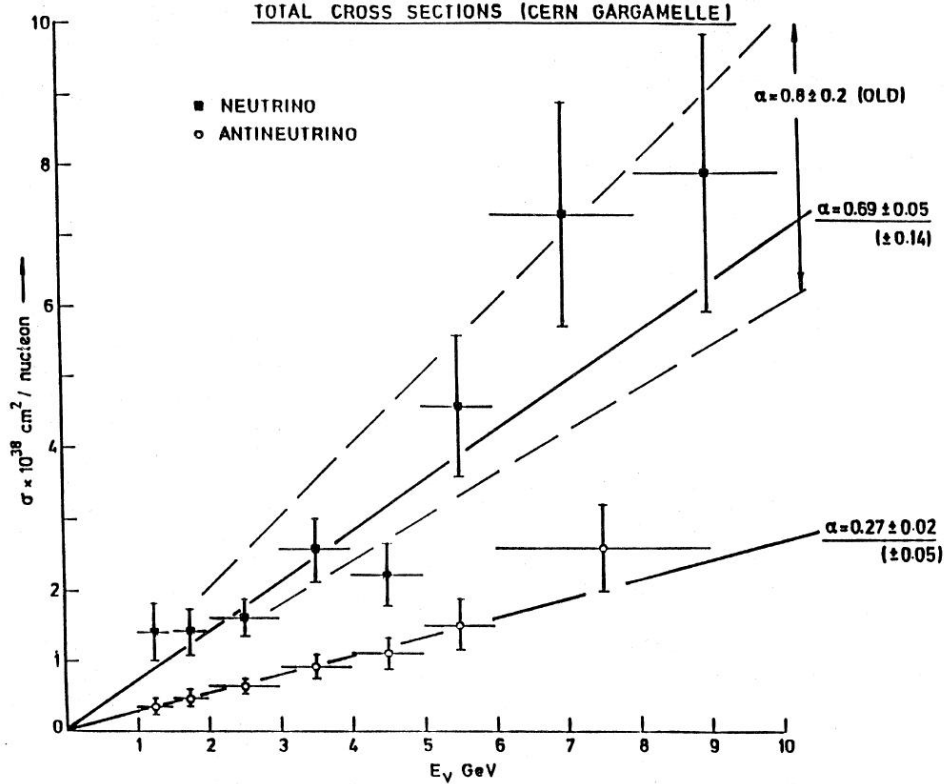


Figure 1: Neutrino-nucleon and antineutrino-nucleon cross-sections measured as a function of energy at the CERN 24 GeV Synchrotron with the use of the heavy-liquid bubble chamber “Gargamelle” [4, 7]

In the DIS experiments, by probing the nucleon using leptons, the short-distance structure of the nucleon can be studied. For a long time DIS with charged lepton beams has been the crucial instrument for this study. The process of the deep-inelastic charged-lepton scattering can be considered in the one-photon exchange approximation presented by the Feynman diagram shown in Figure 2. On the diagram  $(E, \vec{k})$  and  $(E', \vec{k}')$  are the 4-momenta of the incident and final lepton, respectively. Initially, the target nucleon of mass  $M$  is at rest in the laboratory system. The  $q = (\nu, \vec{q})$  is the 4-momentum transfer carried by the exchanged virtual photon;  $W$  and  $(E^*, \vec{p}^*)$  are the invariant mass and 4-momentum of the

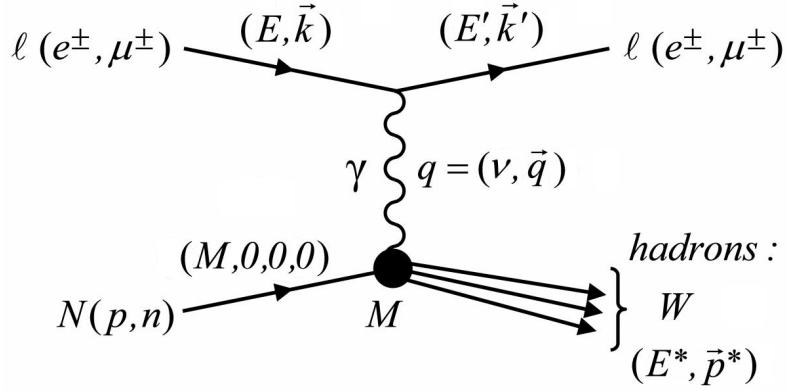


Figure 2: Feynman diagram for deep-inelastic charged-lepton scattering from a nucleon (kinematic quantities are defined in the text)

final state recoiling hadrons, respectively. One of the most important kinematic variables in the process is the square of the 4-momentum transferred to the target nucleon by the exchanged photon,  $q^2 = -2EE'(1 - \cos\theta)$ , where  $E$  is the energy of the incident lepton,  $E'$  is the energy of the final lepton, and  $\theta$  is the scattering angle, all defined in the laboratory frame. Even if the magnitude of  $q^2$  is measured in the laboratory system, its numerical value is the same in all inertial frames. To avoid using negative quantity  $q^2$ , it is common to define the positive 4-momentum transfer  $Q^2 \equiv -q^2$ .

It can be shown that

$$Q^2 = 2M\nu + M^2 - W^2, \quad (8)$$

where  $W^2 = E^{*2} - \vec{p}^{*2}$  is the square of the invariant mass of the final hadron state, and  $\nu$  is the energy transfer,  $\nu = E - E' = E^* - M$ . In the case of  $W = M$ , Equation 8 becomes  $Q^2 = 2M\nu$ , which is true for elastic scattering. Another important kinematic variable of the deep-inelastic scattering is Bjorken- $x$ , defined

as

$$x = \frac{Q^2}{2M\nu}, (0 < x < 1). \quad (9)$$

The range of  $0 < x < 1$  represents the physical region liable to inelastic scattering. For elastic scattering we have:  $x = 1$ . It is important to note that increasing  $Q^2$  directly implies decreasing the wavelength (or resolution) of the “probe” — at sufficiently large  $Q^2$  the nucleon constituents start to be revealed, and the nucleon is not seen anymore as a single whole unit.

The DIS differential cross-section for unpolarized charged-lepton scattering from unpolarized nucleons in terms of  $\nu$  and  $Q^2$  is given by [8]

$$\frac{d^2\sigma}{dQ^2 d\nu} = \frac{4\pi\alpha^2}{Q^4} \cdot \frac{E'}{EM} \left( W_2(\nu, Q^2) \cos^2 \frac{\theta}{2} + 2W_1(\nu, Q^2) \sin^2 \frac{\theta}{2} \right). \quad (10)$$

Without the term in the brackets, Equation 10 resembles the Rutherford scattering formula for scattering on a point-like target particle ( $d\sigma/dQ^2 = 4\pi\alpha^2/Q^4$ ). The term in the brackets arises because the nucleon has a structure. The functions  $W_1$  and  $W_2$  are called structure functions. Two such functions are required to describe the process, because there are two possible polarization states (longitudinal and transverse) of the virtual photon.

In the Bjorken limit, in which  $Q^2$  and  $\nu$  are approaching  $\infty$ , while  $Q^2/\nu$  is kept fixed, the two quantities  $W_1$  and  $W_2$  become functions only of the Bjorken- $x$  variable (see Equation 9), that is

$$\begin{aligned} W_1(\nu, Q^2) &\longrightarrow F_1(x) \\ \frac{\nu W_2(\nu, Q^2)}{M} &\longrightarrow F_2(x). \end{aligned} \quad (11)$$

Or in other words, as Bjorken suggested, if the lepton-parton scattering is point-like, then the structure functions cannot depend on  $Q^2$  and are purely functions of  $x$ . This concept is called scale invariance. Scale invariance is valid in the  $Q^2$  range of several  $\text{GeV}^2$  and more.

Let us consider a target nucleon of mass  $M$  and of 4-momentum  $P$  in a frame approaching the infinite-momentum frame. In this frame the nucleon can be considered as consisting of a parallel stream (the transverse momentum of any parton is negligible) of asymptotically free, point-like partons with 4-momenta  $xP$  ( $0 < x < 1$ ). Thus the incoming lepton “sees” and scatters from the partons, which are non-interacting with each other during the time the virtual photon is exchanged. This nucleon structure model is called the parton model of Feynman, and the diagram of this model is shown in Figure 3. Since the originally called partons

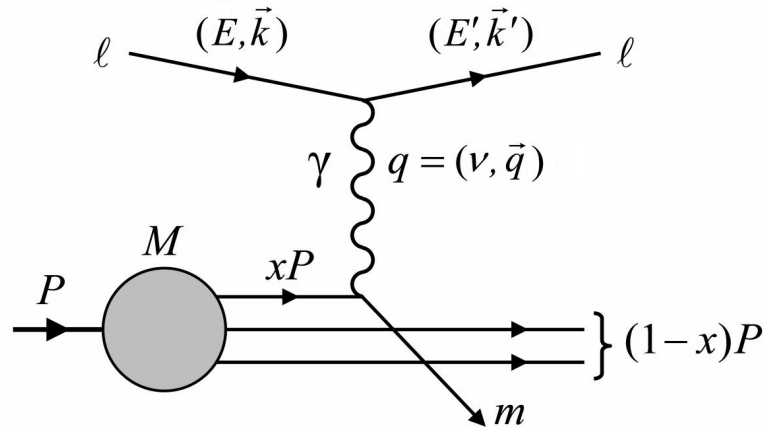


Figure 3: Deep Inelastic lepton-nucleon Scattering in the parton model

later were identified with the quarks, this model is also called Quark-Parton Model.

Suppose that one parton of mass  $m$  is scattered elastically by absorbing the

4-momentum  $q$  from the scattered lepton (see Figure 3):

$$(xP + q)^2 = m^2. \quad (12)$$

Taking that  $|x^2P^2| = x^2M^2 \ll |q^2|$ , and neglecting parton mass  $m$ , it follows from Equation 12 that

$$x = \frac{-q^2}{2P \cdot q} = \frac{Q^2}{2P \cdot q}, \quad (13)$$

where we used  $Q^2 \equiv -q^2$ . In the laboratory frame, where the nucleon is at rest, it is easy to show that  $P \cdot q = M\nu$ . Thus, from Equation 13 one gets Equation 9 for the Bjorken- $x$  variable. Hence the Bjorken- $x$  represents the fraction of a nucleon momentum carried by the parton, and functions  $F_1(x)$  and  $F_2(x)$  give a measure of the fractional momentum distribution of the partons, weighted by the squares of their charges. Furthermore, for a parton, one gets  $Q^2 = 2m\nu$  because of elastic scattering. Thus  $x = Q^2/2M\nu = m/M$ , so  $x$  in principle can be also interpreted as the fractional mass of the nucleon carried by the parton in the laboratory system, and functions  $F_1(x)$  and  $F_2(x)$  give a measure of the effective mass distribution of the parton constituents. Though, it is important to note, that this simple parton model is only valid in the approach, when an energy-momentum transfer from the lepton to the nucleon is very large.

In the parton-model framework, the spin-independent structure function  $F_2(x)$  is given by

$$F_2(x) = \sum_i e_i^2 x q_i(x), \quad (14)$$

where  $i$  is a parton type (quark and anti-quark flavors:  $i = u, \bar{u}, d, \bar{d}, s, \bar{s}, \dots$ ), and

$e_i$  is the charge of a parton  $i$ . The parton densities,  $q_i(x)$ , give the probability for finding a parton of type  $i$  in the nucleon, which carries fraction  $x$  of the momentum of the nucleon. The expression for  $F_1(x)$  is subject to the spin of the partons. It is  $F_1(x) = 0$  for partons with spin=0 and  $2xF_1(x) = F_2(x)$  for partons with spin= $\frac{1}{2}$ . For the quarks (spin= $\frac{1}{2}$ ), the second choice is valid, hence from Equation 14 it follows that

$$F_1(x) = \frac{1}{2} \sum_i e_i^2 q_i(x). \quad (15)$$

If the lepton beams and target nucleons are polarized, i.e., they have certain spin orientation, the spin structure of the nucleon becomes accessible in the DIS experiments. The polarized DIS differential cross-section for polarized charged-lepton scattering from a polarized nucleon in terms of  $\nu$  and  $Q^2$  is expressed as [8]

$$\frac{d^2\sigma^{\uparrow\downarrow}}{dQ^2 d\nu} - \frac{d^2\sigma^{\uparrow\uparrow}}{dQ^2 d\nu} = \frac{4\pi\alpha^2}{Q^2} \cdot \frac{1}{E^2} [M(E + E' \cos \theta)G_1(\nu, Q^2) - Q^2 G_2(\nu, Q^2)], \quad (16)$$

where  $\sigma^{\uparrow\uparrow}$  and  $\sigma^{\uparrow\downarrow}$  are the cross-sections for the lepton and nucleon spins being parallel and antiparallel and  $G_1$  and  $G_2$  are the spin-dependent structure functions, which carry the information on the nucleon spin structure. All other kinematic variables are defined as in Figure 2. Of course, adding the cross-section terms  $d^2\sigma^{\uparrow\downarrow}/dQ^2 d\nu$  and  $d^2\sigma^{\uparrow\uparrow}/dQ^2 d\nu$  of Equation 16 gives the unpolarized DIS differential cross-section  $d^2\sigma/dQ^2 d\nu$  as the function of the spin-independent structure functions  $W_1$  and  $W_2$  from Equation 10.

In the Bjorken limit, similar to the unpolarized case (see Equation 11), the spin-

dependent structure functions,  $G_1$  and  $G_2$ , become functions only of the Bjorken- $x$ :

$$\begin{aligned} M^2\nu G_1(\nu, Q^2) &\longrightarrow g_1(x) \\ M\nu^2 G_2(\nu, Q^2) &\longrightarrow g_2(x). \end{aligned} \tag{17}$$

The functions  $g_1(x)$  and  $g_2(x)$  can be expressed in terms of polarized parton densities. If we define  $q_i^+(x)$  ( $q_i^-(x)$ ) as the probability of finding a parton of type  $i$  in a nucleon of given helicity, which carries a fraction  $x$  of the nucleon momentum and has the same (opposite) helicity as the parent nucleon, then the function  $g_1(x)$  is given by

$$g_1(x) = \frac{1}{2} \sum_i e_i^2 [q_i^+(x) - q_i^-(x)] = \frac{1}{2} \sum_i e_i^2 \Delta q_i(x), \tag{18}$$

where again  $i$  is a parton type,  $i = u, \bar{u}, d, \bar{d}, s, \bar{s}, \dots$ , and  $e_i$  is the charge of a parton  $i$ . Of course, as one can expect:  $q_i(x) = q_i^+(x) + q_i^-(x)$ .

Experimentally, the spin-dependent structure function  $g_1(x)$  can be extracted by measuring asymmetries of the scattering cross-section in the polarized DIS experiments. In the case of longitudinally polarized lepton beams and longitudinally polarized target nucleons, the experimental longitudinal lepton-nucleon asymmetry is defined as

$$A = \frac{d\sigma^{\uparrow\downarrow} - d\sigma^{\uparrow\uparrow}}{d\sigma^{\uparrow\downarrow} + d\sigma^{\uparrow\uparrow}}, \tag{19}$$

where  $\sigma^{\uparrow\uparrow}$  and  $\sigma^{\uparrow\downarrow}$  are the cross-sections for the scattering processes, when the lepton and nucleon spins aligned and antialigned. The measured lepton-nucleon asymmetry  $A$  is related to the virtual photon asymmetry  $A_1$  [6], assuming perfect

beam and target polarizations, by

$$A \approx DA_1. \quad (20)$$

The depolarization factor,  $D$ , is approximately equal to  $\nu/E$  ( $\nu$  is the energy of the virtual photon and  $E$  is the initial lepton energy). The virtual photon asymmetry  $A_1$  is given by

$$A_1 = \frac{\sigma_{1/2} - \sigma_{3/2}}{\sigma_{1/2} + \sigma_{3/2}}, \quad (21)$$

where  $\sigma_{1/2}$  and  $\sigma_{3/2}$  are the photoabsorption cross-sections with the total photon-nucleon angular momentum  $J_z = \frac{1}{2}$  and  $J_z = \frac{3}{2}$ , respectively.

The photoabsorption process can be understood in the Breit framework. The Breit frame is defined as the infinite momentum frame in which a quark reverses its momentum by absorbing a photon. In the Breit frame, the quark can only absorb the virtual photon when the total angular momentum of the photon-quark pair is  $J_z = \pm\frac{1}{2}$ , that is, when the quark's spin is anti-parallel to the virtual photon's spin. The quark does not absorb the photon in the  $J_z = \pm\frac{3}{2}$  photon-quark state, when the quark's spin is parallel to the virtual photon's spin, because of the conservation of angular momentum. The photoabsorption process is illustrated in Figure 4. The quarks participating in the photoabsorption process are shown by dashed arrows; solid arrows indicate quarks not participating in the photoabsorption process. In the upper case of the total photon-nucleon angular momentum  $J_z = \frac{3}{2}$ , the virtual photon is only absorbed by the quarks with the spin antialigned with the spin of the nucleon, thus  $\sigma_{3/2} \propto \sum_i e_i^2 q_i^-(x)$ . In the lower case of the total photon-nucleon

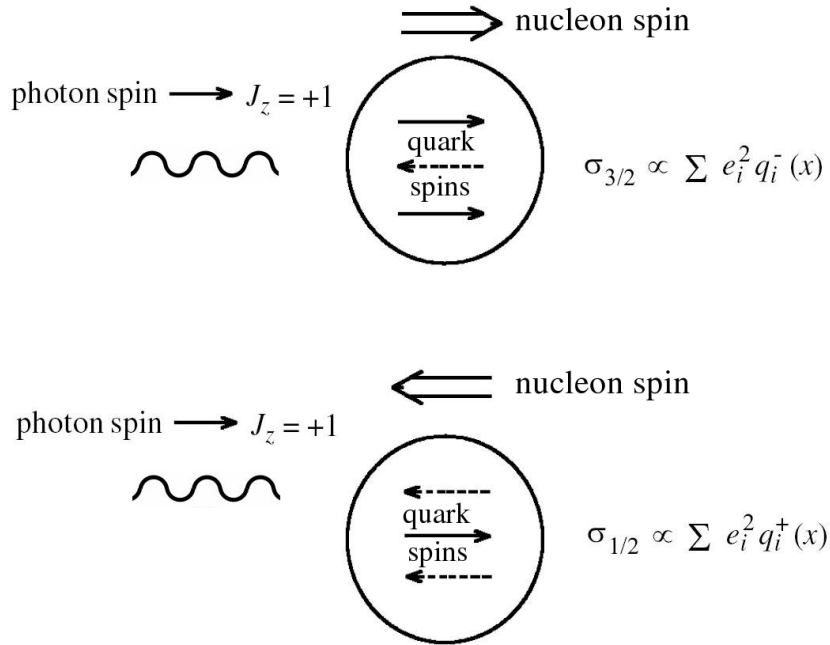


Figure 4: Drawing explaining the process of the absorption of the virtual-photon by quarks with the spin aligned or antialigned with the parent nucleon spin [9]

angular momentum  $J_z = \frac{1}{2}$ , the virtual photon is only absorbed by the quarks with the spin aligned with the spin of the nucleon, thus  $\sigma_{1/2} \propto \sum_i e_i^2 q_i^+(x)$ .

Hence Equation 21 turns into

$$A_1 = \frac{\sigma_{1/2} - \sigma_{3/2}}{\sigma_{1/2} + \sigma_{3/2}} = \frac{\sum_i e_i^2 q_i^+(x) - \sum_i e_i^2 q_i^-(x)}{\sum_i e_i^2 q_i^+(x) + \sum_i e_i^2 q_i^-(x)} = \frac{\sum_i e_i^2 \Delta q_i(x)}{\sum_i e_i^2 q_i(x)} = \frac{g_1(x)}{F_1(x)}, \quad (22)$$

where Equations 15 and 18 have been used. The spin-independent structure function  $F_1(x)$  is measured in unpolarized DIS experiments. Thus, measuring asymmetries in the polarized DIS experiments, one obtains the spin-dependent structure function  $g_1(x)$  from Equation 22.

There are several important relations for the integrals of the spin-dependent structure functions over  $x$  called sum rules. They are obtained within the Quark-Parton Model and have been tested experimentally. These sum rules relate integrals

over the measured spin-dependent structure functions  $g_1(x)$  to the neutron and hyperon  $\beta$ -decay measurements. One of them, the most fundamental, is the Bjorken sum rule [10, 11],

$$\int_0^1 g_1^p(x)dx - \int_0^1 g_1^n(x)dx = \frac{1}{6} \left| \frac{g_A}{g_V} \right|, \quad (23)$$

where  $g_A/g_V$  is the ratio of the axial-vector and vector weak coupling constants measured in the neutron  $\beta$ -decay. The spin-dependent structure functions  $g_1^p(x)$  and  $g_1^n(x)$  correspond to the proton and neutron, respectively. The value of the Bjorken sum rule integral determined without QCD radiative corrections [9] is  $0.211 \pm 0.001$ . Separate sum rules for the proton and the neutron were derived by Ellis and Jaffe, assuming that the strange quark polarization is zero ( $\Delta s + \Delta \bar{s} = 0$ ), [12, 13]:

$$\int_0^1 g_1^p(x)dx = \frac{1}{12} \left( \frac{g_A}{g_V} \right) \left[ 1 + \frac{5}{3} \cdot \frac{3F/D - 1}{F/D + 1} \right] = 0.186 \pm 0.004, \quad (24)$$

$$\int_0^1 g_1^n(x)dx = \frac{1}{12} \left( \frac{g_A}{g_V} \right) \left[ -1 + \frac{5}{3} \cdot \frac{3F/D - 1}{F/D + 1} \right] = -0.025 \pm 0.004, \quad (25)$$

where F and D are the symmetric and antisymmetric couplings obtained from the hyperon  $\beta$ -decays:  $\Lambda \rightarrow pe^- \bar{\nu}_e$  and  $\Sigma^- \rightarrow ne^- \bar{\nu}_e$ ;  $F + D = g_A/g_V$ .

The leading-order Quark-Parton Model result for the integral of the spin-dependent structure function  $g_1(x)$  (see Equation 18) is

$$\int_0^1 g_1(x)dx = \frac{1}{2} \int_0^1 \sum_i e_i^2 \Delta q_i(x) dx, \quad (26)$$

where  $i$  is for three active quark flavors,  $i = u, \bar{u}, d, \bar{d}, s, \bar{s}$ . Hence, the integrals of

$g_1^p(x)$  and  $g_1^n(x)$  are functions of  $\Delta\mathcal{U}$ ,  $\Delta\mathcal{D}$ , and  $\Delta\mathcal{S}$  (quarks and antiquarks added):

$$\Delta\mathcal{Q} = \int_0^1 [(q^+(x) - q^-(x)) + (\bar{q}^+(x) - \bar{q}^-(x))] dx \quad (27)$$

for the flavors  $u$ ,  $d$  and  $s$ . Thus, one can use the Ellis-Jaffe sum rules (or either of the two in combination with the Bjorken sum rule) to extract  $\Delta\mathcal{U}$  and  $\Delta\mathcal{D}$  separately.

$\Delta\mathcal{S}$  then can be extracted from the violation of the Ellis-Jaffe sum rule,

$$\int_0^1 g_1^p(x) dx = \frac{1}{12} \left( \frac{g_A}{g_V} \right) \left[ 1 + \frac{5}{3} \cdot \frac{3F/D - 1}{F/D + 1} \right] + \frac{1}{3} \Delta\mathcal{S}, \quad (28)$$

$$\int_0^1 g_1^n(x) dx = \frac{1}{12} \left( \frac{g_A}{g_V} \right) \left[ -1 + \frac{5}{3} \cdot \frac{3F/D - 1}{F/D + 1} \right] + \frac{1}{3} \Delta\mathcal{S}. \quad (29)$$

Hence, one can evaluate the total fraction of the spin of the proton carried by the quarks

$$\Delta\Sigma = \Delta\mathcal{U} + \Delta\mathcal{D} + \Delta\mathcal{S}. \quad (30)$$

It has been discovered in the polarized DIS experiments that  $\frac{1}{2}\Delta\Sigma \neq \frac{1}{2}$ . It was first demonstrated in the European Muon Collaboration (EMC) experiment [14, 15] that only a fraction of the proton spin was carried by the quarks. Other experiments at the Stanford Linear Accelerator Center (SLAC), as well as HERMES (HERa MEasurement of Spin) and SMC (Spin Muon Collaboration) experiments [16, 17, 18, 19, 20, 21, 22] have confirmed the EMC measurements and discovery. On average only about 30% of the proton spin is originated from the quarks and antiquarks in the proton. This is much smaller fraction than it was expected from the static Quark Model of the proton. Thus, the DIS data demonstrate that there is a deficit between the spin carried by the quarks and antiquarks and the spin of the proton. This phenomenon was called the “spin deficit” (or the “spin crisis”).

The spin deficit can be carried by the gluons and orbital angular momentum of the proton constituents. In the polarized DIS experiments, it is difficult to access the polarized gluon distribution experimentally, because gluons do not couple to photons at the leading order. Next-to-Leading-Order (NLO) QCD studies of the  $Q^2$  dependence of the function  $g_1(x, Q^2)$  based on the data from the inclusive DIS experiments allowed first estimations of the gluon spin contribution  $\Delta G$  to the proton spin though with very large uncertainties [6]. The extracted NLO QCD values for  $\Delta G$  are typically positive but the corresponding uncertainties are often 50–100% of the value. A DIS experiment, HERMES, is capable to study the semi-inclusive scattering process  $\vec{e}(\vec{\gamma})\vec{p} \rightarrow h^+h^-X$  with  $h = \pi, K$ , which in principle can be used to access  $\Delta G$ . Figure 5 shows the longitudinal spin asymmetry, reported by the HERMES collaboration [23], for the photoproduction of pairs of hadrons with relatively high transverse momentum,  $p_T$ . A cut of  $p_T^{h_1} > 1.5$  GeV/ $c$  was imposed on the  $p_T$  of one of the hadron pair participants. The average  $Q^2$  of the measurements is  $0.06$  (GeV/ $c$ )<sup>2</sup>. A gluon polarization has been evaluated based on the measured asymmetry from Figure 5 and is shown in Figure 6. The extracted gluon polarization is  $\langle \Delta G/G \rangle = 0.41 \pm 0.18 \pm 0.03$  at a moderate  $x_G$  ( $\langle x_G \rangle = 0.17$ ). The sensitivity of the measured asymmetry to the polarized gluon distribution is also shown in Figures 5 and 6. Because of low transverse momenta involved in the process investigated by HERMES, it is difficult to interpret the data in terms of a hard-scattering concept. Thus, the measurement of  $\Delta G$  remains one of the most exciting tasks for high-energy experiments with polarized proton-proton collisions.

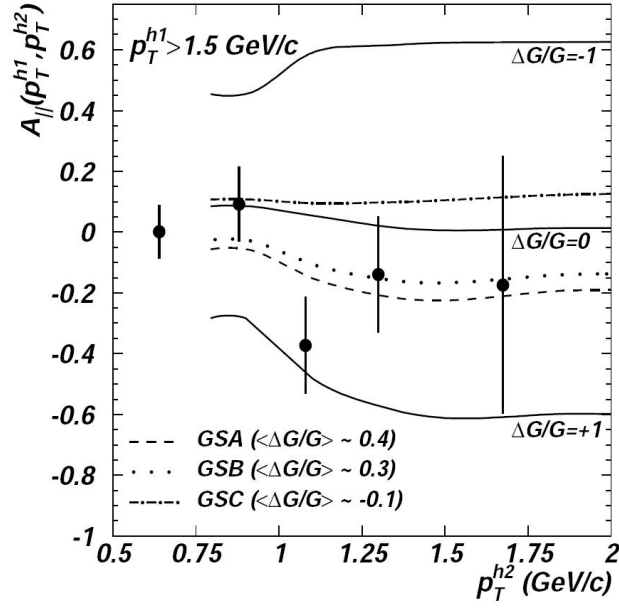


Figure 5: HERMES double-helicity asymmetry versus transverse momentum of one of the hadron pair participant [6]

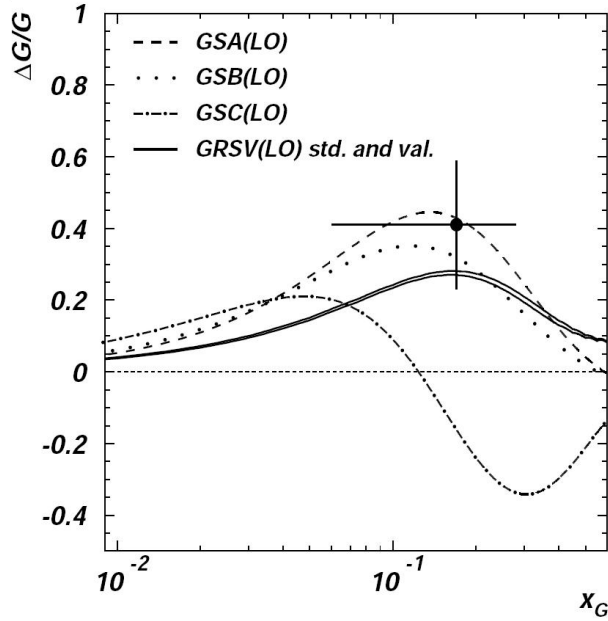


Figure 6: Gluon polarization extracted from HERMES semi-inclusive data [6]

### 2.3 Kinematics of a Proton-Proton Collision

Consider the collision of two protons of energy  $E$  each, with incident 4-momenta  $P_1$  and  $P_2$  (Figure 7). Within the parton-model framework, this collision can be

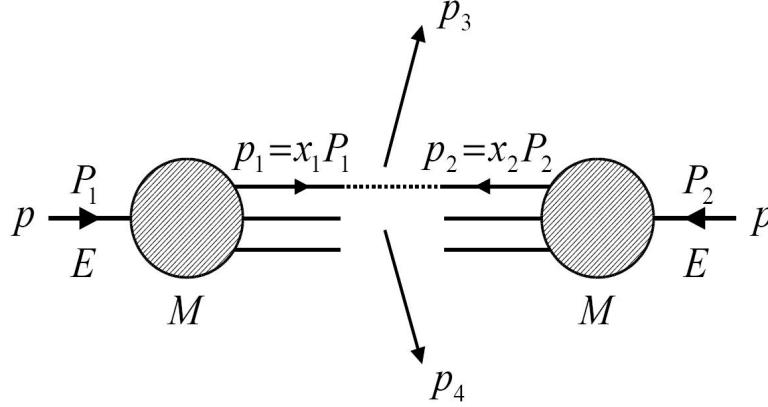


Figure 7: Kinematics of a  $p - p$  collision

considered as a collision of the partons comprising the protons. Let  $p_1$  and  $p_2$  be the 4-momenta of two colliding partons (one from each proton) in the initial state before the collision. Each parton carries the fraction of the parent proton momentum  $x_1$  and  $x_2$ , thus  $p_1 = x_1P_1$  and  $p_2 = x_2P_2$ . The 4-momentum transfer in the parton collision is  $q = p_3 - p_1 = p_2 - p_4$ , where  $p_3$  and  $p_4$  are the 4-momenta of two partons in the final state. If one observes and measures the final state  $p_3$  and  $p_4$ , the parton kinematics of the hard scattering can be reconstructed, and one can determine the unknown parton momentum fractions  $x_1, x_2$ .

The invariant mass of the colliding partons,  $m_{p_1p_2}$ , is

$$m_{p_1p_2}^2 = (p_1 + p_2)^2 = 2P_1P_2x_1x_2 + x_1^2M^2 + x_2^2M^2, \quad (31)$$

where  $M$  is the proton mass. The square of the total center-of-mass system (CMS)

energy for the proton-proton pair is  $E^{*2} \equiv s$ ,

$$s = (P_1 + P_2)^2 = 2P_1P_2 + M^2 + M^2. \quad (32)$$

If  $s \gg M^2$  and  $m_{p_1p_2}^2 \gg x^2M^2$ , Equations 31 and 32 become  $m_{p_1p_2}^2 \approx 2P_1P_2x_1x_2$  and  $s \approx 2P_1P_2$ . Hence, it follows that

$$m_{p_1p_2}^2 = x_1x_2s. \quad (33)$$

One can define a variable  $\tau$  as a ratio of the square of the invariant mass of the colliding partons and the square of the total CMS energy for the proton-proton pair,

$$\tau \equiv \frac{m_{p_1p_2}^2}{s} = x_1x_2. \quad (34)$$

Neglecting all particle masses, from energy-momentum conservation it follows

$$(p_3 + p_4)^2 = (x_1P_1 + x_2P_2)^2 \approx 4x_1x_2E^2, \quad (35)$$

and

$$\tau \equiv x_1x_2 = \frac{(p_3 + p_4)^2}{4E^2}. \quad (36)$$

Momentum conservation along the beam direction ( $z$ -axis) gives

$$x_1 - x_2 = \frac{(p_{3z} + p_{4z})}{E}. \quad (37)$$

Let us define

$$x_F \equiv x_1 - x_2, \quad (38)$$

where  $x_F$  is Feynman  $x$ . The two-equation system,

$$\begin{aligned} x_1 - x_2 &= x_F \\ x_1x_2 &= \tau, \end{aligned} \quad (39)$$

has solutions

$$x_1^{(1,2)} = \frac{1}{2}(x_F \pm \sqrt{x_F^2 + 4\tau}), \quad (40)$$

$$x_2^{(1,2)} = \frac{1}{2}(-x_F \pm \sqrt{x_F^2 + 4\tau}), \quad (41)$$

where

$$x_F = \frac{(p_{3z} + p_{4z})}{E}, \quad (42)$$

$$\tau = \frac{(p_3 + p_4)^2}{4E^2}. \quad (43)$$

Thus, one can reconstruct  $x_1$  and  $x_2$ . And one can obtain  $x_1$  and  $x_2$  in terms of the known kinematic quantities  $E$ ,  $p_3$ , and  $p_4$ .

## 2.4 Spin-Dependent Parton Densities and Cross Sections in Polarized Proton-Proton Collisions

At RHIC, polarized protons are collided at center-of-mass energies of  $\sqrt{s} = 200\text{-}500$  GeV. One mainly considers relatively rare inelastic events with a final state produced at very large transverse momentum,  $p_T$ , of a few GeV or more. The production of the large- $p_T$  particle in the final state means that the particle itself or particle's parents are produced in underlying short-distance hard-scattering processes. The hard-scattering processes are governed by the strong interaction and can be described by perturbative Quantum Chromodynamics (pQCD). A parton model along with pQCD is a key concept which one can use to describe much of the spin physics.

Figure 8 shows the production of a hadron with large  $p_T$  in a collision of unpolarized protons:  $pp \rightarrow hX$ . The QCD factorization theorem states that the cross

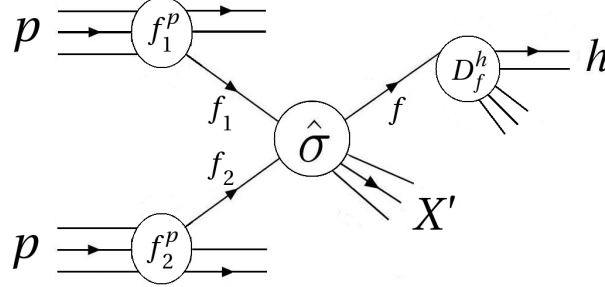


Figure 8: Production of a hadron with large  $p_T$  in a  $p - p$  collision

section of this process can be represented as the product of separate long-distance and short-distance parts. In perturbative QCD, the factorized cross section of the process can be written as [24]

$$\begin{aligned} \frac{d\sigma^{pp \rightarrow hX}}{d\mathcal{P}} &= \sum_{f_1, f_2, f} \int dx_1 dx_2 dz f_1^p(x_1, \mu^2) f_2^p(x_2, \mu^2) \\ &\times \frac{d\hat{\sigma}^{f_1 f_2 \rightarrow f X'}}{d\mathcal{P}}(x_1 p_1, x_2 p_2, p_h/z, \mu) D_f^h(z, \mu^2), \end{aligned} \quad (44)$$

where the sum is over all contributing partonic channels  $f_1 f_2 \rightarrow f X'$ ,  $p_1$  and  $p_2$  are the momenta of the incoming protons, and  $\mathcal{P}$  stands for any appropriate set of the kinematic variables of the process. The long-distance part is represented by the parton distribution functions. The parton distribution function, or the parton density,  $f_i^p(x, \mu^2)$  is the probability density for finding a parton of type  $f_i$  in the proton, carrying fraction  $x$  of the momentum of the proton. The parton-to-hadron fragmentation function  $D_f^h(z, \mu^2)$  is the probability density for finding a hadron  $h$  with momentum fraction  $z$  produced in the fragmentation of parton  $f$ . The  $\hat{\sigma}^{f_1 f_2 \rightarrow f X'}$

are the hard-scattering cross sections of the partonic subprocesses in which initial partons  $f_1$  and  $f_2$  produce a final-state parton  $f$  and unobserved  $X'$ . These partonic subprocess cross-sections  $\hat{\sigma}^{f_1 f_2 \rightarrow f X'}$  give the short-distance information describing the hard interactions; they are computable in pQCD as perturbation series in the strong coupling constant  $\alpha_s$ .  $\mu$  is the unphysical mass scale, or the factorization scale, arising in calculations of the higher-order corrections for the  $\hat{\sigma}^{f_1 f_2 \rightarrow f X'}$ . The parton distribution function  $f_i^p(x, \mu^2)$  and the fragmentation function  $D_f^h(z, \mu^2)$  represent internal universal characteristics of the proton and of the hadronization mechanism, respectively. They are not calculable in QCD at present, but they have universality: once extracted from the data in one process, they can be exploited to make certain predictions for other hard processes. Therefore, the idea is to extract the universal, that is, the same in all reactions, parton distribution functions from experimental data, using precise theoretical calculations of the short-distance partonic subprocess cross sections.

From now on, let us consider a hard  $p - p$  collision with incident protons having certain spin orientation. Figure 8 can still be used to depict this collision, keeping in mind that the incoming protons, and hence all process participants, are polarized. In this case, one can anticipate extracting information about spin distributions of the proton constituents, quarks and gluons, in a polarized proton. That is, one can expect to obtain spin-dependent (or “polarized”) parton distribution functions, also known as polarized parton densities. Longitudinally polarized (“helicity-weighted”) parton densities are denoted as  $\Delta f(x, \mu^2)$ , and transversely

polarized parton densities are denoted as  $\delta f(x, \mu^2)$ . Longitudinally polarized parton distribution functions give information on the probability of finding a particular parton type ( $f = u, \bar{u}, d, \bar{d}, \dots, g$ ) with positive helicity in a nucleon of positive helicity, minus the probability for finding it with negative helicity. Accordingly, transversely polarized parton distribution functions are the differences of the distribution functions of quarks (or antiquarks) with transverse spin aligned and anti-aligned with the transverse (relative to the proton momentum) proton spin. Note that no corresponding transversely polarized distribution function exists for the massless gluons.

Table 1 shows the possible parton distribution functions containing spin information [25, 26]. In this table, labels  $+, -$  stand for helicities (longitudinal polariza-

Table 1: Quark and gluon parton densities containing spin information

Polarization	Quarks	Antiquarks	Gluons
Unpolarized	$q \equiv q_+^+ + q_+^- \equiv q_\uparrow^\uparrow + q_\uparrow^\downarrow$	$\bar{q} \equiv \bar{q}_+^+ + \bar{q}_+^- \equiv \bar{q}_\uparrow^\uparrow + \bar{q}_\uparrow^\downarrow$	$g \equiv g_+^+ + g_+^-$
Longitudinal	$\Delta q = q_+^+ - q_+^-$	$\Delta \bar{q} = \bar{q}_+^+ - \bar{q}_+^-$	$\Delta g = g_+^+ - g_+^-$
Transverse	$\delta q = q_\uparrow^\uparrow - q_\uparrow^\downarrow$	$\delta \bar{q} = \bar{q}_\uparrow^\uparrow - \bar{q}_\uparrow^\downarrow$	—

tions), labels  $\uparrow, \downarrow$  stand for transverse polarizations, superscripts relate to partons, and subscripts relate to the parent hadron. For brevity, the argument  $(x, \mu^2)$  of the parton densities has been omitted. A table with the similar structure can be composed for polarized fragmentation functions  $D_f^h$  [27], because information about

the polarization of the observed final-state hadron can be used to obtain knowledge of the polarization of the parton fragmenting into this hadron.

The spin asymmetries measured in the deep-inelastic scattering of longitudinally polarized leptons from longitudinally polarized nucleons gave the first information about longitudinally polarized distribution functions of the nucleon. DIS is sensitive only to the quark and antiquark polarized densities ( $\Delta q$  and  $\Delta\bar{q}$ ) for each flavor. Furthermore, charged-lepton DIS is not capable of giving information separately for quark and antiquark polarized densities, measuring only the sums  $\Delta\mathcal{Q}(x, Q^2) \equiv \Delta q(x, Q^2) + \Delta\bar{q}(x, Q^2)$  for each flavor. High-energy experiments with polarized nucleon collisions complement the knowledge obtained from the DIS experiments. The polarized nucleon collision experiments can measure quark and antiquark polarized densities separately to achieve a full flavor separation of the polarized sea, can measure gluon polarization  $\Delta g$ , as well as provide an opportunity to extract transversely polarized parton densities  $\delta q$  and  $\delta\bar{q}$ .

By definition the amount of the spin of the proton carried by the parton of the type  $f$  is given by the integrals of the distribution functions  $\Delta f(x, \mu^2)$ , shown in Table 1, over all Bjorken- $x$ , multiplied by the spin of the parton  $f$ . Thus, the gluon polarization in the proton is

$$\Delta G = \int_0^1 dx \Delta g(x, \mu^2), \quad (45)$$

and the proton-spin sum rule becomes

$$\frac{1}{2} = \int_0^1 dx \left[ \frac{1}{2} \sum_q (\Delta q(x, \mu^2) + \Delta\bar{q}(x, \mu^2)) + \Delta g(x, \mu^2) \right] + L(\mu^2), \quad (46)$$

where  $L$  is the orbital angular momentum of quarks and gluons in the proton [28, 29, 30].

The cross section for longitudinally polarized  $p - p$  collisions can be factorized as well. Taking into account all possible longitudinal polarizations of the incident protons, the cross section can be written as [31]

$$\begin{aligned} \frac{d\Delta\sigma^{pp\rightarrow hX}}{d\mathcal{P}} &\equiv \frac{1}{4} \left[ \frac{d\sigma_{++}^{pp\rightarrow hX}}{d\mathcal{P}} + \frac{d\sigma_{--}^{pp\rightarrow hX}}{d\mathcal{P}} - \frac{d\sigma_{+-}^{pp\rightarrow hX}}{d\mathcal{P}} - \frac{d\sigma_{-+}^{pp\rightarrow hX}}{d\mathcal{P}} \right] \\ &= \sum_{f_1, f_2, f} \int dx_1 dx_2 dz \Delta f_1^p(x_1, \mu^2) \Delta f_2^p(x_2, \mu^2) \\ &\quad \times \frac{d\Delta\hat{\sigma}^{f_1 f_2 \rightarrow f X'}}{d\mathcal{P}}(x_1, p_1, x_2, p_2, p_h/z, \mu) D_f^h(z, \mu^2), \end{aligned} \quad (47)$$

where

$$\frac{d\Delta\hat{\sigma}^{f_1 f_2 \rightarrow f X'}}{d\mathcal{P}} \equiv \frac{1}{4} \left[ \frac{d\hat{\sigma}_{++}^{f_1 f_2 \rightarrow f X'}}{d\mathcal{P}} + \frac{d\hat{\sigma}_{--}^{f_1 f_2 \rightarrow f X'}}{d\mathcal{P}} - \frac{d\hat{\sigma}_{+-}^{f_1 f_2 \rightarrow f X'}}{d\mathcal{P}} - \frac{d\hat{\sigma}_{-+}^{f_1 f_2 \rightarrow f X'}}{d\mathcal{P}} \right]. \quad (48)$$

Subscripts in Equation 47 stand for the helicities of the incident protons, and subscripts in Equation 48 stand for the helicities of the incident partons  $f_1$  and  $f_2$ . The “longitudinally polarized” partonic subprocess cross sections  $\Delta\hat{\sigma}^{f_1 f_2 \rightarrow f X'}$  are calculable in pQCD since they are characterized by large momentum transfer. Thus, by measuring the “longitudinally polarized” cross section  $d\Delta\sigma^{pp\rightarrow hX}/d\mathcal{P}$  one can extract the longitudinally polarized parton density  $\Delta f(x, \mu^2)$ , for example  $\Delta g$ .

Note that adding all cross section terms for all possible longitudinal polarization combinations in the first line of Equation 47 gives the unpolarized cross section of Equation 44

$$\frac{d\sigma^{pp\rightarrow hX}}{d\mathcal{P}} \equiv \frac{1}{4} \left[ \frac{d\sigma_{++}^{pp\rightarrow hX}}{d\mathcal{P}} + \frac{d\sigma_{--}^{pp\rightarrow hX}}{d\mathcal{P}} + \frac{d\sigma_{+-}^{pp\rightarrow hX}}{d\mathcal{P}} + \frac{d\sigma_{-+}^{pp\rightarrow hX}}{d\mathcal{P}} \right], \quad (49)$$

with the unpolarized parton densities  $f(x, \mu^2)$  and the unpolarized partonic subprocess cross sections

$$\frac{d\hat{\sigma}_{f_1 f_2 \rightarrow f X'}}{d\mathcal{P}} \equiv \frac{1}{4} \left[ \frac{d\hat{\sigma}_{++}}{d\mathcal{P}} + \frac{d\hat{\sigma}_{--}}{d\mathcal{P}} + \frac{d\hat{\sigma}_{+-}}{d\mathcal{P}} + \frac{d\hat{\sigma}_{-+}}{d\mathcal{P}} \right]. \quad (50)$$

If only one of the incoming protons on Figure 8 is polarized, a single-spin cross section can be defined for this process as  $d\sigma_-^{pp \rightarrow hX} / d\mathcal{P} - d\sigma_+^{pp \rightarrow hX} / d\mathcal{P}$ , although the combination  $d\sigma_-^{pp \rightarrow hX} / d\mathcal{P} - d\sigma_+^{pp \rightarrow hX} / d\mathcal{P}$  can be nonzero only if parity is violated in the hard process [31]. If the latter is in effect, then this cross section will depend on parton densities  $\Delta f_1(x_1, \mu^2)$  and  $f_2(x_2, \mu^2)$ , corresponding to the polarized proton and the unpolarized proton, accordingly.

For transversely polarized incident protons one should change in Equations 47 and 48 labels  $+, -$  for helicities (longitudinal polarizations) to labels  $\uparrow, \downarrow$  for transverse polarizations. This gives the “transversely polarized” cross section, which depends on “transversely polarized” partonic subprocess cross sections and transversely polarized parton densities  $\delta f(x, \mu^2)$ . For the transversely polarized case, the cross section also depends on  $\cos(2\phi)$ , where  $\phi$  is the azimuthal angle of the observed final-state particle [32, 33];  $\phi = 0$  is defined for the scattering in the plane, which is perpendicular to the proton polarization direction.

## 2.5 Asymmetries

The measured quantity in spin physics experiments is the spin asymmetry; it is easier to measure the spin asymmetry than the polarized cross section itself. The

spin asymmetry is the ratio of the polarized cross section over the unpolarized cross section. For the longitudinally polarized case of the  $p - p$  collision from Chapter 2.4, the spin asymmetry is given by

$$A_{LL}^h = \frac{d\Delta\sigma^{pp \rightarrow hX}/d\mathcal{P}}{d\sigma^{pp \rightarrow hX}/d\mathcal{P}}. \quad (51)$$

Subscripts of the spin asymmetry stand for the type of polarization of the incident particles: L for the longitudinal polarization, T for the transverse polarization.  $A_{LL}$  is referred to as double-longitudinal spin asymmetry, also known as double-helicity asymmetry, for two longitudinally polarized initial particles.

The general formula for the double-helicity asymmetry, as a result of Equations 51, 47, and 44, is [24]

$$A_{LL} = \frac{\sum_{f_1, f_2, f} \Delta f_1 \times \Delta f_2 \times \left[ d\hat{\sigma}^{f_1 f_2 \rightarrow fX'} \hat{a}_{LL}^{f_1 f_2 \rightarrow fX'} \right] \times D_f}{\sum_{f_1, f_2, f} f_1 \times f_2 \times \left[ d\hat{\sigma}^{f_1 f_2 \rightarrow fX'} \right] \times D_f}, \quad (52)$$

where  $\hat{a}_{LL}^{f_1 f_2 \rightarrow fX'} = d\Delta\hat{\sigma}^{f_1 f_2 \rightarrow fX'} / d\hat{\sigma}^{f_1 f_2 \rightarrow fX'}$  is the spin asymmetry for the partonic subprocess  $f_1 f_2 \rightarrow fX'$ , also known as the analyzing power of the corresponding reaction. The analyzing powers for different reactions [34] are calculable in pQCD and shown in Figure 9. When only one partonic subprocess is involved, as it follows from Equation 52, the double-helicity asymmetry is proportional to the polarization of the quarks or gluons that collide and to the analyzing power of the subprocess:

$$A_{LL}(x_1, x_2) = \frac{\Delta f_1(x_1)}{f_1(x_1)} \times \frac{\Delta f_2(x_2)}{f_2(x_2)} \times \hat{a}_{LL}^{f_1 f_2 \rightarrow fX'}. \quad (53)$$

$\Delta f_1(x_1)/f_1(x_1)$  is the polarization of quark or gluon 1, which carries the fraction  $x_1$  of the proton momentum, for a proton polarization of 100%.  $\Delta f_2(x_2)/f_2(x_2)$  represents the other colliding quark or gluon.

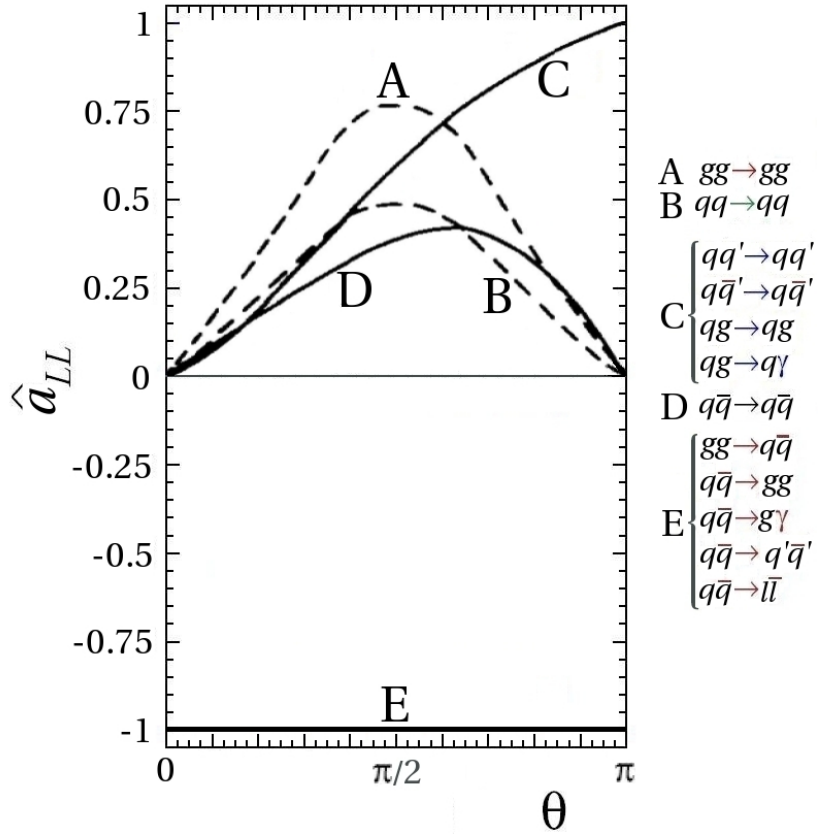


Figure 9: Longitudinal polarization analyzing powers for different partonic reactions vs. the partonic center-of-mass system scattering angle [34]

Thus, according to pQCD, as it follows from Equation 53, the double-helicity asymmetry,  $A_{LL}$ , is sensitive to the polarized gluon distribution in the nucleon,  $\Delta g(x)$ , if gluon-gluon processes dominate all other processes in a particular particle production. The corresponding analyzing power,  $\hat{a}_{LL}$ , for the gluon-gluon subprocess is given in Figure 9. Note that longitudinally polarized beams are required for the gluon polarization studies in the nucleon.

Experimentally, in a collider various asymmetries can be measured: for longitudinally polarized beams, for transversely polarized beams, with both beams polarized, and with only one beam polarized. At RHIC for both proton beams

longitudinally polarized we can measure the double-helicity asymmetry as

$$A_{LL} = \frac{\sigma_{++} + \sigma_{--} - \sigma_{+-} - \sigma_{-+}}{\sigma_{++} + \sigma_{--} + \sigma_{+-} + \sigma_{-+}}, \quad (54)$$

where  $\sigma_{++}$ ,  $\sigma_{--}$ ,  $\sigma_{+-}$  and  $\sigma_{-+}$  are the cross sections of a particular process for all four possible beam-helicity configurations. Since the cross section can be obtained by dividing the experimental yield,  $N$  (the observed number of events), by the integrated luminosity,  $L$  (defined in Chapter 5.2), for the corresponding type of crossing,  $A_{LL}$  can be expressed as

$$A_{LL} = \frac{1}{|\langle P_B P_Y \rangle|} \times \frac{\frac{N_{++}}{L_{++}} + \frac{N_{--}}{L_{--}} - \frac{N_{+-}}{L_{+-}} - \frac{N_{-+}}{L_{-+}}}{\frac{N_{++}}{L_{++}} + \frac{N_{--}}{L_{--}} + \frac{N_{+-}}{L_{+-}} + \frac{N_{-+}}{L_{-+}}}, \quad (55)$$

where  $P_B$  and  $P_Y$  are the polarizations of the RHIC “blue” and “yellow” beams (see Chapter 5.1). Since the proton beams are not purely polarized,  $A_{LL}$  is normalized by the beam polarizations. The beam polarization  $P_{beam}$  is defined as

$$P_{beam} = \frac{B_+ - B_-}{B_+ + B_-}, \quad (56)$$

where  $B_+(B_-)$  is the number of protons in the beam bunch with  $+( -)$  helicity. Thus, when one expects the beam polarization to be, for example, 70%, it means that  $P_{beam} = 0.7$ .

If only one of the colliding beams is polarized longitudinally, and the other beam is unpolarized (or when summing over both polarization states of the other beam), the single-spin (parity-violating) asymmetry can be defined as

$$A_L = \frac{\sigma_+ - \sigma_-}{\sigma_+ + \sigma_-}, \quad (57)$$

or

$$A_L = \frac{1}{P} \times \frac{\frac{N_+}{L_+} - \frac{N_-}{L_-}}{\frac{N_+}{L_+} + \frac{N_-}{L_-}}, \quad (58)$$

where  $N_+$  and  $N_-$  represent the experimental yields observed from polarized protons with positive helicity and negative helicity, respectively, normalized by the luminosity, and  $P$  is the polarization of the polarized beam. Similarly, transversely polarized spin asymmetries  $A_{TT}$  and  $A_N$  can be expressed for transversely polarized beam collisions by using labels  $\uparrow, \downarrow$  for transverse polarizations instead of labels  $+, -$  for helicities in the equations above for the longitudinal polarization.

## 2.6 Asymmetry Errors

The statistical error of the double-helicity asymmetry measurement is given by [24]

$$\Delta A_{LL} = \sqrt{\frac{1}{NP_1^2 P_2^2} - \frac{1}{N} A_{LL}^2}, \quad (59)$$

where  $N = N_{++} + N_{--} + N_{+-} + N_{-+}$  is the total measured yield for all four possible beam-helicity configurations. Here it is supposed that the statistical errors for the luminosity and the beam polarization measurements are negligible. The single-spin asymmetry error is

$$\Delta A_L = \sqrt{\frac{1}{NP^2} - \frac{1}{N} A_L^2}. \quad (60)$$

If the asymmetry is not large, it follows from Equations 59 and 60 that

$$\Delta A_{LL} = \pm \frac{1}{P_1 P_2 \sqrt{N}}, \text{ and } \Delta A_L = \pm \frac{1}{P \sqrt{N}}. \quad (61)$$

The measured raw asymmetry is the product of the beam polarizations, the quark/gluon polarizations, and the subprocess analyzing power. These raw asymmetries are typically small, and systematic errors of the measurements need to be controlled to reach the proposed sensitivities. The systematic errors, as well as the statistical errors, are discussed in more detail later in the analysis part of the dissertation.

## 2.7 Gluon Polarization Probes at RHIC

As it follows from the proton-spin sum rule (Equation 46), a significant gluon polarization,  $\Delta g$ , in the proton is one of the possible explanations of the spin deficit phenomenon revealed in the polarized DIS experiments, which measured the small quark and antiquark contribution to the proton spin. The inclusive DIS experiments with polarized lepton beams scattered from polarized nucleon targets constrained the gluon polarization within very large uncertainties [6]. In contrast to the DIS experiments, in longitudinally polarized proton-proton collisions at RHIC  $\Delta g$  can be measured to a high degree of accuracy and over an extended range of  $x$ . At RHIC,  $\Delta g$  is accessed directly, because at RHIC energies and luminosity the polarized proton-proton collisions can be simply considered as collisions of polarized gluons and quarks. The polarized gluons and quarks perform as strong interaction probes in the hard-scattering processes with large momentum transfer, which means that the scattering can be described in pQCD formalism. Therefore the measurement of the gluon polarization in the polarized protons at RHIC is one of the main

advantages of the RHIC spin program. In  $p-p$  collisions at RHIC,  $\Delta g$  can be probed with several independent channels involving elementary hard-scattering processes with gluons in the initial state [24]:

- 1) prompt-photon production,  $\vec{p}\vec{p} \rightarrow \gamma X$ ;
- 2) combination of Compton process and Drell-Yan production of lepton pair,  $\vec{p}\vec{p} \rightarrow \gamma^* q X \rightarrow l^- l^+ q X$ ;
- 3) jet and large- $p_T$  hadron production,  $\vec{p}\vec{p} \rightarrow jet(s) X, \pi X$ ;
- 4) heavy-flavor production,  $\vec{p}\vec{p} \rightarrow c\bar{c} X, b\bar{b} X$ .

All these key methods used to probe the gluon polarization in the proton are discussed below. The last one, heavy-flavor production, in particular open charm production, is the subject of this dissertation research. More details on this method are given in Chapter 4.

### 2.7.1 Prompt-Photon Production

For a long time, prompt-photon production has been used as the crucial instrument for determining the unpolarized gluon density, and nowadays it is used to access the polarized gluon density. Prompt photons are the photons produced directly in the partonic hard scatterings. One of the distinguishing features of the prompt photons is a large transverse momentum,  $p_T$ . Figure 10 shows the lowest-order Feynman diagrams for the prompt-photon production: a) quark-gluon Compton process,  $qg \rightarrow \gamma q$ , and b) quark-antiquark annihilation,  $q\bar{q} \rightarrow \gamma g$ . In  $p-p$  collisions, the quark-gluon Compton process dominates  $q\bar{q} \rightarrow \gamma g$  process be-

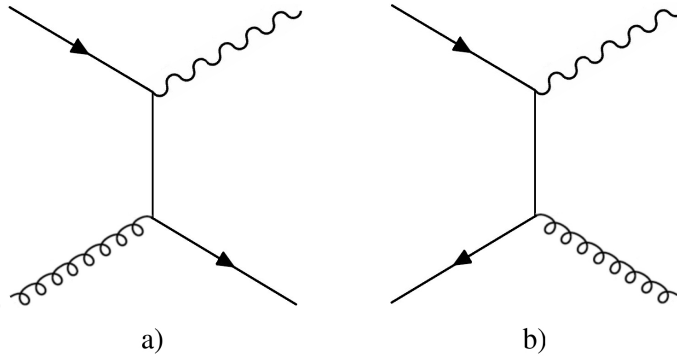


Figure 10: Leading-order Feynman diagrams for the production of a photon in the final state: a) quark-gluon Compton scattering, b)  $q\bar{q}$  annihilation

cause of the smallness of the antiquark distribution functions in the proton. Since the Compton scattering dominates, as it follows from Equations 52 and 53, the double-helicity asymmetry for the prompt-photon production can be written as

$$A_{LL} \approx \frac{\Delta g(x_1)}{g(x_1)} \cdot \left[ \frac{\sum_i e_i^2 \Delta q_i(x_2)}{\sum_i e_i^2 q_i(x_2)} \right] \cdot \hat{a}_{LL}^{gq \rightarrow \gamma q} + \{1 \leftrightarrow 2\}, \quad (62)$$

where the sum is over the quark and antiquark flavors. The term in the square brackets is the same as the virtual photon asymmetry  $A_1$  (Equation 22) measured in the polarized DIS experiments. The analyzing power  $\hat{a}_{LL}$  for  $gq \rightarrow \gamma q$  process is given in Figure 9. Hence, measuring  $A_{LL}$  for prompt-photon production, one can obtain  $\Delta g(x)/g(x)$ .

As it was mentioned above, one of the distinguishing features of the prompt photons produced in the partonic hard scatterings is a large transverse momentum. However, photons with large  $p_T$  can also originate in fragmentation processes, when a parton produced in the hard scattering fragments into a photon and several hadrons. It has been estimated that, for collider energies, approximately half of the

observed photons are produced in the fragmentation processes. Another source of the photon background is  $\gamma$ s from  $\pi^0$  or  $\eta$  decays. Therefore, one needs to develop selection cuts to apply to the photon signal in experiment in order to minimize the influence of the background contributions to extract the prompt-photon production signal. As an example, the most effective cut used to reduce background for the prompt-photon production is so called “isolation” cut [35].

An NLO prediction for the prompt-photon production double-helicity asymmetry [6] as a function of the photon  $p_T$  is presented in Figure 11. The asymmetries

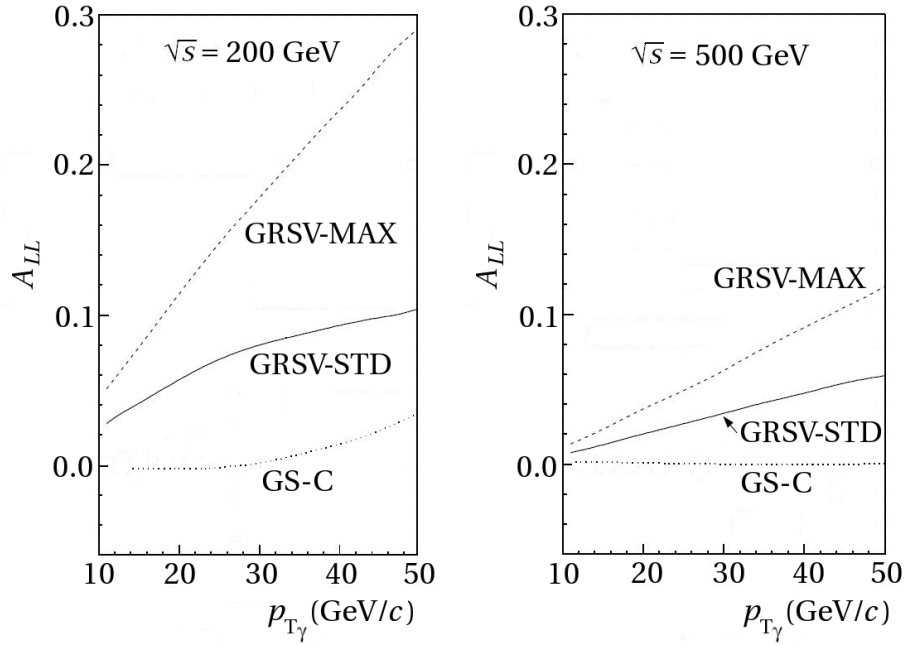


Figure 11: NLO prediction for the prompt-photon production double-helicity asymmetry for different polarized parton density sets [6]

are calculated for the CMS collision energies of  $\sqrt{s} = 200$  GeV and  $\sqrt{s} = 500$  GeV. A medium-pseudorapidity (defined in Chapter 5.2) cut,  $|\eta| < 0.35$ , as well as “isolation” cuts have been applied. Different polarized parton density sets have

been used for the NLO calculations: GRSV-MAX [36], GRSV-STD [36], and GS-C [37]. The quark densities of these sets are all in agreement with the polarized DIS data; the only difference is in the gluon density assumptions. GRSV-MAX assumes a large positive gluon distribution, GS-C contains a small  $\Delta g$ , and GRSV-STD's gluon density is between the other two (see Figure 12). The asymmetry in Figure 11 demonstrates a strong sensitivity to the different  $\Delta g$  — simulations show very different spin asymmetries for different spin-dependent gluon densities.

Figure 12 shows the three above mentioned gluon distribution functions, as well as DSS  $\Delta g$  [38], obtained from NLO fits to the available polarized DIS data. Various

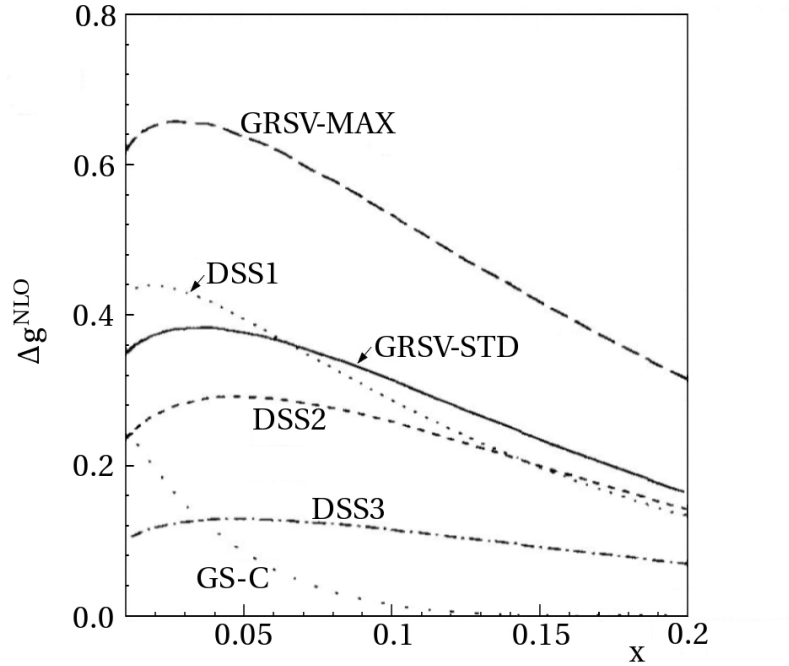


Figure 12: Polarized gluon densities for different NLO sets of polarized parton distribution functions (at  $Q^2 = 100 \text{ GeV}^2$ ) [39]

NLO fits for different polarized parton density sets provide results for  $\Delta g$  at a fixed  $x$  differing by an order of magnitude. Undoubtedly, the real gluon density could be

very dissimilar to all of these distributions.

### 2.7.2 Combination of Compton Process and Drell-Yan Production of Lepton Pair

One can also probe the gluon polarization via the reaction  $qg \rightarrow \gamma^*q \rightarrow l^-l^+q$ , which is the combination of the Compton scattering with a photon off-shell by of order of a few GeV and Drell-Yan production of lepton pair from the photon. The Feynman diagram for this reaction is shown in Figure 13. The advantage of this

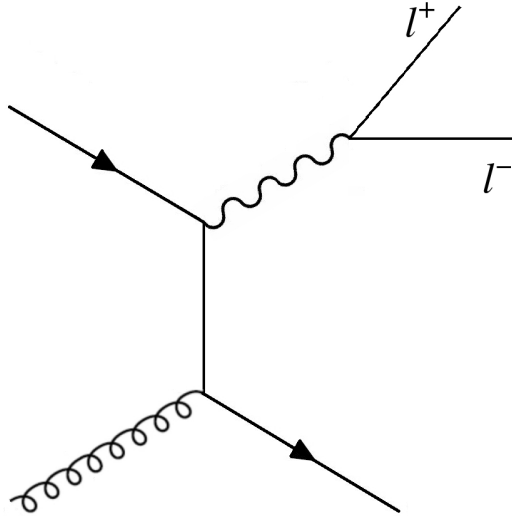


Figure 13: Feynman diagram for combination of Compton Process and Drell-Yan Production of Lepton Pair

method is explicit theoretical description, though the production yield is decreased by the factor of  $10^2 - 10^3$  in comparison to the prompt-photon production yield because of an additional factor  $\alpha_{em}/(3\pi Q^2)$  in the Drell-Yan cross-section, where  $Q$  is the dilepton mass.

### 2.7.3 Jet and Large- $p_T$ Hadron Production

At the CMS collision energy of  $\sqrt{s} = 200\text{-}500$  GeV, jets are produced in abundance and can be distinctly observed. There are many partonic subprocesses which contribute to leading-order jet production, but in accessible kinematical regions the production of the jets is dominated (see [24] and references therein) by gluon-initiated subprocesses, such as the gluon-gluon and quark-gluon partonic subprocesses shown in Figure 14. Thus, by studying jet's properties, one can probe  $\Delta g$ . Jets are investigated by the STAR (see Chapter 5.1) experiment.

In the PHENIX experiment the limited geometrical coverage makes jet exploration difficult, but one can observe large- $p_T$  leading hadrons such as  $\pi^0, \pi^\pm$ , which have origin in the same partonic processes. It is expected that the hadron-production asymmetry has the same level of sensitivity to the polarized gluon distribution as the jet asymmetry.

NLO QCD calculations for jet production double-helicity asymmetry versus the jet transverse momentum [39] are shown in Figure 15, for different polarized parton density sets with different  $\Delta g$  (see Figure 12). The predictions are made for the CMS collision energy of  $\sqrt{s} = 500$  GeV and pseudorapidity range  $|\eta| < 1$ . As seen from Figure 15 the asymmetry is fairly small for all different parton densities; this means that the statistics for jet measurements is required to be fairly large.

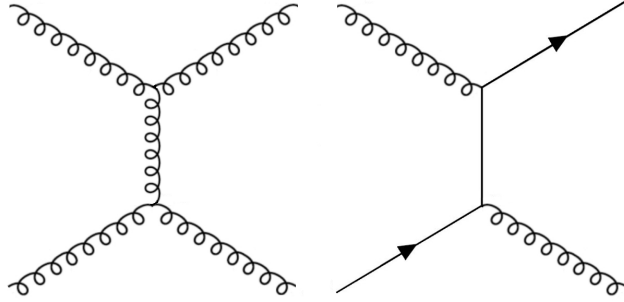


Figure 14: Lowest-order Feynman diagrams of gluon-initiated subprocesses for jet production

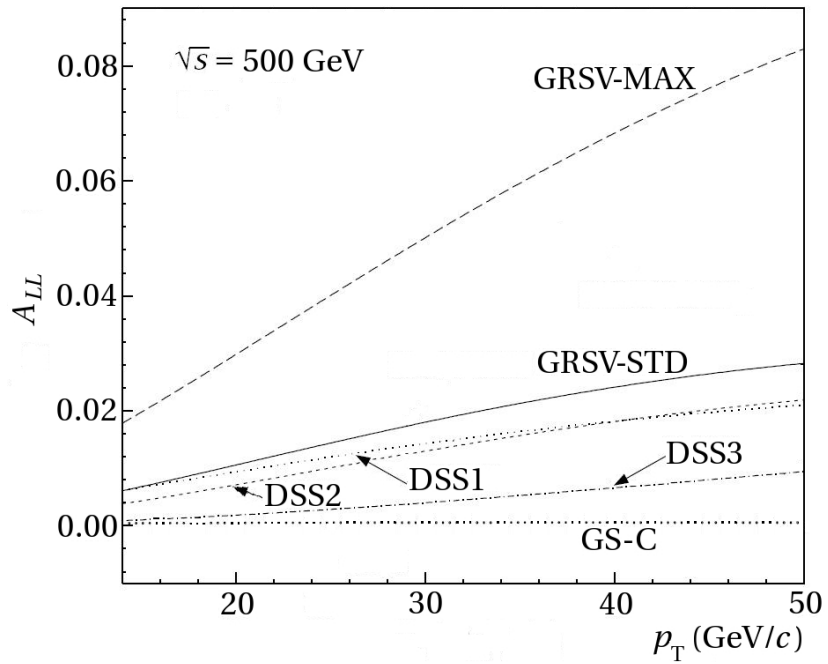


Figure 15: NLO predicted jet production double-helicity asymmetry as a function of jet transverse momentum, for different polarized parton densities [24]

### 2.7.4 $\Delta g$ in Heavy-Flavor Production

In  $p - p$  collisions heavy quark pairs,  $c\bar{c}$  and  $b\bar{b}$ , are produced substantially in gluon-gluon processes,  $gg \rightarrow Q\bar{Q}$ , such as the leading-order gluon-gluon fusion shown in Figure 16. Another channel for heavy-flavor production,  $q\bar{q} \rightarrow Q\bar{Q}$ , is

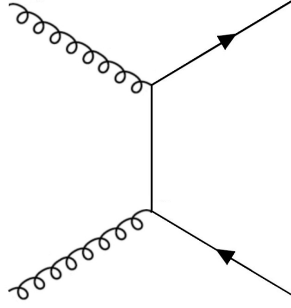


Figure 16: Feynman diagram for heavy quark pair production via gluon-gluon fusion suppressed because of the smallness of the antiquark distribution functions in the proton. Thus, the gluons in the proton can be directly accessed by observing heavy quarks. The lowest-order theoretical calculations, as well as NLO QCD calculations, demonstrated that this method can be used to measure the gluon polarization in polarized  $p - p$  collisions. According to pQCD, since the gluon-gluon processes dominate all other processes for heavy-flavor production, as it follows from Equations 52 and 53, the double-helicity asymmetry  $A_{LL}$  measured in heavy-flavor production is sensitive to the polarized gluon distribution,  $\Delta g(x)$ , in the proton:

$$A_{LL}(x_1, x_2) \approx \frac{\Delta g(x_1)}{g(x_1)} \times \frac{\Delta g(x_2)}{g(x_2)} \times \hat{a}_{LL}^{gg \rightarrow q\bar{q}}, \quad (63)$$

where  $g(x)$  is the unpolarized gluon distribution function,  $\hat{a}_{LL}$  is the analyzing power for  $gg \rightarrow q\bar{q}$  partonic subprocess given in Figure 9; it is maximally negative,

$\hat{a}_{LL} = -1$ . Thus, measuring  $A_{LL}$  for the heavy-flavor production one can obtain  $\Delta g(x)/g(x)$ . Note that longitudinally polarized beams are required for the gluon polarization studies.

Several channels can be used to extract a heavy-flavor production signal from experimental data:  $pp \rightarrow e^\pm X$ ,  $pp \rightarrow \mu^\pm X$ ,  $pp \rightarrow e^+e^- X$ ,  $pp \rightarrow \mu^+\mu^- X$ , and  $pp \rightarrow \mu^\pm e^\mp X$ . It is also possible to use like-sign leptons to extract a bottom production signal: in this case one lepton is produced directly from  $b$ -decay and another from sequential  $c$ -decay. More details on the study of the open heavy-flavor production, when quark and antiquark do not form a bound state, are given in Chapter 4.

The production of heavy quarkonia, the intermediate bound state of the quark-antiquark pair, can also be used to probe  $\Delta g$ . An example of this reaction is presented in Figure 17, where production of  $J/\psi$  from a  $c\bar{c}$  pair is shown with subsequent decay to a lepton pair. The double-helicity asymmetry  $A_{LL}$  for  $J/\psi$

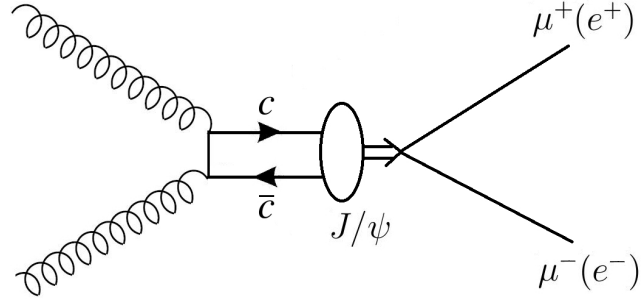


Figure 17: An example of heavy quarkonium ( $J/\psi$ ) production via gluon-gluon fusion, with subsequent decay to a lepton pair; the oval between the  $c\bar{c}$  pair and the  $J/\psi$  represents the formation of the  $J/\psi$  from the  $c\bar{c}$  pair

production can be written as

$$A_{LL}^{J/\psi}(x_1, x_2) \approx \frac{\Delta g(x_1)}{g(x_1)} \times \frac{\Delta g(x_2)}{g(x_2)} \times \hat{a}_{LL}^{gg \rightarrow J/\psi}, \quad (64)$$

where  $\hat{a}_{LL}^{gg \rightarrow J/\psi}$  is the partonic asymmetry for  $J/\psi$  production. The advantage of this channel is a clear signal of the reaction in experimental data due to a relatively large cross-section and small background. However, at present there is no clear understanding of the production mechanism of the heavy quarkonia and hence there is no unambiguous  $\hat{a}_{LL}^{gg \rightarrow J/\psi}$ , which is sensitive to the production mechanism. Thus, it is difficult to make a quantitative investigation of the gluon polarization. Due to ambiguities in the heavy quarkonium production mechanisms,  $\Delta g$  from heavy quarkonium production is highly model-dependent.

### 3 RECENT DOUBLE-HELICITY ASYMMETRY AND POLARIZED GLUON DISTRIBUTION MEASUREMENTS

One of the major goals of the RHIC spin physics program is to measure the polarized gluon distribution  $\Delta g(x)$  over an extended range of momentum fraction  $x$  and evaluate the gluon contribution to the proton spin. High-energy experiments at RHIC have made significant progress toward this goal. Recent measurements at RHIC have substantially narrowed the upper and lower limits for the possible gluon contribution to the proton spin.

As discussed in Chapter 2, processes in polarized  $p - p$  collisions at RHIC with final states produced at very large transverse momentum,  $p_T$ , give access to  $\Delta g(x)$ . The double-helicity asymmetries measured for these processes can be considered in terms of the spin-dependent parton distribution functions, including  $\Delta g(x)$ , and short-distance interaction partonic cross sections, calculable in pQCD. Thus,  $\Delta g(x)$  can be extracted from the experimentally measured double-helicity asymmetries for an  $x$  range determined by the kinematics of a particular experiment. The gluon contribution to the proton spin,  $\Delta G$ , by definition is given by the integral of  $\Delta g(x)$  over all momentum fraction range  $0 \leq x \leq 1$  (see Equation 45).

The spin-dependent cross sections relevant for the  $\Delta g(x)$  measurements at RHIC have been predicted by next-to-leading order (NLO) pQCD [40]. The spin-averaged cross sections for unpolarized  $p - p$  collisions at a center-of-mass energy of  $\sqrt{s} = 200$  GeV have been measured at RHIC for inclusive production of pions at mid-rapidity

at PHENIX [41] and forward rapidity at STAR [42], as well as of jets at STAR [43] and prompt photons at PHENIX [44] at mid-rapidity. The parton distribution functions for the spin-averaged case are known with quite good precision [45, 46, 47, 48, 49]. This has allowed quantitative tests of the theoretical NLO framework. The measured spin-averaged cross sections have been successfully compared numerically with the NLO pQCD predictions [50, 51, 52, 53, 54, 55, 56, 57] showing a remarkable agreement. This has demonstrated the validity of the NLO pQCD application and provided the groundwork for NLO propagation to the polarized case.

To date, RHIC utilizes mainly inclusive processes,  $pp \rightarrow \pi X$  at PHENIX and  $pp \rightarrow jet X$  at STAR, to access the spin-dependent gluon distribution  $\Delta g(x)$ . Recent RHIC results [58, 59, 60, 61, 43, 62] demonstrate that the gluons in the proton have relatively small polarization in the region of momentum fraction from 0.05 to 0.2 accessible at RHIC at present. The most recent double-helicity asymmetry  $A_{LL}$  measurements for mid-rapidity inclusive- $\pi^0$  production at PHENIX and inclusive-jet production at STAR are shown in Figures 18 and 19. The theoretical NLO predictions for  $A_{LL}$  as a function of  $p_T$  [50, 51], shown as well in Figures 18 and 19, correspond to the various polarized gluon distribution functions from the different GRSV models from Glück, Reya, Stratmann, and Vogelsang [63] and the GS-C fit from Gehrmann and Stirling [37]. The “GRSV-std” curve is founded on the best fit among GRSV models to the DIS data, with an integrated gluon contribution to the proton spin (see Equation 45) of  $\Delta G \approx 0.4$  at scale  $Q^2 = 1 \text{ GeV}^2$ . The GRSV curve labeled “ $\Delta g = 0$ ” corresponds to very little gluon polarization,  $\Delta G(\text{at } Q^2 = 1$

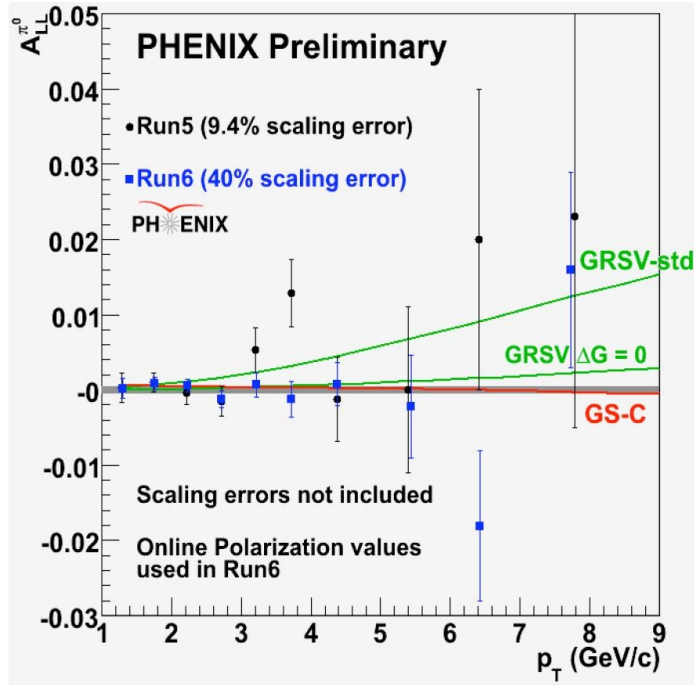


Figure 18: PHENIX inclusive- $\pi^0$   $A_{LL}$  [59, 60, 61]. The NLO curves are addressed in the text

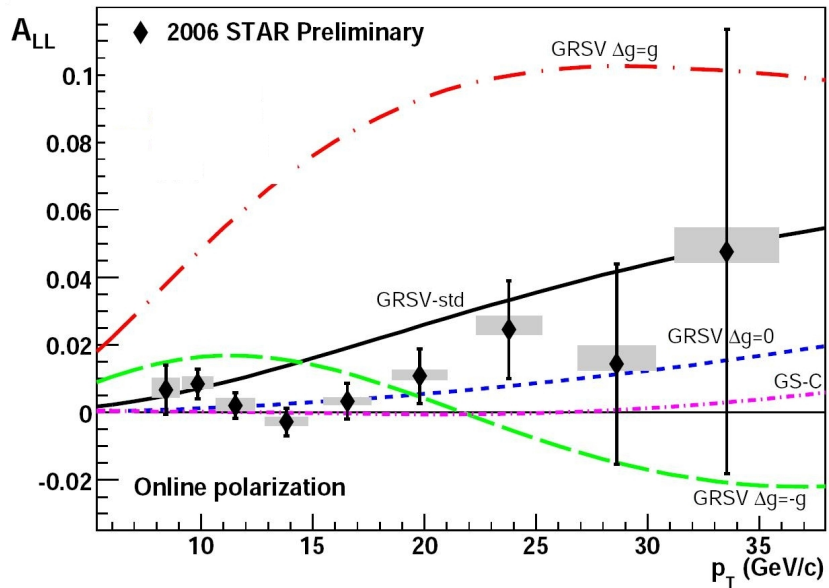


Figure 19: STAR inclusive-jet  $A_{LL}$  [62]. The NLO curves are addressed in the text

GeV<sup>2</sup>)  $\approx 0.1$ . The GS-C fit contributes little and has a node vs.  $x$  in the region of current RHIC sensitivity, but still has a large contribution to the full integral  $\Delta G$  from low momentum fractions  $x$ . Figure 19 shows also the curves for the models with the maximally polarized gluons, aligned ( $\Delta g = g$ ) and anti-aligned ( $\Delta g = -g$ ) with the proton spin, with corresponding  $\Delta G(\text{at } Q^2 = 1 \text{ GeV}^2) \approx 1.9$  and  $\Delta G(\text{at } Q^2 = 1 \text{ GeV}^2) \approx -1.8$ , respectively. As can be seen from the data points, these extreme maximal models are disfavored by the current RHIC measurements.

The most recent RHIC double-helicity asymmetry measurements have been utilized in a novel global analysis of the proton spin structure accomplished by de Florian, Sassot, Stratmann, and Vogelsang (DSSV) [64]. This global analysis combines the asymmetries measured in proton-proton collisions at RHIC with measurements from the inclusive and semi-inclusive DIS experiments to derive the spin-dependent parton distribution functions. The global analysis theoretical calculations are performed at NLO QCD accuracy. Quark, anti-quark, and gluon polarized densities in the proton have been obtained from the combined RHIC and DIS data. The polarized gluon distribution, resulting from the global analysis, is presented in Figure 20. The DSSV polarized gluon density is small in the momentum fraction range from 0.02 to 0.3 and has a node in the  $x$  region accessible presently at RHIC. However, the uncertainty of this distribution, shown as well in Figure 20 as cross-hatched and vertically hatched bands for different levels of confidence, is still quite large. The previous fits from the GRSV [63] and DNS [65] models are shown as well, and they are outside of the DSSV distribution uncertainties. Thus, these earlier NLO

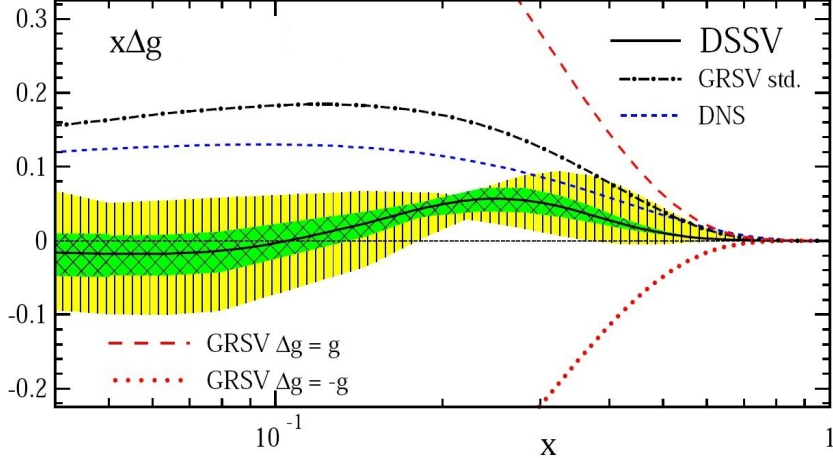


Figure 20: Polarized gluon distribution functions at  $Q^2 = 10 \text{ GeV}^2$  from the global analysis by DSSV [64] and from the prior GRSV and DNS models

fits to the past DIS data, which suggested large or moderate gluon contribution to the proton spin, are not confirmed by the combined recent RHIC and DIS data.

At present, it is not possible to evaluate the integral of  $\Delta g(x)$  over the entire momentum fraction range  $0 \leq x \leq 1$ , in order to make a statement about the total gluon contribution  $\Delta G$  to the proton spin. Thus, to obtain  $\Delta G$ , it is essential to measure  $\Delta g(x)$  with high precision in the accessible  $x$  region, as well as to determine  $\Delta g(x)$  at lower and higher  $x$  values than being accessed presently. There is still a possibility of significant contribution to the full integral of  $\Delta g(x)$  from  $x < 0.02$ . It is not expected that the contribution from  $x > 0.3$  region is large, but in some models  $\Delta g/g$  is sizable in this region.

In the DIS experiments, HERMES at DESY, COMPASS at CERN, and many experiments at Jefferson Laboratory, information on the polarized gluon distribution function is obtained primarily via investigation of the  $Q^2$  dependence of the structure function  $g_1(x, Q^2)$ . This information is a part of the global analysis of

the combined DIS and RHIC data [64]. The results from these lepton scattering experiments are in agreement with the RHIC results. But there is still a large uncertainty in the  $\Delta g(x)$  functional form and sign of the integral  $\Delta G$  presents.

The principal conclusions from the current measurements at RHIC are the following: the range of gluon momentum fraction addressed by the RHIC measurements is from 0.05 to 0.2, and the gluon contribution to the proton spin in this range is not large. The general conclusion for the RHIC and DIS measurements is that the results from the DIS experiments are consistent with the RHIC results. Large gluon contribution to the proton spin in the accessible so far  $x$  region is improbable. But a possible interesting behavior of  $\Delta g(x)$  and the significance of the low- $x$  region are exciting subjects to investigate.

The HERMES, COMPASS, and SMC experiments have performed measurements of  $\Delta g(x)$  via photon-gluon fusion, detecting pairs of hadrons with relatively high  $p_T$  with respect to the virtual photon direction [23, 66, 67, 68]. These measurements are leading order methods, therefore they are not part of the DSSV NLO QCD global analysis. The results of these measurements for  $\Delta g(x)/g(x)$  are consistent with zero within the uncertainty of  $\sim 0.1$  at  $x \sim 0.15$ . This is in agreement with the RHIC results stating a small value of the gluon polarization at this  $x$  region.

COMPASS have used also heavy-flavor, namely, open-charm, production to access  $\Delta g(x)$  from muon-deuteron scattering [69]. These measurements are based on the photon-gluon fusion process tagged by charmed meson production with

subsequent decay to charged  $K$  and  $\pi$ . It was assumed that open-charm production is dominated in leading-order QCD by the photon-gluon fusion process creating a  $c\bar{c}$  pair which fragments mainly into  $D$  mesons. The advantages of this method are that there is no other contributions to the cross section in the lowest order, and that it is less model dependent than previous DIS measurements. But statistics is quite limited. The  $D$  mesons were selected through two decay channels:  $D^0 \rightarrow K^-\pi^+$  (a branching ratio of 3.8%) and  $D^{*(2010)^+} \rightarrow D^0\pi_{slow}^+ \rightarrow K^-\pi^+\pi_{slow}^+$ , and their charge conjugates. The mesons were reconstructed on a combinatorial basis, calculating the invariant mass of all pairs of oppositely charged tracks in a given event. The result for extracted gluon polarization is  $\langle\Delta g/g\rangle = -0.47 \pm 0.44(\text{stat}) \pm 0.15(\text{syst})$  at  $\langle x \rangle \approx 0.11$  and a scale  $\mu^2 \approx 13(\text{GeV}/c)^2$ . This result is shown in Figure 21 along with other, mentioned above, DIS measurements from high  $p_T$  hadron-pair production by COMPASS, HERMES, and SMC. The COMPASS  $\langle\Delta g/g\rangle$  measured in open-charm production is in line with the recent DIS and RHIC results favoring small values of the gluon polarization.

Silicon vertex detectors in PHENIX, the Silicon Vertex Tracker (VTX) covering the central rapidity and the Forward Silicon Vertex Tracker (FVTX) covering the forward rapidity, are under construction. They will significantly advance the studies of the heavy-quark (charm and bottom quark) production by measuring the displaced decay vertex. Heavy quarks, along with the forward rapidity region physics capabilities, permit to measure the gluon polarization at lower and higher  $x$  values than so far accessible. In this dissertation research, an attempt to access the

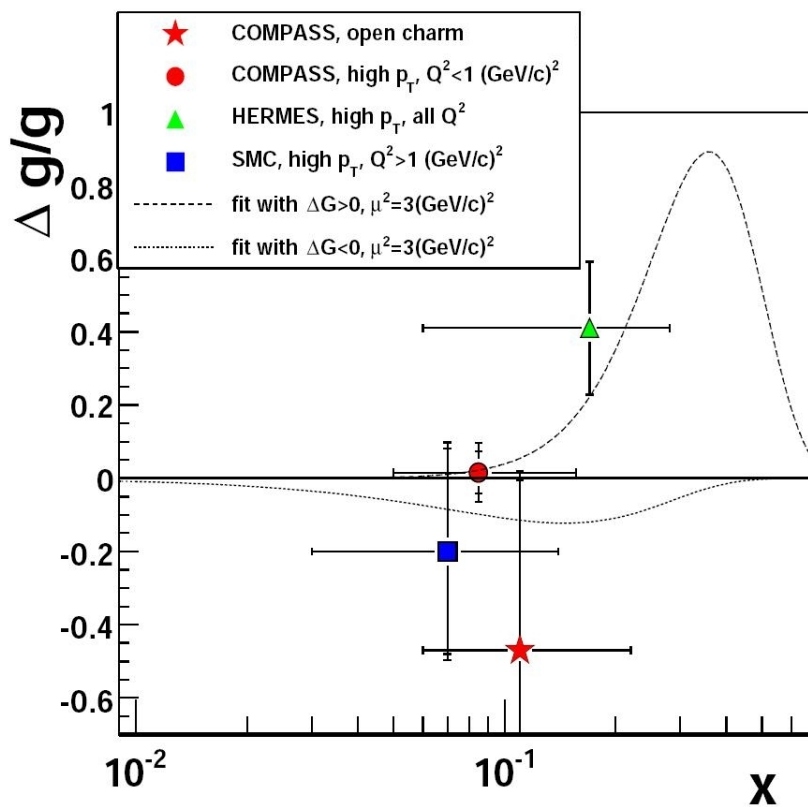


Figure 21:  $\langle \Delta g/g \rangle$  from open-charm and high  $p_T$  hadron pair production measured by COMPASS, HERMES, and SMC [69]

gluon polarization in the proton via open-charm production has been made using current capabilities of the PHENIX detector.

## 4 HEAVY-FLAVOR PRODUCTION

Heavy-flavor (charm and bottom) production represents a crucial test of QCD. Since the production of charm quark and anti-quark pairs,  $c\bar{c}$ , and bottom quark and anti-quark pairs,  $b\bar{b}$ , at RHIC energies is dominated by gluon-gluon processes, heavy-flavor production in polarized  $p - p$  collisions directly probes the polarized gluon distribution  $\Delta g(x)$  and, hence, the gluon polarization  $\Delta G$ . Furthermore, measurements of heavy-flavor production in  $p-p$  reactions supply with groundwork for exploration of the hot and dense matter in heavy ion collisions. Thus, a good understanding of the reaction mechanism for heavy-flavor production is of great importance.

Heavy quarks do not serve as valence flavors of the commonly used beam particles; they are primarily produced in the hard scattering underlying subprocesses in collision events. Therefore, they are excellent probes of the underlying hard dynamics. At any center-of-mass energy, the large masses of the heavy quarks,  $m_c = 1.27_{-0.11}^{+0.07}$  GeV/ $c^2$  and  $m_b = 4.20_{-0.07}^{+0.17}$  GeV/ $c^2$  (in the  $\overline{MS}$  scheme) [3], set conditions for the hard scale of an event, thereby implying the validity of the pQCD application. Heavy-flavor production can be treated by NLO pQCD, especially at high  $p_T$ , and even at small momenta. Hence, pQCD theoretical predictions of the heavy quark production are supposed to be reliable over the full momentum range addressed at high energy collider experiments. In particular, due to the heavy-quark large masses relative to the  $u$ ,  $d$ , and  $s$  quark masses, it is feasible to calculate total

heavy-flavor production cross sections, which is difficult to accomplish in the case of lighter flavors.

#### 4.1 Theoretical Predictions for Heavy-Flavor Production

In the lowest order (LO) in the strong coupling  $\alpha_s$ ,  $\mathcal{O}(\alpha_s^2)$ , charm and bottom quark pairs are produced in  $p - p$  collisions via two parton-parton underlying hard-scattering subprocesses: gluon-gluon fusion,  $gg \rightarrow Q\bar{Q}$ , and quark-antiquark annihilation,  $q\bar{q} \rightarrow Q\bar{Q}$ , depicted in Figure 22. The spin-dependence of the LO

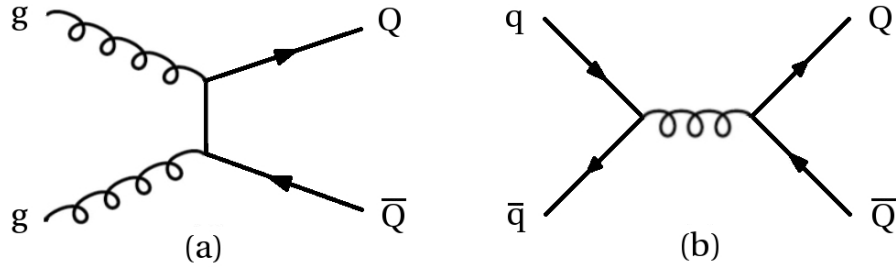


Figure 22: Leading-order Feynman diagrams for heavy-flavor production: a) gluon-gluon fusion, b)  $q\bar{q}$  annihilation

subprocesses for heavy quark production has been examined in [70, 71]. The cross section for the subprocess  $q\bar{q} \rightarrow Q\bar{Q}$ , with  $q_1, q_2$  the momenta of the incoming quark-antiquark pair and  $k_1, k_2$  the momenta of the outgoing heavy quark and antiquark of mass  $m$ , is given by

$$\frac{d\hat{\sigma}}{dt} = \frac{4\pi\alpha_s^2}{9\hat{s}^2} \left[ \frac{\tilde{t}^2 + \tilde{u}^2 + 2m^2\hat{s}}{\hat{s}^2} \right], \quad (65)$$

where

$$\tilde{t} \equiv m^2 - \hat{t}, \quad \tilde{u} \equiv m^2 - \hat{u}, \quad (66)$$

$$\hat{s} = (q_1 + q_2)^2, \quad \hat{t} = (q_1 - k_1)^2, \quad \hat{u} = (q_1 - k_2)^2. \quad (67)$$

As it was discussed in Chapter 2.5, the double-longitudinal spin asymmetry for a partonic subprocess is defined by

$$\hat{a}_{LL} \equiv \frac{d\hat{\sigma}_{++} - d\hat{\sigma}_{+-}}{d\hat{\sigma}_{++} + d\hat{\sigma}_{+-}}, \quad (68)$$

where + and – correspond to the helicity of the incident partons. Then, for the  $q\bar{q}$  annihilation subprocess, because of helicity conservation and the assumption that the initial state quarks are massless, it follows that

$$\hat{a}_{LL}(q\bar{q} \rightarrow Q\bar{Q}) = -1. \quad (69)$$

The unpolarized (averaged over spins) cross section for the gluon-gluon fusion subprocess, with  $q_1, q_2$  the momenta of the incoming gluons and  $k_1, k_2$  the momenta of the outgoing heavy quark-antiquark pair, can be written in terms of the variables defined in Equations 66 and 67 as

$$\begin{aligned} \frac{d\hat{\sigma}}{dt} &= \frac{\pi\alpha_s^2}{8\hat{s}^2} \left( \frac{4}{3\tilde{u}\tilde{t}} - \frac{3}{\hat{s}^2} \right) \left[ (\tilde{t}^2 + \tilde{u}^2) + \left( \frac{4m^2\hat{s}}{\tilde{u}\tilde{t}} \right) (\tilde{u}\tilde{t} - m^2\hat{s}) \right] \\ &= \frac{1}{2} \left( \frac{d\hat{\sigma}_{++}}{dt} + \frac{d\hat{\sigma}_{+-}}{dt} \right). \end{aligned} \quad (70)$$

The difference of the helicity-dependent cross sections is

$$\frac{d\hat{\sigma}_{++}}{dt} - \frac{d\hat{\sigma}_{+-}}{dt} = -\frac{\pi\alpha_s^2}{4\hat{s}^2} \left( \frac{4}{3\tilde{u}\tilde{t}} - \frac{3}{\hat{s}^2} \right) \left[ (\tilde{t}^2 + \tilde{u}^2) - \left( \frac{2m^2\hat{s}}{\tilde{u}\tilde{t}} \right) (\tilde{t}^2 + \tilde{u}^2) \right]. \quad (71)$$

Thus, for the gluon-gluon fusion subprocess, the partonic double-longitudinal spin asymmetry is given by

$$\hat{a}_{LL}(gg \rightarrow Q\bar{Q}) = -\frac{(\tilde{t}^2 + \tilde{u}^2) - 2m^2\hat{s}(\tilde{t}^2 + \tilde{u}^2)/\tilde{u}\tilde{t}}{(\tilde{t}^2 + \tilde{u}^2) + 4m^2\hat{s}(\tilde{u}\tilde{t} - m^2\hat{s})/\tilde{u}\tilde{t}}. \quad (72)$$

Exploiting the following kinematic relations

$$\tilde{t} = \frac{\hat{s}}{2}(1 - \beta y), \quad \tilde{u} = \frac{\hat{s}}{2}(1 + \beta y), \quad (73)$$

where  $y \equiv \cos(\theta^*)$  gives the center-of-mass scattering angle and  $\beta \equiv \sqrt{1 - 4m^2/\hat{s}}$  is the heavy-quark speed, the LO partonic level double-helicity asymmetry,  $\hat{a}_{LL}$ , for the subprocess  $gg \rightarrow Q\bar{Q}$  versus  $y$  for different values of  $\sqrt{\hat{s}}/2m$  is presented in Figure 23 [71]. The solid, dashed, dot-dash, and dotted curves correspond to

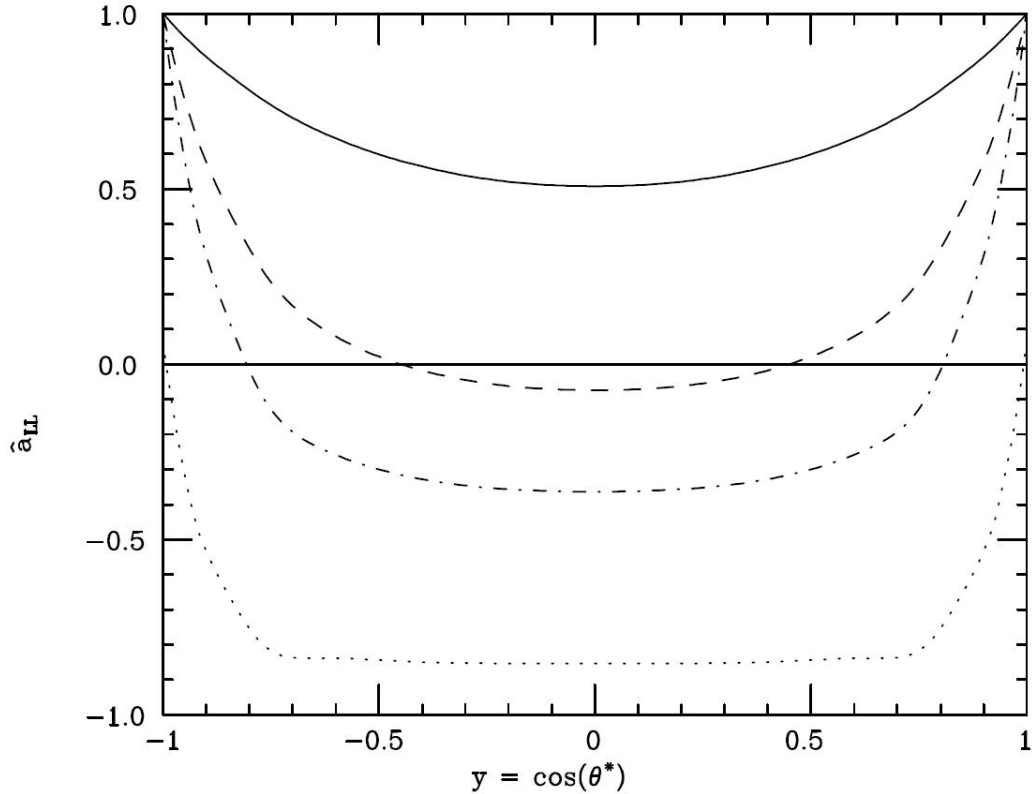


Figure 23: LO partonic level double-helicity asymmetry for gluon-gluon fusion vs. the center-of-mass scattering angle for different values of  $\sqrt{\hat{s}}/2m$  (see text) [71]

$\sqrt{\hat{s}}/2m = 1.1, 1.5, 2,$  and  $5,$  respectively. As seen from Figure 23, near the threshold for  $Q\bar{Q}$  production, where  $\sqrt{\hat{s}} = 2m,$  the LO partonic asymmetry is  $+1$  for the entire  $y$  range. But as the partonic center-of-mass energy is increased and as  $\theta^* \rightarrow \pi/2,$

i.e., when the transverse momentum,  $p_T$ , is increased, the LO gluon-gluon fusion  $\hat{a}_{LL}$  rapidly approaches  $-1$ , changing dramatically the expected magnitude and even sign of the observable asymmetry. Thus, heavy-flavor production is unique in that all contributing LO subprocesses are characterized by a large analyzing power, at least at large  $p_T$ , approaching  $-100\%$ .

The gluon-gluon fusion subprocess dominates the quark-antiquark annihilation subprocess for the heavy-flavor pair production in  $p-p$  collisions in the unpolarized case, and in the polarized case as well. The quark-antiquark annihilation subprocess is suppressed because of the smallness of the antiquark distribution functions in the proton. For  $\sqrt{s} = 200$  GeV  $p-p$  collisions, the leading-order PYTHIA [72, 73, 74] Monte Carlo estimation of the cross-section ratio  $\sigma(gg \rightarrow Q\bar{Q})/\sigma(q\bar{q} \rightarrow Q\bar{Q})$  is 95/5 for the charm production and 85/15 for the bottom production. In contrast with DIS, where gluons participate only as a small correction in the NLO QCD, this makes heavy-flavor production in polarized  $p-p$  collisions one of the promising candidates to study  $\Delta g(x)$ . However, NLO pQCD corrections to the LO subprocesses have to be included for a reliable description of the heavy-flavor production. The full set of the NLO corrections to heavy-quark production for the unpolarized case is available in [75, 76, 77, 78].

The NLO pQCD corrections to the hadroproduction of heavy flavor in polarized  $p-p$  collisions have been computed in [79]. These results can be considered as the first complete order calculations. The  $\mathcal{O}(\alpha_s^3)$  NLO pQCD corrections to heavy-flavor production include three sources: 1) the one-loop virtual corrections to the

LO processes (see examples in Figure 24(a, b)), 2) the real “2 → 3” corrections with an additional gluon in the final state (Figure 24(c, d, e)), and 3) an additional production mechanism,  $gq(\bar{q}) \rightarrow Q\bar{Q}q(\bar{q})$  (example f in Figure 24). Taking

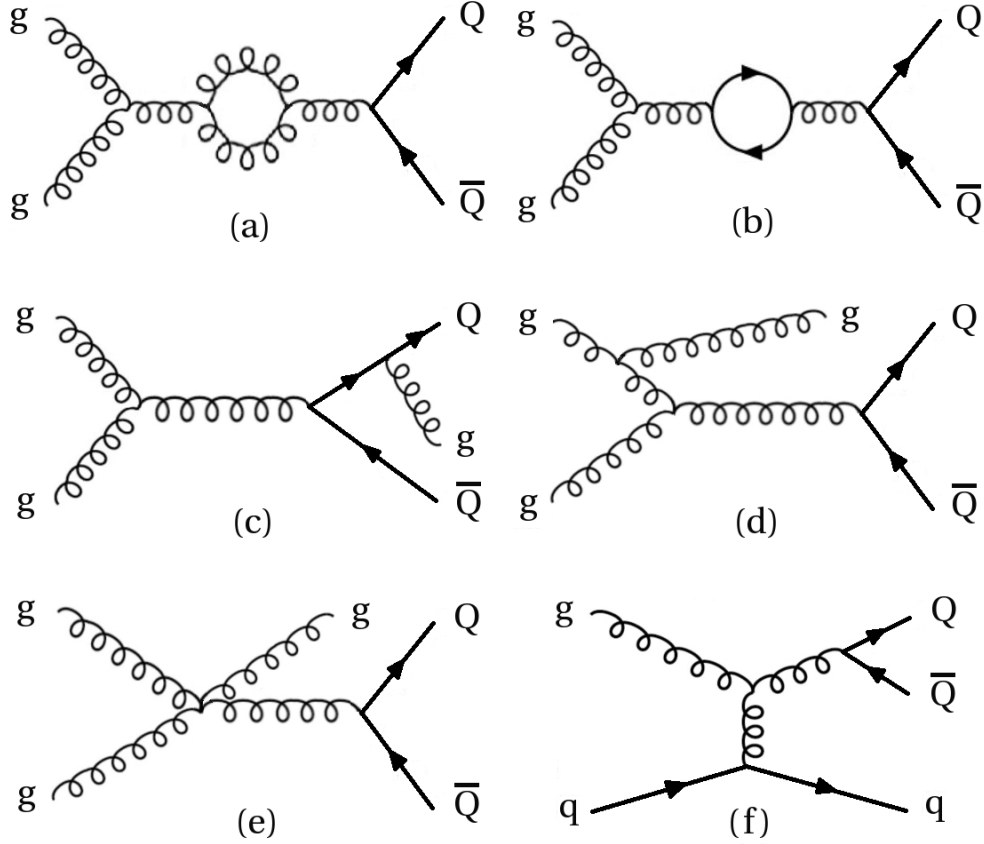


Figure 24: Examples of NLO Feynman diagrams for heavy-flavor production (see text)

in account the NLO pQCD corrections, the total partonic subprocess cross sections  $\hat{\sigma}_{ij}$  for the unpolarized case and  $\Delta\hat{\sigma}_{ij}$  for the polarized case, where  $i, j = q, \bar{q}, g$ , are expressed in terms of LO functions  $f_{ij}^{(0)}$ ,  $\Delta f_{ij}^{(0)}$  and NLO functions  $f_{ij}^{(1)}$ ,  $\Delta f_{ij}^{(1)}$ , respectively, which depend on a scaling variable  $\xi = \hat{s}/(4m^2) - 1$ , where  $\hat{s}$  is the partonic center-of-mass-system energy squared and  $m$  is the heavy quark mass.

Note that taking the ratio of the partonic subprocess cross sections  $\Delta\hat{\sigma}_{ij}$  and  $\hat{\sigma}_{ij}$  gives  $\hat{a}_{LL}^{ij}$ , appearing in Equation 52 and defined in Equation 68, the spin asymmetry for partonic subprocesses, also known as the analyzing power. The NLO corrections to the total partonic  $gg$  cross sections,  $\hat{\sigma}_{gg}$  and  $\Delta\hat{\sigma}_{gg}$ , turn out to be significant; they are demonstrated in Figure 25. This figure shows the unpolarized

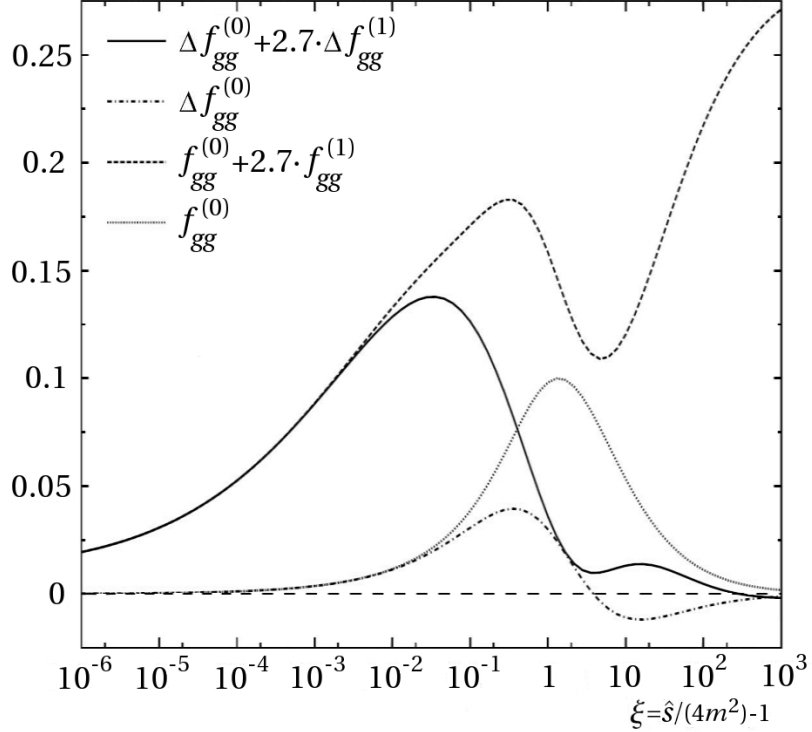


Figure 25:  $(m^2/\alpha_s^2)\hat{\sigma}_{gg}$  and  $(m^2/\alpha_s^2)\Delta\hat{\sigma}_{gg}$  in LO and NLO [79]

and polarized gluon-gluon subprocess cross sections,  $(m^2/\alpha_s^2)\hat{\sigma}_{gg}$  and  $(m^2/\alpha_s^2)\Delta\hat{\sigma}_{gg}$ , in LO and NLO as functions of  $\xi$ . The factor  $4\pi\alpha_s = 2.7$ , multiplying the NLO correction functions, is set as appropriate for charm production. The threshold for  $Q\bar{Q}$  production is at  $\xi = 0$ , where  $\hat{s} = 4m^2$ . At the threshold,  $\hat{\sigma}_{gg}$  and  $\Delta\hat{\sigma}_{gg}$  are equal. While in LO the polarized and unpolarized cross sections approach zero at

the threshold, they tend to a non-zero constant in NLO. In the high energy region,  $\xi \rightarrow \infty$ , the polarized and unpolarized functions behave quite differently. The NLO functions  $f_{gq}$  and  $\Delta f_{gq}$  are numerically much smaller than  $f_{gg}$  and  $\Delta f_{gg}$ , as shown in [79].

The physical, i.e., observed in experiment, total cross section can be obtained by convolving the partonic-subprocess cross sections with the appropriate combinations of parton densities as in Equations 44 and 47. In [79], a prediction for the charm cross section as being measured at PHENIX via detected electrons has been obtained using an “efficiency” function, which models the hadronization, decays of the heavy quarks, and detector geometry. Based on this calculation for the charm cross section, the charm production spin asymmetry at RHIC has been predicted for the various sets of the polarized parton distribution functions with the different assumptions about  $\Delta g(x)$ . These NLO charm spin asymmetries are presented in Figure 26 as functions of  $x_T^{min} = p_T^{min}/p_T^{max}$ , where  $p_T^{max} = \frac{1}{2}\sqrt{s - 4m^2}$  is the upper kinematical limit, and  $s$  is the proton-proton center of mass system energy squared. The asymmetry curves are scaled by  $1/x_T^{min}$  for a better separation. The Gehrman-Stirling set A (GS A) asymmetry, assuming the large gluon polarization, needed to be scaled down by a factor of 0.7 to fit into the same graph with the other predictions. In contrast, the GS C asymmetry, assuming a very small, oscillating  $\Delta g$ , is almost vanishing. The further study of the contributions to the total charm spin asymmetry from different partonic subprocesses ( $gg, gq, q\bar{q}$ ) has demonstrated that, as expected, the major contribution originates from the gluon-

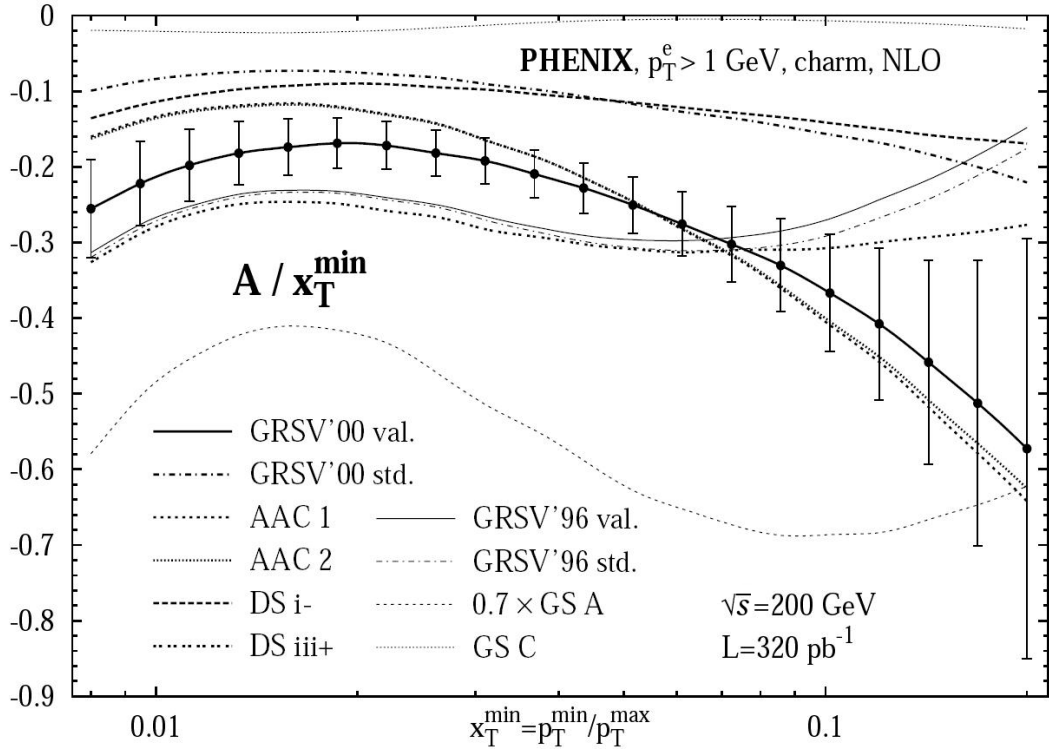


Figure 26: NLO charm spin asymmetry at  $\sqrt{s} = 200$  GeV for PHENIX [79]

gluon fusion. Along with the estimated statistical errors, assuming a luminosity of  $\mathcal{L} = 320 \text{ pb}^{-1}$  (see Figure 26), it is apparent that charm production at RHIC can be used to extract  $\Delta g$  in the proton.

The electron  $p_T$  spectrum originating from heavy-flavor decays in  $p-p$  collisions at RHIC at  $\sqrt{s} = 200$  GeV has been calculated in the fixed-order-plus-next-to-leading-log (FONLL) pQCD approach [80, 81]. As the complement to the full fixed-order NLO results discussed above, the FONLL calculation also resums large perturbative terms proportional to  $\alpha_s^n \log^k(p_T/m)$  to all orders with next-to-leading logarithmic (NLL) accuracy (i.e.,  $k = n, n - 1$ ), where  $m$  is the heavy quark mass. In the calculation,  $m_c = 1.5 \text{ GeV}/c^2$  and  $m_b = 4.75 \text{ GeV}/c^2$  were taken as central

values, and then the masses were varied over the range  $1.3 < m_c < 1.7 \text{ GeV}/c^2$  for charm and  $4.5 < m_b < 5 \text{ GeV}/c^2$  for bottom to evaluate theoretical uncertainties arising from the mass uncertainty. The following predictions for the transverse momentum,  $p_T$ , distributions are calculated in [80, 81]: of the heavy (charm and bottom) quarks,  $Q(c, b)$ , in  $p - p$  collisions at  $\sqrt{s} = 200 \text{ GeV}$ ; of the charm and bottom hadrons resulting from fragmentation of the heavy quarks into the heavy hadrons,  $H_Q(D, B)$ ; and of the electrons produced in the semi-leptonic decays of the hadrons,  $H_Q$ . Based on these predictions, the cross section of electrons from heavy-flavor production can be written in the following convolution form:

$$\frac{E d^3 \sigma_e}{dp^3} = \frac{E_Q d^3 \sigma_Q}{dp_Q^3} \otimes D(Q \rightarrow H_Q) \otimes f(H_Q \rightarrow e). \quad (74)$$

The distribution  $E_Q d^3 \sigma_Q / dp_Q^3$  of the heavy quarks has been calculated in the FONLL approach.  $D(c \rightarrow D)$  and  $D(b \rightarrow B)$  are fragmentation functions for mixtures of charm and bottom hadrons, respectively. The calculated transverse momentum distributions in  $p - p$  collisions at  $\sqrt{s} = 200 \text{ GeV}$  for charm quarks and charm mesons are shown in Figure 27 and for bottom quarks and bottom mesons are shown in Figure 28 [80]. As can be seen from Figures 27 and 28, the bottom quark and  $B$  meson distributions overlap over the whole  $p_T$  range shown, up to 20 GeV. The charm quark and  $D$  meson bands partially overlap up to 9 GeV and then begin to differ for  $p_T > 9 \text{ GeV}$ . The FONLL predictions for the transverse momentum distributions of single electrons from the semi-leptonic decays of the  $D$  and  $B$  mesons are discussed in Chapter 4.2 and are shown in Figure 32 compared

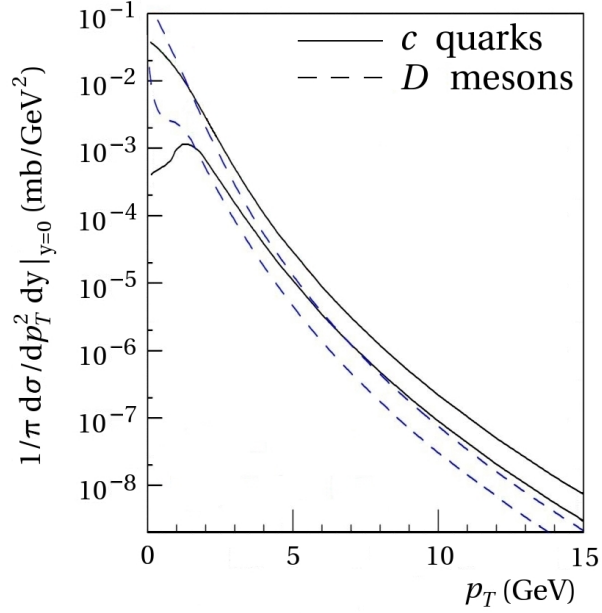


Figure 27: FONLL uncertainty bands for  $c$  quark and  $D$  meson  $p_T$  distributions [80]

to data.

The total charm and bottom quark-antiquark pair production cross sections have been calculated [81] by integrating the total partonic cross sections predicted to NLO and by using CTEQ6M parton densities [49]. The obtained total cross sections as functions of  $p-p$  CMS energy,  $\sqrt{s}$ , are shown in Figure 29. The solid lines are the central results calculated with  $m_c = 1.5 \text{ GeV}/c^2$  and  $m_b = 4.75 \text{ GeV}/c^2$ . The dashed lines represent the uncertainty bands. The dotted line shown for charm case is the result calculated with  $m_c = 1.2 \text{ GeV}/c^2$ . At  $\sqrt{s} = 200 \text{ GeV}$ , the charm and bottom NLO total cross sections are  $\sigma_{c\bar{c}}^{NLO_{nf}} = 301_{-210}^{+1000} \mu\text{b}$  and  $\sigma_{b\bar{b}}^{NLO_{nf}} = 2.06_{-0.81}^{+1.25} \mu\text{b}$ .

The alternative way to account for the higher order processes for heavy-flavor

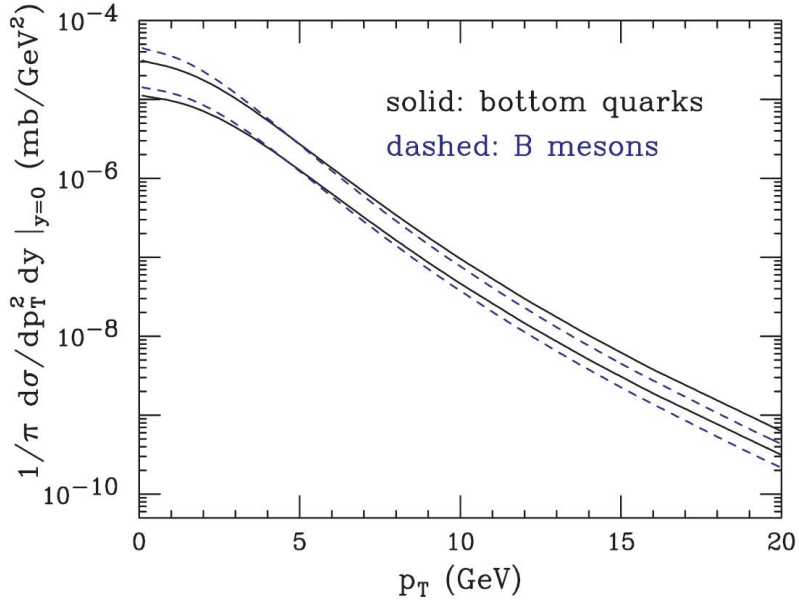


Figure 28: FONLL uncertainty bands for  $b$  quark and  $B$  meson  $p_T$  distributions [80]

production is the parton-shower (PS) framework [82] which exploits a probabilistic approach. The PS approximations differ from those used in the NLO pQCD calculations. In the parton-shower description, the composite  $2 \rightarrow n$  partonic process comprises three phases: initial-state cascades, hard scattering, and final-state cascades. Here the hard scattering is the shortest-distance subprocess with a  $2 \rightarrow 2$  diagram. The partonic processes for heavy-flavor production can be grouped into three different categories in the PS approach: pair creation, flavor excitation, and gluon splitting. Pair creation occurs when the hard-scattering subprocess involves one of the two LO processes shown in Figure 22. An example of the pair creation, with gluon emission, is depicted in Figure 30(a). Parton showers do not affect the production cross sections, but they change kinematics. For example, in the LO,

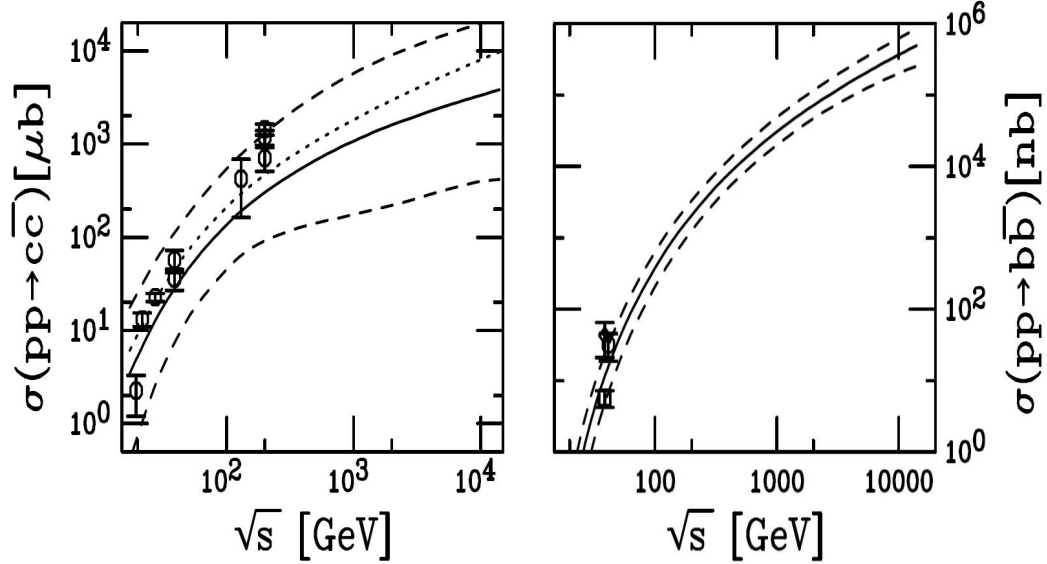


Figure 29: NLO total charm (left-hand side) and bottom (right-hand side) cross sections as functions of  $\sqrt{s}$  [81]

because of momentum conservation the  $Q$  and  $\bar{Q}$  have to be emitted back-to-back in azimuthal angle, while in the PS description the parton shower can carry away some part of momentum (Figure 30(a)). Another category of the heavy-flavor production mechanisms is flavor excitation. This category is characterized by the hard scattering of a heavy flavor coming from one beam particle against a parton of the other beam (Figure 30(b)). If the heavy quark is not a valence flavor, it must originate from a  $g \rightarrow Q\bar{Q}$ . Gluon splitting occurs when a  $g \rightarrow Q\bar{Q}$  appears in the initial- or final-state shower, and no heavy quarks participate in the hard scattering; see Figure 30(c, d). Thus, the three above mentioned categories are classified by the number of heavy flavors in the final state of the hard subprocess: 2 for the pair creation, 1 for the flavor excitation, and 0 for the gluon splitting. The subsequent hadronization process of the outgoing partons from the hard scatterings, of the par-

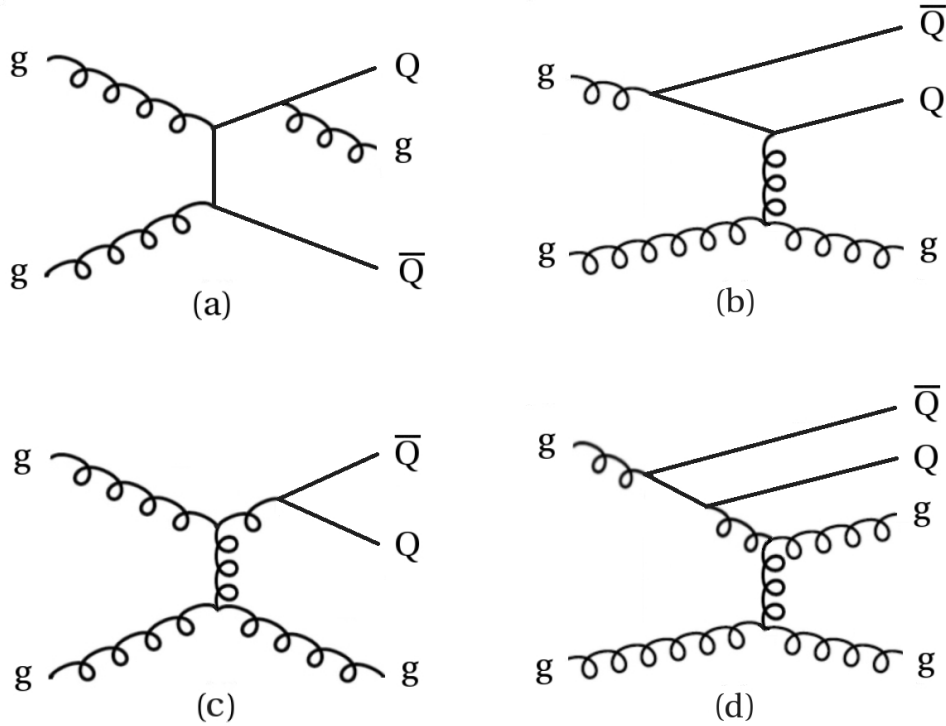


Figure 30: Examples of heavy-flavor production diagrams in parton-shower approach [82]: a) pair creation, b) flavor excitation, c) and d) gluon splitting

tons from the associated showers, and of the beam-remnant partons is performed within the framework of the Lund string fragmentation model [83]. In this string model, a linear confinement potential is implemented by spanning color confinement strings between the partons in a specific order. This couples the hadronization of a heavy quark to the flavor content and momentum of the other string end, often of one of the valence flavors of the incoming beams. The PS approach is implemented in the PYTHIA generator [72, 73, 74], which is used for the simulation studies in this dissertation work.

The total heavy-flavor cross sections in  $p - p$  collisions, both for charm and bottom productions, have been evaluated as functions of the  $p - p$  CMS energy,

$\sqrt{s}$ , in the parton-shower approach using PYTHIA and are presented in Figure 31 [82]. The following heavy-quark masses were chosen for the study:  $m_c = 1.5 \text{ GeV}/c^2$  and  $m_b = 4.8 \text{ GeV}/c^2$ . The presented total cross sections obtained within the PS framework are consistent with the NLO pQCD calculations and with the data values measured at  $\sqrt{s} = 200 \text{ GeV}$  (see Chapter 4.2). The separate contributions from the pair creation, flavor excitation, and gluon splitting production mechanisms are also shown in Figure 31. The total charm cross section at  $\sqrt{s} = 200 \text{ GeV}$  breaks down as the following: the flavor-excitation contribution is  $\sim 65\%$ , the pair-creation contribution is  $\sim 25\%$ , and the gluon-splitting contribution is  $\sim 10\%$ . Thus, at RHIC energies the pair-creation mechanisms including the LO gluon-gluon fusion subprocess account for only a part of the total charm production cross section. The remainder of the charm cross section is contributed by the higher order gluon-gluon processes. Flavor excitation and gluon splitting give significant contributions to the total cross sections at RHIC energies and hence must be included in consideration.

## 4.2 Experimental Measurements of Heavy-Flavor Production

Experiments detect the products of heavy quark (meson) decays, e.g., leptons. Heavy quarks can be identified in the data by methods such as prompt leptons detection, secondary vertices reconstruction, or kinematical constraint usage. Heavy-flavor decays usually are characterized by multi-body kinematics and often proceed through “cascades”; this may make it difficult to reconstruct an event back to the parton level. It is necessary also to apply cuts on the detected particles to provide

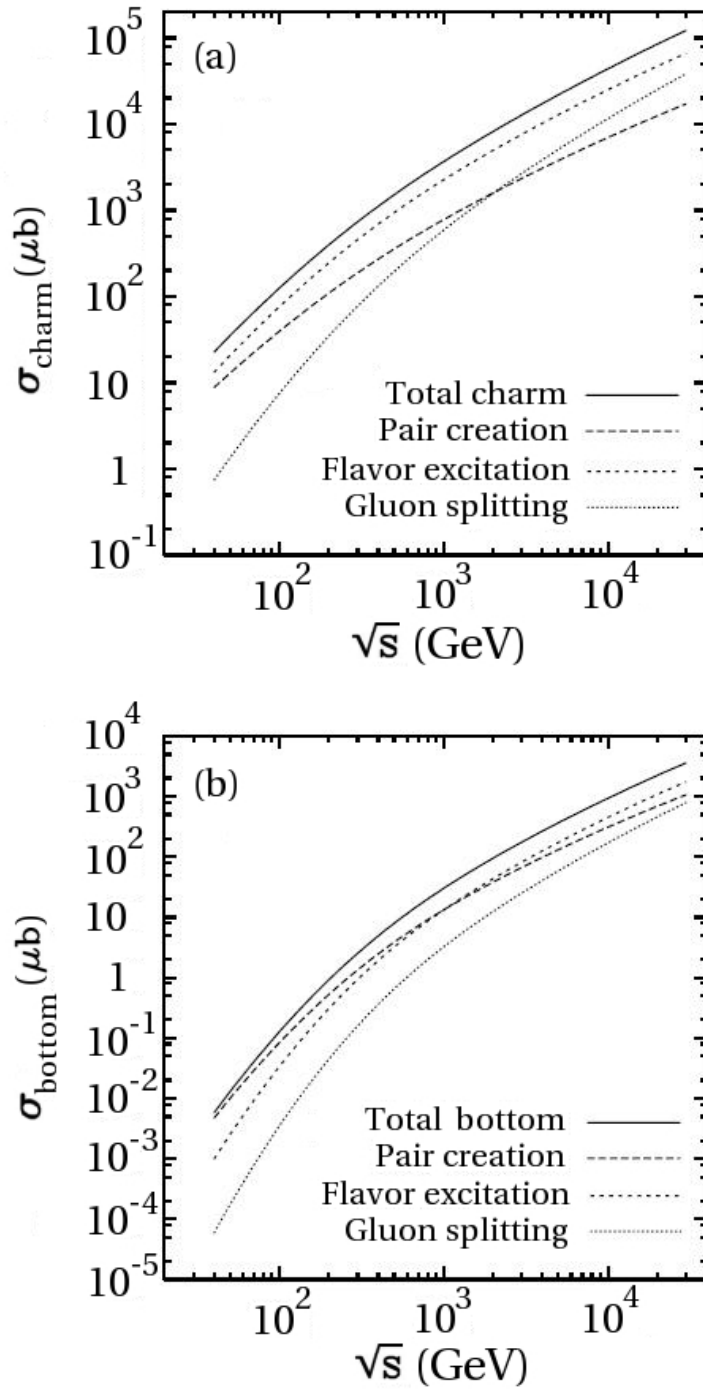


Figure 31: Total charm (a) and bottom (b) production cross sections for  $p - p$  collisions calculated in parton-shower approach using PYTHIA [82]

a correct  $c$  and  $b$  quark separation. One solution is to count on Monte Carlo simulations of heavy-quark decays, for example, on the PYTHIA generator [72, 73], which proved to be successful in comparison with data.

The first open-charm measurements date back to the 1970s, when  $D$  and  $\bar{D}$  mesons were observed for the first time. There are two ways to detect hadrons from open-charm production [81]. First, charm can be observed through semi-leptonic decays of charm mesons to leptons such as  $D \rightarrow Kl\nu_l$ . This way makes it difficult to reconstruct the momentum of the initial  $D$  meson. Second, charm can be detected via decays to charged hadrons such as  $D^0 \rightarrow K^-\pi^+$  (a branching ratio of 3.8% [3]),  $D^+ \rightarrow K^-\pi^+\pi^+$  (9.1% [3]), and their charge conjugates. The second way allows the full momentum reconstruction of the parent meson. Often  $D$  mesons are used alone to measure open charm production, taking into account that, on average, a charm quark has about 60% probability of fragmenting into a  $D^0$ . However, there are other charm hadrons such as the excited  $D$  states,  $D^*$ , which decay mainly to charged and neutral  $D$  mesons, for instance, through  $D^{*+} \rightarrow D^0\pi^+$ . The charm-strange meson,  $D_s$ , can decay to charged hadrons, and semi-leptonically as well. There are also charm baryons such as  $\Lambda_c^+$ , with the lowest mass among charm baryons, which decays mainly to  $\Lambda(uds)$  but also decays to  $pK^-\pi^+$  (a branching ratio of 2.8% [3]) and semi-leptonically with a 4.5% branching ratio [3]. The heavier charm baryons such as  $\Sigma_c$  and their excited states decay through the  $\Lambda_c^+$ . There are also charm-strange baryons, which contribute to the total charm production negligibly.

Charm and bottom production cross sections measured at RHIC [84, 85] and at the Tevatron are in good agreement with pQCD prediction. At the Tevatron, for bottom production, cross section measurements agree well with NLO pQCD calculations [86]; for charm production, cross sections obtained at high  $p_T$  are higher than the theoretical prediction by  $\approx 50\%$ , though this discrepancy is within the theoretical uncertainties [87]. This provides a solid baseline for studying the gluon polarization in the proton via heavy-flavor production.

The invariant differential cross section of electrons from decays of heavy flavor in  $p-p$  collisions at  $\sqrt{s} = 200$  GeV has been measured by the PHENIX experiment at RHIC over the transverse momentum range  $0.3 < p_T < 9.0$  GeV/ $c$  in the central rapidity region  $|\eta| < 0.35$  [85]. The differential cross section for electron production has been calculated using the following formula:

$$E \frac{d^3\sigma}{dp^3} = \frac{1}{\int \mathcal{L} dt} \frac{1}{2\pi p_T} \frac{N_e}{\Delta p_T \Delta y} \frac{1}{\epsilon_{rec}} \frac{1}{\epsilon_{bias}}, \quad (75)$$

where  $N_e$  is the measured electron yield,  $\int \mathcal{L} dt$  is the integrated luminosity for the sample,  $\epsilon_{bias}$  is the probability for an electron event to satisfy the minimum bias trigger condition, and  $\epsilon_{rec}$  includes the geometrical acceptance, track reconstruction and trigger efficiency. The spectrum of electrons from semi-leptonic decays of hadrons carrying heavy flavor was obtained by subtracting two major background contributions from other sources from the inclusive electron spectrum. One of the major background components is the “photonic” background including electrons from Dalitz decays of light mesons and conversion of photons, primarily from

$\pi^0 \rightarrow \gamma\gamma$  decays, in material within the acceptance of the detector, mainly in the beam pipe. Another important background contribution is the “nonphotonic” background including electrons from the remaining  $K_{e3}$  decays and dielectron decays of vector mesons. The background subtraction was performed by two different independent methods, the “cocktail subtraction” method [84, 88, 89] and the “converter subtraction” method [90]. In the cocktail subtraction technique the invariant cross section of electrons from decays of heavy flavor was obtained by subtracting a “cocktail” of electron contributions from other various sources computed using a Monte Carlo event generator of hadron decays. In the converter subtraction technique electron spectra measured with a photon converter (a thin brass sheet of 1.67% of a radiation length) installed temporarily around the beam pipe were compared to measurements without converter. The results of the cocktail subtraction and the converter subtraction methods are in good agreement with each other. Figure 32 shows the invariant differential cross section of electrons from decays of heavy flavor, after subtracting all backgrounds from the inclusive electron spectrum. The statistical and systematic uncertainties are depicted as the error bars and bands, respectively. The obtained electron spectrum from heavy-flavor decays is compared with a fixed-order-plus-next-to-leading-log (FONLL) pQCD prediction [80], discussed in Chapter 4.1. The FONLL pQCD calculations for charm and bottom productions are given separately also, and the contribution of electrons from the secondary  $b$  decays ( $b \rightarrow c \rightarrow e$ ), calculated in FONLL, is shown as well. It is worth to note, that the predicted contribution from bottom decays becomes dominant

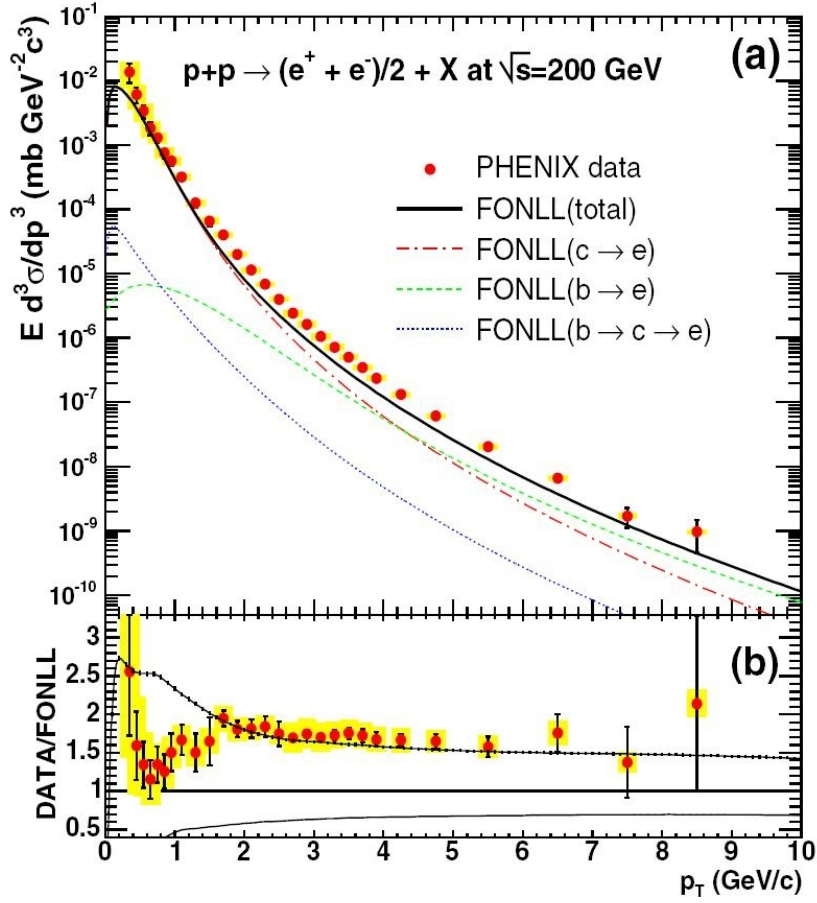


Figure 32: Invariant differential cross section of electrons from decays of heavy flavor (a); ratio of the data to the FONLL calculation (b) [85]

for  $p_T > 4$   $\text{GeV}/c$  and that the contribution to the total rate of the secondary  $b$  decays is negligible. The data are in agreement with FONLL pQCD calculations within the theoretical and experimental uncertainties, with a data-to-theory ratio of  $1.71 \pm 0.02(\text{stat}) \pm 0.18(\text{sys})$  (Figure 32(b)). The upper and lower curves in Figure 32(b) represent the theoretical upper and lower limits, respectively, of the FONLL calculation. The upper limit of the FONLL prediction is compatible with the data.

The total cross section of charm quark-antiquark pair production has been obtained by integrating the heavy-flavor electron cross section and taking into account

a  $c \rightarrow e$  total branching ratio of  $9.5 \pm 1.0\%$ . Using the rapidity distribution from HVQMNR [91] with CTEQ5M parton distribution functions [92] for the extrapolation, the total charm cross section at  $\sqrt{s} = 200$  GeV has been determined to be  $\sigma_{c\bar{c}} = 567 \pm 57(\text{stat}) \pm 193(\text{sys}) \mu\text{b}$ . This value is compatible with the PHENIX measurement for the charm cross section in  $Au - Au$  collisions at the same  $\sqrt{s} = 200$  GeV [90],  $622 \pm 57(\text{stat}) \pm 160(\text{sys}) \mu\text{b}$  per  $NN$  collision. The total charm cross section predicted by FONLL at  $\sqrt{s} = 200$  GeV,  $\sigma_{c\bar{c}}^{\text{FONLL}} = 256_{-146}^{+400} \mu\text{b}$ , [80, 81] is smaller, but it is still compatible with the data within its uncertainty. The corresponding NLO prediction for the charm cross section is  $\sigma_{c\bar{c}}^{\text{NLO}} = 244_{-134}^{+381} \mu\text{b}$  [80, 81]. Note that the analysis in [85] does not allow charm and bottom separation. The FONLL prediction for the total bottom cross section is  $\sigma_{b\bar{b}}^{\text{FONLL}} = 1.87_{-0.67}^{+0.99} \mu\text{b}$ . The fact, that the reported data are in agreement with the FONLL and NLO pQCD predictions within the theoretical and experimental uncertainties, convinces us that an extraction of the gluon polarization in the proton via heavy-flavor production is feasible.

A different method has been used to determine the total charm production cross section via electron-positron pair measurements at PHENIX in  $p - p$  collisions at  $\sqrt{s} = 200$  GeV [93]. The electron-positron mass distribution obtained by subtracting the contributions from  $\pi^0, \eta, \omega, \rho, \phi, \eta', J/\psi$ , and  $\psi'$  mesons from the inclusive  $e^+e^-$  pair mass spectrum is dominated by semi-leptonic decays of charmed hadrons correlated through flavor conservation. Fitting to the data the spectral shapes of the bottom and charm  $e^+e^-$  pairs predicted by PYTHIA, the

heavy-flavor production cross sections at  $\sqrt{s} = 200$  GeV have been estimated to be  $\sigma_{c\bar{c}} = 518 \pm 47(\text{stat}) \pm 135(\text{syst}) \pm 190(\text{model}) \mu\text{b}$  for charm production and  $\sigma_{b\bar{b}} = 3.9 \pm 2.5(\text{stat})_{-2}^{+3}(\text{syst}) \mu\text{b}$  for bottom production. The obtained charm and bottom production cross sections are compatible with the FONLL and NLO pQCD predictions and with the PHENIX measurement of single electrons.

The PHENIX experiment has measured single muon production in  $\sqrt{s} = 200$  GeV  $p$ - $p$  collisions in the forward rapidity region  $1.5 \leq |\eta| \leq 1.8$  over the transverse momentum range  $1 < p_T < 3$  GeV/ $c$  [94]. The data for this measurement were collected in the Run 2001/2 period, when only the South Muon Arm was operational. The limited statistics available for the Run 2001/2 determines the upper limit of the  $p_T$  range. The “vertex-independent” muon spectrum has been statistically extracted by subtracting estimated yields of “decay” muons from light hadron ( $\pi$  and  $K$ ) decays and of fake backgrounds from the inclusive muon yield ( $pp \rightarrow \mu^\pm X$ ). The fake backgrounds are “punch-through” hadrons, which penetrate through the Muon Arm absorber material, reach the deepest Muon Identifier layer and are thus misidentified as muons, and “background tracks,” which are hadrons that decayed into muons within the Muon Arm volume. The contribution of the “decay” muons from the light hadron decays was estimated by fitting the collision vertex histograms using the fact that the yield of the muons from light meson decays before the Muon Arm absorber is vertex-dependent. A data-driven hadron generator that is based on PHENIX midrapidity measurements was used to evaluate contributions from the fake backgrounds. The yield of the “punch-through” hadrons in the deepest

Muon Identifier layer was obtained by a technique in which the yield of the identified hadrons in the shallow Muon Identifier layers was extrapolated to the deepest Muon Identifier layer. On the basis of the data-driven hadron generator simulation, the “background track” yield was estimated to be 5% of the vertex-averaged decay muon yield. The finally extracted “vertex-independent” muon  $p_T$  spectrum for negative muons is shown in Figure 33. Statistical and systematic uncertainties are depicted as error bars and bands, respectively. In the analysis in [94], the muons from the open-charm decays are not measured directly. But it is expected that, in the  $1 < p_T < 3$  GeV/ $c$  range, the extracted “vertex-independent” muon yield, as predicted by PYTHIA, is dominated by the semi-leptonic decays of the heavy flavor mesons from open-charm production, with small contributions from decays of mesons from open bottom (6.9%) and decays of light-vector mesons ( $\rho, \omega, \phi$ ) (8.1%). Contributions from decays of quarkonia and Drell-Yan production are negligible ( $< 0.1\%$ ). In Figure 33, the measured “vertex-independent” negative-muon spectrum is compared to theoretical calculations. The measurements are noticeably higher than the predictions made using the PYTHIA generator (dotted line) [72, 73] and computed in the FONLL pQCD approximation (solid line with systematic error band) [80, 81]. The bottom panel in Figure 33 shows the ratio of the measured spectrum to the FONLL prediction. One can see also that the measured spectrum is harder than the PYTHIA spectrum. It is necessary to note that in the analysis in [94], by default PYTHIA has been tuned to generate only leading order processes for heavy-quark production.

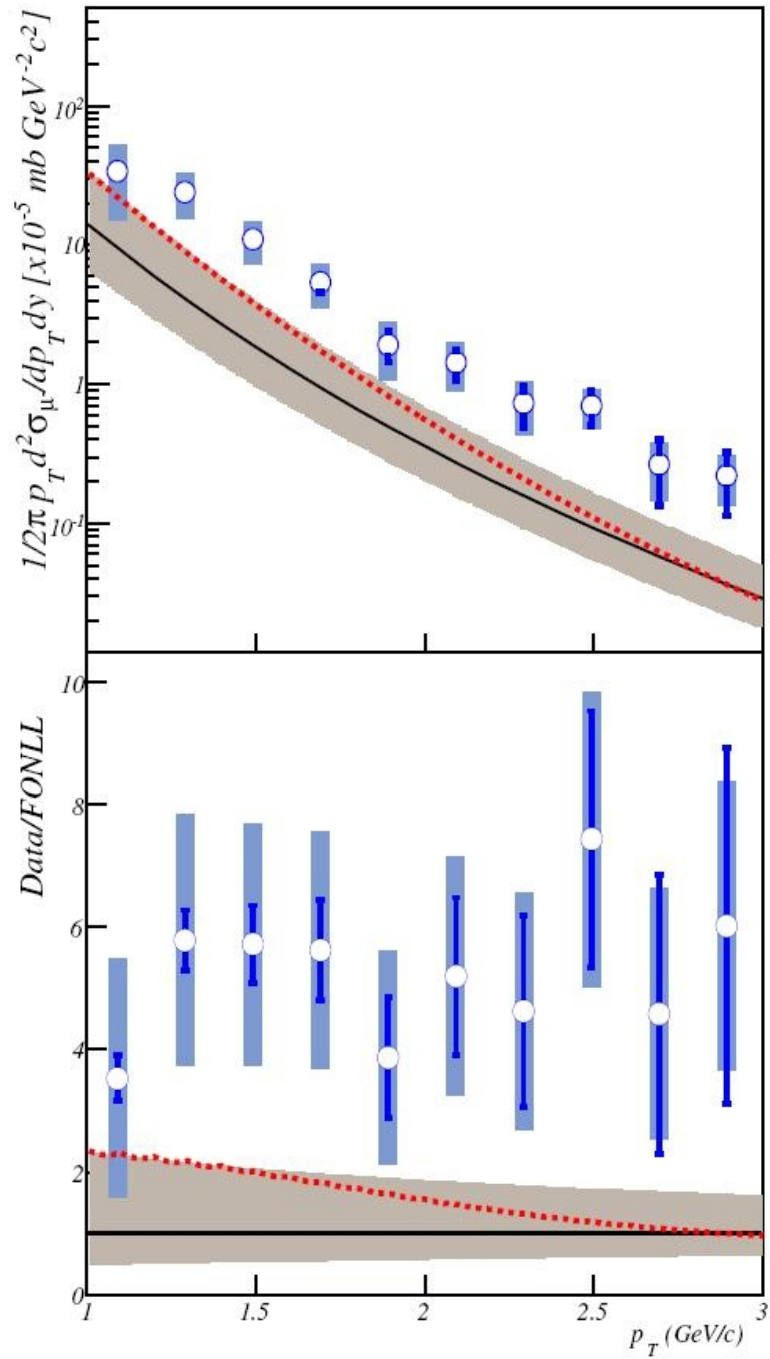


Figure 33:  $p_T$  spectrum of “vertex-independent” negative muons compared to theoretical calculations [94]

### 4.3 Search for Open Charm with a Combined Analysis of Single-Muon Events in the Central and Muon Arms of the PHENIX Detector

Heavy-flavor production is one of the most promising candidates used at RHIC to determine the polarized gluon distribution  $\Delta g(x)$  over a broad range of the momentum fraction  $x$ . As mentioned before, the production of  $c\bar{c}$  pairs in  $p-p$  collisions at the RHIC energy is dominated by gluon-gluon processes. One of the channels, which can be used to extract the open-charm production signal from experimental data, is  $pp \rightarrow \mu^\pm X$ . Therefore, the production of single muons from charm decay in polarized  $p-p$  collisions is expected to be sensitive to the polarized gluon distribution in the proton (Figure 34).

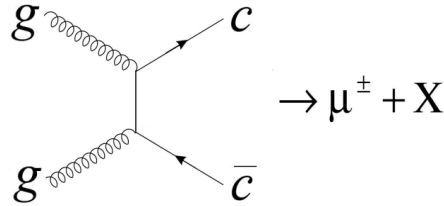


Figure 34: Production of single muons from charm decay used to access gluons in the proton

There are several sources of the inclusive muon candidates, which can be successfully reconstructed to the last Muon Identifier layer of the Muon Arms of the PHENIX Detector:

- 1) open-charm muons — muons originating from semi-leptonic decays of heavy-flavored mesons from open-charm production (one of the possible scenarios of the single muon production starting from gluon-gluon fusion is shown in Figure 35);

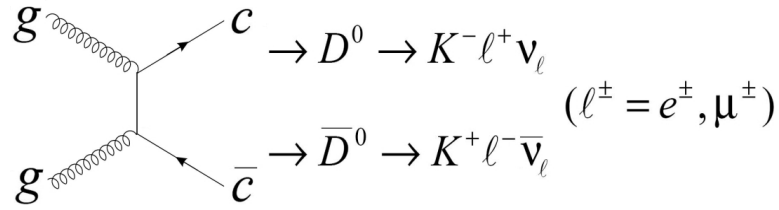


Figure 35: Example of single lepton (muon or electron) production in semi-leptonic decays of heavy-flavored mesons from open charm

- 2) other open-heavy-flavor muons, which originate from bottom quark decays;
- 3) quarkonium muons — muons originating from the decays of the intermediate bound states of the quark-antiquark pair (quarkonium), such as  $J/\psi$  decays;
- 4) decay muons — muons produced primarily in the decays of  $\pi$ s and  $K$ s, which do not have origin in heavy-flavor decays;
- 5) “punch-through” hadrons — hadron tracks, which reach the deepest Muon Identifier layer, have correctly reconstructed momenta, and are thus misidentified as muons;
- 6) background tracks — tracks arising from combinatoric associations of unrelated hits.

For the purpose of accessing the polarized gluon distribution via single muons from charm decay one has to discriminate between open-charm muons and other inclusive muon candidates, which is not a trivial experimental project. One could use an obvious common characteristic of all charmed particles, which is the lifetime of the  $c$  quark. Regardless of what particle is formed or how many strong decays it undergoes, eventually the  $c$  quark has to decay weakly into a strange (or less

frequently, a down) quark, for instance, through  $c \rightarrow s/d + \mu + \nu_\mu$ , with a lifetime of about  $\tau = 1 \text{ ps}$ . Depending on momentum, the  $c$  quark's path length,  $l = c\gamma\tau$  ( $c$  is the speed of light), varies from a fraction of a mm to a few mm. Thus, one could look for secondary vertices separated from the main vertex by these distances. At present, this is outside the capabilities of the PHENIX detector — the vertex resolution is not sufficiently good to proceed with this task. Hence, one has to identify other common features, or combinations of features, of the open-charm events, which can be used to extract an enriched sample from the data.

In this dissertation work we proceed with a combined analysis of the single-muon-triggered events in the Central and Muon Arms of the PHENIX detector in order to search for open charm in the single-muon data. The open-charm content of the single-muon event sample can be enhanced by combining additional event information from the PHENIX Central Arms. This can allow actual tagging of the open-charm muons on an event-by-event basis using developed selection criteria in contrast to the methods which use the yield evaluation for the open-charm muons by excluding different sources of muons from the inclusive muon yield. We take advantage of the several following circumstances. First of all, about 8.2% of the time, one of the members of the  $c\bar{c}$  pair decays into a muon [3]:

$$\frac{\Gamma(c \rightarrow \mu^+ \textit{anything})}{\Gamma(c \rightarrow \textit{anything})} = 8.2 \pm 0.5\%. \quad (76)$$

Further, the presence of a relatively high- $p_T$  muon is one of the characteristic features of the charm events. Because of the large mass, the charm quark is expected

to produce one or more high- $p_T$  decay products, and simulations show that such hadron or lepton tracks often end up in the Central Arms even as a muon is detected in the Muon Arms. Thus, there could be correlations between the muon and other high- $p_T$  tracks, originating in the decay of the same or the companion  $c$  (or  $\bar{c}$ ) quark, in the open-charm events. This can be exploited by performing a combined Central/Muon-detector analysis. The goal of this research is to study the correlations between the high- $p_T$  Muon-Arm tracks at forward rapidity and the Central-Arm charged hadron/lepton tracks at mid rapidity in order to enrich the charm content of the single-muon data. The ultimate goal of the correlation studies is to develop multivariate selection criteria, which can significantly enhance the charm content of a sample of single-muon events, by studying and comparing different kinematic quantities of the Muon-Arm tracks and the Central-Arm tracks. This part of the analysis is described in Chapter 7.

## 5 EXPERIMENTAL SETUP AND DATA ACQUISITION

### 5.1 The RHIC Accelerator Complex

The Relativistic Heavy Ion Collider (RHIC) [95, 96] at Brookhaven National Laboratory (BNL) is capable of accelerating nuclear beams of various ions from protons to gold. An energy of 100 GeV per nucleon is achieved for the heavy ion beams. Proton beams are accelerated up to 250 GeV energy. RHIC accelerates counter-circulating beams in two different rings crossing each other at six interaction regions. Figure 36 represents a schematic view of the RHIC accelerator complex.

RHIC provides an opportunity to study collisions of polarized protons. It is capable of accelerating beams of polarized protons up to 250 GeV with polarizations up to 70%. In 2001, RHIC accomplished the first physics Run colliding beams of polarized protons. RHIC is the first polarized-proton collider and represents an exceptional laboratory for investigating the proton. At present, RHIC also provides the highest energy for  $p-p$  collisions at accelerators. At the RHIC energy and luminosity, the collisions of polarized protons can evidently be considered as collisions of polarized quarks and gluons. The polarized quarks and gluons at RHIC are strongly interacting probes; they supplement the knowledge obtained from the DIS experiments which used polarized lepton probes to investigate the proton spin structure. DIS itself is sensitive only to the combined contributions of quarks and antiquarks of each flavor. The strong-interaction probes at RHIC are sensitive to the gluon polarization,  $\Delta g$ , and can be used for quark spin-flavor separation in

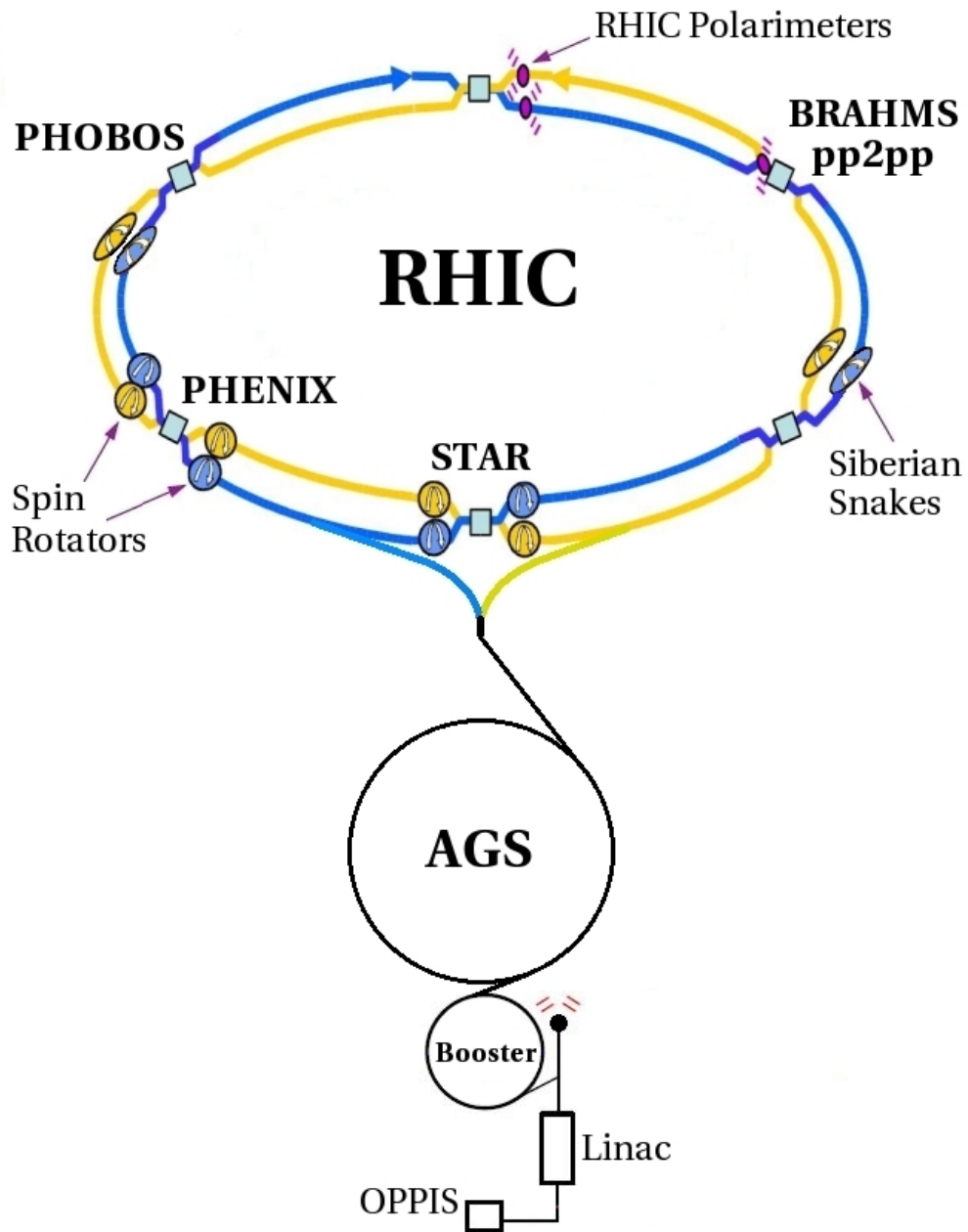


Figure 36: Schematic view of the RHIC accelerator complex

$W^\pm$  boson production. The individual polarizations of the  $u, \bar{u}, d,$  and  $\bar{d}$  quarks in the proton can be measured directly and to a high degree of accuracy using the parity-violating production of the  $W^\pm$  bosons in  $u + \bar{d} \rightarrow W^+ \rightarrow l^+ + \nu$  and  $d + \bar{u} \rightarrow W^- \rightarrow l^- + \bar{\nu}$ .

The RHIC apparatus relevant to the polarized  $p - p$  collisions are illustrated in Figure 36. The route for the proton injection to the RHIC rings starts from an intense polarized  $H^-$  ion source. The source feeds a chain of accelerators: protons are accelerated in the Linac, Booster, and Alternating Gradient Synchrotron (AGS). Then individual proton bunches are injected from the AGS into two RHIC rings at 22 GeV. The beam in the Blue ring runs clockwise and the beam in the Yellow ring runs counter-clockwise. The injection is repeated 120 times for each ring, thus there are 120 bunches in each beam. In each ring the beams of polarized protons are then accelerated to up to 250 GeV for collisions at interaction regions. The perimeters of the rings are 3.843 km, thus one turn at RHIC is roughly  $13 \mu\text{s}$ . The time interval between bunch buckets is 106 ns. Typical bunch length for the proton beam is 60 cm (2 ns). Note, that the bunches are created independently at the source, so that the bunches in the same beam can have alternate polarization sign.

The RHIC design specifications are as follows. The AGS is capable of transferring to RHIC individual bunches of  $2 \times 10^{11}$  protons with 70% polarization. RHIC is capable of colliding beams at center-of-mass energy of  $\sqrt{s} = 50\text{-}500$  GeV. For the highest RHIC center-of-mass energy of  $\sqrt{s} = 500$  GeV the design luminosity is  $\mathcal{L} = 2 \times 10^{32} \text{ s}^{-1} \text{ cm}^{-2}$ . The actual RHIC performance for specific PHENIX runs is

given later in Chapters 6.1 and 6.7.

There are six interaction regions at RHIC called 2, 4, 6, 8, 10, and 12 o'clock, where two bunches of the two beams are collided at an angle of  $0^\circ$ . There are five detectors at RHIC located at four collision points and used to investigate various types of collisions: PHENIX, STAR, BRAHMS, PHOBOS, and pp2pp. Table 2 shows the detectors at the RHIC interaction regions.

Table 2: RHIC experiments

Interaction region (o'clock)	Detector
2	BRAHMS, pp2pp
4	—
6	STAR
8	PHENIX
10	PHOBOS
12	—

All RHIC experiments have spin programs [24]. PHENIX and STAR are the two largest experiments at RHIC. These detectors are quite complementary: STAR (Solenoid Tracker At RHIC) [97] tracks and identifies charged particles within a large solid angle coverage, whereas the strength of the PHENIX is in measuring hadrons, leptons and photons at both high-multiplicity and high-rate environments.

PHENIX and STAR consider spin physics as a major part of their program. These experiments measure gluon and quark polarizations with hard scattering. The BRAHMS and pp2pp experiments share one collision point, the PHOBOS experiment is situated in another interaction region. BRAHMS [98] measures hadrons over wide ranges of rapidity and momentum using two magnetic spectrometers. PHOBOS [99] consists of a large number of silicon detectors surrounding the collision point to measure charged particle multiplicities. Both BRAHMS and PHOBOS measure transverse spin asymmetries. In addition, the pp2pp [100, 101] experiment measures spin dependence in small-angle elastic scattering. The BRAHMS, PHOBOS, and pp2pp experiments successfully accomplished their physics programs by 2006. PHENIX and STAR, two principal RHIC experiments, continue operation improving their capabilities for physics measurements.

There are several polarized-proton-specific tools at RHIC: Polarimeters, Siberian Snakes, and Spin Rotators. Polarimetry [102] at RHIC is based on a polarized hydrogen gas jet target and elastic proton-carbon scattering in the Coulomb-nuclear-interference (CNI) region. The polarized hydrogen gas jet target is used at RHIC to determine the beam polarization precisely. For frequent measurements RHIC uses the proton-carbon CNI scattering to monitor the beam polarization.

Siberian Snakes [103] are installed at RHIC to maintain the proton polarization during acceleration process. The proton spin responds to focusing and error magnetic fields in the rings, and this causes depolarization of the proton beam. In order to avoid the depolarization, strings of superconducting helical dipole magnets

are used to rotate the proton spin  $180^\circ$  around an axis in the horizontal plane each time the beam passes the device. In result, each two passes cancel the cumulative tilts of the spin.

There are also special strings of dipole magnets located before and after the PHENIX and STAR interaction regions which are used to alter the spin orientation from vertical to longitudinal direction relative to the beam. This allows conducting both transverse-spin physics studies at all experiments and longitudinal-spin physics studies at PHENIX and STAR. Longitudinal spin orientation is essential for investigation of the gluon polarization in the proton and parity-violating physics.

## 5.2 Luminosity in the Collider and Other Definitions

In this chapter, the definitions of some variables used to describe Nuclear Physics experiments are given. The event rate,  $N$ , in a collider is proportional to the interaction cross-section  $\sigma_{int}$ :

$$N = \mathcal{L}\sigma_{int}, \quad (77)$$

where the factor of proportionality,  $\mathcal{L}$ , is called the luminosity. For the collision of two bunches containing number of particles  $n_1$  and  $n_2$ , the instantaneous luminosity can be written as

$$\mathcal{L} = f \frac{n_1 n_2}{4\pi\sigma_x\sigma_y}. \quad (78)$$

Here  $f$  is the collision frequency, and  $\sigma_x$  and  $\sigma_y$  are the average width of the bunches in the horizontal and vertical directions.  $\mathcal{L}$  is measured in units of  $\text{cm}^{-2}\text{s}^{-1}$ . The

integrated luminosity can be calculated by integrating the instantaneous luminosity over time:

$$\mathcal{L}_{int} = \int \mathcal{L} dt. \quad (79)$$

The integrated luminosity is usually stated in the inverse units used for cross-sections,  $\text{b}^{-1}$  (inverse barn,  $1 \text{ b} = 10^{-24} \text{ cm}^2$ ).

The rapidity,  $y$ , of a particle is defined by

$$y \equiv \frac{1}{2} \ln \left( \frac{E + p_z}{E - p_z} \right), \quad (80)$$

where  $E$  is the particle energy and  $p_z$  is the  $z$ -component of momentum of the particle (usually along the beam direction).

The pseudorapidity,  $\eta$ , of a particle is defined by

$$\eta \equiv \frac{1}{2} \ln \left( \frac{p + p_z}{p - p_z} \right) = - \ln \tan \left( \frac{\theta}{2} \right), \quad (81)$$

where  $p$  is the scalar value of momentum and  $\theta$  is the polar angle of the particle direction relative to the  $z$ -axis ( $\cos \theta = p_z/p$ ). The pseudorapidity,  $\eta$ , can be measured when the mass,  $m$ , and momentum of the particle are unknown. The pseudorapidity is approximately equal to the rapidity,  $y$ , for  $p \gg m$ .

Helicity,  $\lambda$ , is the projection of the spin,  $\vec{S}$ , of a particle onto the direction of momentum,  $\vec{p}$ , of the particle:

$$\lambda = \frac{\vec{S} \cdot \vec{p}}{|\vec{p}|}. \quad (82)$$

The helicity is positive (also called right-handed), when the spin and the momentum of the particle are aligned, and it is negative (left-handed), when the spin and the momentum are anti-aligned (see Figure 37).

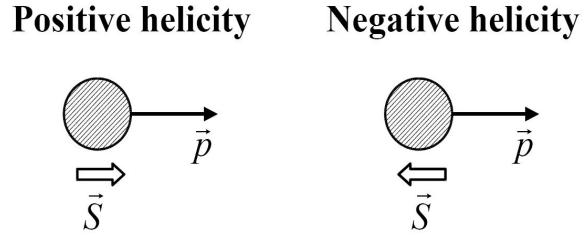


Figure 37: Helicity

### 5.3 The PHENIX Experiment Overview

The Pioneering High Energy Nuclear Interaction eXperiment (PHENIX) [104] performs a study of various types of collisions:  $p - p$ ,  $p - A$ , and  $A - A$ , probing different fundamental features of the strong interaction. Two primary areas of research performed at the PHENIX experiment are:

- 1) to detect the formation of a new phase of matter, a deconfined state of nuclear matter called the Quark Gluon Plasma (QGP) [105], in relativistic heavy ion collisions and to study the properties of the QGP;
- 2) to study the spin structure of the nucleon by determining the contributions from anti-quarks and gluons in polarized proton-proton collisions.

The aim of the first area of research is to study QGP, the state of the universe at the time of order of a  $\mu s$  after the “Big Bang”. It is predicted by Quantum Chromodynamics (QCD) that heavy nuclei collisions at ultrarelativistic energies will cause a phase transition of the nuclei from hadronic matter to a deconfined state of quarks and gluons which will move freely over a volume approximately  $10 \text{ fm}^3$  [105]. Fundamental characteristics of the QGP, Debye screening of QCD

interactions and chiral symmetry restoration, are important components of the PHENIX measurements [104]. The thermal radiation is important as well, because it defines the temperature of the system created in the collisions. The PHENIX advantage is the possibility to study both lepton and hadron signatures in the same experiment. By measuring leptons and prompt photons one can probe directly the QGP phase, whereas measuring hadrons provide complementary information about the later hadronization of the QGP. QGP study is a very broad area of research at the PHENIX experiment, but this dissertation work is devoted to the other primary PHENIX goal: to measure the spin structure of the nucleon.

### 5.3.1 The PHENIX Detector Subsystem Overview

The PHENIX detector consists of a number of subsystems and employs many different detector technologies. Global detectors [106] are used to measure the start time, vertex, and multiplicity of collisions. Two central spectrometers (Central Arms) [107, 108, 109] at central rapidity are instrumented to detect photons, charged leptons, and hadrons. Two forward rapidity spectrometers (Muon Arms) [110] are used to detect muons. A three-dimensional drawing of the PHENIX detector is shown in Figure 38. A summary, including rapidity and azimuthal angle  $\phi$  coverages as well as functional characteristics of the PHENIX detector subsystems used in the analysis of this dissertation work, is given in Table 3. Figure 39 shows the PHENIX detector performance for the detection of various particle species.

The global detectors are used to characterize an event following a collision. The

Table 3: Summary of the PHENIX detector subsystems used in the analysis

Subsystem	$\Delta\eta$	$\Delta\phi$	Function and characteristic
Global detectors:			
Beam-Beam (BBC)	$\pm(3.1 \text{ to } 3.9)$	$360^\circ$	Start time, vertex.
Muon Arms:			
Muon Tracker (MuTrS)	$-1.15 \text{ to } -2.25$	$360^\circ$	Tracking for muons.
Muon Tracker (MuTrN)	$1.15 \text{ to } 2.44$	$360^\circ$	Tracking for muons.
Muon Identifier (MuIDS)	$-1.15 \text{ to } -2.25$	$360^\circ$	$\mu$ /hadron separation.
Muon Identifier (MuIDN)	$1.15 \text{ to } 2.44$	$360^\circ$	$\mu$ /hadron separation.
Central Arms:			
Drift Chambers (DC)	$\pm 0.35$	$90^\circ \times 2$	Tracking for charged hadrons/leptons.
Pad Chambers (PC)	$\pm 0.35$	$90^\circ \times 2$	Pattern recognition, tracking for unbent direction.
Magnets:			
Central (CM)	$\pm 0.35$	$360^\circ$	Up to 1.15 T·m.
Muon (MMS)	$-1.1 \text{ to } -2.2$	$360^\circ$	0.72 T·m for $\eta=2$ .
Muon (MMN)	$1.1 \text{ to } 2.4$	$360^\circ$	0.72 T·m for $\eta=2$ .

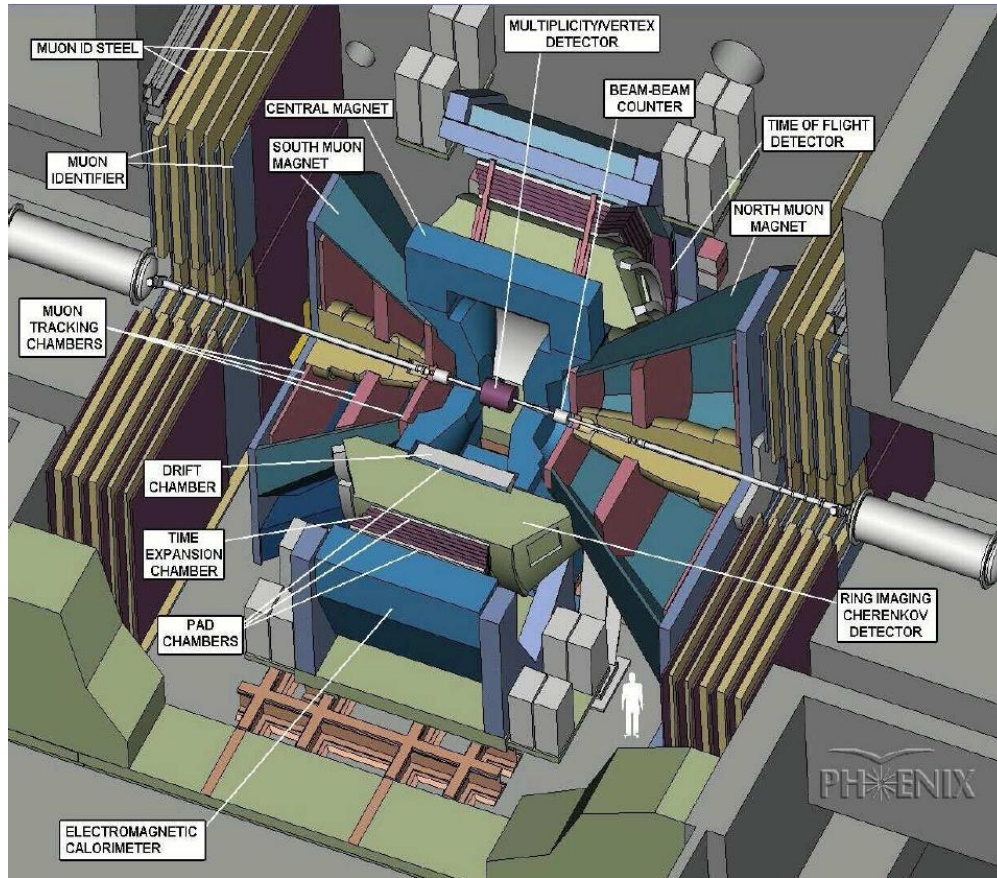


Figure 38: A three-dimensional sectional view drawing of the PHENIX detector with the labeled subsystems [111]

PHENIX experiment utilizes mainly two global detectors: Zero-Degree Calorimeters (ZDC) and Beam-Beam Counters (BBC). A pair of Beam-Beam Counters is positioned 1.4 meters away from the beam-crossing point along the beam axis on either side of the interaction point. The BBC operation is based on the time-of-flight measurements of forward particles produced at glancing angles. The BBCs are used as the primary trigger of beam-beam collisions (the minimum-bias interaction trigger, which requires at least one hit in each BBC). They determine the time origin of the collisions and the collision position along the beam axis (vertex

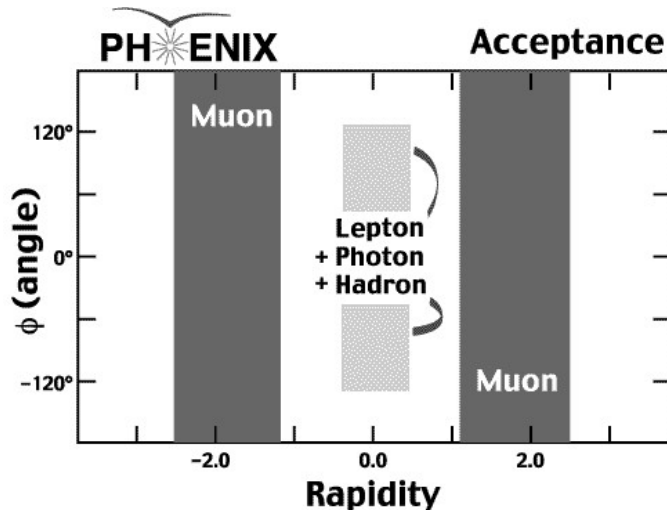


Figure 39: The PHENIX detector performance for the detection of various particle species

position of an event). For  $p - p$  collisions, the BBC vertex resolution is about 2 cm. Each Beam-Beam Counter comprises 64 modules of counter elements. Each counter element includes a radiator of fused quartz 3 cm long and a photomultiplier tube (PMT) of 1 inch diameter. The counter elements are arranged in a cylinder coaxial with the beam. The BBCs measure the arrival times of the fast leading charged particles from beam-beam collisions on both sides of the collision vertex. From the average and the difference of these arrival times the time origin of the collision (the event start time) and the vertex position of the collision along the beam direction ( $z_{vtx}$ ) are determined, respectively.

The North and South Muon Arms cover pseudorapidity ranges of  $-2.25 \leq \eta \leq -1.15$  for the South Arm and  $1.15 \leq \eta \leq 2.44$  for the North Arm and both have full azimuthal coverage. They are coaxial with the beam on opposite sides of the beam-interaction point. Each arm comprises a Muon Tracker (MuTr) followed by a Muon

Identifier (MuID). The Muon Trackers consist of three stations of multi-plane drift chambers which perform precise tracking and measure particle momenta. The Muon Identifiers consist of alternating layers of steel absorbers and tracking layers of the Iarocci-type streamer tubes and serve as a muon trigger. The pion contamination of identified muons is of order  $10^{-4}$ . The MuTr and MuID are described in more detail in Chapter 5.4.

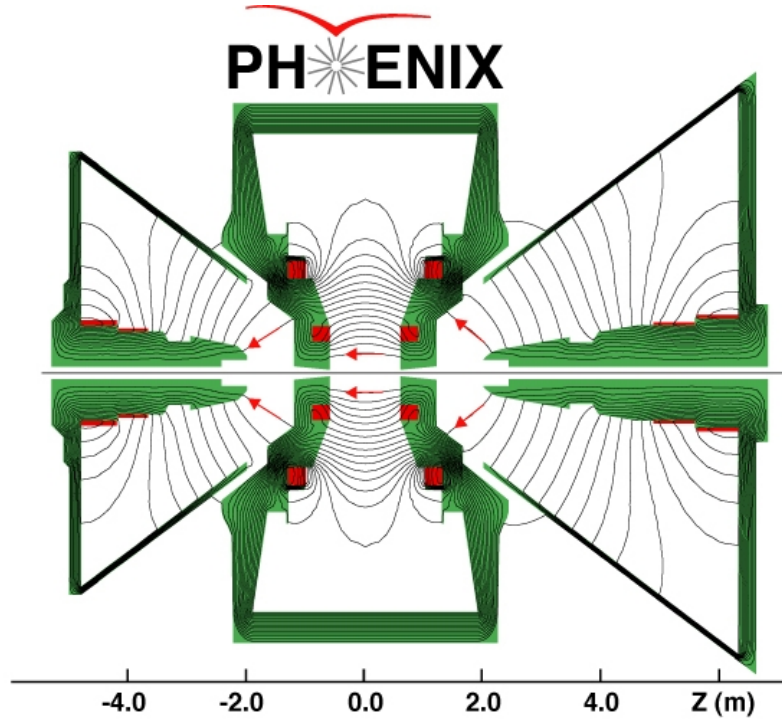
The East and West Central Arms are located with the midpoint at zero rapidity. They comprise a tracking system for charged particles, electromagnetic calorimetry and a particle identification system. The precise tracking is accomplished by means of an intermediate tracker made of Drift Chambers (DC) and Pad Chambers (PC1). Also, the Central Arms consist of a Ring Imaging Cherenkov Detector (RICH), an outer tracker comprised of two Pad Chambers (PC2 and PC3) before and after Time-Expansion Chambers (TEC), Time-Of-Flight scintillators (TOF) and Electromagnetic Calorimeters (EMCal) of the lead-scintillator type (PbSc) and of the lead-glass type (PbGl). The multiwire focusing DC provides high resolution transverse-momentum,  $p_T$ , measurements. Three Pad Chambers PC1, PC2 and PC3 provide a three-dimensional position measurement to aid in pattern recognition and to determine  $p_z/p_T$ . The TEC located between PC2 and PC3 assists in pattern recognition and provides electron-pion separation from energy-loss information. The RICH serves as one of the primary devices for the identification of electrons. It is located between the inner (DC/PC1) and the outer (PC2/TEC/PC3) tracking chambers. The entire region is filled with a Cherenkov radiator gas. The

Cherenkov photons generated by high momentum charged particles are reflected by spherical mirrors placed within the radiator volumes and the photons are focused onto photon detectors placed just behind the PHENIX Central Magnet. The TOF, positioned between the outer tracking chambers and the EMCal, serves to identify hadrons. It consists of 1056 elements of scintillator slats with photomultiplier tube readouts. The primary goal of the EMCal is to identify electrons and photons and to measure their position and energy. Hadrons with kinetic energy of more than about 200 MeV do not produce usually a response in the calorimeter proportional to their full energy, since the calorimeter is thin. Comparison of the momentum of charged particles with the energy response of the calorimeter provides a tag for electron identification. Because from the Central Arms only the tracking information is necessary to the analysis of this dissertation work, data only from the inner tracker, made of the DC and PC1, are acquired for the analysis. The DC is described in more detail in Chapter 5.5.

The detectors described above generally consist of segmented subdetectors so as to have one particle being detected by one subdetector segment. The segmentation or the granularity of the detector is required due to the high multiplicity of events. The occupancy of a detector is the ratio of the number of particles to the number of subdetectors.

There are three magnets in the PHENIX detector. The Central Magnet [112] produces an axial magnetic field for the Central Arms; this magnetic field is parallel to the beam axis. The Muon Magnets provide a radial magnetic field for each Muon

Tracker, which bends particles in the azimuthal direction. Magnet characteristics are given in Table 3. Figure 40 shows the magnetic field lines of the magnetic fields produced by the Central Magnet and the two Muon Magnets.



Magnetic field lines for the two Central Magnet coils in combined (++) mode

Figure 40: Magnetic field produced by the Central Magnet and two Muon Magnets

Events following collisions are collected and stored by means of PHENIX electronics and computing resources [113, 114]. The PHENIX detector has a large number of ADC and TDC channels, and the number of channel counts varies for different subsystems. Front-End Electronics (FEE) were developed for the PHENIX subsystems in order to obtain primary signals from collision events. The FEE is the interface between the PHENIX subsystems and the PHENIX Data Acquisition (DAQ) system. The signals from the FEEs are transferred by means of optical

fibers to the Level-1 trigger, which collects signals from the different PHENIX subsystems and makes a decision to accept or reject an event. The timing of the Level-1 trigger is synchronized with the RHIC master timing system and the trigger works for every beam bunch crossing. After an event is accepted by the Level-1 trigger, the data packets from the different subsystems are collected by event builders which put together the events in the final form. The On-Line Computing System (ONCS) controls the electronics and the data flow. The offline system performs the event reconstruction of the assembled data. This way, raw data are turned into the physics data, which are ready for data analysis.

### 5.3.2 The PHENIX coordinate system

Figure 41 shows the PHENIX coordinate system. The  $z$ -axis is chosen to be

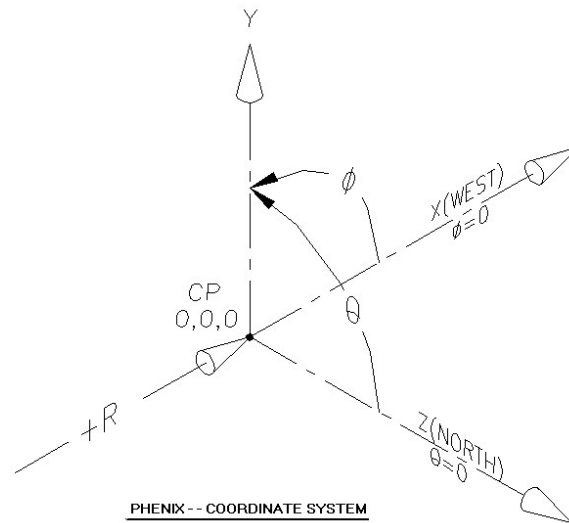


Figure 41: The PHENIX coordinate system

directed along the beam line which runs straight in the PHENIX experimental

area. Positive  $z$ -direction is pointed to the north, i.e., to the North Muon Arm. The polar angle  $\theta$  and azimuthal angle  $\phi$  are defined relative to the  $z$ -axis. The north direction is chosen as  $\theta = 0^\circ$  and the south is chosen as  $\theta = 180^\circ$ . The west direction is chosen as  $\phi = 0^\circ$  and the east is chosen as  $\phi = 180^\circ$ . In this coordinate system, rapidity (pseudorapidity),  $y(\eta)$ , of a particle going to the North Muon Arm is positive, and it is negative if a particle goes to the South Muon Arm. Figure 42 represents a cutaway schematic view of the PHENIX detector with the PHENIX coordinate system axes shown.

#### 5.4 The Muon Arms

The PHENIX Muon Arms [110] serve in detecting muons at forward rapidity ranges with full azimuthal acceptance. They track, identify muons, and provide rejection of pions and kaons with a factor of  $\sim 10^{-3}$ . The PHENIX Muon Arms are designed to explore the decay of vector mesons to dimuon pairs, to allow the investigation of Drell-Yan process and heavy-flavor production. Two Muon Arms are placed along the direction of the beam pipe on each side of the beam interaction point. They are similar in construction except for the size in the  $z$ -direction. Each Muon Arm consists of a Muon Tracker (MuTr) and a Muon Identifier (MuID). In order to improve the performance of the Muon Detectors, absorber shields are placed prior to the first tracking station of the MuTr: 20 cm of copper (the nosecone) and 60 cm of iron (part of the MuTr magnet). These absorbers noticeably reduce the MuTr occupancy and provide the first level of pion rejection. The construction

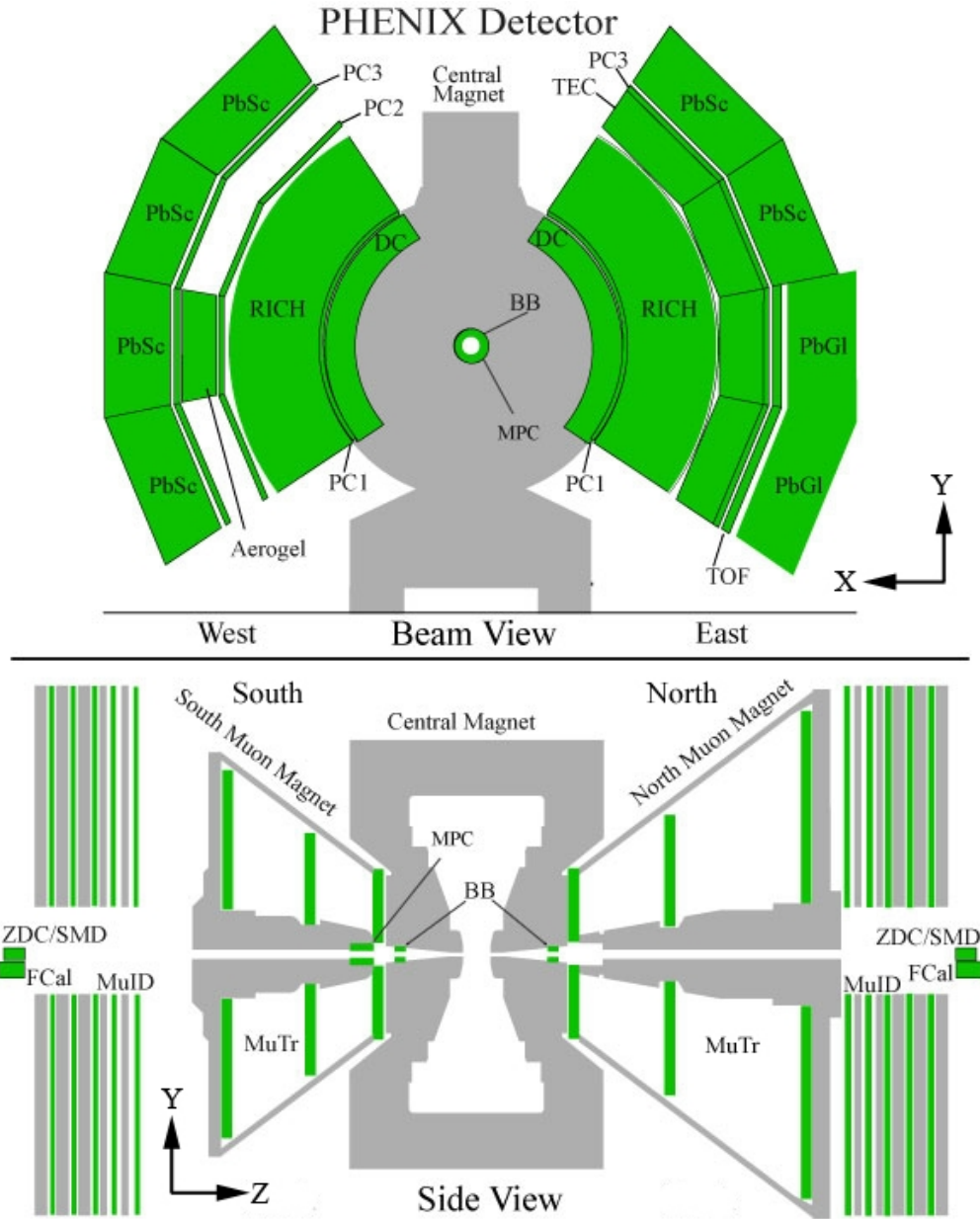


Figure 42: A cutaway schematic view of the PHENIX detector with the PHENIX coordinate system axes

and performance of the MuTr followed by the construction and performance of the MuID are discussed below.

#### 5.4.1 The Muon Tracker

The Muon Tracker consists of three stations of tracking chambers with cathode-strip readout. The cathode-strip orientations and readout planes vary in each station. The stations are installed inside the conical-shaped Muon Magnets described in Chapter 5.3.1 and in more detail in the paper about PHENIX magnets [112]. Each station is arranged in a plane perpendicular to the beam axis. The Muon Tracker construction is shown in Figure 43. Particles originating in the beam inter-

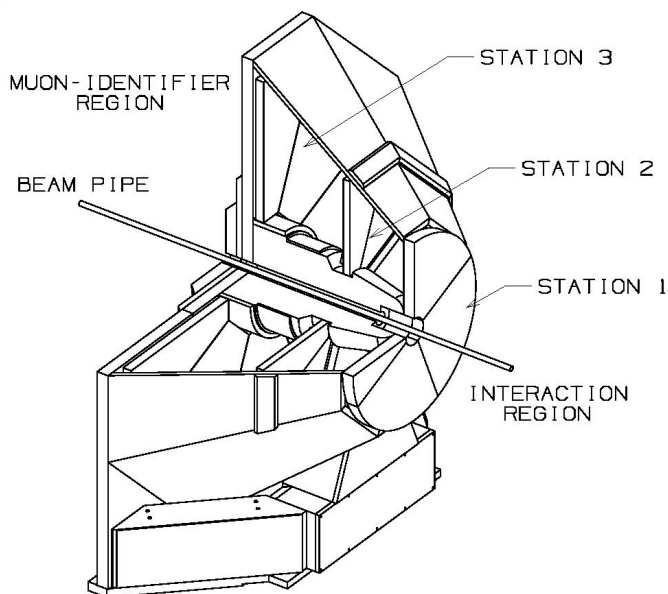


Figure 43: The Muon Arm tracking spectrometer (MuTr) [110]

action region intersect successively the multiple ionization gaps of the stations 1, 2, and 3 and then proceed to the MuID detector. An ionizing particle usually fires three adjoining strips in the cathode planes. The design of the Muon Tracker is

determined by the requirement that the non-stereo cathode planes have to provide 100  $\mu\text{m}$  spacial resolution measurements of the particle trajectories.

Each of the three stations is divided in eight segments called octants, thus making each station comprised of eight cathode-strip chambers (CSC). All CSC include several chamber gaps. Each chamber gap consists of two cathode-strip planes and one intermediate anode plane with a 3.175 mm distance between planes. The cathode-strip planes are made of 5 mm cathode strips with alternate strip readout. The CSC of each of the three stations is uniquely designed. For the mechanical construction of the cathode-strip planes, honeycomb technology was used for stations 1 and 3 and thin foil technology was used for station 2. A cathode pattern of each station was produced with an accuracy of better than 25  $\mu\text{m}$ . The anode planes have alternating structure of 75  $\mu\text{m}$  breadth gold-coated Cu-Be field wires and 20  $\mu\text{m}$  breadth gold-coated tungsten sense wires with a spacing of 10 mm between sense wires. The cathode strips are perpendicular to the anode wires in half of the cathode-strip planes; the other half of the cathode-strip planes have the strips at stereo angles from  $0^\circ$  to  $\pm 11.25^\circ$  relative to the perpendicular strips. The gas mixture of 50% Ar + 30% CO<sub>2</sub> + 20% CF<sub>4</sub> recirculates in the chambers. The typical operating high voltage for the chambers is 1850 V with a gain of  $\sim 2 \times 10^4$ . In these operating conditions, the charge of approximately 100 electrons is produced by a minimum-ionizing particle in the CSC.

The closest station to the interaction region is station 1. That is why the station-1 CSC have several distinctive features. First of all, the station-1 CSC are the

smallest in size — the distance from the inner radius to the outer radius of station 1 is  $\sim 1.25$  m. Second, the chambers have the highest occupancy per strip. Third, they are built up in quadrants (two electrically divided octants combined together). Each quadrant comprises three chamber gaps of the construction discussed above. Thus the quadrant contains 6 cathode-strip planes sandwiched by 3 anode planes. The cathode plane strips were made by laminating honeycomb panels with photo-etched copper clad FR-4.

The demand of good momentum resolution imposes requirements for the thickness of station 2. In order to provide good momentum resolution, the thickness of station 2 has to be  $\leq 0.1\%$  of a radiation length. Therefore the station-2 cathode-strip planes were produced by etching 25-micron mylar foils coated by 600 Å copper layer. Each station-2 CSC consists of three chamber gaps, each containing a pair of cathode foils on either side of an anode wire plane. All three chamber gaps are isolated by ground foils.

Station 3 is the most distant station from the collision region, therefore the station-3 tracking chambers are the largest in size — the distance from the inner radius to the outer radius of the station 3 is  $\sim 2.4$  m. Each station-3 CSC detector consists of two chamber gaps. Thus, each octant contains 4 cathode-strip planes sandwiched by 2 anode-wire planes. The cathode-plane strips were made by mechanically routing shallow lines in the copper clad FR-4 sheets laminated on the honeycomb panels.

An optical alignment system was mounted in order to assist with maintaining

good momentum resolution. The system monitors relative displacements of the chambers to  $\pm 25 \mu\text{m}$ . The configuration of the optical alignment system is shown in Figure 44. Seven optical beam lines circumscribe each octant chamber. Each

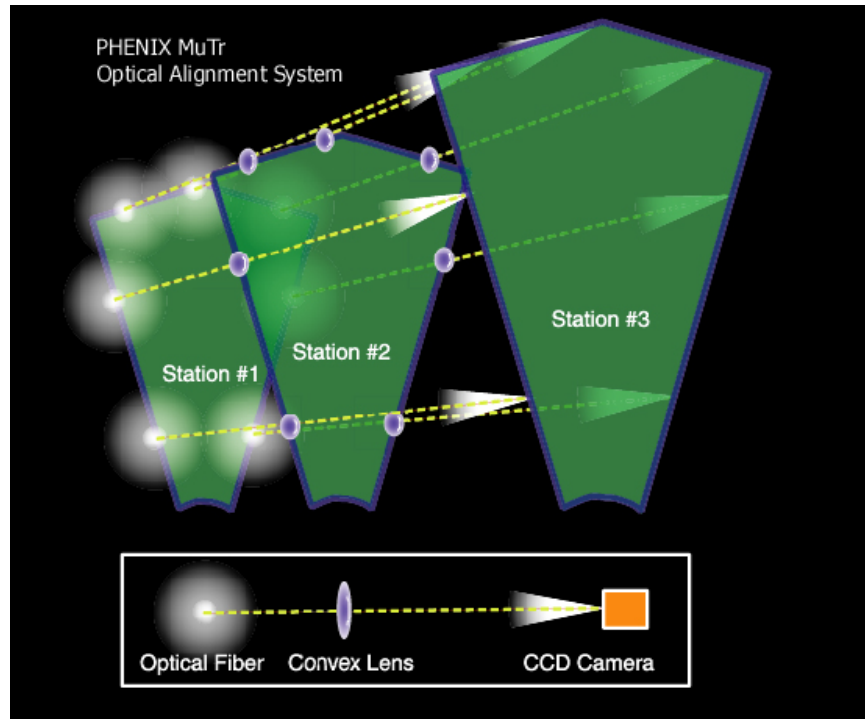


Figure 44: MuTr optical alignment system [115]

optical line comprises an optical-fiber light source at station 1, a convex lens at station 2, and a CCD camera at station 3. Light from the optical fiber is directed from station 1 through the convex lens to the CCD at station 3.

The Muon Tracking Front End Electronics (FEE) obtains primary signals from collision events. Because of space constraints, the FEE are mounted directly on the chambers. The electronics amplifies and collects analog hit information from the MuTr chamber cathode strips. Timing signals traveled on optical fibers (GLink) are translated to copper wires (CLink) right outside the Muon Magnets and transferred

to the electronics by means of 7-m cables. After a Level-1 trigger is received from the PHENIX Granule Timing Module (GTM), all collected signals are digitized and outgoing data are transported via cables to the CLink/GLink interface and then via optical fibers to the PHENIX Data Collection Module (DCM) in the counting house.

Another set of electronics is installed in the racks outside of the Muon Magnets. This electronics includes the high-voltage power supplies, the low-voltage power for the electronics, interfaces for fiber optics, calibration electronics, and auxiliary controls and monitoring.

The temperature of the electronics is very important parameter to control, because some parts of the electronics are very receptive to temperature and the FEEs operate continuously inside the Muon Magnets for very prolonged periods of time. To monitor the electronics temperature, the slow-control system, based in the AR-CNet protocol, is used. To keep the electronics at operating temperature, a water-cooling system is used.

The complete installation of the South Muon Tracker inside the Muon Magnets along with all electronics systems in the PHENIX Experimental Hall was accomplished in January 2001. The North Muon Tracker and accompanying electronics installation in the PHENIX Experimental Hall was completed in August 2002. The detector has been shown to be robust and all systems, including the electronics, the low-voltage system, and the high-voltage system with nominal high voltage of 1850 V, demonstrated stability over long runs of data taking for several years.

Data from cosmic-ray test runs showed that a spacial resolution of  $\sim 100 \mu\text{m}$  was achieved with the station-2 chambers. Clusters in each cathode-strip readout plane were fit to obtain the centroid positions of the hits. The positions from 5 stereo cathode-strip planes were fit by a straight line and projected to the sixth non-stereo cathode plane. The plot in Figure 45 is the difference between the projected straight-line fit and the measured position on the sixth plane. The composite

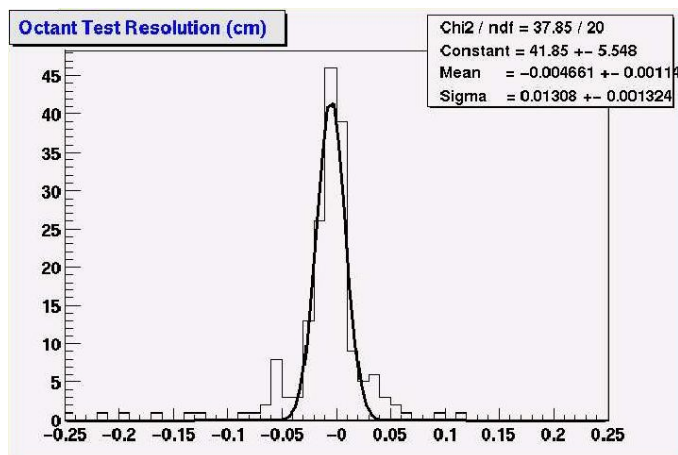


Figure 45: Position resolution measured in cosmic-ray test runs for the station 2 [111]

chamber plus projection error is about  $131 \mu\text{m}$ , which is consistent with the  $100 \mu\text{m}$  spacial resolution. The MuTr provides a momentum resolution of  $\sigma_p/p \approx 5\%$  (almost momentum independent).

#### 5.4.2 The Muon Identifier

The Muon Identifier design requirement for a pion from the vertex to be misidentified as a muon is  $2.5 \times 10^{-4}$ . To provide the required pion rejection, in addition to the nosecone and the Central Magnet material preceding the Muon

Arms, a steel of total depth of 90 cm (5.4 hadronic interaction lengths) is necessary to filter pions. The thickness of the Muon Magnet backplate prior to the North Arm MuID is 30 cm, thus a depth of 60 cm of steel is required inside the MuID volume. Four alternating layers of steel absorbers of thickness 10, 10, 20, and 20 cm are placed in the MuID. These absorber layers, along with the Muon Magnet backplate, form five gaps. Each gap contains MuID panels, described below. Dividing the MuID steel absorber into several layers is determined by the intention to improve the particle trajectory measurements in the MuID. The North Arm MuID and the South Arm MuID are identical in construction except that the South Muon Magnet backplate is 20 cm thick. Both MuIDs are located at the same distance from the collision vertex.

With all the material placed prior to the Muon Arms and inside the Muon Arms, only muons with a minimum average energy of 1.9 GeV at the collision vertex can reach the MuID and only muons with a minimum average energy of 2.7 GeV at the collision vertex are able to reach the last gap (Gap 5) of the MuID.

The basic elements of the MuID are Iarocci tubes. The Iarocci tube is a planar drift tube consisting of 100  $\mu\text{m}$  breadth gold-plated Cu-Be anode wires at the center of long channels surrounded by a graphite-coated plastic cathode. There are 8 channels in a tube. Each individual channel comprises an anode wire and the space around the wire along with the cathode walls. Thus there are 8 anode wires in a tube. In order to increase the service life of the Iarocci tubes, they are used in the proportional mode at 4500 V.

The length of the Iarocci tubes varies in different MuID panels. The typical tube length is a few meters. Therefore, each wire inside the tubes is supported at the center of a channel by plastic spacers located every 50 cm along the tube. The width of the Iarocci tubes is 8.4 cm.

All 8 internal wires inside a tube are connected together. Some tubes are oriented horizontally and some of the tubes are oriented vertically. This provides readout spacing every 8.4 cm both in  $x$  and  $y$  directions forming 8.4 cm square segments. Such a dividing into the readout segments provides sufficient granularity for unambiguous matching of MuID roads to tracks in the MuTr.

The Iarocci tubes are grouped in pairs and staggered by half a channel, thus forming so called two-packs. A signal is read from one or another tube in a two-pack. Roughly half of the two-packs are oriented horizontally and half are oriented vertically inside an aluminum box. This formation is called a MuID panel. There are six panels in each gap located around the square hole for the beam pipe (see Figure 46). The panels are labeled A through F clockwise from the upper left corner. The large panels A, C, D and F are placed at the 4 corners of the gap. Each contains 118 horizontal tubes of length 5200 mm and 128 vertical tubes of length 5010 mm. The small panels B and E are located above and below the square hole. Each contains 90 horizontal tubes of length 2504 mm and 52 vertical tubes of length 3821 mm. The total number of the tubes per gap is 1268 and they cover an area of 13.1 m wide by 10.7 m high in each gap. The total number of the tubes per arm is 6340.

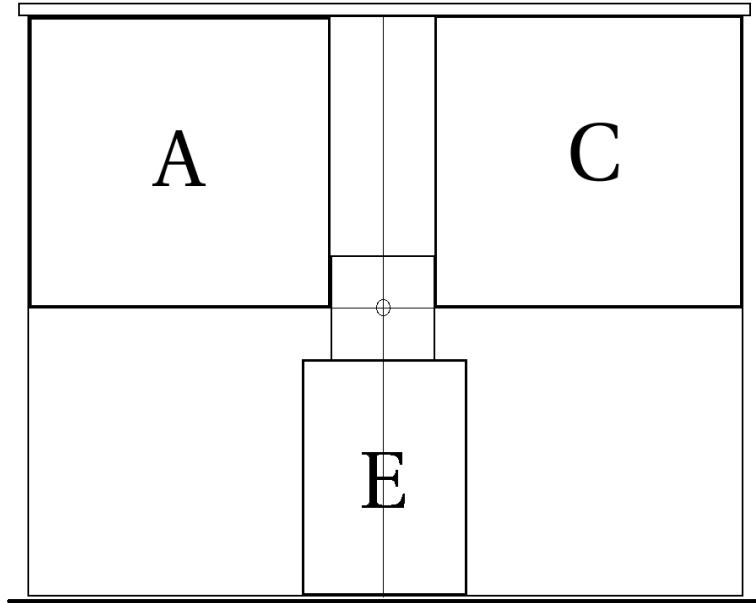


Figure 46: MuID panels in a gap (panels A, C and E shown) around the beam pipe hole (in the center)

To avoid dead spaces, adjoining panels are overlapped along their edges. In this way, the panels A, C and E (see Figure 46) are situated in the plane 10 cm closer to the collision vertex than the plane with the panels B, D and F.

The positions of the MuID panels relative to the vertex have to be controlled better than  $\pm 4$  mm in the horizontal and vertical directions in order to make alignment errors to be negligible in comparison with multiple scattering errors. The positions of the MuID panels in the  $z$ -direction need to be known within a few centimeters with respect to the vertex.

There are two gas volumes in the MuID. One volume is inside the Iarocci tubes. A mixture of  $\text{CO}_2$  and up to 25%  $i\text{-C}_4\text{H}_{10}$  circulates in this volume. Another volume is inside the aluminum boxes surrounding the tubes. This volume is filled

with  $N_2$  to keep the electronics dry and clean and to dilute the flammable gas in the case of a gas leakage from the Iarocci tubes.

The anode wires from two Iarocci tubes of a two-pack are connected into the same amplifier circuit, thus forming one readout channel. Every six readout channels are located on one circuit board of  $8.2 \times 50.4$  cm<sup>2</sup> size. The boards are placed inside the MuID panels at the tube end caps. The Iarocci tube high-voltage-distribution electronics is also mounted on the same in-panel boards, but on the opposite side of the boards to prevent human contact with the high voltage circuits.

Signals from the in-panel boards are transferred via 30 m twisted-pair cables to the out-panel electronics mounted in a set of four crates containing two types of cards: FEMs and ROCs. The FEM cards are the interface between the MuID and the PHENIX online system; they provide the timing and performance control. The ROC cards provide analog processing and synchronization. Thus, in the crates the signals are digitized and synchronized so all signals from the same beam crossing arrive at the same time.

Data from every beam crossing is sent as the Muon-Arm input to the Level-1 trigger. There is an algorithm implemented in the Level-1-trigger system which decides whether there was a candidate for a muon track in the event. This algorithm fits a road to the hits in the MuID panels and projects the road to the collision vertex. After an accept signal is received from the Level-1 trigger, the data from all ROC cards are transferred and assembled by the PHENIX DCM in the counting house.

The MuID performance and reconstruction efficiency were simulated with single-muon events and single-pion events [110]. Table 4 shows the conclusions from the simulations. The low  $\mu$  reconstruction efficiency at 2.0 GeV/ $c$  is caused by the

Table 4: Summary of the MuID performance simulation [110]

$p$ (GeV/ $c$ )	$\mu$ reconstruction efficiency (%)	$\pi$ rejection rate
2.0	$65.3 \pm 1.1$	$(2.0 \pm 1.4) \times 10^{-4}$
3.0	$93.7 \pm 1.4$	$(2.3 \pm 0.5) \times 10^{-3}$
4.0	$96.9 \pm 1.4$	$(2.5 \pm 0.5) \times 10^{-3}$
5.0	$98.1 \pm 1.4$	$(3.7 \pm 0.6) \times 10^{-3}$
10.0	$99.6 \pm 1.4$	$(3.9 \pm 0.7) \times 10^{-3}$

energy loss in the Central Magnet material and MuID absorber. The simulation of the single-pion events was used to evaluate the  $\mu/\pi$  rejection factor. The  $\pi$ -rejection rate shown in the Table 4 is the fraction of the simulated pions which can be misidentified as muons. This rate accounts for the contribution of decay muons from pion decays as well. The fraction of this rate which is not due to the decay muons is consistent with the MuID design requirement of  $2.5 \times 10^{-4}$  for a pion to be misidentified as a muon.

The MuID was constructed and commissioned entirely in the summer of 2001. Later on, a shielding inside the square hole was installed because, during initial data taking, a beam-related background was revealed. Figure 47 indicates the

strong correlation between the total charge collected in the PHENIX BBC and the

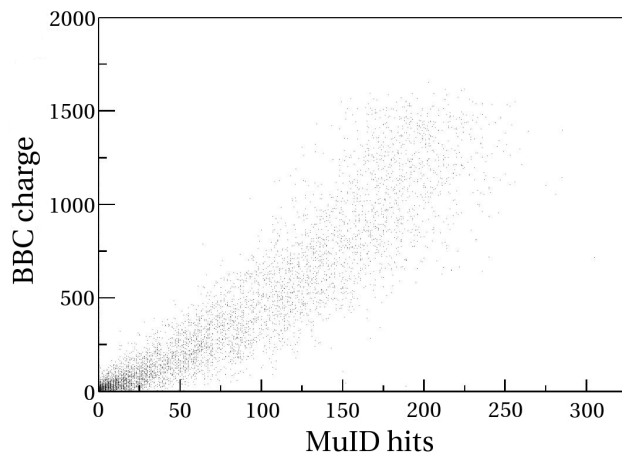


Figure 47: Beam-Beam Counter total charge versus number of hits in the MuID [116]

number of hits in the MuID. This demonstrates that the hits in the MuID are caused by beam collisions.

## 5.5 The Drift Chamber

The low-mass multiwire focusing Drift Chambers (DC) and Pad Chambers 1 (PC1) [107] compose the inner tracking system. The DC provides high resolution measurements of the charged particle trajectories from RHIC collisions in the  $x - y$  plane to obtain the transverse momentum,  $p_T$ , of the particles. The precise measurement of the longitudinal component of the momentum  $p_z$  is performed with the assistance of PC1. The DC also aids in the pattern recognition at high track occupancy, supplying initial position measurements which are used to relate tracks in different PHENIX detector subsystems.

The DCs are located in the two PHENIX Central Arms. The positions of the

DCs and PC1s in the Central Arms are shown on the upper part (Beam View) of the Figure 42. Both DC frames are cylindrically shaped with an inner radius of 2.03 m and an outer radius of 2.47 m from the beam line. Both frames are 2.4 m long along the  $z$ -direction. Figure 48 shows the structure of the DC frame. The

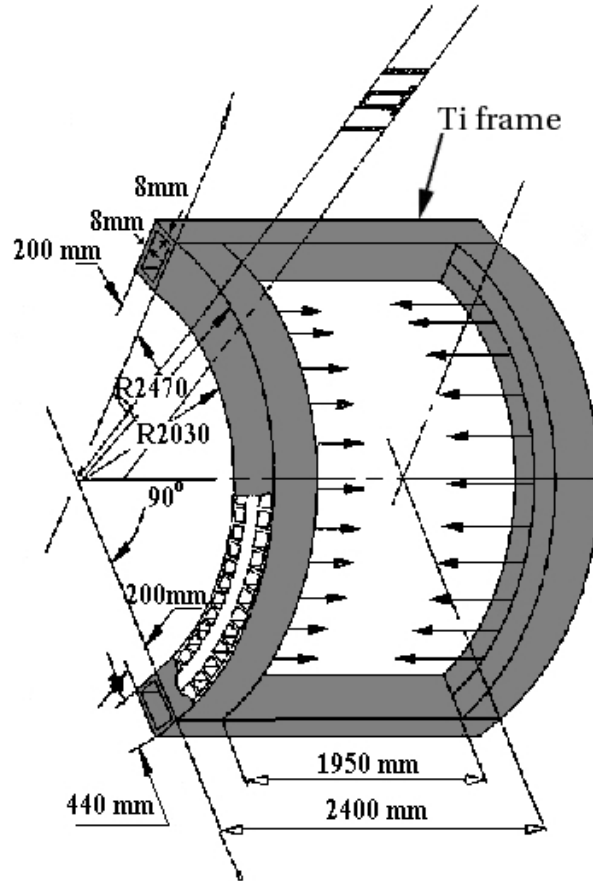


Figure 48: The DC frame structure

azimuthal coverage of the East Central Arm DC and the West Central Arm DC is  $\pi/2$  for each arm. The exact angular location of the DC in the PHENIX coordinate system is  $-34^\circ < \phi < 56^\circ$  for the West Arm and  $125^\circ < \phi < 215^\circ$  for the East Arm. The DC acceptance along the  $z$ -axis is  $\pm 90\text{ cm}$ .

The DC was designed with the following specifications: single-wire resolution better than  $150\ \mu\text{m}$  in  $r - \phi$  ( $x - y$ ) plane, single-wire two-track separation better than 1.5 mm, and spatial resolution in the  $z$ -direction better than 2 mm. The actual performance of the DC after fine adjustment of the electrostatic field in the chamber is as follows: the single-wire resolution is about  $165\ \mu\text{m}$  and the double-track resolution is better than 2 mm. These are very close to the design requirements. The track-finding efficiency is better than 99%.

The East Central Arm DC and the West Central Arm DC are similar in construction. Each DC is assembled inside cylindrical titanium frame (see Figure 48). Al-mylar windows limit the gas volume of the detector in the radial direction. There are 20 equal sectors in each DC inside each titanium frame. The azimuthal-angle  $\phi$  coverage of each individual DC sector is  $4.5^\circ$ . Each sector consists of six wire modules arranged sequentially in the radial direction: X1, U1, V1, X2, U2 and V2 (see Figure 49). Each module comprises 4 anode (sense) planes and 4 cathode planes. Thus, the drift space between the planes is about 2-2.5 cm in the  $\phi$ -direction. There are 12 anode wires in each X module and 4 anode wires in each U and V modules. Thus, there are 40 drift cells (pairs of anode and cathode wires) total in each DC sector.

The wires in the X1 and X2 modules are oriented parallel to the beam line ( $z$ -direction). They assist in the track measurements in the  $r - \phi$  direction. The wires in the U1, V1, U2, and V2 modules are placed with small stereo angles (of about  $6^\circ$ ) relative to the wires in the X modules. This way, the U and V modules assist in

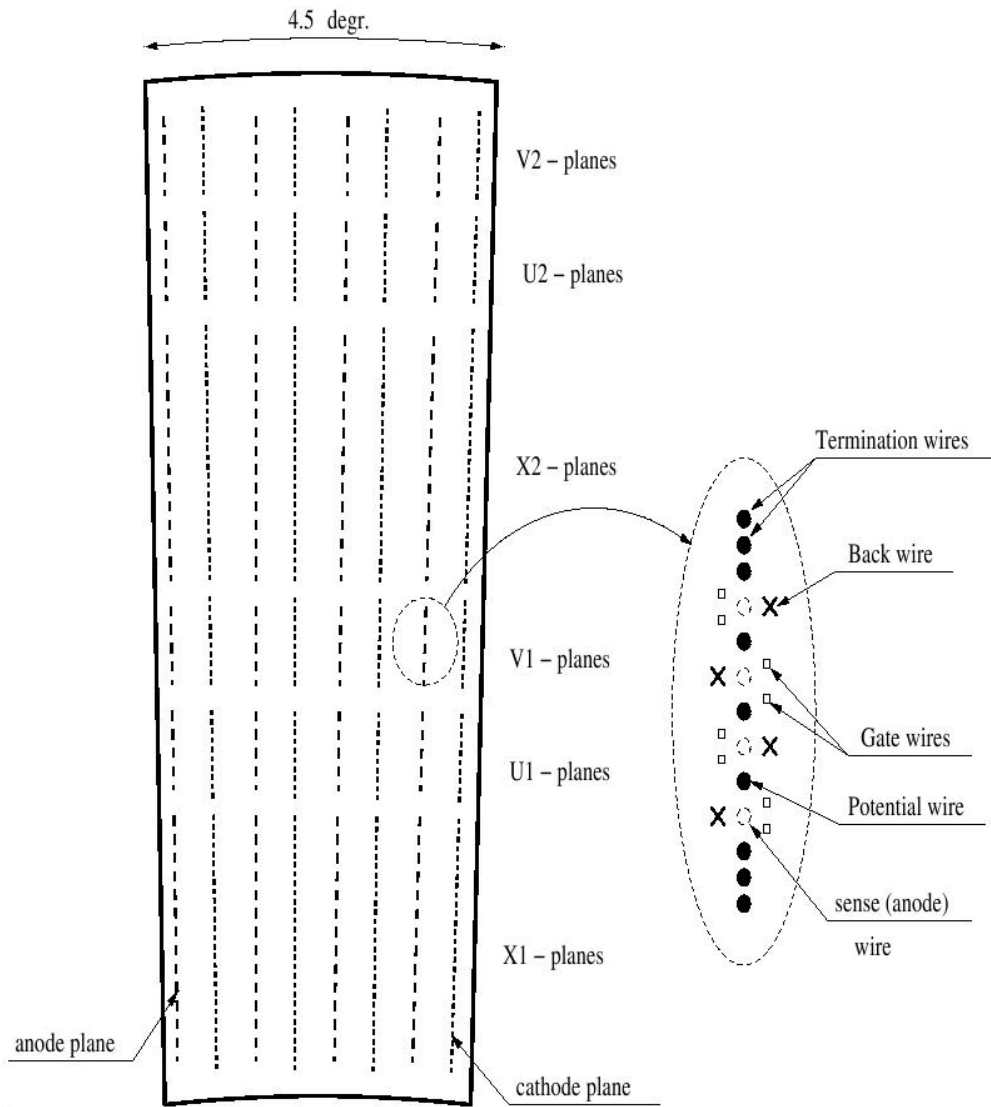


Figure 49: DC sector, side view: wire assembly within a sector and inside the anode plane [107]

the track measurements in the  $z$ -direction. Along with the PC1 measurements this helps to avoid indeterminacy of the track reconstruction in the  $z$ -direction. The orientation of the wires is shown in Figure 50. On one side of the DC, the stereo

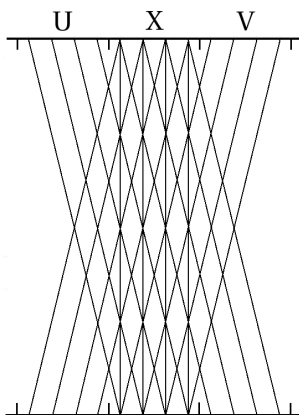


Figure 50: Schematic view (top view) of stereo wire orientation in the DC sectors

wires are fixed in one sector, on another side of the DC, the same stereo wires are fixed in a neighboring sector.

Each anode (sense) wire was cut in the middle into two halves, in order to comply with the specification for the DC to be able to successfully reconstruct up to 500 tracks in an event. This way each half of an anode (sense) wire gives separate readout. Two halves of an anode wire are electrically isolated, being attached in the center to a support made of kapton of  $100 \mu\text{m}$  thickness. This kapton support has very low mass and takes very little space in the fiducial volume of the DC. There are 6500 anode wires in the DC and hence 13000 readout channels.

There are several additional wires surrounding each anode (sense) wire and improving DC performance: Potential, Back, and a couple of Gate wires (see Figure

49). The Potential wire isolates the detection regions of the two neighboring anode (sense) wires from each other by forming a strong electric field. The goal of the Gate wires is to reduce the drift time of electrons from a track, hence decreasing the pulse width. The Back wire helps to minimize left-right indeterminacy by cutting off most of the drift electrons from its side.

There are 4 different potentials applied in such a complex wire configuration within one drift cell: Potential, Back, Gate, and Cathode. Thorough numerical studies have been conducted to choose the optimum regime of the electrostatic field created by these potentials. To comply with all DC design requirements, the actual electrostatic field in the DC chambers requires fine adjustment.

The High Voltage (HV) system powers separately each X module and each pair of U and V modules. Thus, there are 640 HV channels in the DC system. Each sector consumes power of about 80 W, and there is a DC water cooling system in order to remove the heat.

The focusing geometry of the DC has several advantages. First, it helps to minimize the left-right indeterminacy in the  $z$ -coordinate measurement. Second, it decreases the track occupancy of a single wire. And finally, it refines two-track separation by decreasing the pulse width from primary electrons.

The wire tension creates a load of about 4.5 tons to the titanium frame. To minimize consequent deformation, a carboplastic strut 2 inches in diameter was placed in the center of the frame. The potential deformation was studied by setting springs inside the frame before it was packed with the DC modules.

The East Central Arm DC and the West Central Arm DC are two independent gas volumes. These gas volumes are filled with a gas mixture of 50% Ar + 50% Ethane.

The signals from the DC sense (anode) wires are transmitted to electronics installed immediately on the DC frame. Each DC sector has corresponding 4 ASD/TMC cards and one FEM card. The goal of the ASD/TMC cards in each sector is to amplify and digitize the signals from 40 anode wires of each sector. ASD stands for the names of the chips used in the ASD/TMC card: preAmplifier, Shaping amplifier and Discriminator. The output from the Discriminator is sent to a Time Memory Cell (TMC) chip. The Front End Module (FEM) card is a controller of the four ASD/TMC cards. The FEM controls the triggering and readout requests from the PHENIX DAQ travelling through GLink optical fibers, formats the data, and performs slow-control access to parameters of the DC electronics. FPGA chips are used to format the data into packets and transfer the packets to the DCM in the counting house. They are also used to create headers containing information about event and clock counters.

The DC was installed and commissioned prior to the year-2001 PHENIX run. The DC has been shown to be robust over long runs of data taking during several years.

## 6 DOUBLE-HELICITY ASYMMETRY FOR SINGLE-MUON PRODUCTION

RHIC has the capability to provide beams with the bunches alternating in polarization sign in one ring and with pairs of bunches alternating in sign in the other ring, as shown in Figure 51. In this way, experiments collect data from

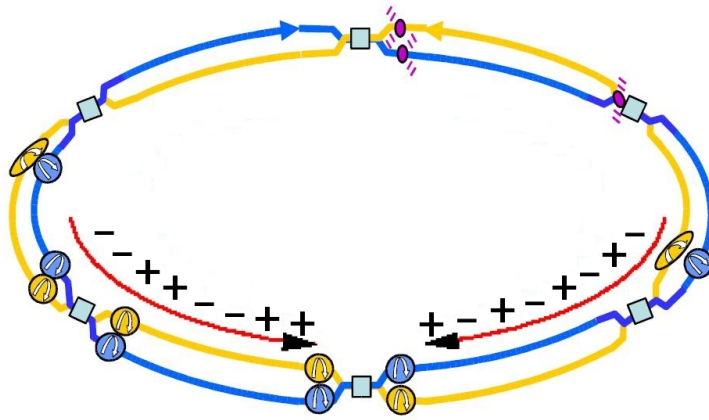


Figure 51: Bunch filling pattern in two RHIC beams representing the spin states of polarized protons

collisions with all four beam-helicity combinations of “Blue”-“Yellow” ring beam polarization signs,  $(++)$ ,  $(+-)$ ,  $(-+)$ , and  $(--)$ , simultaneously.

Asymmetry measurements in the single-muon production are very straightforward. To calculate the double-helicity asymmetry, Equation 55 is used. We need to know the beam polarizations, count the number of signal events (experimental single-muon yield) in collisions for each beam-helicity combination, and monitor the luminosity for the corresponding type of crossings with these combinations of beam spin directions.

## 6.1 2002-2003 RHIC Run 3 Summary

In the 2002-2003 RHIC Run 3, polarized proton beams have been accelerated, stored and collided in RHIC at  $\sqrt{s} = 200$  GeV. Each single proton beam was accelerated to 100 GeV in energy. The proton beams were injected to RHIC with  $0.7 \times 10^{11}$  protons per bunch. In Run 3, RHIC was operated at a 55-bunch per beam mode — there were no actual beam bunches in odd-numbered buckets and, in addition, each beam had a 10-bucket abort gap for the beam cross-check. The average beam polarization for the analyzed data set (after standard PHENIX run-selection procedures for quality assurance were applied) was 37%.

The peak RHIC luminosity reached  $6 \times 10^{30} \text{ cm}^{-2}\text{s}^{-1}$  and the average store luminosity was  $3 \times 10^{30} \text{ cm}^{-2}\text{s}^{-1}$ . Only part of the RHIC delivered integrated luminosity is sampled by the experiments, due to data acquisition live time, experiment uptime, and vertex acceptance. In PHENIX, this fraction is  $\sim 30\%$ .

## 6.2 Data Sample and Triggering

In the RHIC Run 3, data were collected with the PHENIX detector from longitudinally-polarized proton-proton collisions at  $\sqrt{s} = 200$  GeV. The integrated luminosity sampled by PHENIX in the longitudinally-polarized proton-proton collisions was  $0.35 \text{ pb}^{-1}$ .

The decision to accept and store an event was made by the Level-1 Trigger [113] within  $4 \mu\text{s}$  of the collision. The trigger decision was based on the information contributed by the BBC and the MuID triggers. The BBC provided input to the

minimum-bias interaction trigger (MB), which required at least one hit in each BBC counter and a vertex position of a collision within a valid range  $|z_{vtx}| < 38$  cm. The cross section of the MB trigger for  $p - p$  interactions,  $\sigma_{BBC}^{pp}$ , was found to be  $21.8 \pm 2.1$  mb [41]. MuID1D, the MuID trigger, required reconstructed tracks penetrating to the last MuID layer (Gap 5). In the name of the trigger, “1D” at the end stands for at least one track penetrating to the deep (“D”) layer (Gap 5) for an event to be recorded. For the single-muon data sample, we used events selected with the MuID1D trigger with an additional requirement of a coincidence with the MB trigger.

PHENIX runs for the longitudinally-polarized  $p - p$  collisions were chosen for the analysis in this dissertation based on stable detector performance using standard PHENIX procedures for quality assurance (QA). We composed a combined good-run list for the Muon Arm and Central Arm (Drift Chamber) consisting of 44 runs from 20 fills. Two independent QA examinations were performed separately for the Muon Arm and Central Arm.

The list of the good runs for the polarized  $p - p$  Run 3 Muon-Arm data is presented and the Muon-Arm QA procedure is described in [117]. The run selection was based on stable performance of the MuTr High Voltage system, MuID High Voltage system, and MuTr electronics. Some runs were rejected based on examination of the hit distributions and occupancies from online monitoring and the PHENIX logbook. The high-occupancy and high-multiplicity problem in some MuTr data packets was caused by unstable low-voltage-distribution cards. The final

good-run list for the North Muon Arm included 100 runs. The final good-run list for the South Muon Arm contained 127 runs. The combined North/South Muon Arm list of good runs included 54 runs.

In view of prospective studies of the correlations between tracks in the Muon Arms and tracks in the Central Arms, the quality of the Central-Arm data was taken into account, based on the DC and PC1 performance. The QA procedure and results for the Drift Chamber and the first layer of Pad Chamber performance in the polarized  $p - p$  RHIC Run 3 are described in [118]. First, short runs with small number of good quality tracks were removed from the Central-Arm run list. Fourteen runs out of total 227 PHENIX Run-3 runs were rejected because of this reason. Then a check was performed for unacceptable DC/PC1 performance. Some runs were rejected because of unacceptable DC High-Voltage-system performance and others were rejected because of low average track reconstruction efficiency. Twenty-seven runs in total were removed from the Central-Arm run list as a result of the check for unacceptable DC/PC1 performance.

The combined Central/Muon list of the good runs accepted for the current analysis is shown in Table 5. These 44 good runs were selected out of total 227 PHENIX Run-3 runs in the longitudinally-polarized  $p - p$  collisions. The good runs include about 39% of the entire  $p - p$  data. This corresponds to  $0.14 \text{ pb}^{-1}$  of the integrated luminosity.

For the Run-3 analysis, the Muon trigger MWG (Muon Working Group) data files of the `run3pp_v03AG_pro50` and `run3pp_v03AG_pro51` versions have been used.

Table 5: PHENIX Run-3 good run list used in the analysis

fill #	run #
3659	88578
3675	88946
3677	89005
3681	89128, 89135
3682	89211
3691	89303
3693	89323, 89325
3698	89453
3702	89529
3705	89624, 89626, 89629
3708	89646, 89648
3713	89685, 89693, 89695, 89697
3714	89707, 89709, 89713, 89715
3764	91270
3769	91447, 91460, 91462, 91464
3780	91720, 91726, 91729, 91731
3793	91844, 91846, 91848, 91851, 91853
3799	92034
3803	92234, 92242
3810	92440, 92444, 92446

These data files are nanoDST-type files in the ROOT format, where DST stands for Data Summary Tape and ROOT is an object-oriented framework for large-scale data analysis [119]. Only the nanoDSTs for the PHENIX runs from the good-run list (see Table 5) have been included for consideration. The spin information was extracted from the “SpinDataEventOut” Tree in the `MWG_Muon` nanoDSTs. The analysis of the nanoDSTs was accomplished in two steps. First, the `offline/AnalysisTrain/cntmu` package was used to create Trees of selected variables. In the next step, to proceed with the analysis calculations, the Trees were analyzed using specifically developed C++ codes.

The PHENIX Run-3 luminosity data for each type of crossing with the different beam-helicity combinations are available in [120]. In the analysis we used luminosity numbers which were obtained as GL1p scaler sum values from channel (a) of GL1p board 1. The input to the channel (a) of the first GL1p board was from the BBCLL1 trigger with the vertex cut  $|z_{vtx}| < 30$  cm. These luminosity numbers have been used to normalize the muon yields in the asymmetry calculations.

### 6.3 Event and Muon-Arm Track Selection

This Chapter includes information on the event and track selection criteria. Only those collision events which occurred in the vertex range  $|z_{vtx}| < 30$  cm were selected for the analysis.

The reconstruction procedure in the Muon Arms starts from finding “roads.” The “roads” are defined as groups of hits in the MuID which form straight, two-

dimensional lines. Then the “roads” are associated with hits in the MuTr to form “tracks.” Set of cuts has been applied on both track and road characteristics in order to reduce contributions from backgrounds. These standard cuts are given in Table 6. Applying these cuts, only the best-quality Muon-Arm tracks are selected,

Table 6: Muon-Arm track and road cuts

Cut	Setting
Track cuts:	
1) Number of MuTr hits	$n_{hits} \geq 12$ (out of possible 16)
2) Track fit quality	$\chi^2/dof < 15$
Road cuts:	
3) required hit in MuID Gap 5	$\geq 1$

those that penetrate to the most downstream MuID gap with at least one hit in the horizontal or vertical layer associated with the track. This increases the probability for the Muon-Arm tracks to be identified as muons.

Decrease of efficiency for reconstructing the tracks due to high occupancy is negligible in  $p - p$  collisions. Run-to-run reconstruction efficiency variations are insignificant because only the PHENIX runs with stable and similar detector performance were selected.

## 6.4 Beam Polarization

Polarimetry is an important part of the spin measurements. Two types of polarimetry techniques are exploited at RHIC. Both polarimeters use small-angle elastic scattering, with sensitivity to the proton beam polarization from scattering in the Coulomb field of an unpolarized particle (proton or carbon) the magnetic moment of the polarized proton. The first polarimeter, the proton-carbon polarimeter, utilizes scattering from an ultra-thin ( $5 \mu\text{g}/\text{cm}^2$ ) and 10 micron wide carbon ribbon target. This method uses the dominance of the interference between electromagnetic and hadronic amplitudes in the Coulomb-Nuclear Interference (CNI) region. By means of the proton-carbon polarimeter, fast relative polarization measurements are conducted several times during the typical 6-8 hour RHIC fill, with a statistical uncertainty of a few percent. Frequent measurements during a fill allow to track the beam polarization time behavior and also to measure the beam polarization profiles in the transverse plane. The second polarimeter, the H-Jet polarimeter, utilizes scattering from a polarized atomic hydrogen gas target. The H-Jet polarimeter provides absolute polarization measurements accumulating data over the entire fill, with a statistical uncertainty of  $\sim 10\%$ . The H-Jet polarization measurements are used for the precise absolute calibration of the proton-carbon polarimeters. The polarimeters are described in [102].

The polarization measurement values in fills of the 2002-2003 RHIC Run 3 are shown in Figure 52 for the Blue and Yellow beams and can be found on the official

CNI Polarimeter Group web page [121]. Figure 52 shows the final polarization

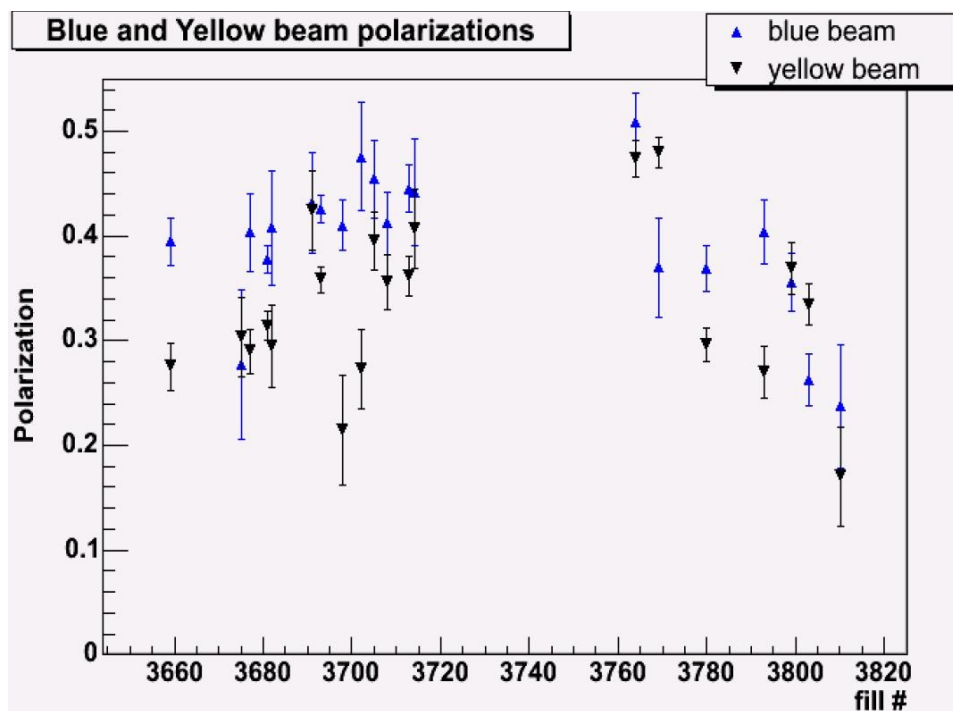


Figure 52: Fill-by-fill polarizations for 100 GeV Blue and Yellow beams in RHIC Run 3

values corrected by the overall rescaling factors: 1.34 for the Blue beam and 1.27 for the Yellow beam [121]. The overall rescaling factors originate from the comparison between the offline and online measurements (1.09 for the Blue beam, 1.05 for the Yellow beam) and from the recalibration of the proton-carbon polarimeters using the polarized gas jet target absolute polarimeter data (1.23 for the Blue beam, 1.21 for the Yellow beam). Only polarization measurements for the analyzed data set are shown in Figure 52. The error bars depicted are statistical uncertainties. The average beam polarization for the analyzed data set was calculated as an average

over the fills weighted by integrated luminosity numbers for every fill:

$$\sqrt{\langle P_B P_Y \rangle}_{Run-3} = \sqrt{\frac{\sum_{fill} (P_B P_Y)_{fill} \cdot L_{fill}}{\sum_{fill} L_{fill}}}. \quad (83)$$

For the weighted average of the uncertainty we used:

$$\sigma_{\sqrt{\langle P_B P_Y \rangle}_{Run-3}} = \frac{1}{2\sqrt{\langle P_B P_Y \rangle}_{Run-3}} \cdot \frac{\sum_{fill} (\sqrt{P_B^2 \sigma_Y^2 + P_Y^2 \sigma_B^2})_{fill} \cdot L_{fill}}{\sum_{fill} L_{fill}}. \quad (84)$$

Using Equations 83 and 84, the average beam polarization for the analyzed data set was found to be  $\sqrt{\langle P_B P_Y \rangle}_{Run-3} = 0.37 \pm 0.02(\text{stat})$ .

The overall relative systematic uncertainties for the polarization measurements in the 2002-2003 RHIC Run 3,  $\Delta P/P$ , were 18.6% for the Blue beam and 16.8% for the Yellow beam. The overall systematic uncertainties were dominated by polarization uncertainties from jet measurements (8.5%), energy-correction uncertainties (9.8%), offline/online adjustments (7.3% for the Blue beam, 9.2% for the Yellow beam), and the proton-carbon polarimeter measurements (10.0% for the Blue beam, 4.0% for the Yellow beam) [121].

The beam polarization profiles in the transverse plane have been measured by the CNI Polarimeter Group with both vertical and horizontal targets. If the polarization profile is not flat over the beam, the H-Jet polarimeter, the proton-carbon polarimeter, and the experiments sample the polarization differently, so this would give a systematic error. The CNI Polarimeter Group confirmed that they found no profile in the measurements, meaning that the beam polarization profiles were consistent with flat.

## 6.5 Asymmetry Measurement Systematic Errors

While the detector performance and beam conditions remain stable with time between reversals of the beam-spin directions, the asymmetry measurements are stable and the errors are mainly statistical. But when reversals of the beam polarization are spread apart in time, and the detector performance and beam conditions vary for the different beam-helicity configurations, false asymmetries appear. At RHIC, with the bunches alternating in polarization sign in one beam and with pairs of bunches alternating in sign in the other beam, experiments collect data from collisions with all four possible beam-helicity combinations simultaneously. Thus, time dependence of the detector performance and variations of the beam conditions for the different beam-helicity configurations are negligible, and asymmetry measurement errors are substantially statistical.

False asymmetries can also arise if the luminosities for collisions with the different beam-helicity configurations are incorrectly measured, which causes non-zero numerator in Equation 55 because of incorrect normalization. It has been established that  $A_{LL}$  of the PHENIX luminosity monitor (BBC) is consistent with zero within the measurement accuracy of  $\delta A_{LL} < 2 \times 10^{-3}$ . The “non-physical” false double-helicity asymmetries between  $(++)$  and  $(--)$  and between  $(+-)$  and  $(-+)$  helicity configurations were evaluated for the analyzed data set as a check of systematic errors and to search for non-zero parity violating asymmetries, if any. The same-sign false double-helicity asymmetry,  $((N_{++}/L_{++}) - (N_{--}/L_{--})) / ((N_{++}/L_{++}) +$

$(N_{--}/L_{--})$ ), shown in Figure 53, and the opposite-sign false double-helicity asymmetry,  $((N_{+-}/L_{+-}) - (N_{-+}/L_{-+})) / ((N_{+-}/L_{+-}) + (N_{-+}/L_{-+}))$ , shown in Figure 54, were consistent with zero, as expected. The calculations of the false double-helicity asymmetries have been performed using the fill-by-fill method described later in Chapter 6.6. No lower- $p_T$  cut has been imposed on the data — all muon tracks with  $p_T^{max} > 0$  GeV/ $c$  were used for the calculation in the lowest  $p_T^{max}$  bin.

Another type of systematic error which must be considered is scale error. The scale errors occur if the beam polarizations are incorrectly measured. In this case, no false asymmetry is created, but the scale of the obtained asymmetry is changed. By scale error it is meant that in the relative asymmetry error ratio of the  $\Delta A_{LL}$  in Equation 61 to the  $A_{LL}$  from Equation 55, the polarization normalization divides out. Thus, the polarization uncertainty has an influence only on the scale of the asymmetry measurement and not on the statistical significance of the measurement. The polarization uncertainties are addressed in Chapter 6.4.

## 6.6 Data Analysis: Results and Discussion

For the analysis in this dissertation, a single-muon data set was selected from the good runs presented in Chapter 6.2. Collision events were chosen collected with the MuID1D trigger and the requirement of having good Muon-Arm track candidates reaching to the deepest MuID layer (Gap 5).

The muon track with maximum transverse momentum  $p_T^{max}$  was selected from each collision event to calculate the experimental yield for each “Blue”-“Yellow”

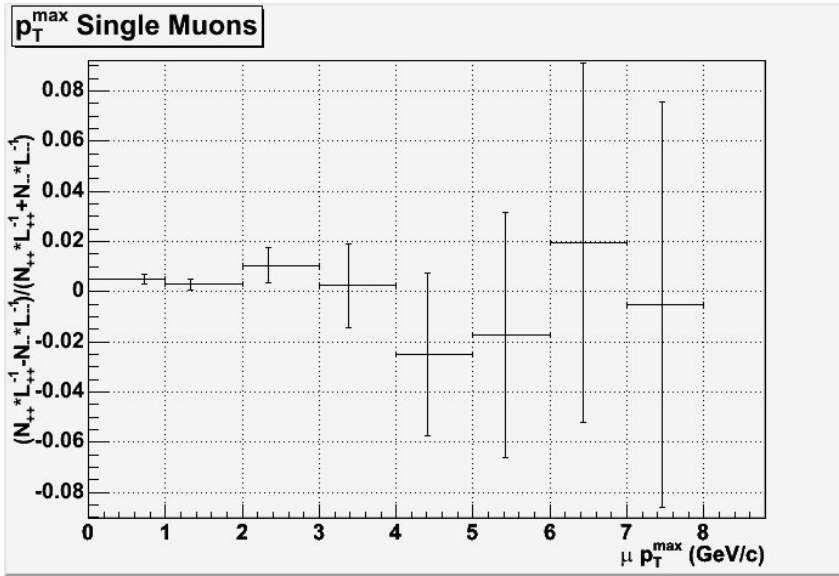


Figure 53: The “non-physical” same-sign double-helicity asymmetry for inclusive single muons

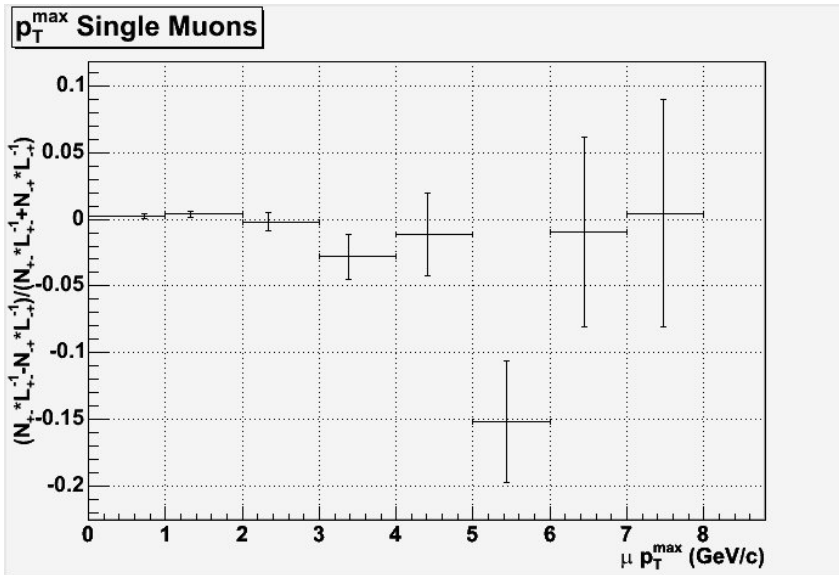


Figure 54: The “non-physical” opposite-sign double-helicity asymmetry for inclusive single muons

ring beam helicity configuration. This selection is performed because muons produced in charm-quark decays are expected to have large  $p_T$ . The  $p_T$  spectrum for muon tracks with the largest transverse momentum in each event, shown in Figure 55, demonstrates the statistics available for the analysis, after standard track-quality cuts were applied to the data. The points in this figure have been

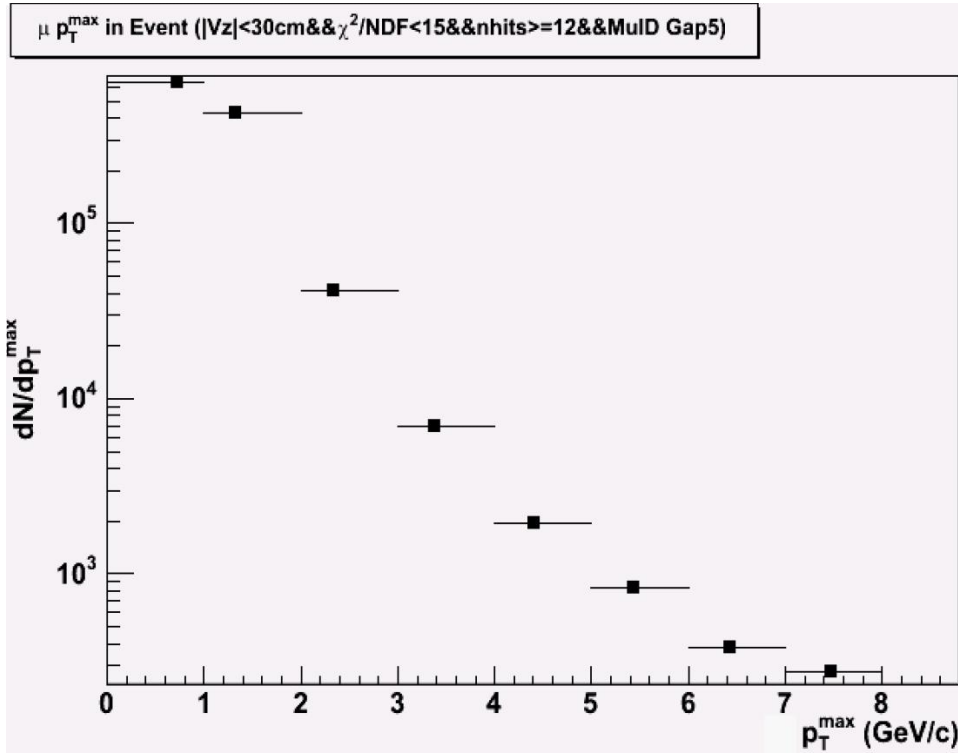


Figure 55:  $p_T$  spectrum for  $\mu$  tracks in the PHENIX Muon Arms with maximum transverse momentum in an event (2002-2003 RHIC Run 3)

located at the average  $p_T$  values of each bin to demonstrate the correct shape of the steeply falling distribution. The horizontal error bars show 1 GeV/c bins. No lower- $p_T$  cut has been imposed on the data — all muon tracks with  $p_T^{\max} > 0$  GeV/c were used for the calculation in the lowest  $p_T^{\max}$  bin.

The double-helicity asymmetry,  $A_{LL}^{\mu}$ , normalized by the beam polarization and

corrected for luminosity, for inclusive single muons versus the largest muon transverse momentum  $p_T^{max}$  in each collision event, was obtained. The results are shown in Figure 56 and are given in Table 7. The measurements were performed for the

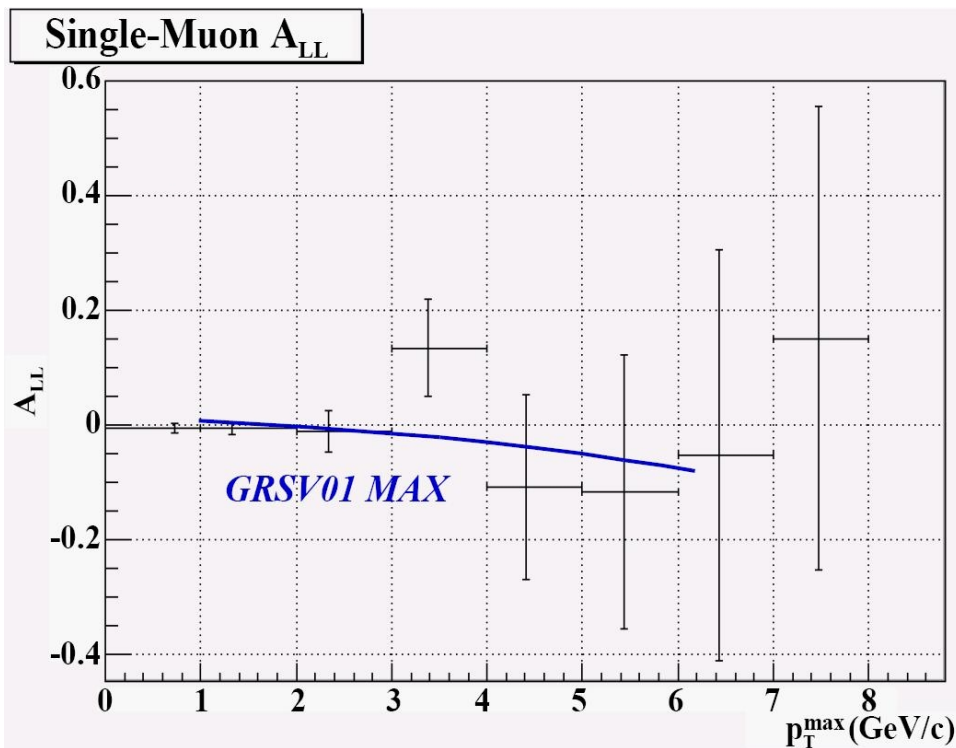


Figure 56:  $A_{LL}^{\mu}$  for inclusive single muons from PHENIX Run-3 (2002-2003) data, compared with theoretical prediction

$p_T$  range up to 8 GeV/c in 8  $p_T$  bins. The points in Figure 56 have been placed at the average  $p_T$  value of each bin. The horizontal error bars show 1 GeV/c bins. No lower- $p_T$  cut has been imposed on the data. The vertical error bars are statistical uncertainties. The scale errors (see Chapter 6.5) are not shown.

The measurements for the double-helicity asymmetry have been performed on a fill-by-fill basis. First, we calculated  $A_{LL}^{fill}$  with statistical uncertainty  $\Delta A_{LL}^{fill}$  using Equation 55 for every fill of the RHIC beam injection, because the detector

Table 7: PHENIX Run-3 inclusive single muon  $A_{LL}^\mu$  values

$p_T$ range (GeV/c)	$A_{LL}^\mu$	$\Delta A_{LL}^\mu$
$0 < p_T^{max} \leq 1$	-0.006	0.009
$1 < p_T^{max} \leq 2$	-0.007	0.011
$2 < p_T^{max} \leq 3$	-0.01	0.04
$3 < p_T^{max} \leq 4$	0.13	0.09
$4 < p_T^{max} \leq 5$	-0.11	0.16
$5 < p_T^{max} \leq 6$	-0.12	0.24
$6 < p_T^{max} \leq 7$	-0.05	0.36
$7 < p_T^{max} \leq 8$	0.15	0.40

performance and beam conditions remain relatively stable within one fill. Then, the final  $A_{LL}^\mu$  value for the entire analyzed data set in each  $p_T$  bin was obtained as a weighted average over the fills. For the weights,  $w_{fill} = 1/(\Delta A_{LL}^{fill})^2$  has been used. For the final uncertainty we used  $1/(\Delta A_{LL}^\mu)^2 = \sum_{fill} (1/(\Delta A_{LL}^{fill})^2)$ .

In Figure 56, the double-helicity asymmetry,  $A_{LL}^\mu$ , is compared with the theoretical prediction for single muons from heavy-flavor production made by the PHENIX LANL group [122] using a PYTHIA simulation and the GRSV01-MAX polarized parton distribution function set. From this comparison, one can see that the Run-3 measurements are statistically too limited to proceed with the gluon polarization measurements. GRSV01-MAX assumes maximally polarized gluons in the proton

and predicts maximal values for the asymmetry. Other predictions, using different polarized parton distribution function sets, give even smaller values for the double-helicity asymmetry than the GRSV01-MAX set does. This can be seen in Figure 57 [122] demonstrating also predictions for the GS-C, GS-A, and GRSV01-STD sets, which assume different, smaller, gluon densities. The main conclusion is that,

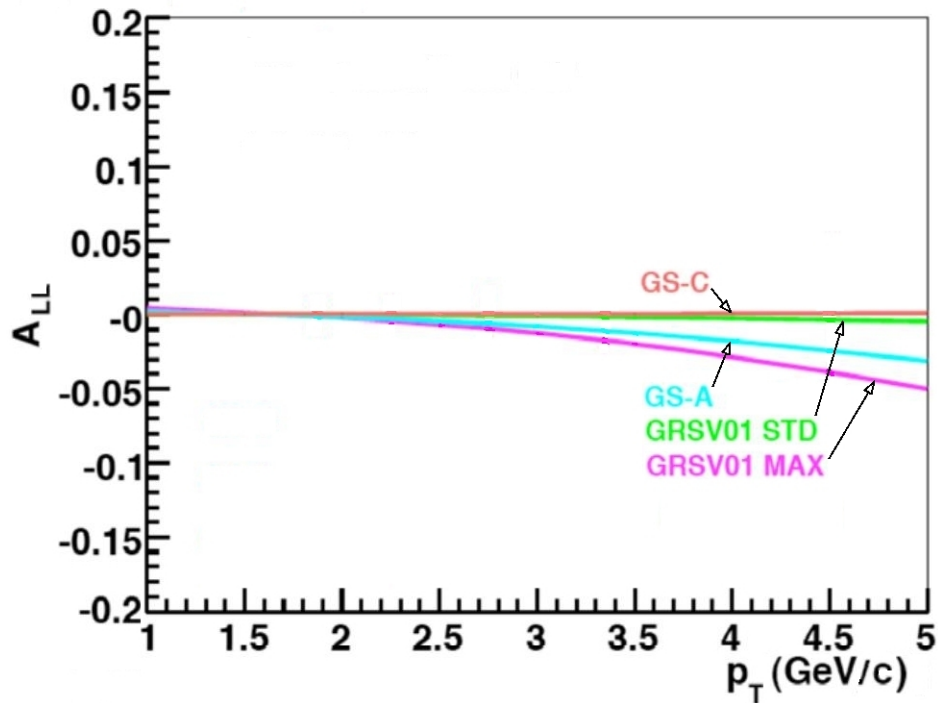


Figure 57:  $A_{LL}^{\mu}$  theoretical predictions for single muons from heavy-flavor production [122] using different polarized parton distribution function sets; GRSV01-MAX curve is the same theoretical prediction curve shown in Figure 56 compared with the measurement results

because of the large statistical uncertainties of the  $A_{LL}^{\mu}$  measurements, it is not possible to constrain the gluon polarization using the PHENIX Run-3 single muon data.

## 6.7 2005-2006 RHIC Run-6 Data

During 2005-2006 RHIC Run 6, data were collected with the PHENIX detector from longitudinally-polarized  $p - p$  collisions at  $\sqrt{s} = 200$  GeV. The proton beams were injected to RHIC with  $1.4 \times 10^{11}$  protons per bunch. In Run 6, RHIC was operated at 111-bunch per beam mode — there were no beam bunches in 9-bucket abort gaps of the beams. The average beam polarization for the RHIC Run 6 was approximately 58%, which is larger by factor of  $\sim 1.6$  than the average beam polarization for the RHIC Run 3. The beam polarization measurement uncertainty has been significantly reduced to  $\Delta P/P < 5\%$ .

The peak RHIC luminosity reached  $28 \times 10^{30} \text{ cm}^{-2}\text{s}^{-1}$  and the average store luminosity was  $18 \times 10^{30} \text{ cm}^{-2}\text{s}^{-1}$ . The integrated luminosity for the longitudinally-polarized  $p - p$  collisions sampled by PHENIX was  $7.5 \text{ pb}^{-1}$ , which gives us approximately 20 times more statistics than we had from the 2002-2003 PHENIX Run-3 longitudinally-polarized  $p - p$  data. Along with the larger beam polarization, this reduces accordingly uncertainties in double-helicity asymmetry measurements in comparison with what we obtained from the PHENIX Run-3 polarized  $p - p$  data.

The PHENIX Run-6 data give the opportunity to analyze combined PHENIX detector Muon and Central-Arm data, which in turn allow to study the correlation between tracks in the Muon Arms and tracks in the Central Arm. The PHENIX “run6pp\_200GeV\_pro74” MWG\_MU files (Muon trigger Muon-Arm data) and the “run6pp\_200GeV\_pro74” CNT\_MU files (Muon trigger Central-Arm data) for the

Run-6 longitudinally-polarized  $p-p$  data are available at the RCF data storage facility called HPSS and are accessible via the PHENIX Analysis Train, the method for running multiple analysis codes on a set of data. The Analysis Train compatible package `offline/AnalysisTrain/cntmu` has been developed, which lets us work with the combined Central/Muon data. The Run-6 combined Central/Muon data files with selected variables from the “run6pp\_200GeV\_pro74” MWG\_MU and CNT\_MU files have been created using the `cntmu` package and are available for the analysis.

QA studies of the Muon-Arm operation performance [123] and of the Central-Arm operation performance [124] have been completed for the Run 6 period with the longitudinally-polarized  $p-p$  collisions at  $\sqrt{s} = 200$  GeV. Most of the rejected runs in the QA examination of the Muon Arms were runs with the following problems: runs with low production rate in the last MuID Gap 5, short runs with time duration less than 8 minutes, runs with too many failed MuTr FEMs, and runs with too many failed HV channels in the MuTr and MuID HV systems. Few runs were eliminated because of zero magnetic field in the runs, and because of GL1 board errors (for spin analyses). Separate QA examinations were completed for the North Muon Arm and for the South Muon Arm. The Central-Arm QA examination was based on the occupancy study in the DC sectors, and runs were eliminated due to DC HV system problems and failed DC sectors. The lists of good runs with stable and similar detector performance can be found at [123] and [124] for the Muon Arms and for the Central Arms, respectively. The final good-run list for the North Muon

Arm consists of 387 runs. The final good-run list for the South Muon Arm contains 377 runs. The Central-Arm good run list includes 401 runs out of the 508 Run-6 longitudinally-polarized  $p - p$  PHENIX runs. The combined Muon/Central Arm list of good runs can be composed from the lists mentioned above.

The raw double-helicity asymmetry,  $A_{LL}^{\mu}$ , for inclusive single muons versus the maximum muon transverse momentum  $p_T^{max}$  in each collision event was obtained based on the fraction of the PHENIX Run-6 longitudinally-polarized  $p - p$  data. The measurements were performed for the muon  $p_T$  range up to 8 GeV/ $c$  in 8  $p_T$  bins. The raw double-helicity asymmetry is not corrected for luminosity and not normalized by beam polarization. The luminosity numbers for each type of crossing with the different beam-helicity combinations and the beam polarization values for every fill need to be included in the analysis to proceed with the asymmetry calculations using the Run-6 data.

## 6.8 Run-6 $A_{LL}^{\mu}$ Predictions

According to Equation 61 for  $\Delta A_{LL}$ , larger RHIC Run-6 beam polarization and PHENIX sampled integrated luminosity reduce significantly the statistical uncertainties in double-helicity asymmetry measurements in comparison with the statistical uncertainties obtained in the Run-3 measurements. Predictions for Run-6 have been made based on the Run-3 measurements using comparison between the Run-6 and Run-3 beam polarization values and the sampled integrated luminosity numbers for the longitudinally-polarized  $p - p$  collisions. For these predictions,

we assumed similar PHENIX detector operation performance during the Run-6 and Run-3 periods. The predicted inclusive muon track  $p_T$  spectrum in Figure 58 shows the expected statistics for the Run-6 analysis. The horizontal error bars demon-

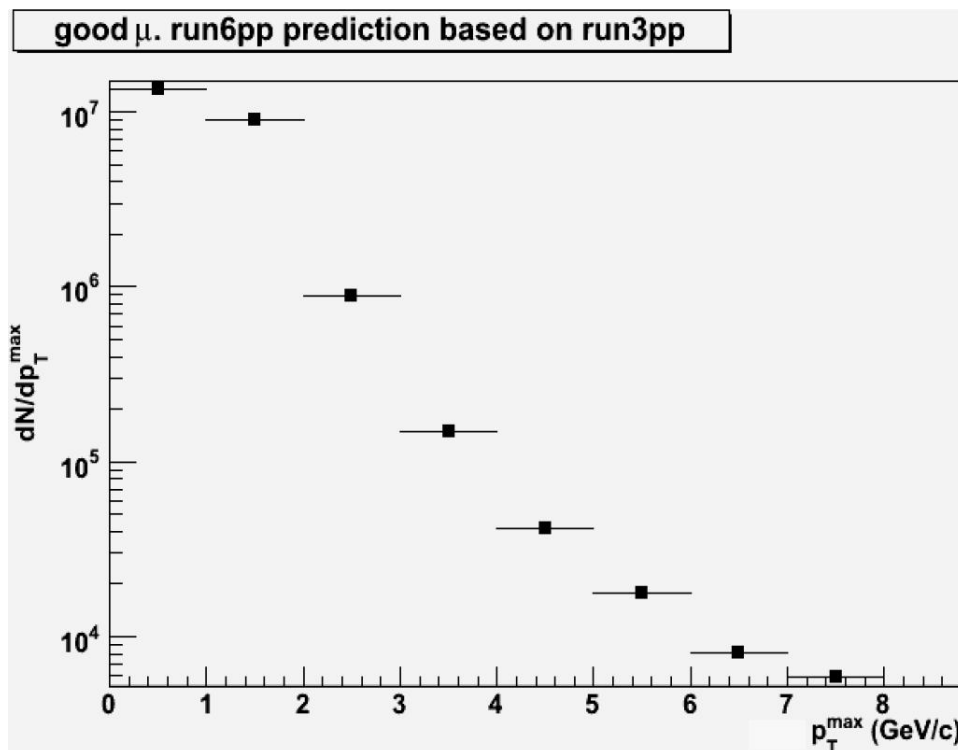


Figure 58: Predicted  $p_T$  spectrum for  $\mu$  tracks in the PHENIX Muon Arms with maximum transverse momentum in an event for 2005-2006 PHENIX Run-6 data

strate 1 GeV/ $c$  bins. Figure 59 shows predicted statistical uncertainties for the Run-6 double-helicity asymmetry measurements for inclusive single muons. The predictions were made for 8 bins of the largest muon transverse momentum  $p_T^{\max}$  in each collision event, for the  $p_T$  range up to 8 GeV/ $c$ . The points in Figure 59 have been placed at zero intentionally because there were no final measurement values obtained for the Run-6 double-helicity asymmetry in the current analysis.

In Figure 59, one can see the double-helicity asymmetry theoretical predictions

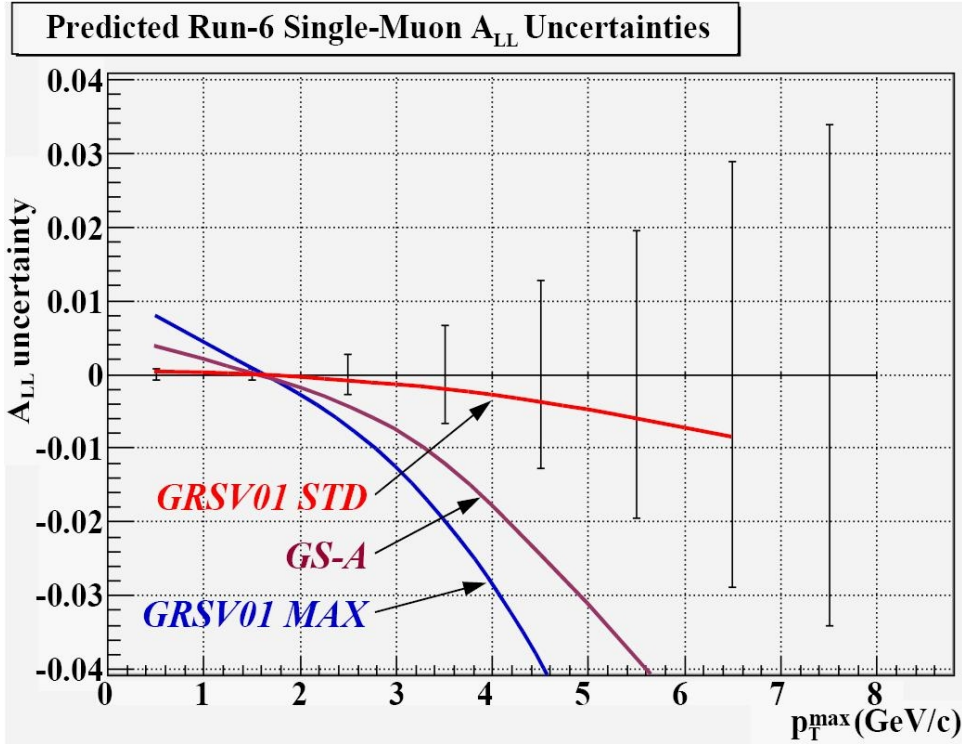


Figure 59: Predicted inclusive single muon  $\Delta A_{LL}^{\mu}$  for PHENIX Run-6 (2005-2006) data, along with  $A_{LL}^{\mu}$  theoretical predictions

for single muons from heavy-flavor production made by the PHENIX LANL group [122] using PYTHIA simulation and various polarized parton distribution function sets assuming different gluon polarized densities. The theoretical predictions for GRSV01-MAX, GS-A, and GRSV01-STD sets are shown. The GRSV01-MAX polarized parton distribution function set assumes maximally polarized gluons in the proton. The GRSV01-STD is based on the best fit among GRSV models to the DIS data. From Figure 59, one can see that the prospective Run-6 measurements will still be statistically limited. It could be possible to make some discrimination but still will be difficult to put constraints on the gluon polarization. Note also that the Run-6 data predictions are made for inclusive single muons which in addition to the

heavy-flavor single muons include several other sources of single muon production discussed in Chapter 4.3.

## 7 SEARCH FOR OPEN CHARM

The double-helicity asymmetry,  $A_{LL}^{\mu}$ , measured in the PHENIX Run 3 and predicted for the PHENIX Run 6 and presented in Chapter 6, is for inclusive single muons. There are several types of inclusive muon candidates penetrating to the last MuID layer, described in Chapter 4.3: open-charm muons (which we are interested in), other open heavy-flavor muons, quarkonium muons, muons produced in the decays of  $\pi$ s and  $K$ s which do not have heavy-flavor origin, “punch-through” hadrons, and background tracks. Our intention is to measure the double-helicity asymmetry for the open-charm muons in order to access the polarized gluon distribution in the proton. How to discriminate between the open-charm muons and other inclusive muon candidates? The idea in this dissertation work, as discussed in Chapter 4.3, is to study track correlations in the PHENIX Muon and Central Arms analyzing the combined single-muon triggered events. This can lead to the actual tagging of the open-charm muons on an event-by-event basis using developed selection criteria.

In order to develop discriminants and selection cuts for enriching the charm content of the sample of single-muon events, a full multistage Monte Carlo simulation, including the detailed PHENIX detector geometry and response, has been conducted to investigate correlations between muon tracks in the Muon Arms and charged hadron/lepton tracks in the Central Arms of the PHENIX detector. The tracks involved in the correlation studies are depicted in Figure 60. The multistage simulation included: the standard PYTHIA event generator simulation, detector

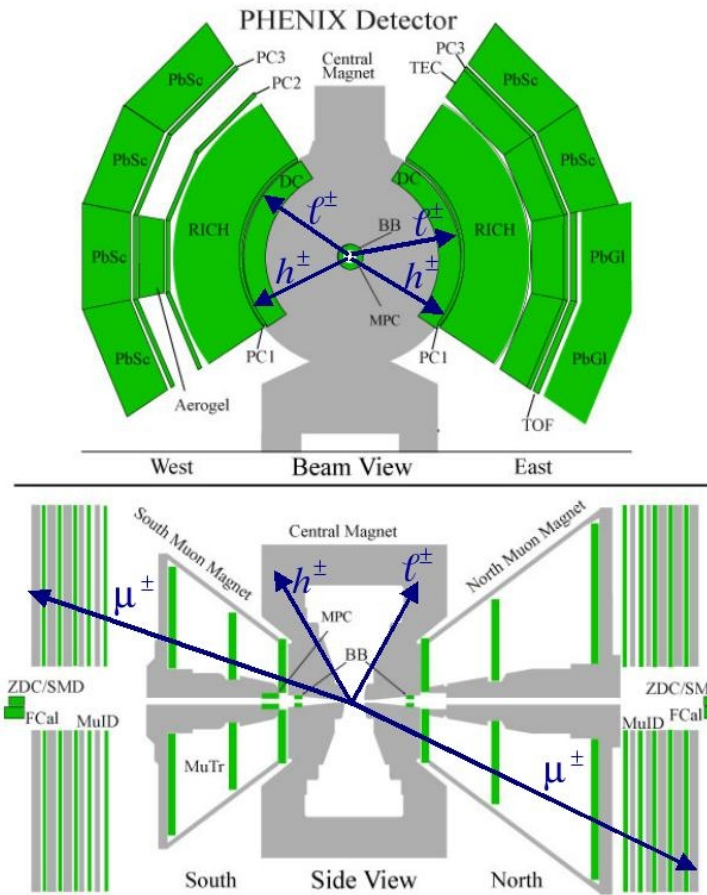


Figure 60: Tracks in the PHENIX Muon and Central Arms involved in the track correlation studies

response for both the Central and Muon Arms of the PHENIX detector using the simulation package PISA (PHENIX Integrated Simulation Application) specifically developed for PHENIX, and the reconstruction chain which is used for the reconstruction of the real data as well. In this way, the PHENIX detector acceptance and reconstruction efficiencies were taken into account in the simulation. A code was developed to track particle ancestry through all simulation stages, which let us know the origin of the reconstructed particles. Three separate simulation outputs have been produced and compared: for open charm ( $c\bar{c}$ ) events, for bottom ( $b\bar{b}$ )

events and for minimum-bias (i.e. mostly light-quark) events. The objective is to develop multivariate selection criteria which can significantly enhance the charm content of a sample of single-muon events without reducing the statistical power of the sample to unacceptable levels, by studying and comparing different kinematic quantities of the Muon-Arm tracks and the Central-Arm tracks.

## 7.1 Simulation

In order to study track correlations, the multistage simulation has been run together both for the Central Arms (DC/PC1) and the Muon Arms. The stages of the simulation are shown in Figure 61. The four stages, with short descriptions, are:

- 1) PYTHIA — the generator of high energy physics events which is initialized for  $p - p$  collisions at  $\sqrt{s} = 200$  GeV;
- 2) PISA — the program which simulates the PHENIX detector and tracks particles through the PHENIX subsystems;
- 3) Data reconstruction chain — the software which simulates with as much realism as possible the signals from the PHENIX subsystems, then reconstructs these signals using the same software used for the real data;
- 4) Analysis code — the `cntmusimAnc` code which we developed to work with the combined data from the Central Arms and the Muon Arms and adapted to the simulation project.

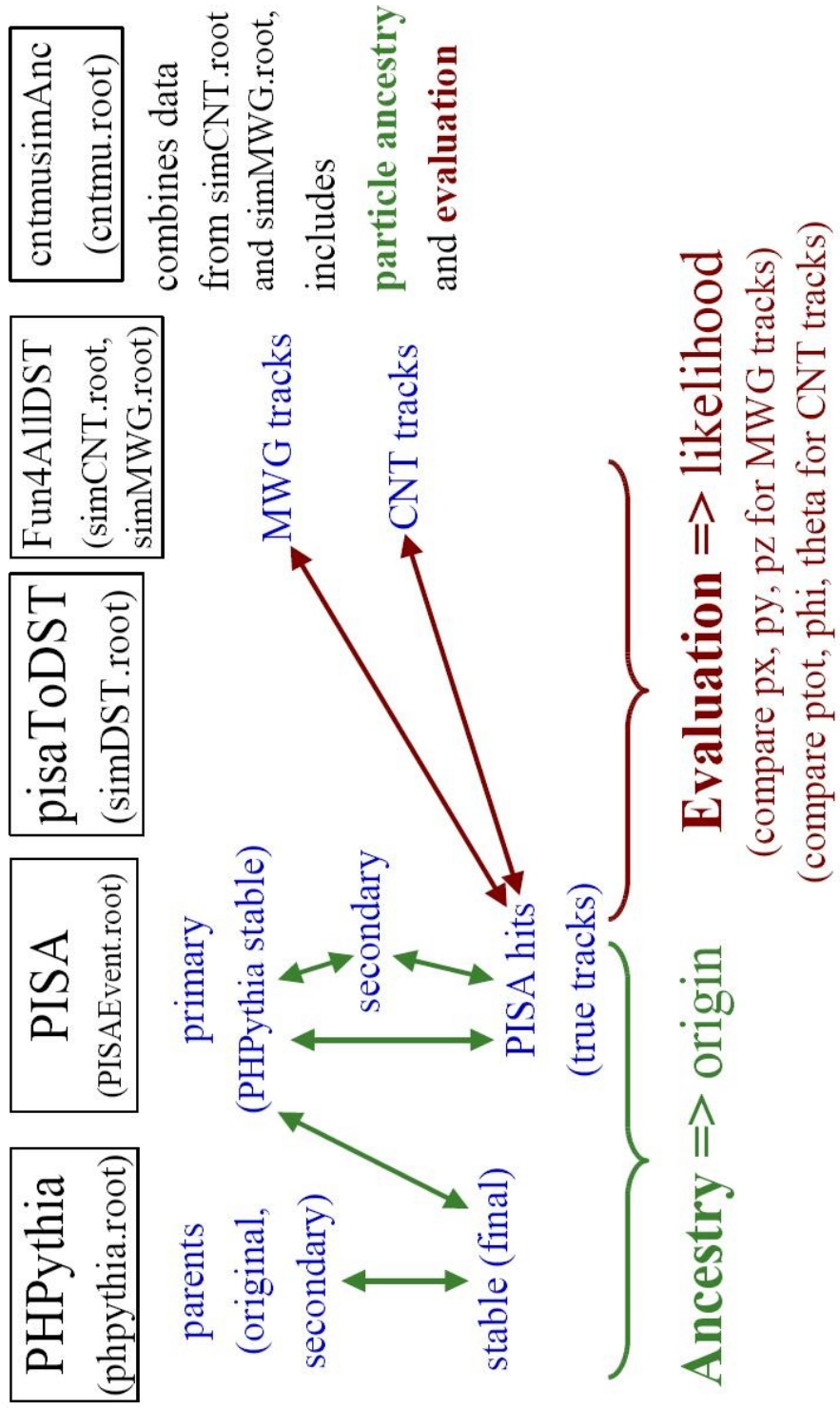


Figure 61: Multistage simulation chain and ancestry tracking

In the following chapters, the simulation stages, as well as the produced simulation outputs, are described in detail.

### 7.1.1 Monte Carlo Event Generation

To generate collision events we used the PHPythia package [125]. The PHPythia package adapts the PYTHIA event generator to the PHENIX software environment. This way a user can run PYTHIA interfaced to the PHENIX Fun4All framework and PISA. The PHENIX Fun4All framework is the universal PHENIX shell for processing of data. The PYTHIA event generator is a Monte Carlo code simulating the experimental high energy events following the QCD theoretical concepts. The PHPythia package has been installed and configured in the directory `/direct/phenix+u/workarea/stepanov/phpythia/event_gen/`.

With the PHPythia package we generated events using PYTHIA version 6.410 with the switches and parameters listed in Table 8. The meaning of each switch and parameter is defined in the fullest detail in the PYTHIA manual [126]. Note that we used the CTEQ5L parton distribution function (PDF) set [92] available in PYTHIA.

In the current analysis simulation, PYTHIA has been initialized to generate  $p-p$  collisions at 200 GeV center-of-mass energy. A single  $p-p$  collision is referred to as an event. An event is characterized by the position coordinates of the collision point called the vertex. In the simulation, an event is considered as a list of the original, secondary, and final particles with their types, energies, momenta, the

Table 8: PYTHIA switches and parameters, default for the analysis

Switch/Parameter	Setting	Meaning
MSEL	1	Minimum-bias collisions
PMAS(4,1)	1.5	$m_c$ (GeV/ $c^2$ )
PMAS(5,1)	4.8	$m_b$ (GeV/ $c^2$ )
MSTP(32)	8	Hard scattering scale, $Q^2$
MSTP(33)	1	Use common K-factor
PARP(31)	1	Common K-factor multiplying hard processes
MSTP(51)	7	Select CTEQ5L PDF library
MSTP(52)	1	Use internal PYTHIA PDF libraries
MSTP(91)	1	Use Gaussian distribution for intrinsic $k_T$
PARP(91)	1.5	Width of $k_T$ distribution in GeV/ $c$
PARP(93)	5.0	Maximum $k_T$ value in GeV/ $c$

position coordinates of production and the time of production.

### 7.1.2 Detector Simulation and Data Reconstruction Chain

The PHENIX-specific PISA detector-simulation package [127] was used to simulate detector response. The PISA is the GEANT-based Monte Carlo program using the FLUKA [128] hadronic interaction package. GEANT [129] is the package simulating the detector geometry and the interactions of particles with the materi-

als of the detectors and the magnetic fields. PISA has been installed and configured in `/direct/phenix+u/workarea/stepanov/cntmusim/pisa_run6/`.

Using GEANT, the PISA program tracked particles generated by the PYTHIA event generator through the active areas of each detector subsystem involved in the analysis and produced the hits in the detector. Both the primary particles and their secondaries were tracked within an event. All particles and secondaries in the event were tracked until they stopped or escaped the detector volume. This part of the simulation was the most time-consuming. The output from PISA was so called a “hits file” (`PISAEvent.root`) which stored the specific event-by-event hit data produced by the tracked particles in the selected active detector subsystems. These raw hit detector data contained information about the particle type, its hit positions, its momentum and energy, and the time of flight from the interaction vertex to the detector.

The simulated detector response was thoroughly tuned to match the real detector. The measured detector performance, including the overall acceptance and efficiency, was incorporated in the detector response simulation. Complete and accurate fiducial cuts were applied to remove detector-active-area discrepancies between real data and simulation. As the reference run for the detector response simulation we chose run #201869 which was present in both Muon-Arm and Central-Arm PHENIX Run-6 good-run lists.

PISA is configured in the sense of the event selection, the detector geometry layout for the active and passive elements, and the tracking options. The most

important configuration file is `pisa.kumac`. The first part of the `pisa.kumac` file configured for the current analysis is given in Figure 62. This part specifies the options for energy and momentum thresholds, magnetic field, active detector volumes, interaction types, etc. A leading asterisk `*` represents a comment line. The selection of the magnetic field map in PISA is done with the `MAGF` control line. The “3D++” magnetic field option stands for the magnetic field configuration used in the PHENIX Run 6 when both the inner and the outer Central-Arm magnet coils have the same polarity. For the description of the `pisa.kumac` control options in the fullest detail, one can refer to the PISA Primer Manual [130]. In the second part of the `pisa.kumac` file, given in Figure 63, PISA allows a user to select which subsystems of the PHENIX detector need to be involved into an event simulation. The first two detector parameters are detector name and install-or-not-install option. Any of the detector subsystem can be included or excluded by the ON/OFF switch (the second parameter). ITR stands for the Intermediate Tracker, consisting of DC and PC1. As one can see, we included in the current analysis simulation only the BBC, ITR, MuTr (“MUM”), and MuID (“MUI”) detectors, which are crucial for the analysis. We also kept the MVD (“VER”) detector installed, because it is the inner detector close to the collision point, and its material has to be present physically in order to reproduce correctly real experiment conditions. All other detectors are outer detectors relative to the BBC, ITR, MuTr, MuID, and MVD, and they can be excluded harmlessly from the consideration, since the backward particle scattering from the outer detectors back to the inner detectors is a highly

```

* PISA kumac file for Central Arm and Muon Arm
*
*           Aerogel control line default is ON as of Run5
*           TOF-West control line default is ON as of Run7
*
*           Change default to Run4 3D++ map, use helium bag, East + West
Arm Photon Shields
*           Use +1.0 scale factor for 3D++ field
*           NTC is absent as of Run5
*           MVD is absent as of Run7 (to be replaced by HBD in this radia
l region)
*
SETRHIC 6 2           ! Run6
*
* Random number seeds (using internal GEANT seeds from 001 to 215)
*           keep the second input as 0 all the time, change only the first
*
RNDM 001 0
*
* Tracking thresholds
*
CUTS  .001 .001 .010 .010 .010 .001 .001 1.e+4 1.e+4 .010 4.e-7
*
* NOTE: As of December 1, 1999 the compressed ZEBRA output format is not used by
default
*           The FOUT line will be used only if the SWIT(1) value is changed to 6 in
gffgo.dat
*
FOUT 'phnx.dat.cZ'           ! Name of output hits file
FPAR 'phnx.par'             ! Name of namelist parameter file for geometry
STEE 'KINE' 'HITS' 'DIGI'   ! Output data structure control
DOUT 'DIGI'                 ! Output data structure control
MAGF '3D++' 1.00 0001 0.0 0.0
GEOP 'ENDC' 'CENT' 'PIPE' 'NOSE' 'PLUG' 'BCOL' 'HBAG' 'PHSH'
DCAY 1                     ! GEANT command for decay on
ANNI 1                     ! GEANT command for annihilation on
BREM 1                     ! GEANT command for bremsstrahlung on
COMP 1                     ! GEANT command for Compton scattering on
LOSS 2                     ! GEANT command for Landau fluctuations on
DRAY 0                     ! GEANT command for Delta no ray (Landau is on)
HADR 4                     ! GEANT command for hadrons using FLUKA
MULS 1                     ! GEANT command for multiple scattering on
PAIR 1                     ! GEANT command for pair production on
PHOT 1                     ! GEANT command for photoelectric effect on
MUNU 0                     ! GEANT recommendation when HADR 4 is used

```

Figure 62: PISA configuration file `pisa.kumac` for the current analysis simulation

```

*****
*
*       To install a detector turn the switch 'ON'
*
*****
*
* central arm detectors
*
* SVX is off by default because its an "upgrade" detector
* FCL and ZDC are off by default except for dedicated simulations
ZDC 'OFF' 'FULL' 'ETOT' 'FULL' 'ZCAL' 'FRG1' 'HBOO' 37.89
SVX 'OFF' 'FULL' 'P_ID' 'FULL' 'ELEM' 'NEUT' ! This is the Silicon Vertex Tracker (upgrade)
FCL 'OFF' 'FULL' 'P_ID' 'FULL' 'ELEM' ! This is the FCL (forward calorimeter)
VER 'ON' 'FULL' 'P_ID' 'FULL' 'VCAL' 'STCK' ! MVD on with track stack used
BBC 'ON' 'FULL' 'ETOT' 'FULL' 'BCAL' 'STCK' ! BBC on with track stack used
NTC 'OFF' 'FULL' 'P_ID' 'FULL' 'ELEM' ! This is the NTC
TZR 'OFF' 'FULL' 'P_ID' 'FULL' 'ELEM' ! This is the TZR
ITR 'ON' 'IT96' 'ETOT' 'FULL' 'TRKS' ! Latest version of Dch and PC1
CRK 'OFF' 'FULL' 'P_PZ' 'FULL' 'CCAL' 'CO2 ' ! RICH with CO2 radiator gas
PAD 'OFF' 'PC98' 'P_ID' 'FULL' 'PCAL' ! Latest version of PC2/PC3
AER 'OFF' 'FULL' 'P_ID' 'FULL' 'ELEM' ! This is the AER (aerogel counter)
TFW 'OFF' 'FULL' 'P_ID' 'FULL' 'ELEM' ! This is the TFW (TOF-West)
TRD 'OFF' 'FULL' 'P_ID' 'FULL' 'TCAL' ! This is the TEC
TOF 'OFF' 'FULL' 'P_ID' 'FULL' 'FCAL' 0.0 0.0 ! Time of Flight
EMC 'OFF' 'FULL' 'FULL' 'FULL' 'ECAL' 'AUAU' 'CTRK' ! EMCal, H.I. with Cerenkov
*
* forward rapidity (muon arms) detectors
MUM 'ON' 'FULL' 'ETOT' 'FULL' 'MCAL' 0. 0. 0. 'STCK' 'NNEU' ! Muon trackers
MUI 'ON' 'FULL' 'ETOT' 'FULL' 'NCAL' 0. 0. 0. 'STCK' 'NNEU' ! Muon identifier
*
* MUPC is off by default because its an "upgrade" detector
MUPC 'OFF' 'FULL' 'P_ID' 'FULL' 'PCAL' ! Pad chamber for Muon Trigger
RLT 'OFF' 'FULL' 'P_ID' 'FULL' 'PCAL' ! Relative Luminosity Telescope

```

Figure 63: The second part of the pisa.kumac file for the current analysis simulation

unlikely event. The benefits of having the outer detectors excluded from the simulation are significantly reduced time of the simulation running and reduced size of the output file, since the current analysis does not require information from the outer detectors.

Before being handled by PISA, the events from the PYTHIA generator were processed first through another PISA configuration file, the so called kinematic filter file `event.par`. In the `event.par`, a user can set various kinematic cuts and particle identity cuts, if desired. The `event.par` file configured for the current analysis is given in Figure 64. Most of the variables have obvious meanings. Using

```

$epar
y_min = -1.e+20,
y_max = +1.e+20,
p_min = 0.00,
p_max = +1.e+20,
pt_min = 0.00,
pt_max = +1.e+20,
the_min = 0.00,
the_max = 180.00,
phi_min = -180.00,
phi_max = +180.00,
xyz0_input = 0.0, 0.0, 0.0,
vrms = 0.025, 0.025, +22.0,
north_south = 0,
nskip_evt = 0,
t0cent = 0.0,
t0width = 0.0,
$end

```

Figure 64: PISA kinematic filter file `event.par` for the current analysis simulation

the corresponding RMS of the distributions of the data, “vrms,” we spread the simulated collision vertex with a Gaussian distribution of a  $\sigma = 22$  cm in the  $z$  direction and  $\sigma = 0.025$  cm in the  $x$  and  $y$  directions, with the center of the

distribution at the “xyz0.input = 0.0, 0.0, 0.0”. This has to be done because PYTHIA generates events exactly at a (0.0, 0.0, 0.0) interaction point, while in the experiment the interaction region in PHENIX of the two beam bunches has a spread with a sigma of approximately 22 cm in the  $z$  direction.

The “hits file,” `PISAEvent.root`, was handled by the next stage program called `pisaToDST` which modeled with as much realism as possible what would be the real electronic signals from the detector subsystems and produced data in the same layout as from the PHENIX Data Acquisition system. The `pisaToDST` stage also reconstructed the simulated data. Simulated events were processed through the entire PHENIX reconstruction chain as with real data. The `pisaToDST` program uses exactly the same software as for the real data reconstruction. The `pisaToDST` stage was also time-consuming but faster than the PISA stage. The output from this stage was written to `simDST.root` file which stored the simulated event-by-event data in an identical format as in the DST (Data Summary Tape) files which are the PHENIX real-data files. The last data reconstruction stage, `Fun4AllDST`, divided the simulated data into `simCNT` (Central-Arm data) and `simMWG` (Muon-Arm data) files, as was done for the real data. This last stage proceeded much faster than the preceding simulation stages. The whole simulation data reconstruction chain has been installed and configured in `/direct/phenix+u/workarea/stepanov/cntmusim/pisaToDST_run6/`.

### 7.1.3 Multistage Simulation Chain and Ancestry Tracking

The scheme of the multistage simulation chain used in the current analysis simulation is depicted in Figure 61. All simulation stages described in the previous chapters are shown along with the output files produced at every stage. The whole multistage simulation chain has been installed and configured in the directory `/direct/phenix+u/workarea/stepanov/cntmusim/`.

On the last stage we used the `cntmusimAnc` analysis code. This code was developed on the basis of the `offline/AnalysisTrain/cntmu` package to work with the combined data from the Central Arms (`simCNT.root`) and the Muon Arms (`simMWG.root`) and specifically upgraded for the simulation to track particle ancestry through all simulation stages, which let us know the origin of all reconstructed particles in the simulation output. The `cntmusimAnc` analysis code has been installed and configured in `/direct/phenix+u/workarea/stepanov/cntmusimAnc/`.

The ancestry tracking part of the `cntmusimAnc` analysis code includes two subdivisions: the particle ancestry tracking itself and the evaluation part. In order to develop discriminants to distinguish between the open-charm muons and other inclusive muon candidates, we need to know the origins of the detected particles producing hits in the PHENIX subsystems. The `cntmusimAnc` analysis code provides the track ancestry capability. On the PYTHIA and PISA stages, the particle ancestry tracking establishes direct and unambiguous relations between original (parent or primary) particles and their descendant (daughter or secondary) parti-

cles. That is, for every PISA track in the “hits file” it is possible to establish its proton constituent origin. The established relations are shown as double arrows in Figure 61.

As regards the reconstruction stage, it is not possible to establish direct relations between the reconstructed tracks and their origins. The evaluation part of the ancestry tracking code produces an event-by-event association between the reconstructed tracks in the simulated DSTs (`simCNT.root` and `simMWG.root`) and the true tracks in the PISA “hits file.” In other words, the evaluation part correlates the “signal” information in the DSTs with the exact particle information known from the PISA tracking program and the PYTHIA event generation. This is done by comparing different kinematic variables of the reconstructed tracks in the simulated DSTs with the same variables of the true tracks in the PISA “hits file.” For muon tracks in the `simMWG.root` DST, we used comparison of the  $p_x$ ,  $p_y$ , and  $p_z$  variables which contained information about the  $p_x$ ,  $p_y$ , and  $p_z$  momentum components. For every reconstructed track, we calculated a likelihood for all PISA true tracks in an event as:

$$L_{MWG}^{true/rec} = \prod_{i=x,y,z} \frac{1}{\sqrt{2\pi}\sigma_i} \exp\left(-\frac{(p_i^{true} - p_i^{rec})^2}{2\sigma_i^2}\right), \quad (85)$$

where  $p_i^{rec}$  ( $i = x, y, z$ ) stands for the momentum components of the reconstructed track,  $p_i^{true}$  ( $i = x, y, z$ ) stands for the momentum components of the PISA true track, and  $\sigma_x$ ,  $\sigma_y$ ,  $\sigma_z$  are momentum reconstruction errors for  $p_x$ ,  $p_y$ , and  $p_z$ , respectively. The momentum reconstruction errors were extracted from the diagonal

elements of the covariance matrix stored in the `simMWG.root` and returned from the Kalman filter fit used for momentum reconstruction in the Muon Arms. Maximum likelihood from Equation 85 picks the best match among the PISA true tracks, the most probable track among all PISA true tracks to turn out to be original track for the reconstructed track. For the Central-Arm tracks, we compared variables  $ptot$ ,  $phi$ , and  $theta$  which contained information about total momentum  $p$ , azimuth angle  $\phi$ , and polar angle  $\theta$ . We calculated the likelihood as:

$$L_{CNT}^{true/rec} = \frac{1}{\sqrt{2\pi}\sigma_p} \exp\left(-\frac{(p^{true} - p^{rec})^2}{2\sigma_p^2}\right), \quad (86)$$

and cut on the azimuth and polar angle deviations,  $|\phi^{true} - \phi^{rec}|$  and  $|\theta^{true} - \theta^{rec}|$ . For the standard deviation,  $\sigma_p$ , we used the momentum resolution of the DC/PC1 tracker,  $\sigma_p/p \approx 0.7\% + 0.9\%p$  [85]. We selected the best match to the reconstructed track among the PISA true tracks with the maximum likelihood and the azimuth and polar angle deviations less than nominal values. The nominal value both for the azimuth and polar angle deviations was  $10^\circ$ . This nominal value was determined from studies of the evaluation algorithm performance.

Information such as the particle ancestry and the reconstruction evaluation is not available in the real data. But we need this information in the simulation data in order to proceed with the track correlation studies. Thus, the simulation data files have additional variables compared to what we have in the real data files. These additional variables contain information which is used to evaluate the performance of the event reconstruction of the simulated events and to track

particle ancestry through all simulation stages up to the original collided proton constituents. For every reconstructed track we store a *likelihood* variable, which is the output from the evaluation algorithm (Equations 85 and 86). The *likelihood* variable contains information about quality of the track reconstruction, that is, how well the reconstructed track is matched to the PISA true track. For ghost reconstructed tracks, for which the evaluation algorithm could not find any match among the PISA true tracks, we assigned  $likelihood = 0$ . The ancestry tracking yields the variable *origin*. The values of the *origin* variable depending on the detected particle origin are presented in Table 9.

Table 9: Variable *origin* from ancestry tracking

Origin	Variable <i>origin</i>
light-quark decay	1
$c\bar{c}$ decay	4
$b\bar{b}$ decay	5

Samples of  $c\bar{c}$ , minimum-bias (i.e. mostly light-quark), as well as  $b\bar{b}$  events, were produced with the use of the multistage simulation chain. For the  $c\bar{c}$  sample and the minimum-bias sample, we produced  $14 \times 10^6$  events and  $13.1 \times 10^6$  events, respectively. In addition we produced  $2 \times 10^5$  events for the bottom quark sample for the intended  $b\bar{b}$  production study, but we did not use this sample in the current analysis extensively because of its limited statistics.

### 7.1.4 Minimum-bias Modeling

The sample of minimum-bias (i.e. mostly light-quark) events was generated in order to be compared to the sample of open-charm events. On the first (PYTHIA simulation) stage we used the switches and parameters listed in Table 8. With the switch MSEL set to 1, minimum-bias collisions were generated with QCD hard scattering processes enabled, though single and double diffractive and elastic scattering processes were excluded from the event generation.

A full test simulation including only the diffractive processes turned on has been run. This simulation indicated that less than 0.05% of the generated diffractive events produced muon tracks which were reconstructed in the Muon Arms and passed good quality cuts. This test justifies the exclusion of the single and double diffractive scattering processes from the minimum-bias simulation.

The total and elastic cross sections for  $p - p$  collisions at 200 GeV center-of-mass energy are  $\sigma_{pp}^{total} = 52.0 \pm 0.5$  mb and  $\sigma_{pp}^{elastic} = 10 \pm 1$  mb, respectively [3]. Hence, inelastic  $p - p$  cross section is  $\sigma_{pp}^{inelastic} = \sigma_{pp}^{total} - \sigma_{pp}^{elastic} = 42.0 \pm 1.2$  mb. The total cross section for single and double diffractive scattering processes is  $\sigma_{pp}^{diff.} = 11.5 \pm 0.5$  mb [131]. Thus, the resulting inelastic cross section for non-diffractive  $p - p$  collisions generated in the current minimum-bias modeling is  $\sigma_{pp}^{inel.,non-diffr.} = \sigma_{pp}^{total} - \sigma_{pp}^{elastic} - \sigma_{pp}^{diff.} = 30.5 \pm 1.3$  mb.

Figure 65 demonstrates the agreement between the simulation results and real data. The figure shows the single-muon  $p_T$  spectra in the PHENIX Muon Arms ob-

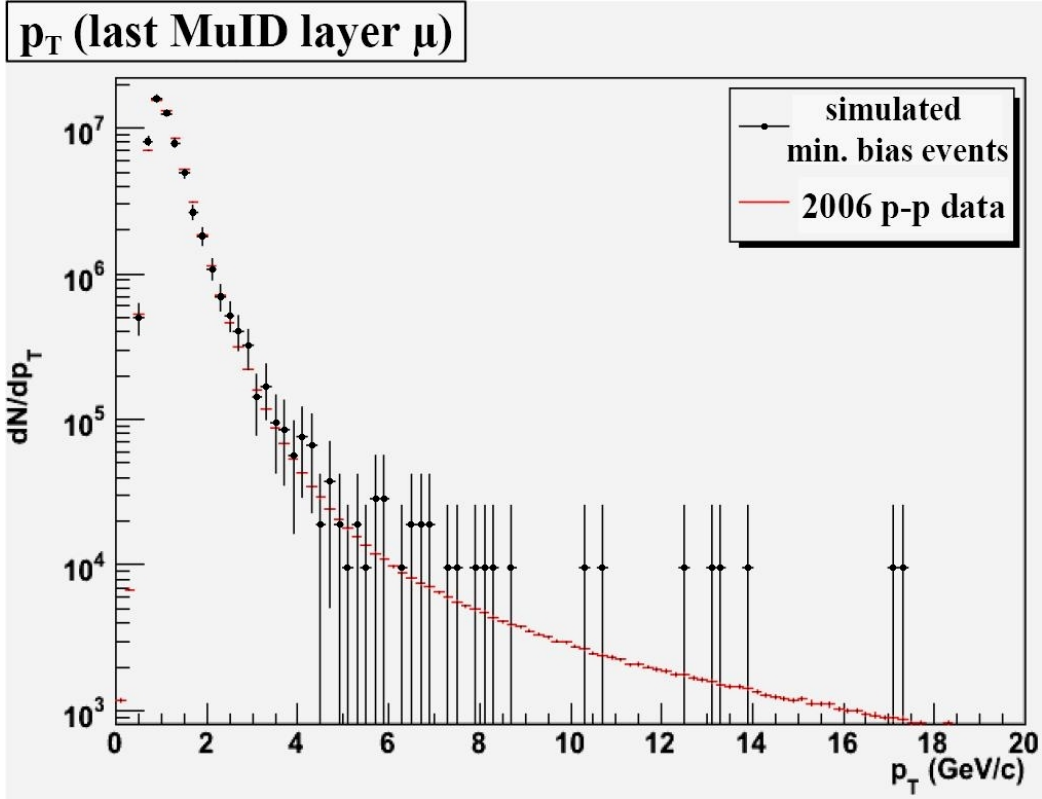


Figure 65: Minimum-bias simulation single-muon  $p_T$  spectrum compared to single-muon  $p_T$  spectrum from the PHENIX Run-6  $p - p$  data

tained from the simulated minimum-bias sample and from the 2005-2006 PHENIX Run-6 data collected from longitudinally-polarized  $p - p$  collisions at  $\sqrt{s} = 200$  GeV. The simulation spectrum was normalized at  $p_T = 1$  GeV/ $c$ . One can see that the simulation is in good accord with the real data.

### 7.1.5 Charm Modeling

For the sample of  $c\bar{c}$  events, we generated another PYTHIA minimum-bias sample using the same PYTHIA simulation switches and parameters which are listed in Table 8. Then the  $c\bar{c}$  events were selected from the PYTHIA minimum-bias sample and processed through the rest of the multistage simulation chain (PISA

and data reconstruction chain).

When PYTHIA is run with the charm ( $c\bar{c}$ ) production selected (the switch MSEL set to 4), only the leading-order charm production mechanisms, gluon-gluon fusion and quark-antiquark annihilation, shown in Figure 22, are involved in the simulation. It is known that the lowest-order PYTHIA calculations (MSEL=4) fail to describe well single-electron and single-muon production from charm quarks produced with large  $p_T$ . As discussed in Chapter 4.1, the leading-order processes account only for a small fraction of the total charm production cross section. The remainder of the cross section results from the higher-order charm-production mechanisms shown in Figure 30. The higher-order charm-production processes are included in a simulation when PYTHIA is run with the switch MSEL set to 1, with the hard scattering processes enabled. The pair creation and flavor excitation mechanisms can be switched on individually by a user to occur in each event in PYTHIA, but the gluon splitting cannot be switched on individually by a user. Thus, to include all of the higher-order charm-production processes in PYTHIA simulation, one has to simulate hard interactions fully with the switch MSEL set to 1. For the total charm production cross section, PYTHIA gives  $\sigma_{c\bar{c}} = 666 \mu\text{b}$ .

## 7.2 Central-Arm Track Selection

Tracks from the Central East and West Arms have been analyzed in the simulation project. The momentum of each track is determined by the inner DC/PC1 tracker. No particle-identification detectors have been involved in the simulation

project, but it is possible to assert from the simulation output which particle produced a track. Cuts have been applied on the Central-Arm track parameters in order to reduce contributions from backgrounds. These standard cuts are listed in Table 10. Applying these cuts, only the best-quality Central-Arm (DC/PC1)

Table 10: Central-Arm (DC/PC1) track cuts

Cut	Setting
1) Drift Chamber track quality	63
2) DC/PC1 fiducial cut	$ zed  < 75$ cm

tracks are selected.

### 7.3 Simulation Data Analysis: Track Correlation Study

Correlations of kinematic variables between the highest- $p_T$  Muon-Arm track and high- $p_T$  Central-Arm tracks have been studied, with the help of the simulation, in order to develop discriminants and multivariate selection criteria that favor open-charm events. Analysis of  $c\bar{c}$  pair decay products in the output from the multistage simulation has been done. Two separate sets of the simulation output files, one for charm, another for minimum-bias events, were compared. The goal was to discriminate between open-charm and minimum-bias events. For the current simulation analysis, the events were selected in both sets of the simulation files with at least one muon track per event in either arm (North or South) of the Muon

spectrometer and at least one charged track in the same event in the Central Arm. The same event and track-selection cuts which were used for the real data were also applied to the simulated data. Only the best-quality muon tracks (see Chapter 6.3) which reach the deepest Muon Identifier layer and the best-quality Central-Arm tracks (see Chapter 7.2) were selected for the current simulation analysis.

The studies reported in the following chapters indicate a somewhat increased tendency in charm events for the maximum- $p_T$  Central-Arm track to be produced back-to-back in azimuthal angle  $\phi$  with the maximum- $p_T$  Muon-Arm track. Additional studies involve correlations between the  $p_T$  of the muon track and the  $p_T$  of the particles detected in the Central Arms including combinations of variables, described later.

### 7.3.1 Simulation Studies of Azimuthal-Angle Correlations

Studies of the azimuthal-angle correlation of muons at forward rapidity (in the Muon Arms) with mid-rapidity particles (in the Central Arms) for open-charm events in the PHENIX detector were performed using the simulation output data. The azimuthal-angle correlations of the maximum- $p_T$  Central-Arm and Muon-Arm tracks have been studied and compared for the  $c\bar{c}$  events and the minimum-bias events. For this analysis, from each event we selected the Muon-Arm track with the maximum transverse momentum,  $p_T^{\mu(max)}$ , and the Central-Arm track with the maximum transverse momentum,  $p_T^{h/l(max)}$ .

The distributions of the azimuthal angle between the maximum- $p_T$  Muon-Arm

track and the maximum- $p_T$  Central-Arm track,  $\Delta\phi = \left| \phi_{p_T^{\mu(max)}} - \phi_{p_T^{h/l(max)}} \right|$ , both for the open-charm events and for the minimum-bias events, are shown in Figures 66 and 67, respectively. Applying the cut  $likelihood > 0.0$ , we excluded the ghost tracks from the analysis. From the open-charm sample, we selected only particles originating in  $c\bar{c}$  decays. From the minimum-bias sample, we selected only particles originating in light-quark decays ( $origin = 1$ ). The  $\Delta\phi$  distributions showed a peak around  $180^\circ$  both for the open-charm events and for the minimum-bias events. But the ratio of these two distributions demonstrated some preference for the open-charm events around  $180^\circ$ . The ratio, along with the linear fit to the ratio, is shown in Figure 68. The fitting parameter  $p1$  given in the box in Figure 68 refers to the slope of the linear fit. Based on the value of the  $p1$  parameter, there is some small increase in the tendency for the charm events to have the maximum- $p_T$  mid-rapidity particles (in the Central Arms) and forward-rapidity muons (in the Muon Arms) emitted back-to-back in azimuthal angle  $\phi$ .

Further we have studied the azimuthal-angle correlations of the maximum- $p_T$  Central-Arm and Muon-Arm tracks as a function of the Muon-Arm track  $p_T$ , and the obtained distributions have also been compared for  $c\bar{c}$  events and minimum-bias events. Figures 69, 70, 71, and 72 show the distributions of the azimuthal angle between the maximum- $p_T$  Muon-Arm track and the maximum- $p_T$  Central-Arm track in the different Muon-Arm track  $p_T$  bins for the open-charm sample. Figures 73, 74, 75, and 76 demonstrate the  $\Delta\phi$  distributions in the different Muon-Arm track  $p_T$  bins for the minimum-bias sample. Again, we excluded the ghost

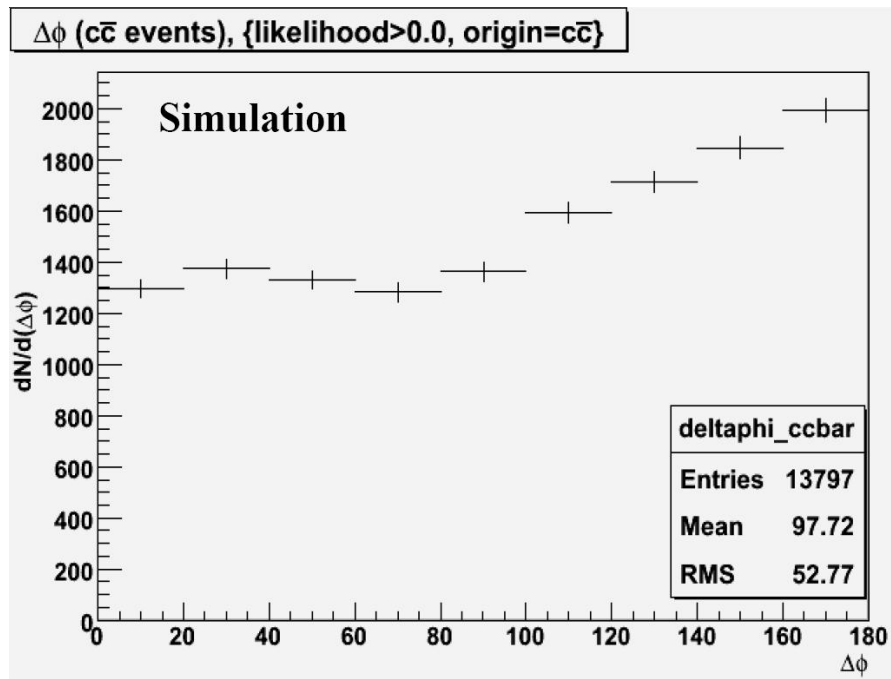


Figure 66: Azimuthal angle between maximum- $p_T$  Muon-Arm track and maximum- $p_T$  Central-Arm track for  $c\bar{c}$  events

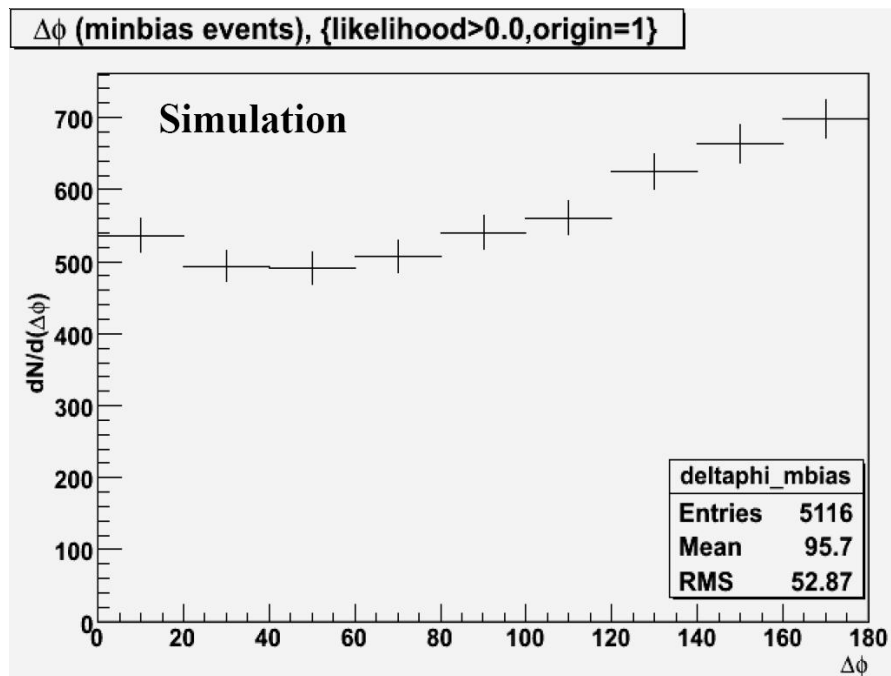


Figure 67: Azimuthal angle between maximum- $p_T$  Muon-Arm track and maximum- $p_T$  Central-Arm track for minimum-bias events

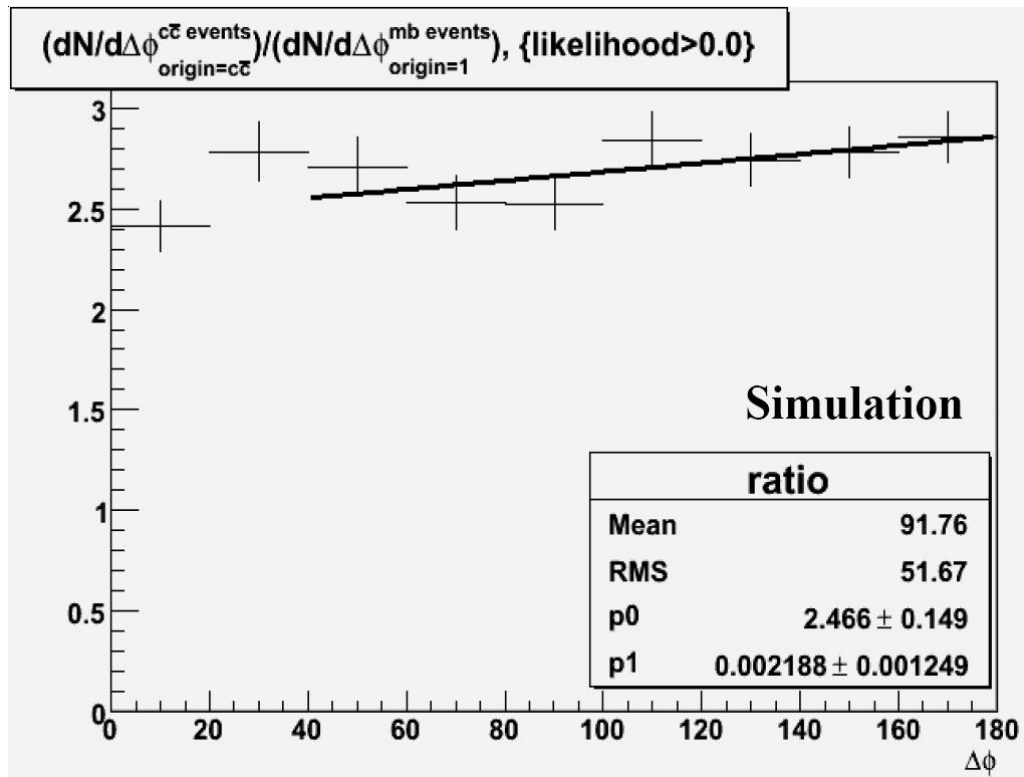


Figure 68: Ratio of two distributions — open-charm  $\Delta\phi$  distribution over minimum-bias  $\Delta\phi$  distribution

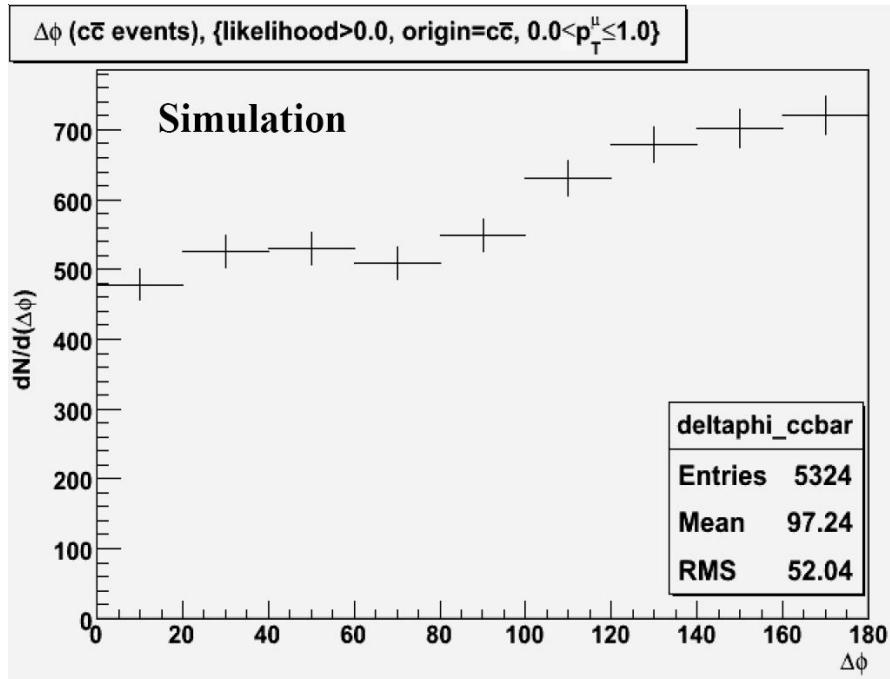


Figure 69: Azimuthal angle between maximum- $p_T$  Muon-Arm and Central-Arm tracks for  $0.0 < p_T^{\mu(max)} \leq 1.0$  GeV/ $c$  ( $c\bar{c}$  events)

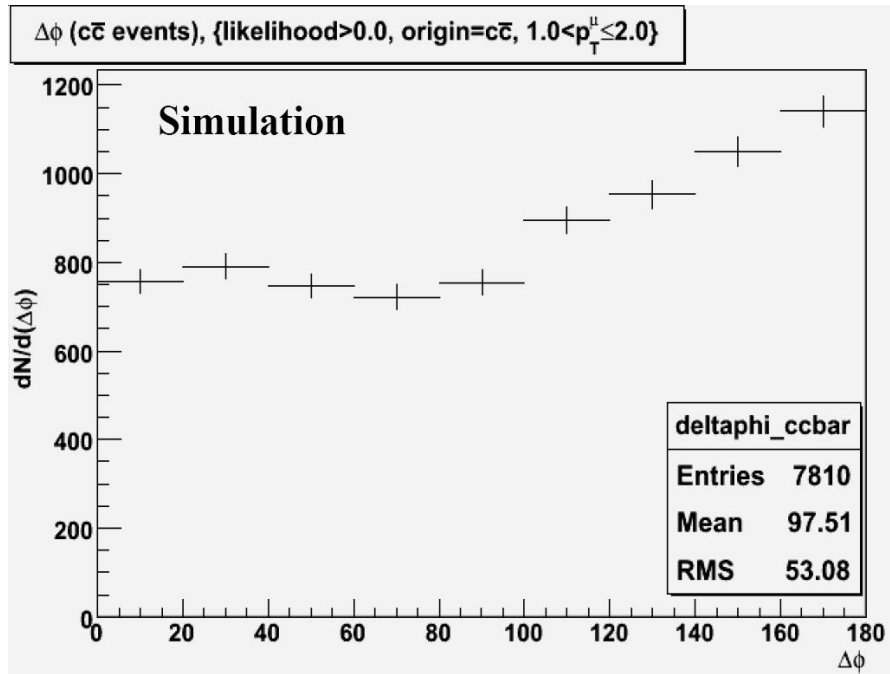


Figure 70: Azimuthal angle between maximum- $p_T$  Muon-Arm and Central-Arm tracks for  $1.0 < p_T^{\mu(max)} \leq 2.0$  GeV/ $c$  ( $c\bar{c}$  events)

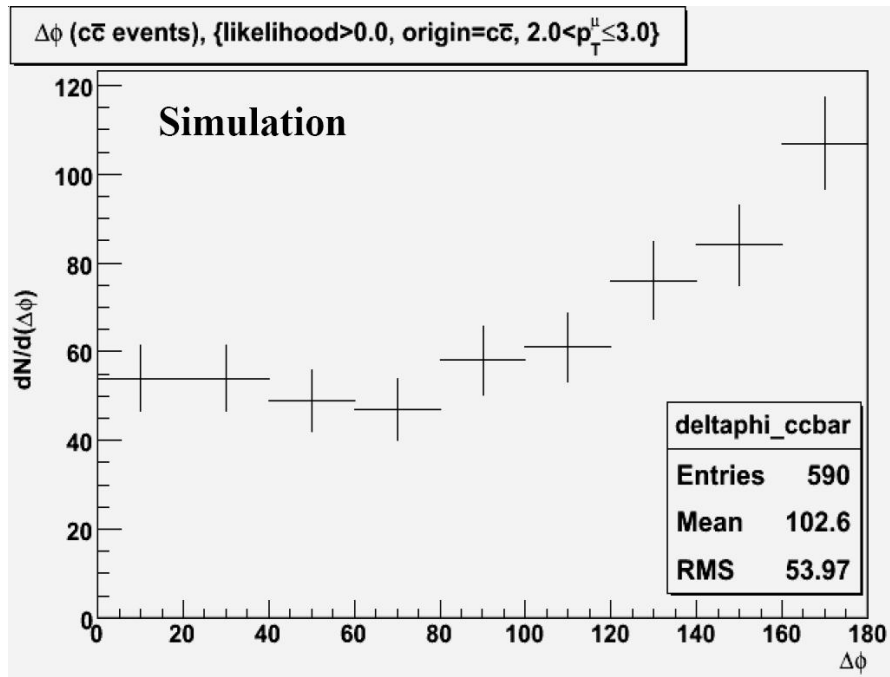


Figure 71: Azimuthal angle between maximum- $p_T$  Muon-Arm and Central-Arm tracks for  $2.0 < p_T^{\mu(max)} \leq 3.0$  GeV/c ( $c\bar{c}$  events)

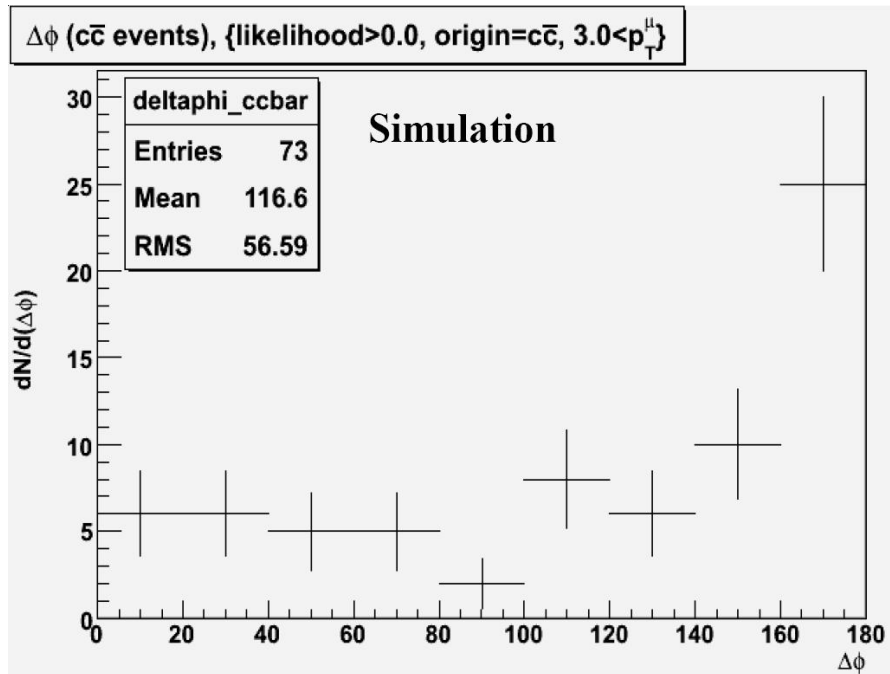


Figure 72: Azimuthal angle between maximum- $p_T$  Muon-Arm and Central-Arm tracks for  $3.0 \text{ GeV}/c < p_T^{\mu(max)}$  ( $c\bar{c}$  events)

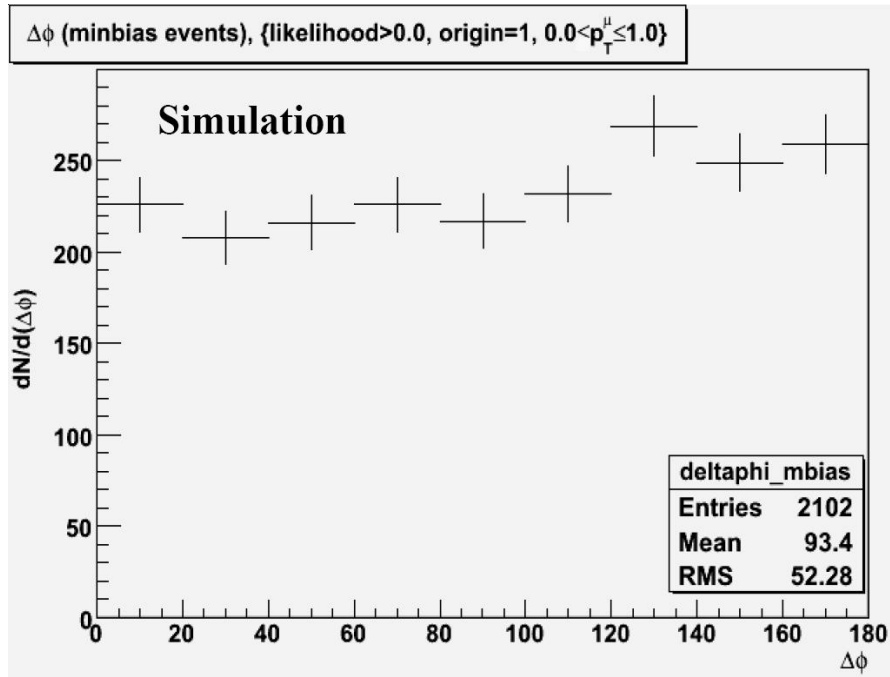


Figure 73: Azimuthal angle between maximum- $p_T$  Muon-Arm and Central-Arm tracks for  $0.0 < p_T^{\mu(max)} \leq 1.0$  GeV/ $c$  (minimum-bias events)

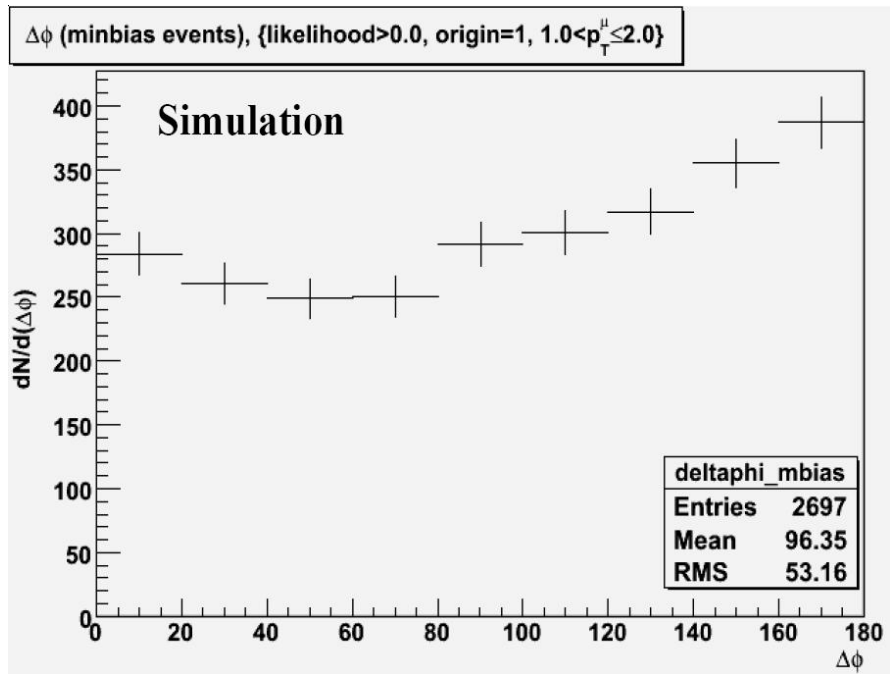


Figure 74: Azimuthal angle between maximum- $p_T$  Muon-Arm and Central-Arm tracks for  $1.0 < p_T^{\mu(max)} \leq 2.0$  GeV/ $c$  (minimum-bias events)

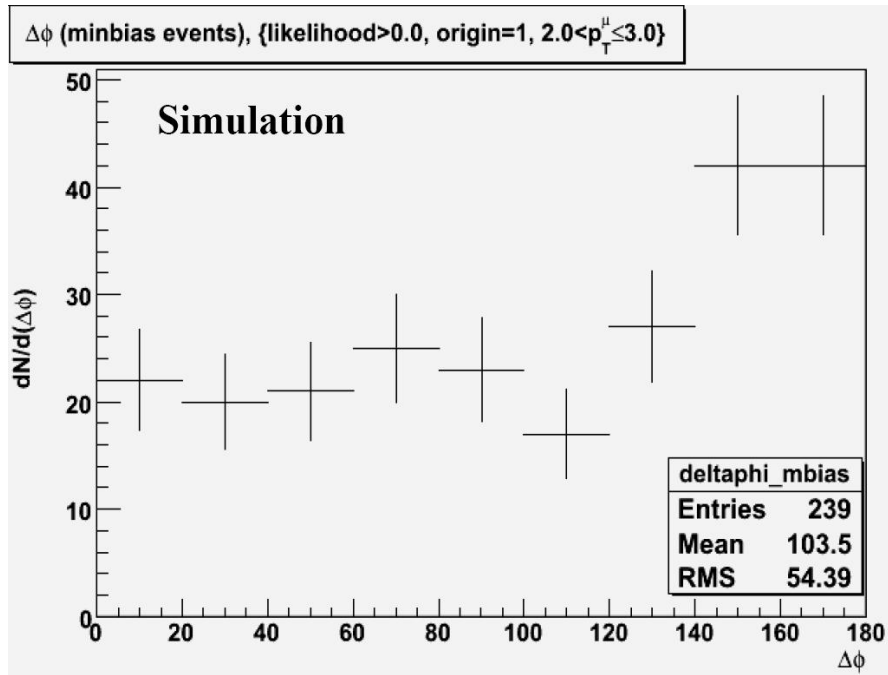


Figure 75: Azimuthal angle between maximum- $p_T$  Muon-Arm and Central-Arm tracks for  $2.0 < p_T^{\mu(max)} \leq 3.0$  GeV/c (minimum-bias events)

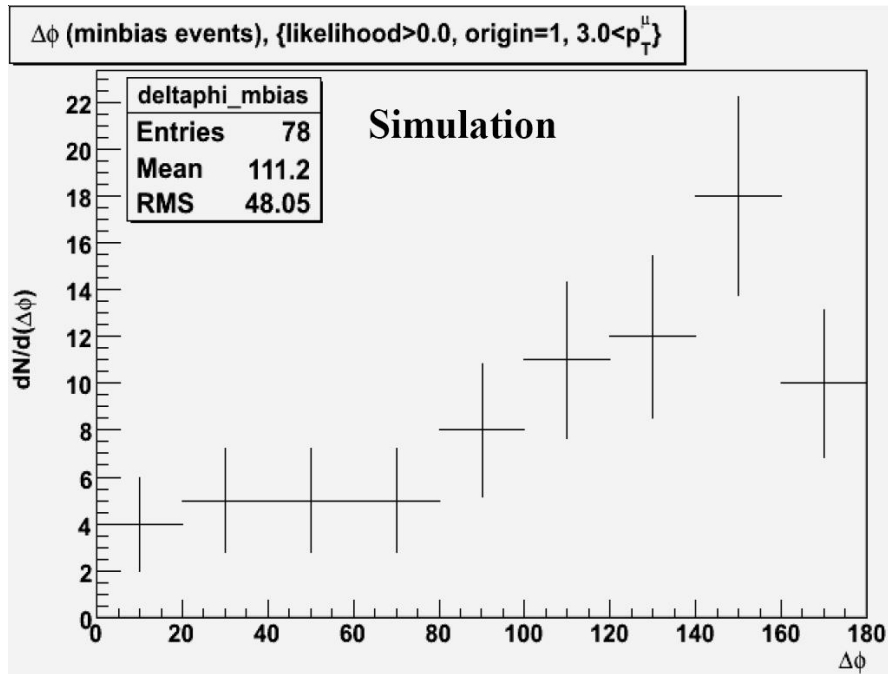


Figure 76: Azimuthal angle between maximum- $p_T$  Muon-Arm and Central-Arm tracks for  $3.0 \text{ GeV}/c < p_T^{\mu(max)} < 3.5$  GeV/c (minimum-bias events)

tracks from the analysis (the cut  $likelihood > 0.0$ ), from the open-charm sample we selected only particles originating in  $c\bar{c}$  decays, and from the minimum-bias sample we selected only particles originating in light-quark decays ( $origin = 1$ ). From the figures, one can see that the larger the Muon-Arm track  $p_T$ , the steeper and narrower the  $\Delta\phi$  distribution peak around  $180^\circ$ , both for the open-charm events and for the minimum-bias events. The ratios of the open-charm  $\Delta\phi$  distributions over the minimum-bias  $\Delta\phi$  distributions for the different Muon-Arm track  $p_T$  bins, along with the linear fits to the ratios, are shown in Figures 77, 78, 79, and 80. The fitting parameter  $p1$ , referring to the slope of the linear fit, is given in Table 11 for the different Muon-Arm track  $p_T$ . From the table one can see that the slope

Table 11: Parameter  $p1$  referring to the slope of the linear fit

Muon-Arm track $p_T$ , GeV/ $c$	slope, $p1$
$0.0 < p_T^{\mu(max)} \leq 1.0$	$0.0038 \pm 0.0019$
$1.0 < p_T^{\mu(max)} \leq 2.0$	$0.0011 \pm 0.0018$
$2.0 < p_T^{\mu(max)} \leq 3.0$	$0.0015 \pm 0.005$
$3.0 < p_T^{\mu(max)}$	$0.003 \pm 0.004$

of the fit is non-zero only for the low Muon-Arm track  $p_T$ , below 1 GeV/ $c$ . For the larger Muon-Arm track  $p_T$ , the slope is zero within uncertainties. Thus, based on the value of the  $p1$  parameter, the conclusion from the simulation study is that only for the low- $p_T$  muon tracks there is an increased preference for the charm events to

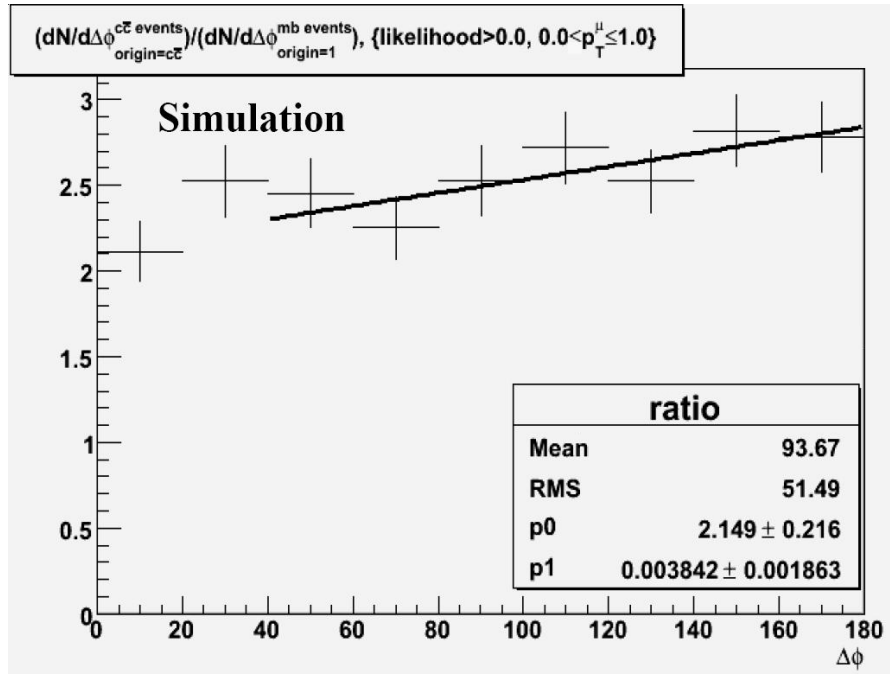


Figure 77: Open-charm  $\Delta\phi$  distribution over minimum-bias  $\Delta\phi$  distribution ratio for  $0.0 < p_T^{\mu(max)} \leq 1.0 \text{ GeV}/c$

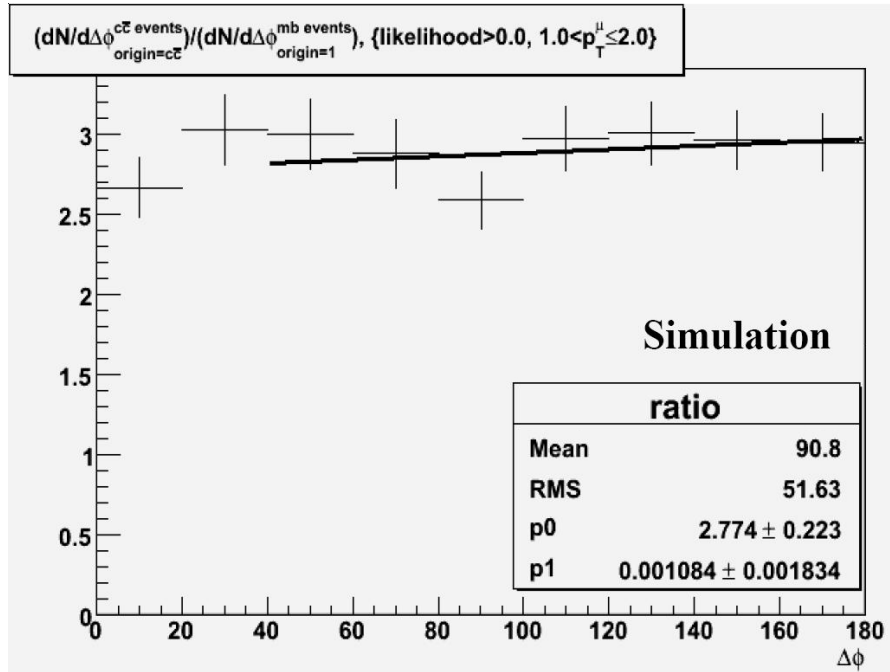


Figure 78: Open-charm  $\Delta\phi$  distribution over minimum-bias  $\Delta\phi$  distribution ratio for  $1.0 < p_T^{\mu(max)} \leq 2.0 \text{ GeV}/c$

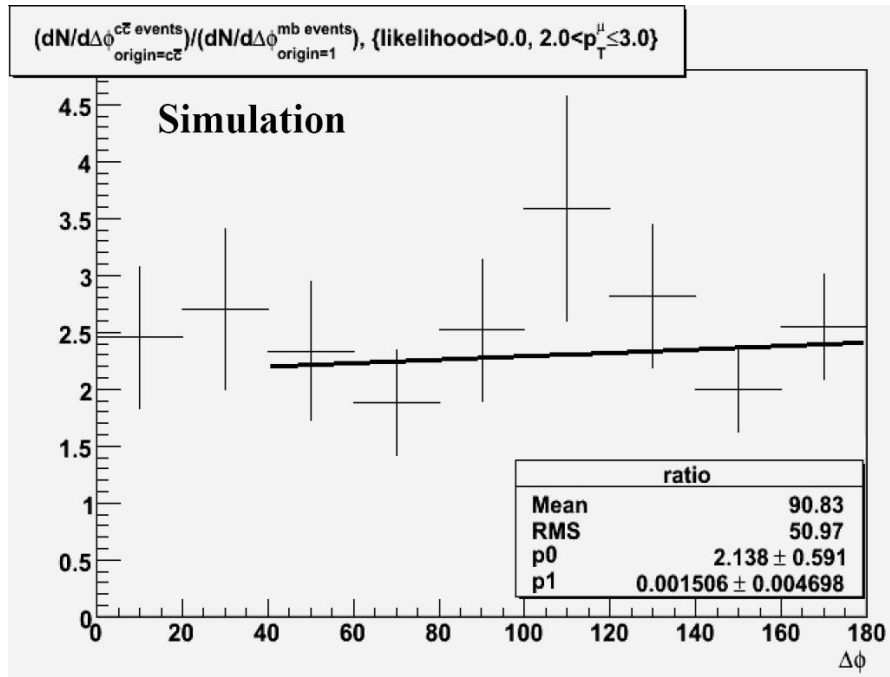


Figure 79: Open-charm  $\Delta\phi$  distribution over minimum-bias  $\Delta\phi$  distribution ratio for  $2.0 < p_T^{\mu(max)} \leq 3.0$  GeV/c

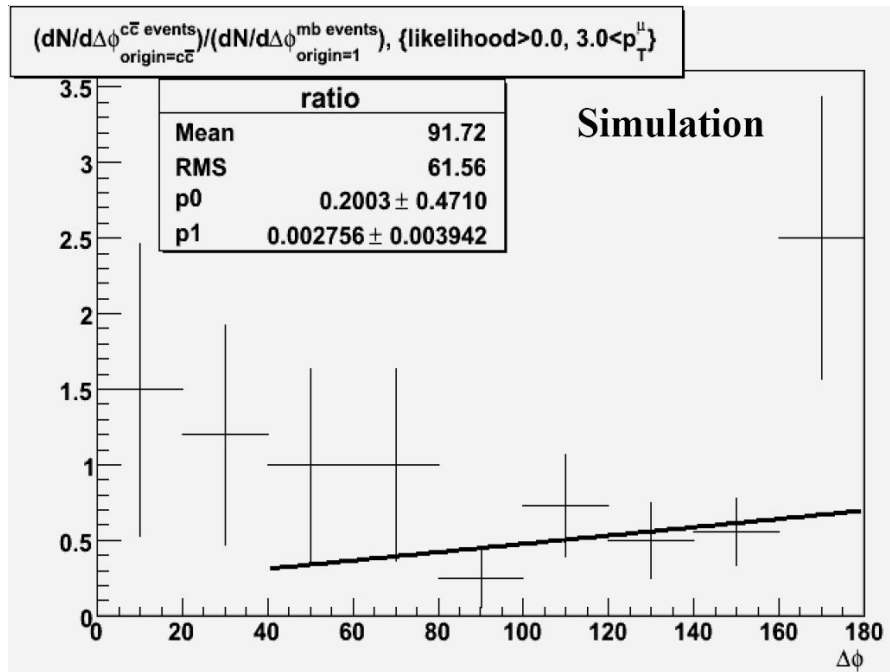


Figure 80: Open-charm  $\Delta\phi$  distribution over minimum-bias  $\Delta\phi$  distribution ratio for  $3.0 \text{ GeV}/c < p_T^{\mu(max)}$

have the maximum- $p_T$  mid-rapidity particles and forward rapidity muons emitted back-to-back in azimuthal angle  $\phi$ .

As opposed to the simulation including higher-order charm-production mechanisms, which indicates some increased tendency for charm events to have the maximum- $p_T$  Central-Arm and Muon-Arm tracks emitted back-to-back only when the Muon-Arm track has a  $p_T$  below 1 GeV/ $c$ , a leading-order simulation indicates stronger tendency for charm events to have the maximum- $p_T$  mid-rapidity particles and forward rapidity muons emitted back-to-back in azimuthal angle  $\phi$ . The leading-order simulation included only LO charm-production mechanisms with the PYTHIA switch MSEL set to 4. Figures 81, 82, and 83 show the distributions of the azimuthal angle between the maximum- $p_T$  Muon-Arm track and the maximum- $p_T$  Central-Arm track both for the LO charm production and for the minimum-bias production, and the ratio of these two distributions, respectively. Figures 84, 85, 86, and 87 show the LO charm production  $\Delta\phi$  distributions for the different Muon-Arm track  $p_T$  bins. Again, the larger the Muon-Arm track  $p_T$ , the steeper and narrower the  $\Delta\phi$  distribution peak around  $180^\circ$ . The ratios of the LO charm production  $\Delta\phi$  distributions over the minimum-bias  $\Delta\phi$  distributions for the different Muon-Arm track  $p_T$  bins, along with the linear fits to the ratios, are shown in Figures 88, 89, 90, and 91. The data for the slope-fitting parameter  $p1$  from Figures 88, 89, 90, and 91 are summarized in Table 12. From Table 12, one can see that, except for the highest Muon-Arm track  $p_T$  bin, there is a stronger tendency for the LO charm production simulated events to have the maximum- $p_T$  mid-rapidity par-

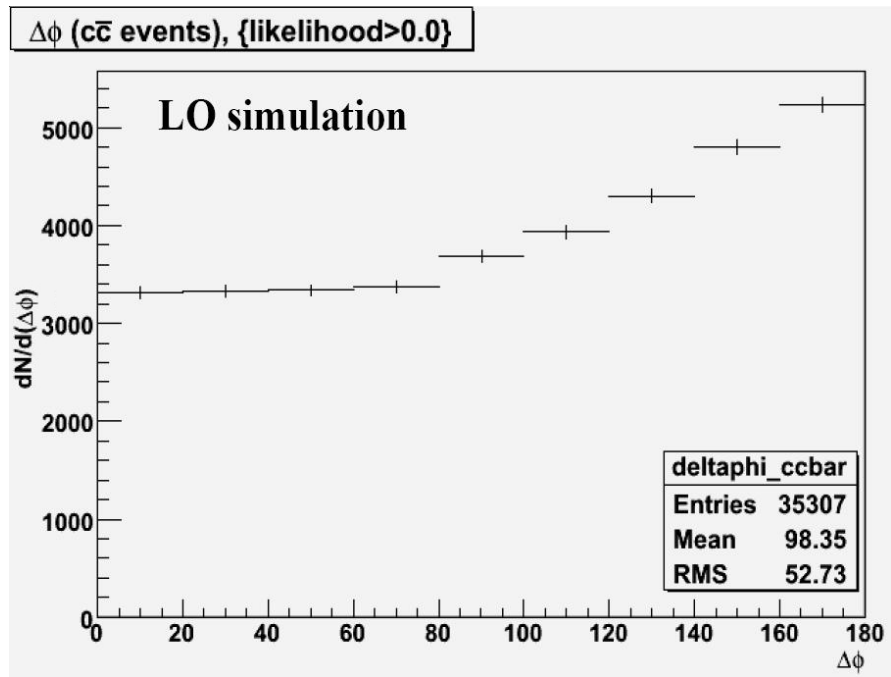


Figure 81: Azimuthal angle between maximum- $p_T$  Muon-Arm track and maximum- $p_T$  Central-Arm track for LO charm production

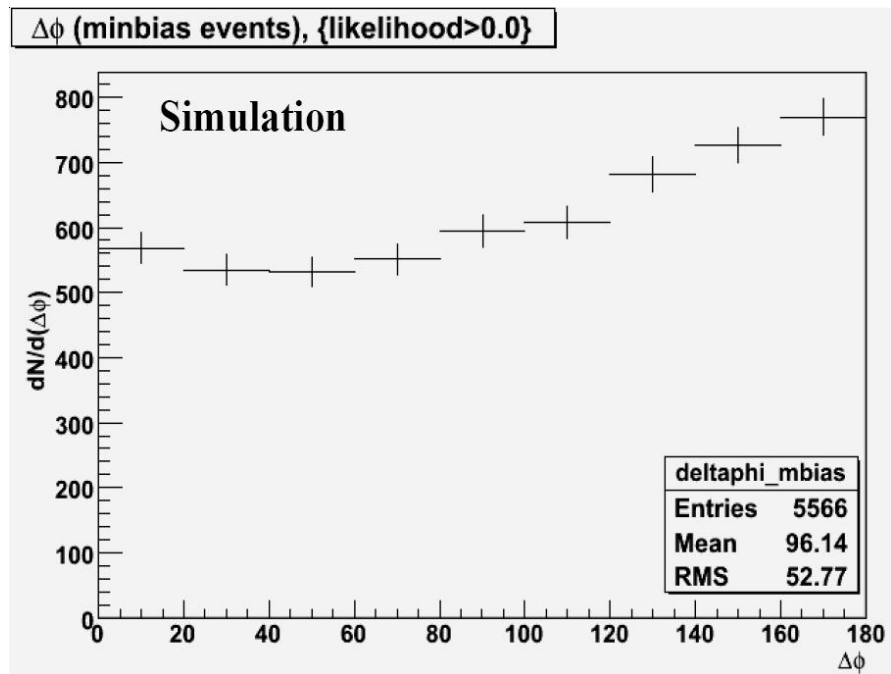


Figure 82: Azimuthal angle between maximum- $p_T$  Muon-Arm track and maximum- $p_T$  Central-Arm track for minimum-bias events (no origin cuts)

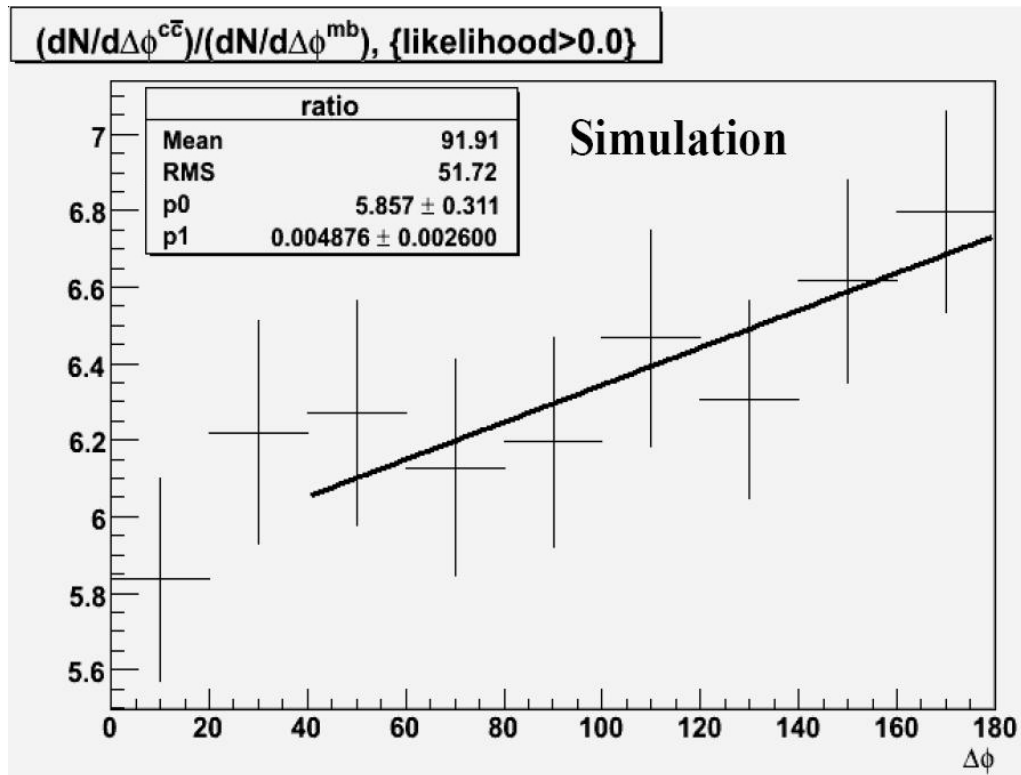


Figure 83: Ratio of two distributions — LO charm  $\Delta\phi$  distribution over minimum-bias  $\Delta\phi$  distribution

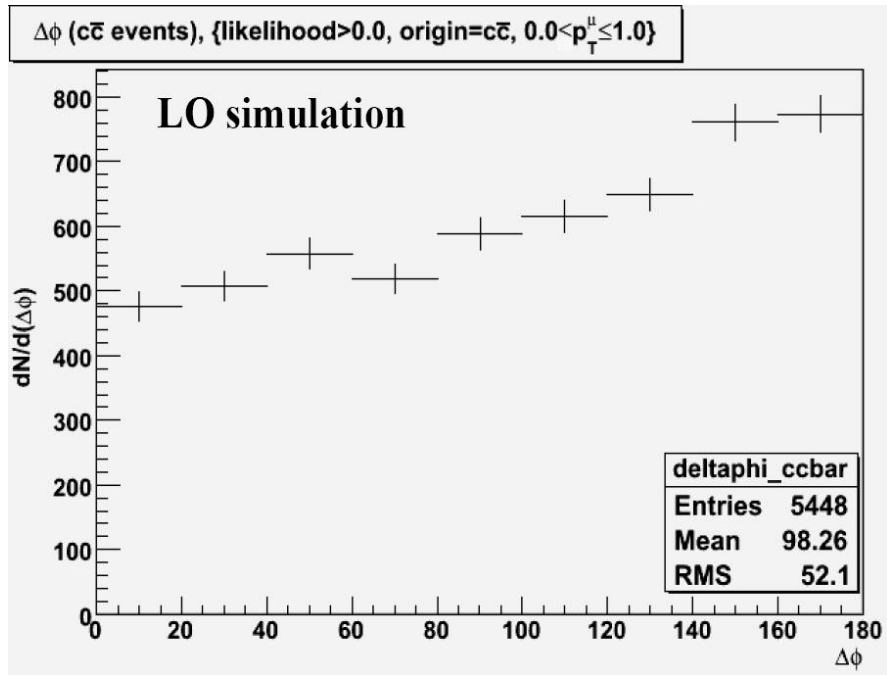


Figure 84: Azimuthal angle between maximum- $p_T$  Muon-Arm and Central-Arm tracks for  $0.0 < p_T^{\mu(max)} \leq 1.0$  GeV/c (LO  $c\bar{c}$  production)

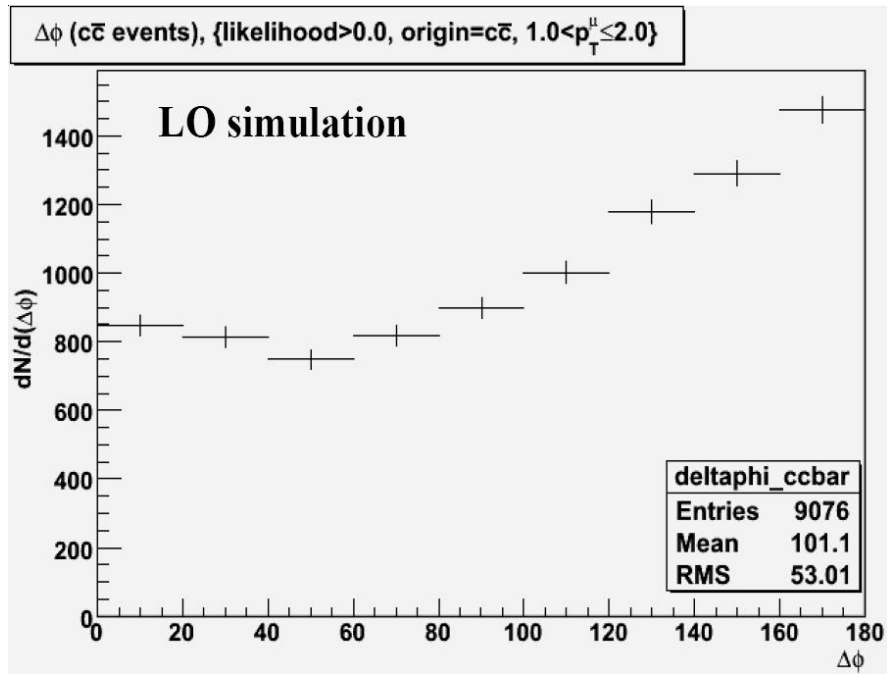


Figure 85: Azimuthal angle between maximum- $p_T$  Muon-Arm and Central-Arm tracks for  $1.0 < p_T^{\mu(max)} \leq 2.0$  GeV/c (LO  $c\bar{c}$  production)

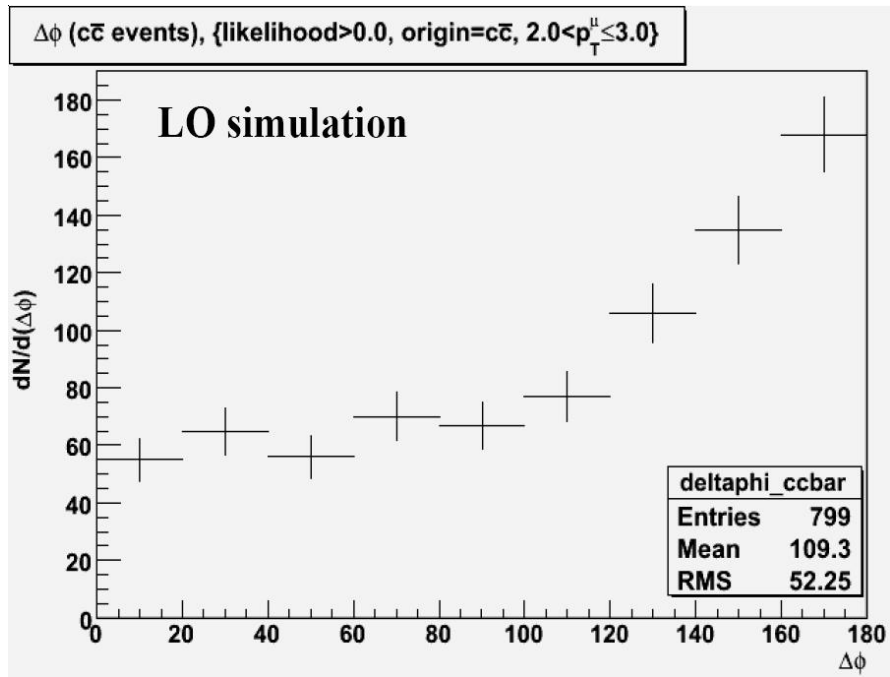


Figure 86: Azimuthal angle between maximum- $p_T$  Muon-Arm and Central-Arm tracks for  $2.0 < p_T^{\mu(max)} \leq 3.0$  GeV/c (LO  $c\bar{c}$  production)

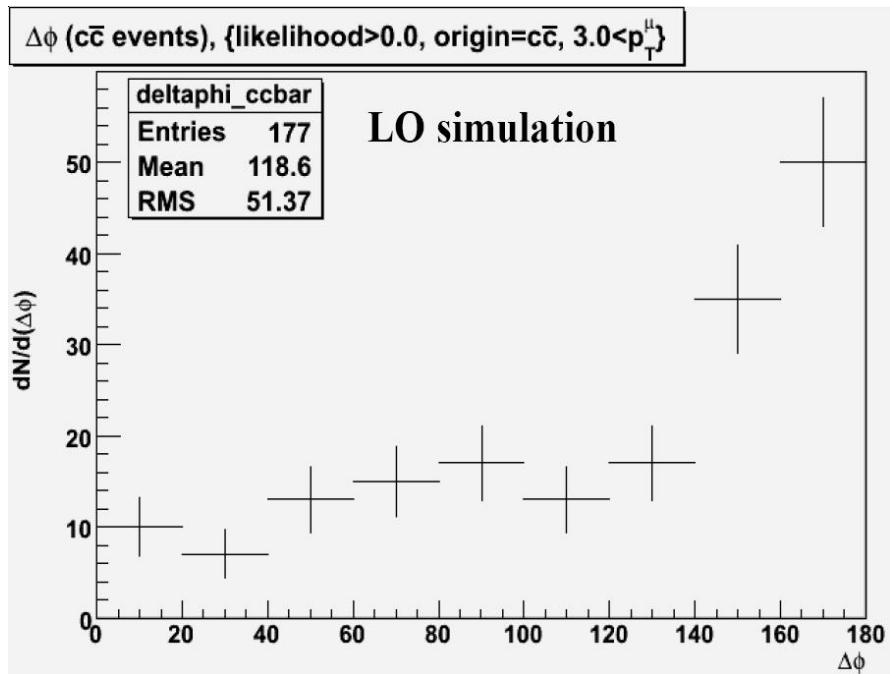


Figure 87: Azimuthal angle between maximum- $p_T$  Muon-Arm and Central-Arm tracks for  $3.0 \text{ GeV}/c < p_T^{\mu(max)}$  (LO  $c\bar{c}$  production)

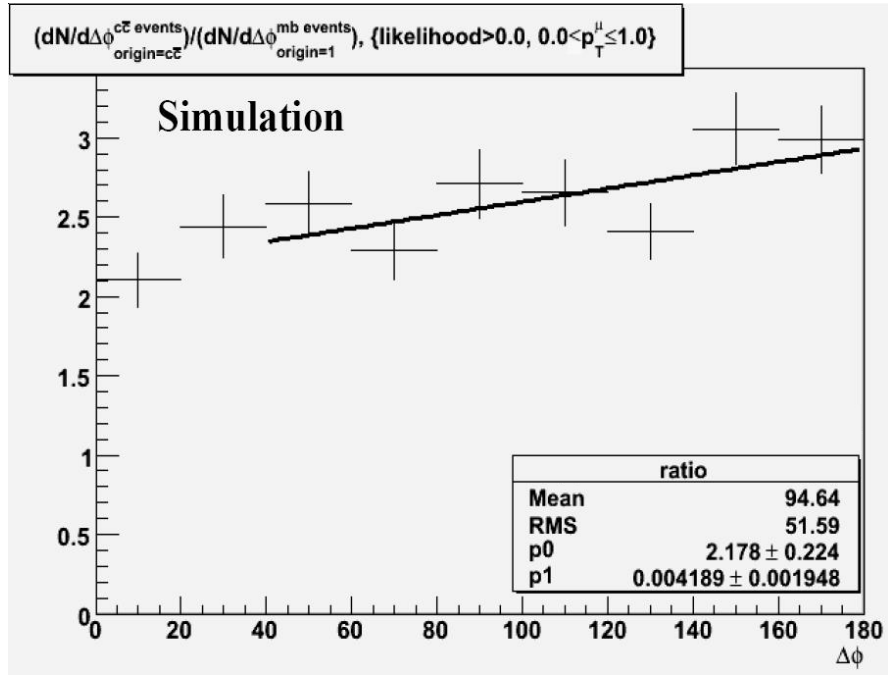


Figure 88: LO charm production  $\Delta\phi$  distribution over minimum-bias  $\Delta\phi$  distribution ratio for  $0.0 < p_T^{\mu(max)} \leq 1.0 \text{ GeV}/c$

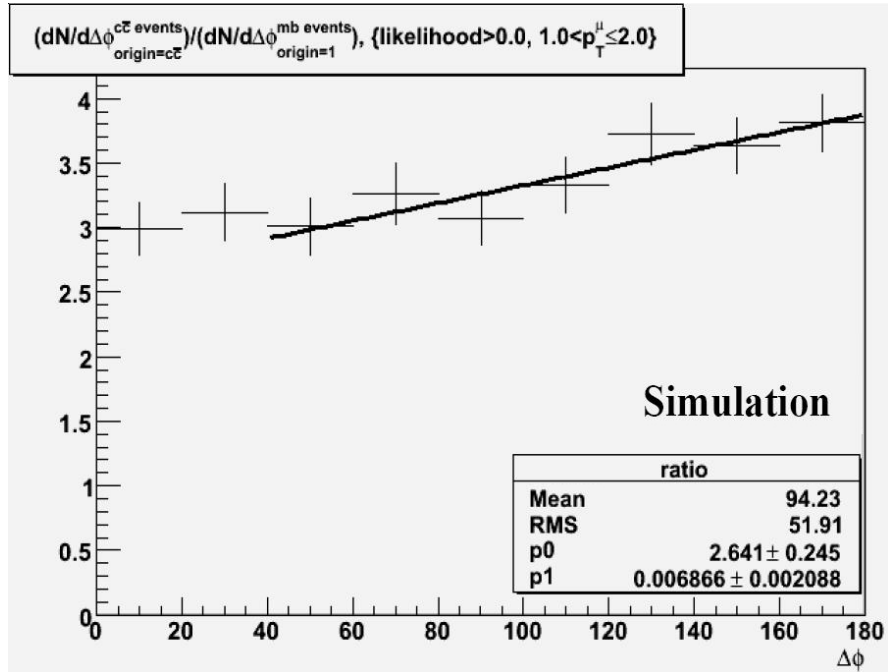


Figure 89: LO charm production  $\Delta\phi$  distribution over minimum-bias  $\Delta\phi$  distribution ratio for  $1.0 < p_T^{\mu(max)} \leq 2.0 \text{ GeV}/c$

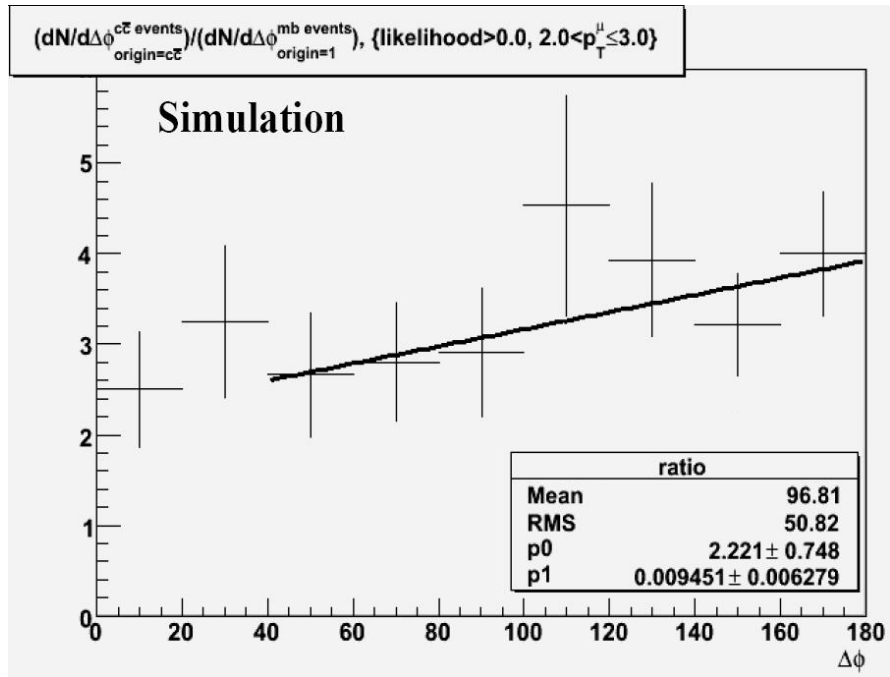


Figure 90: LO charm production  $\Delta\phi$  distribution over minimum-bias  $\Delta\phi$  distribution ratio for  $2.0 < p_T^{\mu(max)} \leq 3.0$  GeV/c

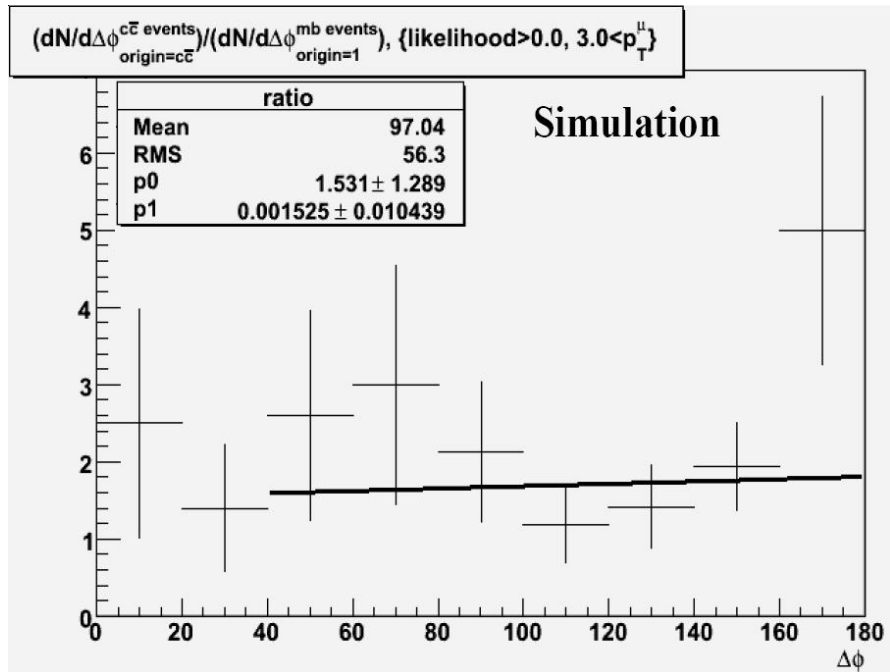


Figure 91: LO charm production  $\Delta\phi$  distribution over minimum-bias  $\Delta\phi$  distribution ratio for  $3.0$  GeV/c  $< p_T^{\mu(max)}$

Table 12: Slope parameter  $p1$  for LO charm simulation

Muon-Arm track $p_T$ , GeV/ $c$	slope, $p1$
$0.0 < p_T^{\mu(max)} \leq 1.0$	$0.0042 \pm 0.0019$
$1.0 < p_T^{\mu(max)} \leq 2.0$	$0.007 \pm 0.002$
$2.0 < p_T^{\mu(max)} \leq 3.0$	$0.009 \pm 0.006$
$3.0 < p_T^{\mu(max)}$	$0.0015 \pm 0.01$

ticles and forward rapidity muons emitted back-to-back in azimuthal angle  $\phi$  than that found for the full charm production simulation. This can be explained by the fact that, in the LO, because of momentum conservation, the  $c$  and  $\bar{c}$  quarks (and the particles produced in their consequent decays) have to be emitted back-to-back in azimuthal angle, but in the higher-order charm-production processes, the parton shower additionally produced in a hard scattering can carry away some part of the momentum. As an illustration, consider an example in Figure 30(a), where we show one of the higher-order charm-production processes called pair creation, with the additional gluon emitted. This additional parton shower emission introduces smearing of the  $\Delta\phi$  correlation. Therefore, the  $\Delta\phi$  distribution for the full charm-production simulation is more smeared than that for the LO charm production simulated events.

To summarize the azimuthal-angle correlation study, we found that the full simulation including higher-order charm-production mechanisms indicates stronger

tendency for charm events to have the maximum- $p_T$  mid-rapidity particles and forward-rapidity muon tracks emitted back-to-back in azimuthal angle  $\phi$  only for the low muon-track  $p_T$ , below 1 GeV/ $c$ . But even in the latter case, the enhancement is very small. Thus, the conclusion is that it is not possible to use  $\phi$  correlation alone to develop selection criteria to discriminate between the open-charm and the minimum-bias events. But it is possible to do this in combination with other variables.

### 7.3.2 Simulation Studies of $p_T$ Correlations

To gain further insight into the track correlations, we studied transverse-momentum correlations between the  $p_T$  of the Muon-Arm track and the  $p_T$  of the charged hadrons and leptons detected in the Central Arms. For a start, we investigated correlations of  $p_T^{\mu(max)}$  vs.  $p_T^{h/l(max)}$ , the maximum Muon-Arm track  $p_T$  against the maximum Central-Arm track (hadron or lepton)  $p_T$ , both for the open-charm events and for the minimum-bias events. As mentioned before, the charm events are expected to produce tracks with larger-than-average  $p_T$ . We plotted  $p_T^{\mu(max)}$  vs.  $p_T^{h/l(max)}$  two-dimensional histograms in order to quantify in which kinematical ( $p_T$ ) regions the open-charm production processes contribute more than all other (minimum-bias) processes. These two-dimensional histograms are shown in Figure 92, for the open-charm sample (upper plot) and for the minimum-bias sample (lower plot). It is difficult to observe any significant distinctions between the distributions examining the histograms: there are no obvious  $p_T$  regions where

the  $c\bar{c}$  events substantially dominate over the minimum-bias events. Therefore, we produced the tables shown in Figure 93 for the percentage of the events surviving the two-dimensional cuts applied both to the Muon-Arm track maximum  $p_T$  and to the Central-Arm track maximum  $p_T$ . In Figure 93, the upper table and the lower table correspond to the open-charm sample and to the minimum-bias sample, respectively. As an example, the number 42.94% in the table for  $c\bar{c}$  events in the second column from the left and in the fourth row from the bottom is the fraction of the total number of the  $c\bar{c}$  events with  $p_T^{\mu(max)} \geq 0.75$  GeV/ $c$  and  $p_T^{h/l(max)} \geq 0.5$  GeV/ $c$ . Comparing numbers from the two tables in Figure 93 for the corresponding set of the cuts, we were still unable to find any kinematical  $p_T$  regions where contributions from the open-charm sample were significantly larger than contributions from the minimum-bias sample. Moreover, contrary to our expectations, there are regions where the minimum-bias events slightly dominate over the open-charm events. This issue is addressed later in Chapter 7.4.

Because the charm quark can produce more than one high- $p_T$  decay products, we investigated correlations of  $p_T^{\mu(max)}$  vs.  $\sum p_T^{h/l}$ , the sum of the transverse momenta of the several hadron/lepton tracks in the Central Arm with the largest  $p_T$  values. Again, the goal was to quantify in which kinematical  $p_T$  regions the open-charm production processes contribute more than all other (minimum-bias) processes. First, we investigated events on the plane of  $p_T^{\mu(max)}$  vs.  $\sum_{n=3} p_T^{h/l}$ , the sum for the three Central-Arm tracks. Figure 94 shows the histograms for this type of transverse momentum correlation both for the open-charm events and for

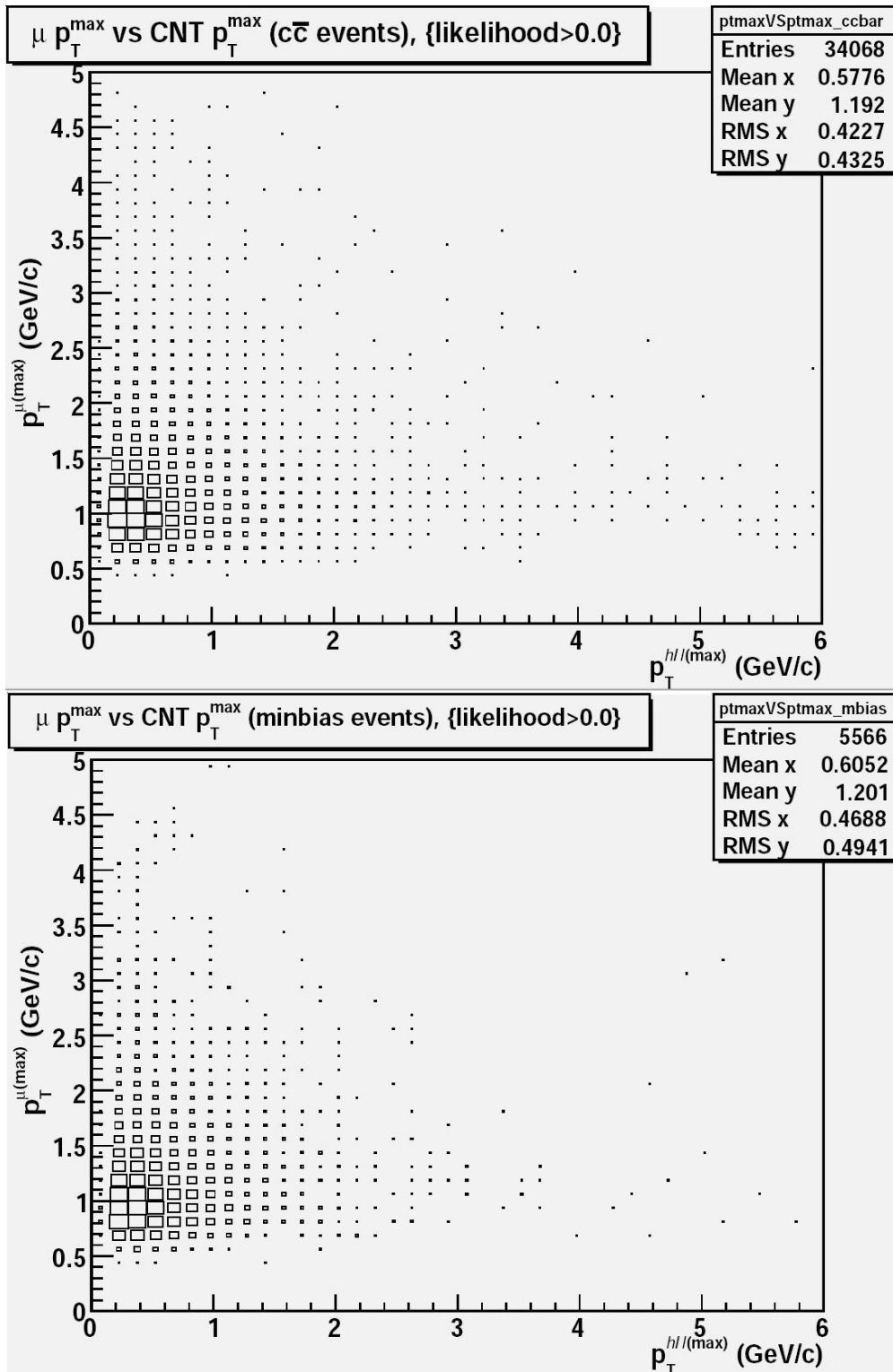


Figure 92:  $c\bar{c}$  and minimum-bias 2-dimensional histograms — maximum Muon-Arm track  $p_T$  against maximum Central-Arm track  $p_T$

<b><math>c\bar{c}</math> events</b>									
$\geq 4.75$	0.07%	0.04%	0.02%	0.01%	0.01%	0.00%	0.00%	0.00%	0.00%
$\geq 4.50$	0.10%	0.05%	0.03%	0.01%	0.01%	0.00%	0.00%	0.00%	0.00%
$\geq 4.25$	0.14%	0.07%	0.04%	0.02%	0.01%	0.00%	0.00%	0.00%	0.00%
$\geq 4.00$	0.19%	0.09%	0.04%	0.02%	0.01%	0.01%	0.01%	0.01%	0.00%
$\geq 3.75$	0.26%	0.14%	0.06%	0.03%	0.01%	0.01%	0.01%	0.01%	0.01%
$\geq 3.50$	0.34%	0.18%	0.07%	0.04%	0.02%	0.01%	0.01%	0.01%	0.01%
$\geq 3.25$	0.48%	0.28%	0.10%	0.05%	0.03%	0.01%	0.01%	0.01%	0.01%
$\geq 3.00$	0.66%	0.38%	0.12%	0.07%	0.04%	0.02%	0.02%	0.02%	0.01%
$\geq 2.75$	1.02%	0.55%	0.18%	0.09%	0.06%	0.04%	0.03%	0.02%	0.02%
$\geq 2.50$	1.69%	0.87%	0.28%	0.13%	0.08%	0.06%	0.05%	0.04%	0.03%
$\geq 2.25$	2.81%	1.43%	0.45%	0.18%	0.11%	0.08%	0.06%	0.05%	0.04%
$\geq 2.00$	5.06%	2.57%	0.76%	0.29%	0.17%	0.12%	0.09%	0.08%	0.07%
$\geq 1.75$	9.21%	4.56%	1.24%	0.45%	0.25%	0.16%	0.11%	0.10%	0.08%
$\geq 1.50$	17.74%	8.66%	2.36%	0.79%	0.41%	0.24%	0.18%	0.16%	0.14%
$\geq 1.25$	33.97%	16.22%	4.18%	1.35%	0.67%	0.40%	0.31%	0.27%	0.24%
$\geq 1.00$	61.48%	28.86%	7.31%	2.37%	1.16%	0.69%	0.54%	0.48%	0.43%
$\geq 0.75$	92.65%	42.94%	10.70%	3.30%	1.59%	0.97%	0.77%	0.69%	0.64%
$\geq 0.50$	99.95%	46.25%	11.49%	3.54%	1.71%	1.04%	0.85%	0.74%	0.68%
$\geq 0.25$	100.00%	46.27%	11.49%	3.54%	1.71%	1.04%	0.85%	0.74%	0.68%
$> 0.00$	100.00%	46.27%	11.49%	3.54%	1.71%	1.04%	0.85%	0.74%	0.68%
	$> 0.0$	$\geq 0.5$	$\geq 1.0$	$\geq 1.5$	$\geq 2.0$	$\geq 2.5$	$\geq 3.0$	$\geq 3.5$	$\geq 4.0$
	$p_T^{hl(max)}$ in the Central Arm (GeV/c)								
<b>minbias events</b>									
$\geq 4.75$	0.41%	0.22%	0.09%	0.04%	0.02%	0.02%	0.00%	0.00%	0.00%
$\geq 4.50$	0.43%	0.23%	0.09%	0.04%	0.02%	0.02%	0.00%	0.00%	0.00%
$\geq 4.25$	0.56%	0.31%	0.09%	0.04%	0.02%	0.02%	0.00%	0.00%	0.00%
$\geq 4.00$	0.74%	0.38%	0.11%	0.05%	0.02%	0.02%	0.00%	0.00%	0.00%
$\geq 3.75$	0.86%	0.41%	0.14%	0.07%	0.02%	0.02%	0.00%	0.00%	0.00%
$\geq 3.50$	0.99%	0.47%	0.14%	0.07%	0.02%	0.02%	0.00%	0.00%	0.00%
$\geq 3.25$	1.13%	0.54%	0.16%	0.09%	0.02%	0.02%	0.00%	0.00%	0.00%
$\geq 3.00$	1.62%	0.75%	0.23%	0.16%	0.07%	0.07%	0.05%	0.05%	0.05%
$\geq 2.75$	2.14%	1.04%	0.38%	0.23%	0.09%	0.07%	0.05%	0.05%	0.05%
$\geq 2.50$	3.09%	1.58%	0.65%	0.34%	0.18%	0.13%	0.07%	0.07%	0.07%
$\geq 2.25$	4.22%	2.10%	0.86%	0.45%	0.20%	0.14%	0.07%	0.07%	0.07%
$\geq 2.00$	6.61%	3.23%	1.28%	0.61%	0.27%	0.18%	0.11%	0.11%	0.11%
$\geq 1.75$	10.73%	5.12%	1.89%	0.86%	0.40%	0.27%	0.18%	0.16%	0.16%
$\geq 1.50$	18.36%	9.22%	3.20%	1.28%	0.59%	0.40%	0.25%	0.23%	0.23%
$\geq 1.25$	33.54%	16.35%	5.41%	2.10%	0.93%	0.59%	0.38%	0.32%	0.29%
$\geq 1.00$	59.67%	28.96%	8.91%	3.41%	1.62%	1.11%	0.81%	0.66%	0.56%
$\geq 0.75$	91.11%	43.44%	12.43%	4.60%	2.10%	1.46%	1.02%	0.86%	0.74%
$\geq 0.50$	99.93%	47.23%	13.35%	4.96%	2.32%	1.55%	1.11%	0.95%	0.81%
$\geq 0.25$	100.00%	47.27%	13.37%	4.96%	2.32%	1.55%	1.11%	0.95%	0.81%
$> 0.00$	100.00%	47.27%	13.37%	4.96%	2.32%	1.55%	1.11%	0.95%	0.81%
	$> 0.0$	$\geq 0.5$	$\geq 1.0$	$\geq 1.5$	$\geq 2.0$	$\geq 2.5$	$\geq 3.0$	$\geq 3.5$	$\geq 4.0$
	$p_T^{hl(max)}$ in the Central Arm (GeV/c)								

Figure 93: Two-dimensional cut tables for Figure 92 — upper table for  $c\bar{c}$  events, lower table for minimum-bias events

the minimum-bias events. Figure 95 shows the tables with the percentage numbers of the events surviving the two-dimensional cuts applied both to  $p_T^{\mu(max)}$  and to  $\sum_{n=3} p_T^{h/l}$ . As in the previous transverse momentum correlation study, we did not observe any kinematical  $p_T$  regions where contributions from the open-charm sample were significantly larger than contributions from the minimum-bias sample. Figures 96, 97 and Figures 98, 99 show the two-dimensional histograms and the two-dimensional cut tables for the correlations of  $p_T^{\mu(max)}$  vs.  $\sum_{n=4} p_T^{h/l}$  (the sum for the four Central-Arm tracks with the largest  $p_T$  values) and of  $p_T^{\mu(max)}$  vs.  $\sum_{n=5} p_T^{h/l}$  (the sum for the five Central-Arm tracks with the largest  $p_T$  values), respectively. Still, with these types of transverse momentum correlations, no significant enrichment in charm content was observed.

We also investigated events on the plane of  $p_T^{h/l(max)}$  vs.  $\sum_{n=3} p_T^{h/l}$ , the maximum Central-Arm track  $p_T$  against the sum of the transverse momenta of the three Central-Arm tracks with the largest  $p_T$  values in the same event, for different  $p_T^{\mu(max)}$  bins and for the entire Muon-Arm track maximum  $p_T$  range. Figures 100, 101, 102, 103, 104, 105, 106, and 107 show the two-dimensional histograms and the two-dimensional cut tables for this type of the Central-Arm track transverse momentum correlation for all  $p_T^{\mu(max)}$ , for  $0.0 < p_T^{\mu(max)} < 1.0$  GeV/ $c$ ,  $1.0 \leq p_T^{\mu(max)} < 2.0$  GeV/ $c$ , and  $2.0 \leq p_T^{\mu(max)}$  GeV/ $c$  ranges, respectively. Again, in this study no significant differences between the open-charm sample and the minimum-bias sample were found.

To summarize the study, no kinematical  $p_T$  regions where contributions from the

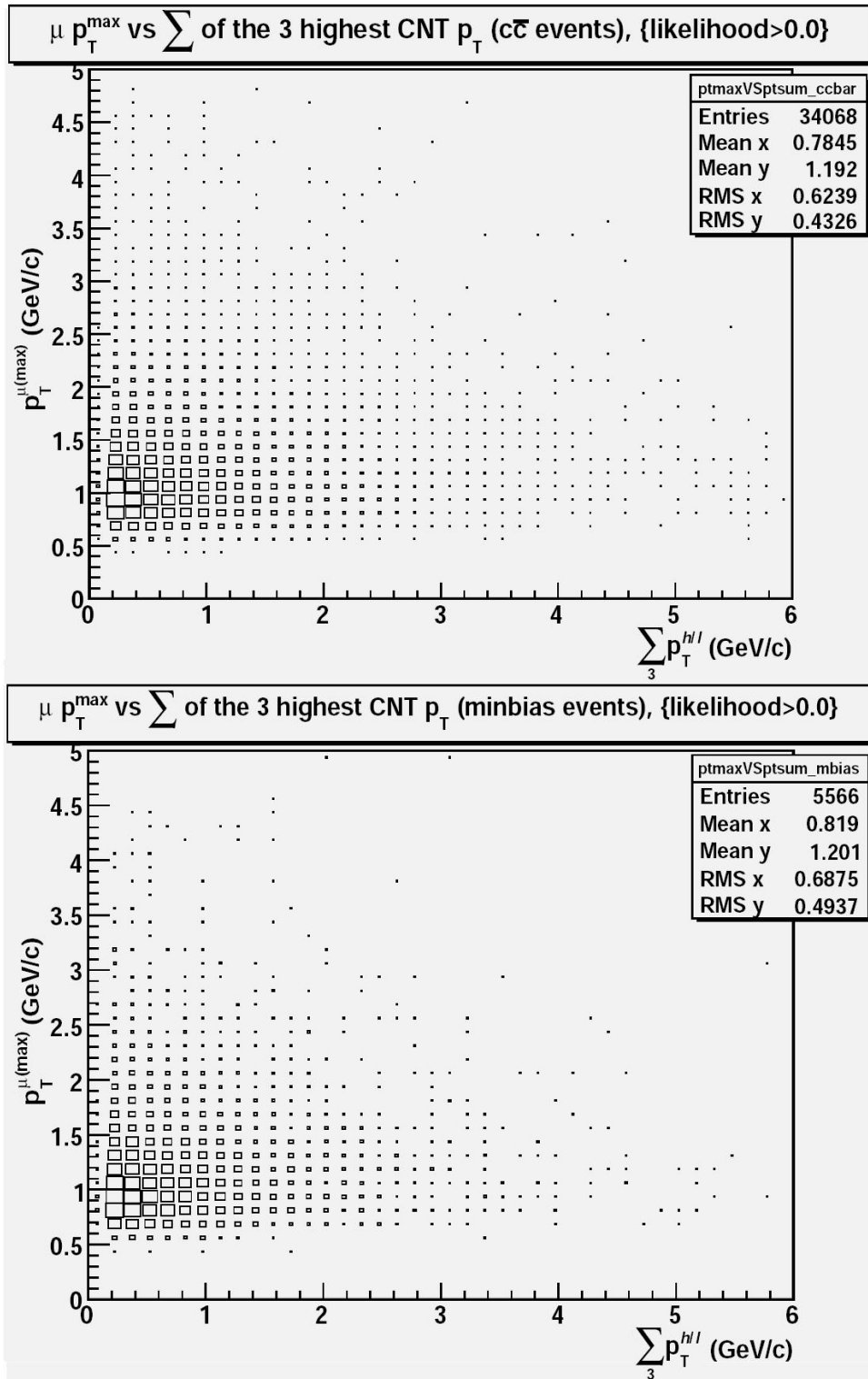


Figure 94: Maximum Muon-Arm track  $p_T$  against the sum of the transverse momenta of 3 Central-Arm tracks with the largest  $p_T$  values

<b><math>c\bar{c}</math> events</b>									
$\geq 4.75$	0.07%	0.04%	0.03%	0.02%	0.01%	0.01%	0.00%	0.00%	0.00%
$\geq 4.50$	0.10%	0.06%	0.04%	0.02%	0.02%	0.01%	0.01%	0.00%	0.00%
$\geq 4.25$	0.14%	0.09%	0.05%	0.03%	0.02%	0.01%	0.01%	0.00%	0.00%
$\geq 4.00$	0.19%	0.12%	0.06%	0.04%	0.03%	0.02%	0.01%	0.01%	0.01%
$\geq 3.75$	0.26%	0.17%	0.10%	0.06%	0.05%	0.03%	0.01%	0.01%	0.01%
$\geq 3.50$	0.34%	0.23%	0.12%	0.08%	0.06%	0.03%	0.01%	0.01%	0.01%
$\geq 3.25$	0.48%	0.34%	0.19%	0.11%	0.08%	0.04%	0.02%	0.02%	0.01%
$\geq 3.00$	0.66%	0.47%	0.25%	0.15%	0.10%	0.05%	0.03%	0.03%	0.02%
$\geq 2.75$	1.02%	0.68%	0.36%	0.21%	0.13%	0.07%	0.04%	0.04%	0.03%
$\geq 2.50$	1.69%	1.08%	0.56%	0.32%	0.19%	0.10%	0.07%	0.06%	0.05%
$\geq 2.25$	2.81%	1.78%	0.89%	0.45%	0.26%	0.15%	0.10%	0.07%	0.06%
$\geq 2.00$	5.06%	3.23%	1.57%	0.76%	0.40%	0.22%	0.16%	0.13%	0.11%
$\geq 1.75$	9.21%	5.74%	2.76%	1.33%	0.66%	0.35%	0.22%	0.17%	0.14%
$\geq 1.50$	17.74%	10.95%	5.20%	2.42%	1.21%	0.65%	0.41%	0.28%	0.22%
$\geq 1.25$	33.97%	20.59%	9.45%	4.26%	2.04%	1.05%	0.65%	0.45%	0.36%
$\geq 1.00$	61.48%	36.77%	16.68%	7.30%	3.48%	1.77%	1.09%	0.76%	0.60%
$\geq 0.75$	92.65%	54.97%	24.78%	10.70%	4.95%	2.52%	1.53%	1.08%	0.87%
$\geq 0.50$	99.95%	59.21%	26.58%	11.50%	5.31%	2.69%	1.63%	1.15%	0.93%
$> 0.00$	100.00%	59.24%	26.60%	11.50%	5.31%	2.69%	1.63%	1.15%	0.93%
	$> 0.0$	$\geq 0.5$	$\geq 1.0$	$\geq 1.5$	$\geq 2.0$	$\geq 2.5$	$\geq 3.0$	$\geq 3.5$	$\geq 4.0$
	$\sum_3 p_T^{hl}$ in the Central Arm (GeV/c)								
<b>minbias events</b>									
$\geq 4.75$	0.41%	0.25%	0.16%	0.13%	0.11%	0.07%	0.05%	0.02%	0.02%
$\geq 4.50$	0.43%	0.27%	0.18%	0.14%	0.11%	0.07%	0.05%	0.02%	0.02%
$\geq 4.25$	0.56%	0.36%	0.23%	0.16%	0.11%	0.07%	0.05%	0.02%	0.02%
$\geq 4.00$	0.74%	0.47%	0.27%	0.18%	0.11%	0.07%	0.05%	0.02%	0.02%
$\geq 3.75$	0.86%	0.56%	0.31%	0.22%	0.13%	0.09%	0.05%	0.02%	0.02%
$\geq 3.50$	0.99%	0.63%	0.34%	0.23%	0.13%	0.09%	0.05%	0.02%	0.02%
$\geq 3.25$	1.13%	0.72%	0.38%	0.27%	0.13%	0.09%	0.05%	0.02%	0.02%
$\geq 3.00$	1.62%	1.01%	0.54%	0.36%	0.20%	0.14%	0.11%	0.07%	0.07%
$\geq 2.75$	2.14%	1.37%	0.75%	0.52%	0.29%	0.20%	0.13%	0.09%	0.07%
$\geq 2.50$	3.09%	1.98%	1.15%	0.77%	0.45%	0.32%	0.20%	0.13%	0.11%
$\geq 2.25$	4.22%	2.64%	1.51%	0.95%	0.52%	0.38%	0.23%	0.14%	0.13%
$\geq 2.00$	6.61%	4.11%	2.32%	1.44%	0.74%	0.56%	0.36%	0.23%	0.18%
$\geq 1.75$	10.73%	6.72%	3.52%	2.05%	1.02%	0.74%	0.50%	0.32%	0.27%
$\geq 1.50$	18.36%	11.50%	6.16%	3.29%	1.74%	1.08%	0.72%	0.45%	0.40%
$\geq 1.25$	33.54%	20.54%	10.51%	5.41%	2.82%	1.63%	1.08%	0.66%	0.52%
$\geq 1.00$	59.67%	36.54%	17.55%	8.77%	4.60%	2.73%	1.78%	1.17%	0.95%
$\geq 0.75$	91.11%	54.89%	25.71%	12.41%	6.43%	3.68%	2.43%	1.63%	1.28%
$\geq 0.50$	99.93%	60.13%	27.88%	13.24%	6.93%	3.99%	2.62%	1.78%	1.38%
$\geq 0.25$	100.00%	60.19%	27.90%	13.26%	6.93%	3.99%	2.62%	1.78%	1.38%
$> 0.00$	100.00%	60.19%	27.90%	13.26%	6.93%	3.99%	2.62%	1.78%	1.38%
	$> 0.0$	$\geq 0.5$	$\geq 1.0$	$\geq 1.5$	$\geq 2.0$	$\geq 2.5$	$\geq 3.0$	$\geq 3.5$	$\geq 4.0$
	$\sum_3 p_T^{hl}$ in the Central Arm (GeV/c)								

Figure 95: Two-dimensional cut tables for Figure 94 — upper table for  $c\bar{c}$  events, lower table for minimum-bias events

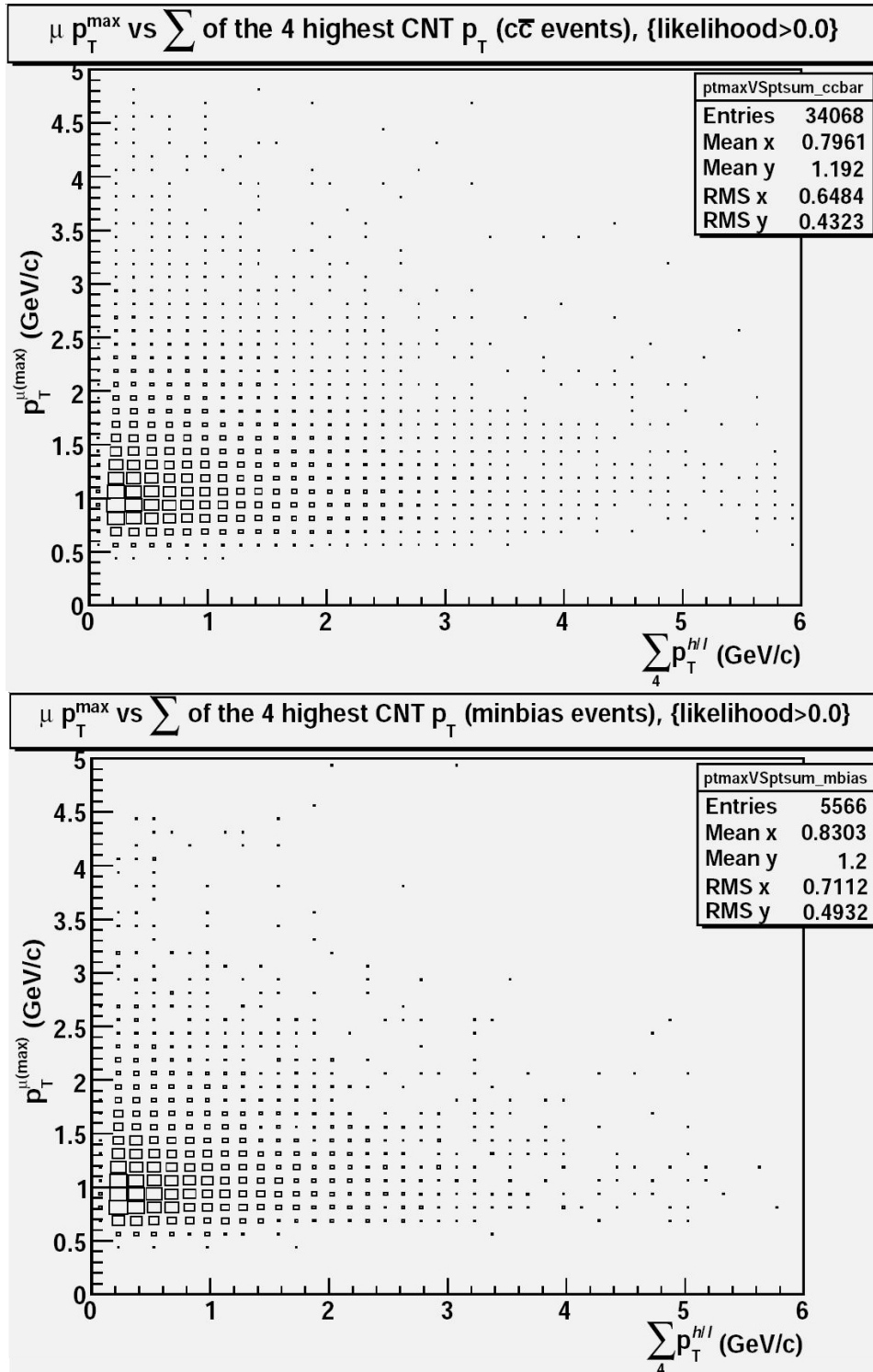


Figure 96: Maximum Muon-Arm track  $p_T$  against the sum of the transverse momenta of 4 Central-Arm tracks with the largest  $p_T$  values

<b><math>c\bar{c}</math> events</b>									
$\geq 4.75$	0.07%	0.04%	0.03%	0.02%	0.01%	0.01%	0.00%	0.00%	0.00%
$\geq 4.50$	0.10%	0.06%	0.04%	0.02%	0.02%	0.01%	0.01%	0.00%	0.00%
$\geq 4.25$	0.14%	0.09%	0.05%	0.03%	0.02%	0.01%	0.01%	0.00%	0.00%
$\geq 4.00$	0.19%	0.12%	0.06%	0.04%	0.03%	0.02%	0.01%	0.01%	0.01%
$\geq 3.75$	0.26%	0.17%	0.10%	0.06%	0.05%	0.04%	0.01%	0.01%	0.01%
$\geq 3.50$	0.34%	0.23%	0.12%	0.08%	0.06%	0.04%	0.02%	0.01%	0.01%
$\geq 3.25$	0.48%	0.34%	0.19%	0.11%	0.08%	0.05%	0.03%	0.02%	0.01%
$\geq 3.00$	0.66%	0.47%	0.25%	0.15%	0.10%	0.06%	0.04%	0.03%	0.02%
$\geq 2.75$	1.02%	0.68%	0.36%	0.21%	0.13%	0.08%	0.05%	0.04%	0.03%
$\geq 2.50$	1.69%	1.08%	0.57%	0.33%	0.20%	0.11%	0.07%	0.06%	0.05%
$\geq 2.25$	2.81%	1.78%	0.90%	0.47%	0.29%	0.17%	0.11%	0.08%	0.07%
$\geq 2.00$	5.06%	3.23%	1.59%	0.79%	0.44%	0.25%	0.17%	0.14%	0.11%
$\geq 1.75$	9.21%	5.74%	2.78%	1.40%	0.75%	0.41%	0.25%	0.18%	0.14%
$\geq 1.50$	17.74%	10.95%	5.24%	2.56%	1.38%	0.74%	0.47%	0.33%	0.25%
$\geq 1.25$	33.97%	20.59%	9.52%	4.52%	2.30%	1.19%	0.75%	0.52%	0.41%
$\geq 1.00$	61.48%	36.77%	16.83%	7.73%	3.87%	2.03%	1.24%	0.86%	0.67%
$\geq 0.75$	92.65%	54.97%	24.99%	11.35%	5.52%	2.89%	1.74%	1.20%	0.95%
$\geq 0.50$	99.95%	59.21%	26.81%	12.21%	5.92%	3.09%	1.86%	1.30%	1.01%
$\geq 0.25$	100.00%	59.24%	26.83%	12.21%	5.92%	3.09%	1.86%	1.30%	1.01%
$> 0.00$	100.00%	59.24%	26.83%	12.21%	5.92%	3.09%	1.86%	1.30%	1.01%
	$> 0.0$	$\geq 0.5$	$\geq 1.0$	$\geq 1.5$	$\geq 2.0$	$\geq 2.5$	$\geq 3.0$	$\geq 3.5$	$\geq 4.0$
	$\sum_4 p_T^{h/l}$ in the Central Arm (GeV/c)								
<b>minbias events</b>									
$\geq 4.75$	0.41%	0.25%	0.16%	0.13%	0.11%	0.09%	0.05%	0.02%	0.02%
$\geq 4.50$	0.43%	0.27%	0.18%	0.14%	0.11%	0.09%	0.05%	0.02%	0.02%
$\geq 4.25$	0.56%	0.36%	0.23%	0.16%	0.11%	0.09%	0.05%	0.02%	0.02%
$\geq 4.00$	0.74%	0.47%	0.27%	0.18%	0.11%	0.09%	0.05%	0.02%	0.02%
$\geq 3.75$	0.86%	0.56%	0.31%	0.22%	0.13%	0.11%	0.05%	0.02%	0.02%
$\geq 3.50$	0.99%	0.63%	0.34%	0.23%	0.13%	0.11%	0.05%	0.02%	0.02%
$\geq 3.25$	1.13%	0.72%	0.38%	0.27%	0.13%	0.11%	0.05%	0.02%	0.02%
$\geq 3.00$	1.62%	1.01%	0.54%	0.36%	0.22%	0.16%	0.11%	0.07%	0.07%
$\geq 2.75$	2.14%	1.37%	0.75%	0.52%	0.31%	0.22%	0.13%	0.09%	0.07%
$\geq 2.50$	3.09%	1.98%	1.15%	0.77%	0.47%	0.36%	0.22%	0.13%	0.11%
$\geq 2.25$	4.22%	2.64%	1.51%	0.97%	0.54%	0.41%	0.25%	0.14%	0.13%
$\geq 2.00$	6.61%	4.11%	2.32%	1.46%	0.77%	0.59%	0.38%	0.23%	0.20%
$\geq 1.75$	10.73%	6.72%	3.54%	2.10%	1.10%	0.79%	0.56%	0.34%	0.29%
$\geq 1.50$	18.36%	11.50%	6.18%	3.34%	1.87%	1.20%	0.79%	0.50%	0.41%
$\geq 1.25$	33.54%	20.54%	10.55%	5.55%	3.02%	1.83%	1.20%	0.77%	0.57%
$\geq 1.00$	59.67%	36.54%	17.59%	9.09%	4.98%	3.00%	1.92%	1.33%	1.04%
$\geq 0.75$	91.11%	54.89%	25.82%	12.95%	7.06%	4.19%	2.64%	1.87%	1.44%
$\geq 0.50$	99.93%	60.13%	28.03%	13.82%	7.64%	4.55%	2.84%	2.01%	1.58%
$\geq 0.25$	100.00%	60.19%	28.05%	13.83%	7.64%	4.55%	2.84%	2.01%	1.58%
$> 0.00$	100.00%	60.19%	28.05%	13.83%	7.64%	4.55%	2.84%	2.01%	1.58%
	$> 0.0$	$\geq 0.5$	$\geq 1.0$	$\geq 1.5$	$\geq 2.0$	$\geq 2.5$	$\geq 3.0$	$\geq 3.5$	$\geq 4.0$
	$\sum_4 p_T^{h/l}$ in the Central Arm (GeV/c)								

Figure 97: Two-dimensional cut tables for Figure 96 — upper table for  $c\bar{c}$  events, lower table for minimum-bias events

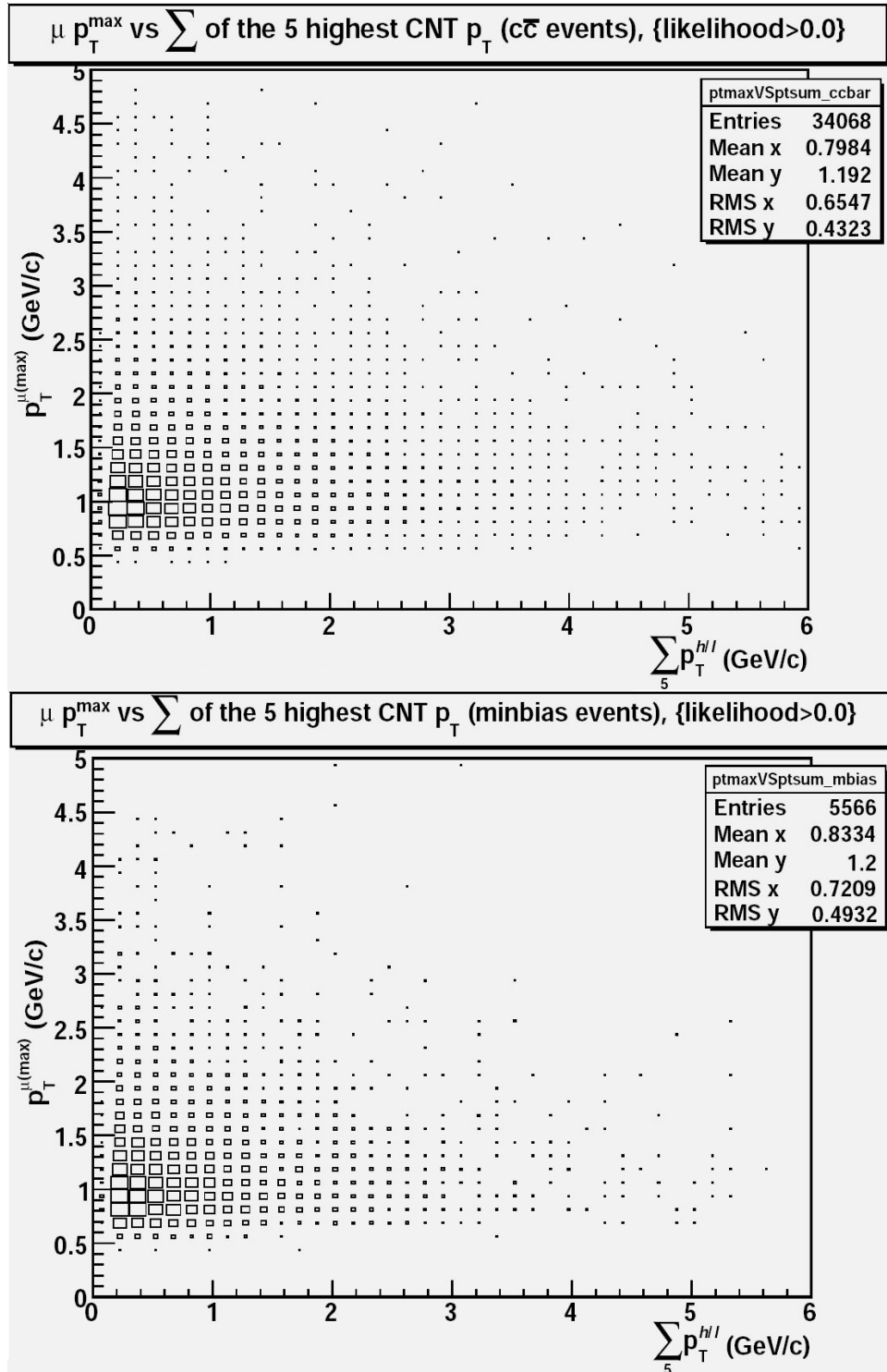


Figure 98: Maximum Muon-Arm track  $p_T$  against the sum of the transverse momenta of 5 Central-Arm tracks with the largest  $p_T$  values

<b><math>c\bar{c}</math> events</b>									
$\geq 4.75$	0.07%	0.04%	0.03%	0.02%	0.01%	0.01%	0.00%	0.00%	0.00%
$\geq 4.50$	0.10%	0.06%	0.04%	0.02%	0.02%	0.01%	0.01%	0.00%	0.00%
$\geq 4.25$	0.14%	0.09%	0.05%	0.03%	0.02%	0.01%	0.01%	0.00%	0.00%
$\geq 4.00$	0.19%	0.12%	0.06%	0.04%	0.03%	0.02%	0.01%	0.01%	0.01%
$\geq 3.75$	0.26%	0.17%	0.10%	0.06%	0.05%	0.04%	0.01%	0.01%	0.01%
$\geq 3.50$	0.34%	0.23%	0.12%	0.08%	0.06%	0.04%	0.02%	0.01%	0.01%
$\geq 3.25$	0.48%	0.34%	0.19%	0.11%	0.08%	0.05%	0.03%	0.02%	0.01%
$\geq 3.00$	0.66%	0.47%	0.26%	0.15%	0.10%	0.06%	0.04%	0.03%	0.02%
$\geq 2.75$	1.02%	0.68%	0.37%	0.21%	0.13%	0.08%	0.05%	0.04%	0.03%
$\geq 2.50$	1.69%	1.08%	0.57%	0.33%	0.20%	0.11%	0.08%	0.06%	0.05%
$\geq 2.25$	2.81%	1.78%	0.90%	0.47%	0.29%	0.17%	0.12%	0.08%	0.07%
$\geq 2.00$	5.06%	3.23%	1.59%	0.79%	0.45%	0.25%	0.18%	0.14%	0.11%
$\geq 1.75$	9.21%	5.74%	2.79%	1.40%	0.77%	0.41%	0.26%	0.18%	0.14%
$\geq 1.50$	17.74%	10.95%	5.24%	2.56%	1.41%	0.76%	0.49%	0.34%	0.26%
$\geq 1.25$	33.97%	20.59%	9.53%	4.53%	2.36%	1.24%	0.77%	0.53%	0.41%
$\geq 1.00$	61.48%	36.77%	16.84%	7.76%	3.98%	2.10%	1.29%	0.90%	0.68%
$\geq 0.75$	92.65%	54.97%	25.00%	11.39%	5.66%	2.99%	1.83%	1.26%	0.98%
$\geq 0.50$	99.95%	59.21%	26.82%	12.26%	6.08%	3.18%	1.95%	1.35%	1.04%
$\geq 0.25$	100.00%	59.24%	26.83%	12.26%	6.08%	3.18%	1.95%	1.35%	1.04%
$> 0.00$	100.00%	59.24%	26.83%	12.26%	6.08%	3.18%	1.95%	1.35%	1.04%
	$> 0.0$	$\geq 0.5$	$\geq 1.0$	$\geq 1.5$	$\geq 2.0$	$\geq 2.5$	$\geq 3.0$	$\geq 3.5$	$\geq 4.0$
	$\sum_5 p_T^{h/l}$ in the Central Arm (GeV/c)								
<b>minbias events</b>									
$\geq 4.75$	0.41%	0.25%	0.16%	0.13%	0.11%	0.09%	0.09%	0.02%	0.02%
$\geq 4.50$	0.43%	0.27%	0.18%	0.14%	0.13%	0.09%	0.09%	0.02%	0.02%
$\geq 4.25$	0.56%	0.36%	0.23%	0.16%	0.13%	0.09%	0.09%	0.02%	0.02%
$\geq 4.00$	0.74%	0.47%	0.27%	0.18%	0.13%	0.09%	0.09%	0.02%	0.02%
$\geq 3.75$	0.86%	0.56%	0.31%	0.22%	0.14%	0.11%	0.09%	0.02%	0.02%
$\geq 3.50$	0.99%	0.63%	0.34%	0.23%	0.14%	0.11%	0.09%	0.02%	0.02%
$\geq 3.25$	1.13%	0.72%	0.38%	0.27%	0.14%	0.11%	0.09%	0.02%	0.02%
$\geq 3.00$	1.62%	1.01%	0.54%	0.36%	0.23%	0.18%	0.14%	0.07%	0.07%
$\geq 2.75$	2.14%	1.37%	0.75%	0.52%	0.32%	0.23%	0.16%	0.09%	0.07%
$\geq 2.50$	3.09%	1.98%	1.15%	0.77%	0.49%	0.38%	0.25%	0.16%	0.11%
$\geq 2.25$	4.22%	2.64%	1.51%	0.97%	0.56%	0.43%	0.29%	0.18%	0.13%
$\geq 2.00$	6.61%	4.11%	2.32%	1.46%	0.81%	0.61%	0.41%	0.27%	0.20%
$\geq 1.75$	10.73%	6.72%	3.54%	2.10%	1.15%	0.81%	0.59%	0.38%	0.31%
$\geq 1.50$	18.36%	11.50%	6.18%	3.34%	1.92%	1.24%	0.86%	0.54%	0.45%
$\geq 1.25$	33.54%	20.54%	10.55%	5.55%	3.11%	1.90%	1.29%	0.88%	0.63%
$\geq 1.00$	59.67%	36.54%	17.59%	9.09%	5.07%	3.11%	2.07%	1.47%	1.10%
$\geq 0.75$	91.11%	54.89%	25.82%	12.95%	7.22%	4.33%	2.80%	2.03%	1.53%
$\geq 0.50$	99.93%	60.13%	28.03%	13.82%	7.80%	4.69%	3.00%	2.17%	1.67%
$\geq 0.25$	100.00%	60.19%	28.05%	13.83%	7.80%	4.69%	3.00%	2.17%	1.67%
$> 0.00$	100.00%	60.19%	28.05%	13.83%	7.80%	4.69%	3.00%	2.17%	1.67%
	$> 0.0$	$\geq 0.5$	$\geq 1.0$	$\geq 1.5$	$\geq 2.0$	$\geq 2.5$	$\geq 3.0$	$\geq 3.5$	$\geq 4.0$
	$\sum_5 p_T^{h/l}$ in the Central Arm (GeV/c)								

Figure 99: Two-dimensional cut tables for Figure 98 — upper table for  $c\bar{c}$  events, lower table for minimum-bias events

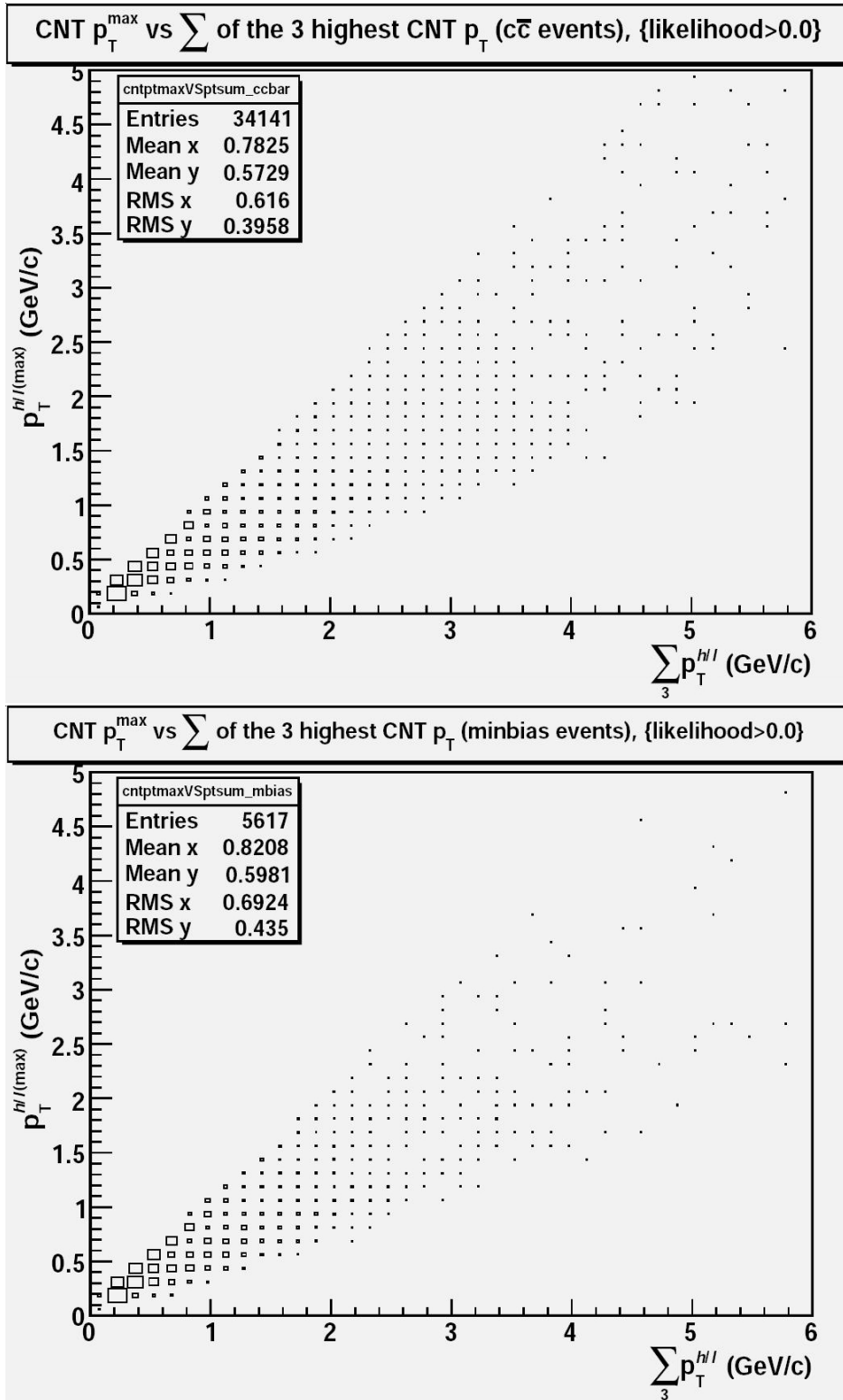


Figure 100: Maximum Central-Arm track  $p_T$  vs. the sum of the  $p_T$  of 3 Central-Arm tracks with the largest  $p_T$  values for all  $p_T^{\mu(max)}$

c $\bar{c}$ events									
$\geq 4.75$	0.63%	0.63%	0.63%	0.63%	0.63%	0.63%	0.63%	0.63%	0.63%
$\geq 4.50$	0.64%	0.64%	0.64%	0.64%	0.64%	0.64%	0.64%	0.64%	0.64%
$\geq 4.25$	0.66%	0.66%	0.66%	0.66%	0.66%	0.66%	0.66%	0.66%	0.66%
$\geq 4.00$	0.69%	0.69%	0.69%	0.69%	0.69%	0.69%	0.69%	0.69%	0.69%
$\geq 3.75$	0.70%	0.70%	0.70%	0.70%	0.70%	0.70%	0.70%	0.70%	0.70%
$\geq 3.50$	0.75%	0.75%	0.75%	0.75%	0.75%	0.75%	0.75%	0.75%	0.74%
$\geq 3.25$	0.79%	0.79%	0.79%	0.79%	0.79%	0.79%	0.79%	0.78%	0.77%
$\geq 3.00$	0.85%	0.85%	0.85%	0.85%	0.85%	0.85%	0.85%	0.83%	0.79%
$\geq 2.75$	0.91%	0.91%	0.91%	0.91%	0.91%	0.91%	0.89%	0.85%	0.80%
$\geq 2.50$	1.05%	1.05%	1.05%	1.05%	1.05%	1.05%	0.98%	0.90%	0.83%
$\geq 2.25$	1.28%	1.28%	1.28%	1.28%	1.28%	1.20%	1.07%	0.95%	0.86%
$\geq 2.00$	1.71%	1.71%	1.71%	1.71%	1.71%	1.44%	1.22%	1.02%	0.90%
$\geq 1.75$	2.38%	2.38%	2.38%	2.38%	2.16%	1.71%	1.36%	1.08%	0.92%
$\geq 1.50$	3.55%	3.55%	3.55%	3.55%	2.79%	2.08%	1.51%	1.14%	0.93%
$\geq 1.25$	6.23%	6.23%	6.23%	5.34%	3.72%	2.44%	1.62%	1.16%	0.93%
$\geq 1.00$	11.49%	11.49%	11.49%	7.77%	4.73%	2.68%	1.64%	1.16%	0.93%
$\geq 0.75$	22.97%	22.97%	18.05%	10.42%	5.30%	2.70%	1.64%	1.16%	0.93%
$\geq 0.50$	46.25%	46.25%	25.30%	11.50%	5.32%	2.70%	1.64%	1.16%	0.93%
$\geq 0.25$	84.91%	59.08%	26.59%	11.50%	5.32%	2.70%	1.64%	1.16%	0.93%
$> 0.00$	100.00%	59.24%	26.59%	11.50%	5.32%	2.70%	1.64%	1.16%	0.93%
	$> 0.0$	$\geq 0.5$	$\geq 1.0$	$\geq 1.5$	$\geq 2.0$	$\geq 2.5$	$\geq 3.0$	$\geq 3.5$	$\geq 4.0$
	$\sum_3 p_T^{h/l}$ in the Central Arm (GeV/c)								
minbias events									
$\geq 4.75$	0.75%	0.75%	0.75%	0.75%	0.75%	0.75%	0.75%	0.75%	0.75%
$\geq 4.50$	0.78%	0.78%	0.78%	0.78%	0.78%	0.78%	0.78%	0.78%	0.78%
$\geq 4.25$	0.80%	0.80%	0.80%	0.80%	0.80%	0.80%	0.80%	0.80%	0.80%
$\geq 4.00$	0.82%	0.82%	0.82%	0.82%	0.82%	0.82%	0.82%	0.82%	0.82%
$\geq 3.75$	0.84%	0.84%	0.84%	0.84%	0.84%	0.84%	0.84%	0.84%	0.84%
$\geq 3.50$	0.96%	0.96%	0.96%	0.96%	0.96%	0.96%	0.96%	0.96%	0.94%
$\geq 3.25$	1.01%	1.01%	1.01%	1.01%	1.01%	1.01%	1.01%	1.00%	0.96%
$\geq 3.00$	1.12%	1.12%	1.12%	1.12%	1.12%	1.12%	1.12%	1.05%	1.00%
$\geq 2.75$	1.26%	1.26%	1.26%	1.26%	1.26%	1.26%	1.21%	1.09%	1.03%
$\geq 2.50$	1.55%	1.55%	1.55%	1.55%	1.55%	1.55%	1.42%	1.28%	1.19%
$\geq 2.25$	1.87%	1.87%	1.87%	1.87%	1.87%	1.78%	1.62%	1.44%	1.28%
$\geq 2.00$	2.33%	2.33%	2.33%	2.33%	2.33%	2.08%	1.78%	1.51%	1.32%
$\geq 1.75$	3.44%	3.44%	3.44%	3.44%	3.17%	2.63%	2.03%	1.60%	1.34%
$\geq 1.50$	4.97%	4.97%	4.97%	4.97%	4.11%	3.12%	2.39%	1.76%	1.37%
$\geq 1.25$	7.69%	7.69%	7.69%	6.94%	5.18%	3.63%	2.58%	1.80%	1.39%
$\geq 1.00$	13.41%	13.41%	13.41%	9.60%	6.43%	4.01%	2.63%	1.80%	1.39%
$\geq 0.75$	24.89%	24.89%	20.03%	12.43%	6.96%	4.02%	2.63%	1.80%	1.39%
$\geq 0.50$	47.25%	47.25%	26.74%	13.35%	6.98%	4.02%	2.63%	1.80%	1.39%
$\geq 0.25$	85.67%	59.89%	27.90%	13.35%	6.98%	4.02%	2.63%	1.80%	1.39%
$> 0.00$	100.00%	60.10%	27.90%	13.35%	6.98%	4.02%	2.63%	1.80%	1.39%
	$> 0.0$	$\geq 0.5$	$\geq 1.0$	$\geq 1.5$	$\geq 2.0$	$\geq 2.5$	$\geq 3.0$	$\geq 3.5$	$\geq 4.0$
	$\sum_3 p_T^{h/l}$ in the Central Arm (GeV/c)								

Figure 101: Two-dimensional cut tables for Figure 100 — upper table for  $c\bar{c}$  events, lower table for minimum-bias events

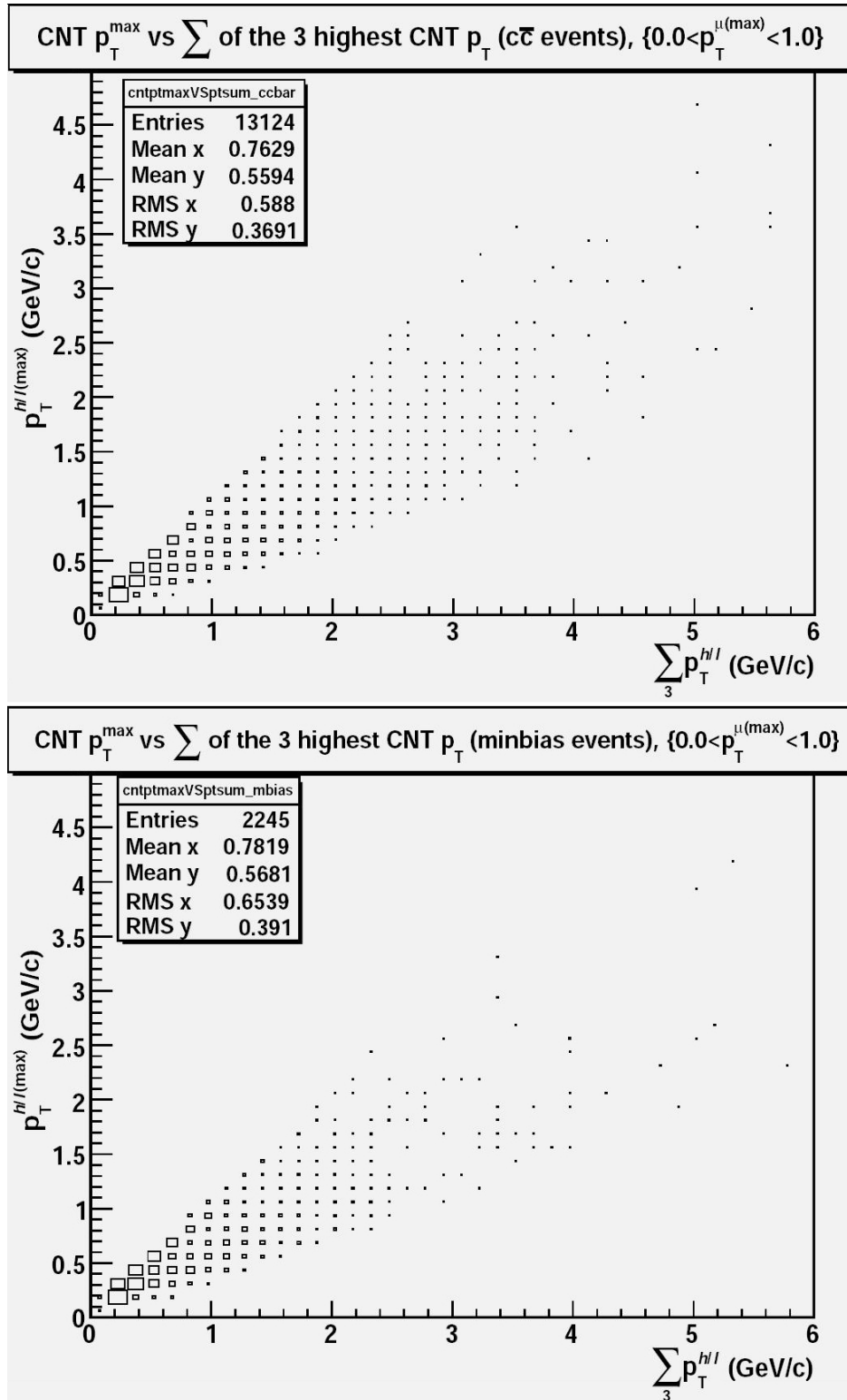


Figure 102: Maximum Central-Arm track  $p_T$  vs. the sum of the  $p_T$  of 3 Central-Arm tracks with the largest  $p_T$  values for  $0.0 < p_T^{\mu(\max)} < 1.0$  GeV/c

<b><math>c\bar{c}</math> events</b>									
$\geq 4.75$	0.63%	0.63%	0.63%	0.63%	0.63%	0.63%	0.63%	0.63%	0.63%
$\geq 4.50$	0.64%	0.64%	0.64%	0.64%	0.64%	0.64%	0.64%	0.64%	0.64%
$\geq 4.25$	0.65%	0.65%	0.65%	0.65%	0.65%	0.65%	0.65%	0.65%	0.65%
$\geq 4.00$	0.66%	0.66%	0.66%	0.66%	0.66%	0.66%	0.66%	0.66%	0.66%
$\geq 3.75$	0.66%	0.66%	0.66%	0.66%	0.66%	0.66%	0.66%	0.66%	0.66%
$\geq 3.50$	0.69%	0.69%	0.69%	0.69%	0.69%	0.69%	0.69%	0.69%	0.69%
$\geq 3.25$	0.73%	0.73%	0.73%	0.73%	0.73%	0.73%	0.73%	0.72%	0.72%
$\geq 3.00$	0.80%	0.80%	0.80%	0.80%	0.80%	0.80%	0.80%	0.77%	0.74%
$\geq 2.75$	0.81%	0.81%	0.81%	0.81%	0.81%	0.81%	0.81%	0.78%	0.75%
$\geq 2.50$	0.90%	0.90%	0.90%	0.90%	0.90%	0.90%	0.88%	0.82%	0.77%
$\geq 2.25$	1.09%	1.09%	1.09%	1.09%	1.09%	1.04%	0.98%	0.87%	0.79%
$\geq 2.00$	1.42%	1.42%	1.42%	1.42%	1.42%	1.19%	1.09%	0.92%	0.82%
$\geq 1.75$	2.02%	2.02%	2.02%	2.02%	1.78%	1.43%	1.20%	0.96%	0.83%
$\geq 1.50$	3.04%	3.04%	3.04%	3.04%	2.35%	1.79%	1.30%	0.99%	0.84%
$\geq 1.25$	5.68%	5.68%	5.68%	4.81%	3.23%	2.12%	1.37%	1.01%	0.85%
$\geq 1.00$	10.85%	10.85%	10.85%	7.35%	4.26%	2.38%	1.39%	1.01%	0.85%
$\geq 0.75$	21.79%	21.79%	17.20%	9.76%	4.75%	2.41%	1.39%	1.01%	0.85%
$\geq 0.50$	45.20%	45.20%	24.61%	10.90%	4.75%	2.41%	1.39%	1.01%	0.85%
$\geq 0.25$	84.68%	58.15%	25.74%	10.90%	4.75%	2.41%	1.39%	1.01%	0.85%
$> 0.00$	100.00%	58.31%	25.74%	10.90%	4.75%	2.41%	1.39%	1.01%	0.85%
	$> 0.0$	$\geq 0.5$	$\geq 1.0$	$\geq 1.5$	$\geq 2.0$	$\geq 2.5$	$\geq 3.0$	$\geq 3.5$	$\geq 4.0$
	$\sum_3 p_T^{h/l}$ in the Central Arm (GeV/c)								
<b>minbias events</b>									
$\geq 4.75$	0.53%	0.53%	0.53%	0.53%	0.53%	0.53%	0.53%	0.53%	0.53%
$\geq 4.50$	0.58%	0.58%	0.58%	0.58%	0.58%	0.58%	0.58%	0.58%	0.58%
$\geq 4.25$	0.58%	0.58%	0.58%	0.58%	0.58%	0.58%	0.58%	0.58%	0.58%
$\geq 4.00$	0.62%	0.62%	0.62%	0.62%	0.62%	0.62%	0.62%	0.62%	0.62%
$\geq 3.75$	0.67%	0.67%	0.67%	0.67%	0.67%	0.67%	0.67%	0.67%	0.67%
$\geq 3.50$	0.71%	0.71%	0.71%	0.71%	0.71%	0.71%	0.71%	0.71%	0.71%
$\geq 3.25$	0.76%	0.76%	0.76%	0.76%	0.76%	0.76%	0.76%	0.71%	0.71%
$\geq 3.00$	0.76%	0.76%	0.76%	0.76%	0.76%	0.76%	0.76%	0.71%	0.71%
$\geq 2.75$	0.80%	0.80%	0.80%	0.80%	0.80%	0.80%	0.80%	0.71%	0.71%
$\geq 2.50$	1.07%	1.07%	1.07%	1.07%	1.07%	1.07%	1.02%	0.89%	0.85%
$\geq 2.25$	1.25%	1.25%	1.25%	1.25%	1.25%	1.20%	1.16%	1.02%	0.98%
$\geq 2.00$	1.74%	1.74%	1.74%	1.74%	1.74%	1.51%	1.34%	1.11%	1.02%
$\geq 1.75$	2.58%	2.58%	2.58%	2.58%	2.45%	2.09%	1.56%	1.25%	1.07%
$\geq 1.50$	3.83%	3.83%	3.83%	3.83%	3.30%	2.58%	1.96%	1.47%	1.07%
$\geq 1.25$	5.92%	5.92%	5.92%	5.17%	3.88%	2.72%	2.05%	1.51%	1.07%
$\geq 1.00$	11.05%	11.05%	11.05%	7.75%	5.12%	3.12%	2.09%	1.51%	1.07%
$\geq 0.75$	22.27%	22.27%	17.37%	10.20%	5.79%	3.12%	2.09%	1.51%	1.07%
$\geq 0.50$	45.39%	45.39%	24.45%	11.14%	5.79%	3.12%	2.09%	1.51%	1.07%
$\geq 0.25$	85.08%	58.22%	25.66%	11.14%	5.79%	3.12%	2.09%	1.51%	1.07%
$> 0.00$	100.00%	58.62%	25.66%	11.14%	5.79%	3.12%	2.09%	1.51%	1.07%
	$> 0.0$	$\geq 0.5$	$\geq 1.0$	$\geq 1.5$	$\geq 2.0$	$\geq 2.5$	$\geq 3.0$	$\geq 3.5$	$\geq 4.0$
	$\sum_3 p_T^{h/l}$ in the Central Arm (GeV/c)								

Figure 103: Two-dimensional cut tables for Figure 102 — upper table for  $c\bar{c}$  events, lower table for minimum-bias events

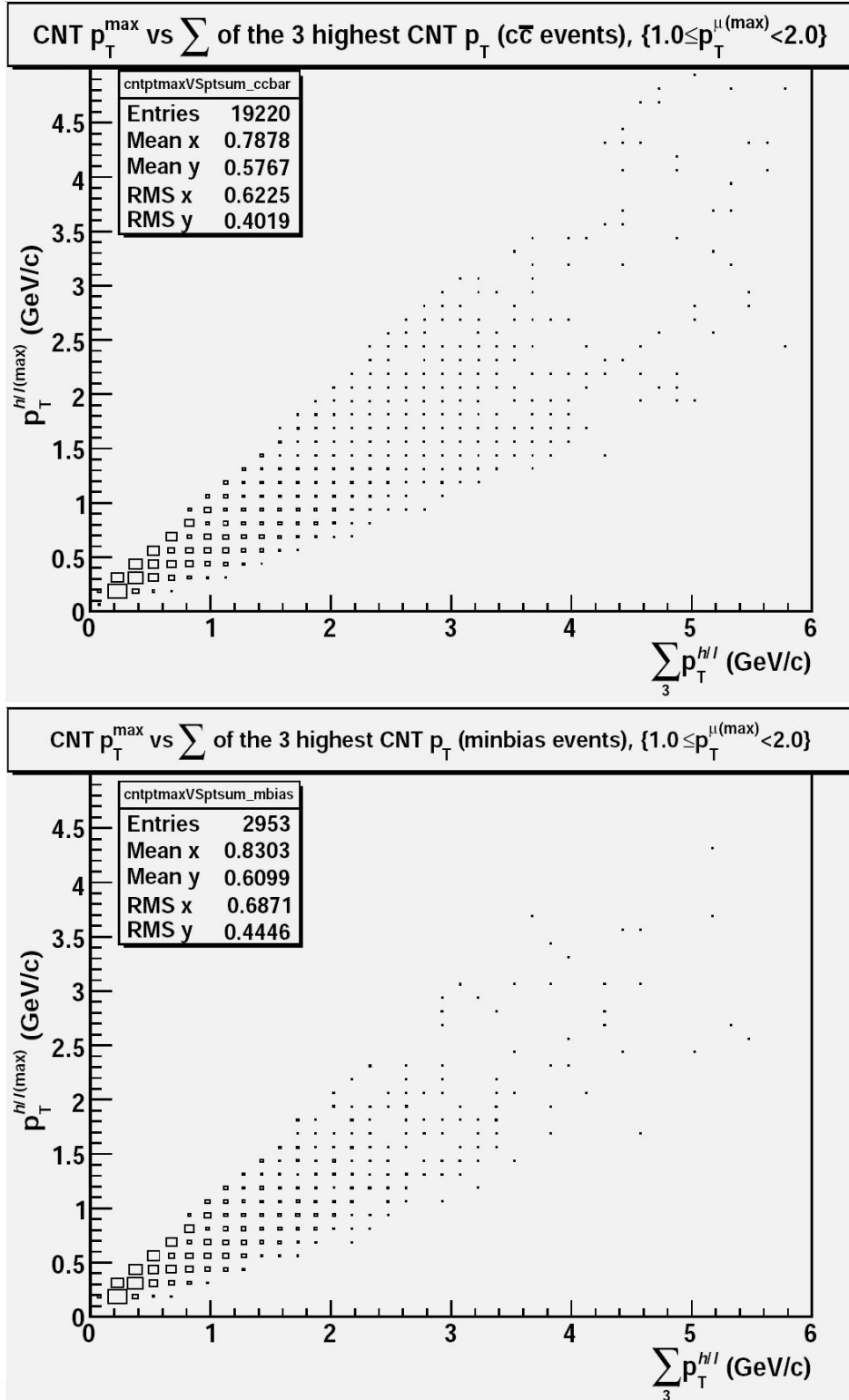


Figure 104: Maximum Central-Arm track  $p_T$  vs. the sum of the  $p_T$  of 3 Central-Arm tracks with the largest  $p_T$  values for  $1.0 \leq p_T^{\mu(\max)} < 2.0$  GeV/c

c $\bar{c}$ events									
$\geq 4.75$	0.58%	0.58%	0.58%	0.58%	0.58%	0.58%	0.58%	0.58%	0.58%
$\geq 4.50$	0.59%	0.59%	0.59%	0.59%	0.59%	0.59%	0.59%	0.59%	0.59%
$\geq 4.25$	0.62%	0.62%	0.62%	0.62%	0.62%	0.62%	0.62%	0.62%	0.62%
$\geq 4.00$	0.65%	0.65%	0.65%	0.65%	0.65%	0.65%	0.65%	0.65%	0.65%
$\geq 3.75$	0.66%	0.66%	0.66%	0.66%	0.66%	0.66%	0.66%	0.66%	0.66%
$\geq 3.50$	0.70%	0.70%	0.70%	0.70%	0.70%	0.70%	0.70%	0.70%	0.70%
$\geq 3.25$	0.73%	0.73%	0.73%	0.73%	0.73%	0.73%	0.73%	0.73%	0.72%
$\geq 3.00$	0.79%	0.79%	0.79%	0.79%	0.79%	0.79%	0.79%	0.76%	0.73%
$\geq 2.75$	0.86%	0.86%	0.86%	0.86%	0.86%	0.86%	0.83%	0.79%	0.75%
$\geq 2.50$	1.01%	1.01%	1.01%	1.01%	1.01%	1.01%	0.92%	0.83%	0.78%
$\geq 2.25$	1.26%	1.26%	1.26%	1.26%	1.26%	1.18%	1.01%	0.88%	0.81%
$\geq 2.00$	1.76%	1.76%	1.76%	1.76%	1.76%	1.46%	1.17%	0.95%	0.85%
$\geq 1.75$	2.46%	2.46%	2.46%	2.46%	2.26%	1.75%	1.33%	1.03%	0.87%
$\geq 1.50$	3.68%	3.68%	3.68%	3.68%	2.91%	2.13%	1.52%	1.11%	0.87%
$\geq 1.25$	6.34%	6.34%	6.34%	5.45%	3.86%	2.50%	1.64%	1.13%	0.88%
$\geq 1.00$	11.60%	11.60%	11.60%	7.75%	4.82%	2.72%	1.66%	1.13%	0.88%
$\geq 0.75$	23.43%	23.43%	18.30%	10.57%	5.43%	2.74%	1.66%	1.13%	0.88%
$\geq 0.50$	46.59%	46.59%	25.41%	11.60%	5.46%	2.74%	1.66%	1.13%	0.88%
$\geq 0.25$	84.90%	59.33%	26.79%	11.60%	5.46%	2.74%	1.66%	1.13%	0.88%
$> 0.00$	100.00%	59.46%	26.79%	11.60%	5.46%	2.74%	1.66%	1.13%	0.88%
	$> 0.0$	$\geq 0.5$	$\geq 1.0$	$\geq 1.5$	$\geq 2.0$	$\geq 2.5$	$\geq 3.0$	$\geq 3.5$	$\geq 4.0$
	$\sum_3 p_T^{hl}$ in the Central Arm (GeV/c)								
minbias events									
$\geq 4.75$	0.81%	0.81%	0.81%	0.81%	0.81%	0.81%	0.81%	0.81%	0.81%
$\geq 4.50$	0.81%	0.81%	0.81%	0.81%	0.81%	0.81%	0.81%	0.81%	0.81%
$\geq 4.25$	0.85%	0.85%	0.85%	0.85%	0.85%	0.85%	0.85%	0.85%	0.85%
$\geq 4.00$	0.85%	0.85%	0.85%	0.85%	0.85%	0.85%	0.85%	0.85%	0.85%
$\geq 3.75$	0.85%	0.85%	0.85%	0.85%	0.85%	0.85%	0.85%	0.85%	0.85%
$\geq 3.50$	1.05%	1.05%	1.05%	1.05%	1.05%	1.05%	1.05%	1.05%	1.02%
$\geq 3.25$	1.12%	1.12%	1.12%	1.12%	1.12%	1.12%	1.12%	1.12%	1.05%
$\geq 3.00$	1.32%	1.32%	1.32%	1.32%	1.32%	1.32%	1.32%	1.22%	1.12%
$\geq 2.75$	1.56%	1.56%	1.56%	1.56%	1.56%	1.56%	1.46%	1.29%	1.19%
$\geq 2.50$	1.76%	1.76%	1.76%	1.76%	1.76%	1.76%	1.63%	1.46%	1.32%
$\geq 2.25$	2.10%	2.10%	2.10%	2.10%	2.10%	2.00%	1.79%	1.59%	1.39%
$\geq 2.00$	2.54%	2.54%	2.54%	2.54%	2.54%	2.30%	1.93%	1.66%	1.42%
$\geq 1.75$	3.73%	3.73%	3.73%	3.73%	3.39%	2.81%	2.20%	1.69%	1.42%
$\geq 1.50$	5.28%	5.28%	5.28%	5.28%	4.37%	3.22%	2.44%	1.76%	1.46%
$\geq 1.25$	8.20%	8.20%	8.20%	7.45%	5.66%	3.83%	2.64%	1.76%	1.46%
$\geq 1.00$	14.39%	14.39%	14.39%	10.06%	6.77%	4.06%	2.68%	1.76%	1.46%
$\geq 0.75$	26.11%	26.11%	21.20%	13.07%	7.25%	4.10%	2.68%	1.76%	1.46%
$\geq 0.50$	48.49%	48.49%	27.60%	13.82%	7.28%	4.10%	2.68%	1.76%	1.46%
$\geq 0.25$	85.84%	61.02%	28.72%	13.82%	7.28%	4.10%	2.68%	1.76%	1.46%
$> 0.00$	100.00%	61.12%	28.72%	13.82%	7.28%	4.10%	2.68%	1.76%	1.46%
	$> 0.0$	$\geq 0.5$	$\geq 1.0$	$\geq 1.5$	$\geq 2.0$	$\geq 2.5$	$\geq 3.0$	$\geq 3.5$	$\geq 4.0$
	$\sum_3 p_T^{hl}$ in the Central Arm (GeV/c)								

Figure 105: Two-dimensional cut tables for Figure 104 — upper table for  $c\bar{c}$  events, lower table for minimum-bias events

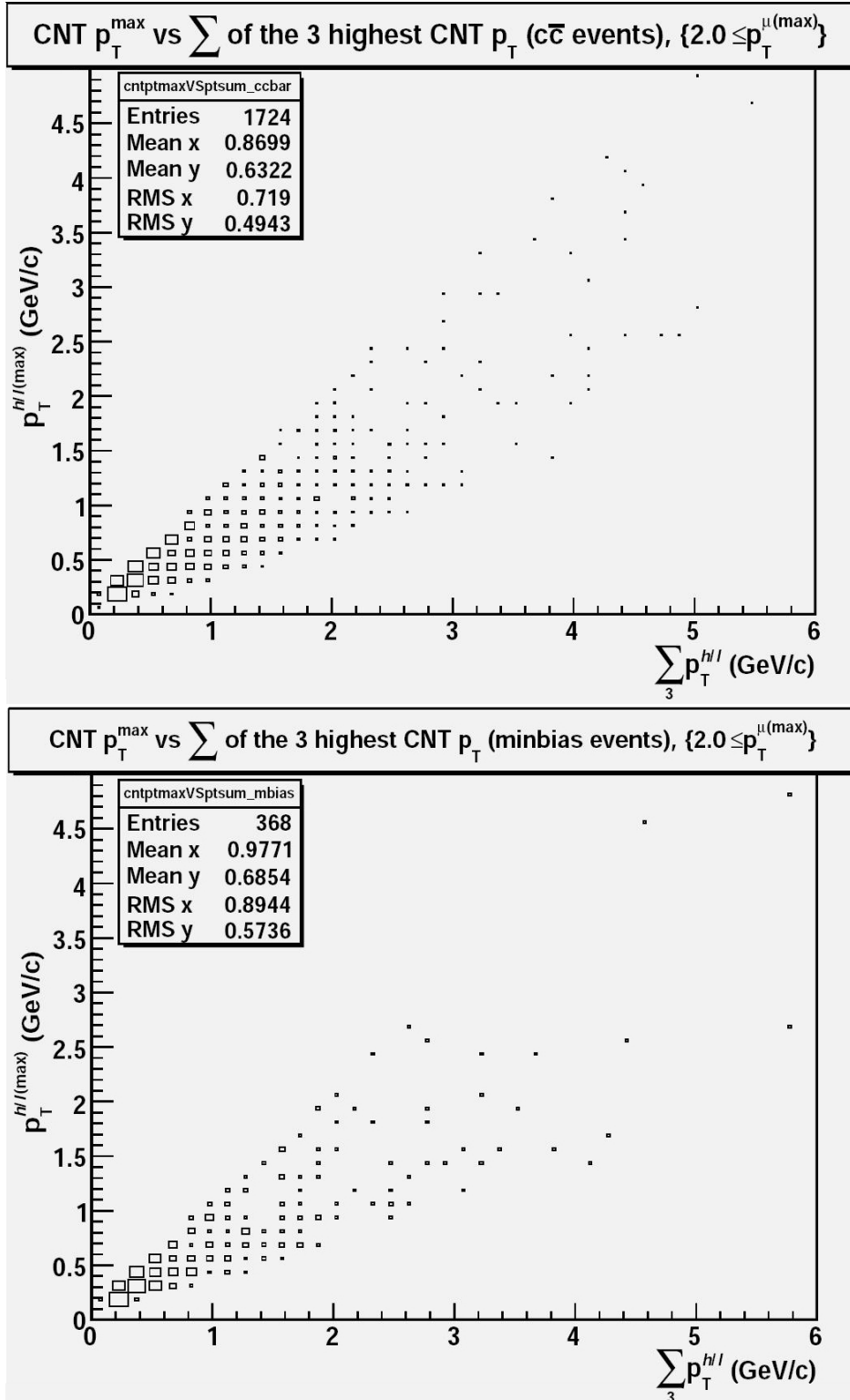


Figure 106: Maximum Central-Arm track  $p_T$  vs. the sum of the  $p_T$  of 3 Central-Arm tracks with the largest  $p_T$  values for  $2.0 \text{ GeV}/c \leq p_T^{\mu(\max)}$

<b><math>c\bar{c}</math> events</b>									
$\geq 4.75$	1.16%	1.16%	1.16%	1.16%	1.16%	1.16%	1.16%	1.16%	1.16%
$\geq 4.50$	1.22%	1.22%	1.22%	1.22%	1.22%	1.22%	1.22%	1.22%	1.22%
$\geq 4.25$	1.22%	1.22%	1.22%	1.22%	1.22%	1.22%	1.22%	1.22%	1.22%
$\geq 4.00$	1.33%	1.33%	1.33%	1.33%	1.33%	1.33%	1.33%	1.33%	1.33%
$\geq 3.75$	1.45%	1.45%	1.45%	1.45%	1.45%	1.45%	1.45%	1.45%	1.39%
$\geq 3.50$	1.57%	1.57%	1.57%	1.57%	1.57%	1.57%	1.57%	1.57%	1.51%
$\geq 3.25$	1.80%	1.80%	1.80%	1.80%	1.80%	1.80%	1.80%	1.74%	1.62%
$\geq 3.00$	1.86%	1.86%	1.86%	1.86%	1.86%	1.86%	1.86%	1.80%	1.68%
$\geq 2.75$	2.09%	2.09%	2.09%	2.09%	2.09%	2.09%	2.03%	1.86%	1.74%
$\geq 2.50$	2.38%	2.38%	2.38%	2.38%	2.38%	2.38%	2.26%	2.09%	1.91%
$\geq 2.25$	2.78%	2.78%	2.78%	2.78%	2.78%	2.67%	2.38%	2.15%	1.97%
$\geq 2.00$	3.36%	3.36%	3.36%	3.36%	3.36%	2.96%	2.67%	2.32%	2.09%
$\geq 1.75$	4.18%	4.18%	4.18%	4.18%	3.83%	3.31%	2.84%	2.44%	2.09%
$\geq 1.50$	5.74%	5.74%	5.74%	5.74%	4.64%	3.60%	2.90%	2.44%	2.09%
$\geq 1.25$	8.93%	8.93%	8.93%	7.83%	5.74%	4.00%	3.02%	2.49%	2.09%
$\geq 1.00$	15.08%	15.08%	15.08%	11.02%	7.08%	4.29%	3.07%	2.49%	2.09%
$\geq 0.75$	26.97%	26.97%	21.87%	13.69%	7.89%	4.41%	3.07%	2.49%	2.09%
$\geq 0.50$	50.81%	50.81%	29.47%	14.97%	7.89%	4.41%	3.07%	2.49%	2.09%
$\geq 0.25$	86.83%	63.52%	30.97%	14.97%	7.89%	4.41%	3.07%	2.49%	2.09%
$> 0.00$	100.00%	63.81%	30.97%	14.97%	7.89%	4.41%	3.07%	2.49%	2.09%
	$> 0.0$	$\geq 0.5$	$\geq 1.0$	$\geq 1.5$	$\geq 2.0$	$\geq 2.5$	$\geq 3.0$	$\geq 3.5$	$\geq 4.0$
	$\sum_3 p_T^{h/l}$ in the Central Arm (GeV/c)								
<b>minbias events</b>									
$\geq 4.75$	1.36%	1.36%	1.36%	1.36%	1.36%	1.36%	1.36%	1.36%	1.36%
$\geq 4.50$	1.63%	1.63%	1.63%	1.63%	1.63%	1.63%	1.63%	1.63%	1.63%
$\geq 4.25$	1.63%	1.63%	1.63%	1.63%	1.63%	1.63%	1.63%	1.63%	1.63%
$\geq 4.00$	1.63%	1.63%	1.63%	1.63%	1.63%	1.63%	1.63%	1.63%	1.63%
$\geq 3.75$	1.63%	1.63%	1.63%	1.63%	1.63%	1.63%	1.63%	1.63%	1.63%
$\geq 3.50$	1.63%	1.63%	1.63%	1.63%	1.63%	1.63%	1.63%	1.63%	1.63%
$\geq 3.25$	1.63%	1.63%	1.63%	1.63%	1.63%	1.63%	1.63%	1.63%	1.63%
$\geq 3.00$	1.63%	1.63%	1.63%	1.63%	1.63%	1.63%	1.63%	1.63%	1.63%
$\geq 2.75$	1.63%	1.63%	1.63%	1.63%	1.63%	1.63%	1.63%	1.63%	1.63%
$\geq 2.50$	2.72%	2.72%	2.72%	2.72%	2.72%	2.72%	2.17%	2.17%	2.17%
$\geq 2.25$	3.53%	3.53%	3.53%	3.53%	3.53%	3.26%	2.72%	2.45%	2.17%
$\geq 2.00$	4.08%	4.08%	4.08%	4.08%	4.08%	3.53%	2.99%	2.45%	2.17%
$\geq 1.75$	6.25%	6.25%	6.25%	6.25%	5.71%	4.35%	3.26%	2.72%	2.17%
$\geq 1.50$	9.24%	9.24%	9.24%	9.24%	6.79%	5.43%	4.35%	3.26%	2.45%
$\geq 1.25$	13.59%	13.59%	13.59%	12.77%	8.70%	7.34%	5.16%	3.53%	2.72%
$\geq 1.00$	19.29%	19.29%	19.29%	16.03%	10.87%	8.42%	5.43%	3.53%	2.72%
$\geq 0.75$	30.16%	30.16%	26.09%	19.29%	11.14%	8.42%	5.43%	3.53%	2.72%
$\geq 0.50$	48.91%	48.91%	33.97%	21.74%	11.14%	8.42%	5.43%	3.53%	2.72%
$\geq 0.25$	88.32%	62.23%	35.05%	21.74%	11.14%	8.42%	5.43%	3.53%	2.72%
$> 0.00$	100.00%	62.23%	35.05%	21.74%	11.14%	8.42%	5.43%	3.53%	2.72%
	$> 0.0$	$\geq 0.5$	$\geq 1.0$	$\geq 1.5$	$\geq 2.0$	$\geq 2.5$	$\geq 3.0$	$\geq 3.5$	$\geq 4.0$
	$\sum_3 p_T^{h/l}$ in the Central Arm (GeV/c)								

Figure 107: Two-dimensional cut tables for Figure 106 — upper table for  $c\bar{c}$  events, lower table for minimum-bias events

open-charm sample were significantly larger than contributions from the minimum-bias sample were observed in the transverse momentum correlations. Furthermore, there are kinematical  $p_T$  regions where the minimum-bias events slightly dominate over the open-charm events. This is a logical consequence of the harder muon  $p_T$  spectrum for the minimum-bias events than that for the  $c\bar{c}$  events, observed in the following study in Chapter 7.4.

#### 7.4 Single-Muon $p_T$ Spectra

A study was performed comparing single-muon  $p_T$  spectra in the PHENIX Muon Arms for the minimum-bias simulation sample, for the open-charm simulation sample, and for the bottom simulation sample. The three single-muon  $p_T$  distributions are shown in Figure 108. The minimum-bias and the  $c\bar{c}$   $p_T$  distributions were normalized as follows. The  $c\bar{c}$  distribution was normalized relative to the  $b\bar{b}$  distribution using the normalization factor:

$$R_{c\bar{c}/b\bar{b}} = \frac{\sigma_{c\bar{c}}}{\sigma_{b\bar{b}}} \times \frac{N_{b\bar{b}}^{gen.events}}{N_{c\bar{c}}^{gen.events}}, \quad (87)$$

where for the calculation we adopted  $\sigma_{c\bar{c}} = 567 \pm 57(\text{stat}) \pm 193(\text{sys}) \mu\text{b}$  [85] and  $\sigma_{b\bar{b}} = 3.9 \pm 2.5(\text{stat})_{-2}^{+3}(\text{sys}) \mu\text{b}$  [93], the measured at PHENIX charm production and bottom production cross sections, respectively.  $N_{c\bar{c}}^{gen.events} = 14 \times 10^6$  and  $N_{b\bar{b}}^{gen.events} = 2 \times 10^5$  are the numbers of generated events for each simulation sample. The minimum-bias  $p_T$  distribution was normalized relative to the  $c\bar{c}$  distribution

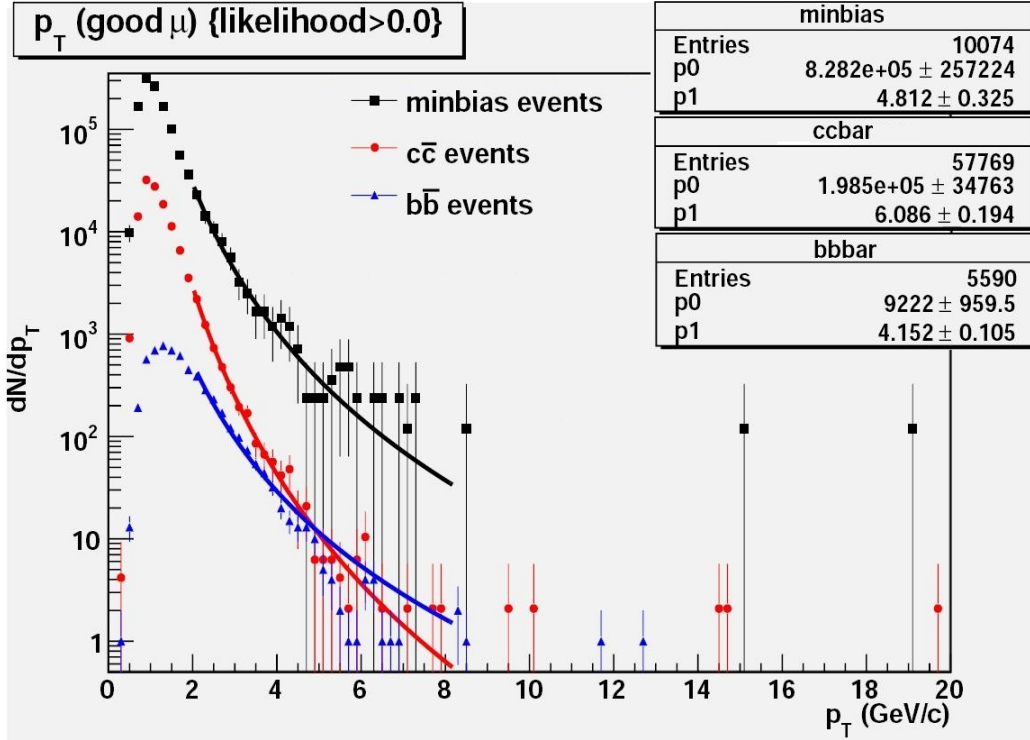


Figure 108: Single-muon  $p_T$  spectra in the Muon Arms for the minimum-bias (squares), the open-charm (circles), and the bottom (triangles) simulation samples

using the normalization factor:

$$R_{min.bias/c\bar{c}} = \frac{\sigma_{pp}^{total} - \sigma_{pp}^{elastic} - \sigma_{pp}^{diffr.}}{\sigma_{c\bar{c}}} \times \frac{N_{c\bar{c}}^{gen.events}}{N_{min.bias}^{gen.events}}, \quad (88)$$

where the cross sections are given in Chapter 7.1.4, and  $N_{min.bias}^{gen.events} = 13.1 \times 10^6$  is the number of generated events in the minimum-bias sample. The spectra were fitted using a power-law function:  $p0 \times p_T^{-p1}$ . The fitting parameters, including the power parameter  $p1$ , can be found in the statistical boxes in Figure 108.

The single-muon  $p_T$  spectrum in the PHENIX Muon Arms for the  $c\bar{c}$  events appears to be softer than that for the minimum-bias events, which is contrary to our expectations and to what has been predicted in [132]. The simulation results in [132] demonstrated that the single-muon  $p_T$  spectrum in the Muon Arms above 2

GeV/ $c$  is dominated by open-charm production. Though it is worth to note about that study that the simulation, used in that analysis, was not complete. First, no complete minimum-bias sample was generated, thus, the heavy-flavor production was compared with only one competing channel — muons from pion and kaon decays. Second, the simulation did not include the PHENIX detector response, simply exploiting the South Muon Arm acceptance cuts,  $12^\circ < \theta < 35^\circ$ . The modeling using the PISA package in [132] was very statistically limited.

One can see, comparing the  $p_1$  parameters, that the  $b\bar{b}$   $p_T$  distribution is harder than the other two distributions. It is also remarkable that the contribution from the bottom decays to the total heavy-flavor production rate becomes dominant for  $p_T > 4.8$  GeV/ $c$ . However the  $b\bar{b}$  event generation used in the current simulation analysis included only LO production mechanisms, with the MSEL switch set to 5, and statistics was not sufficient for detailed studies. Full simulation, including higher-order bottom production mechanisms with much higher statistics, is required to proceed with the  $b\bar{b}$  production simulation analysis. Based on the  $b\bar{b}$  event characteristics, the prospective study of the  $b\bar{b}$  production looks promising, provided that we have enough statistics in the future experiments.

## 7.5 Multivariate Likelihood Function

From the previous chapters it follows that it is hard to use  $\phi$  and  $p_T$  correlations by themselves to develop selection criteria for the open-charm muons. This makes nearly impossible an observation of a charm signal in a sample of single-muon events

using these variables, but it could be possible to do this in combination with other variables. Hopefully, charm events have some other distinguishing features which can be employed to help to differentiate the open-charm muons from other inclusive muon candidates. But it is probably hard to obtain sufficient signal-to-background separation in order to develop discriminants using any variable alone. Therefore, it is more efficient to incorporate many such variables into a combined multivariate discriminant. The combined multivariate discriminant can benefit from various distinctions between the open-charm muons and other inclusive muon candidates giving in the end multivariate selection criteria with much higher signal-to-background separation than any variable alone can give. Thus, the ultimate goal of the correlation studies is to develop multivariate selection criteria which can significantly enhance the charm content of a sample of single-muon events, by studying and comparing different kinematic quantities of the Muon-Arm tracks (at forward rapidity) and the Central-Arm tracks (at mid rapidity).

It also follows from the current track correlation study that it is impossible to tag clearly open-charm muons using cut-based selection criteria. A way out is to assign a probability or level of confidence for every muon to originate in charm decays. This can be accomplished by additional studies which involve likelihood calculations. In this chapter we give a short introduction to a multivariate likelihood function technique which can be exploited in the analysis and has been used at other experiments, e.g., at the CDF experiment at the Fermilab Tevatron [133].

In the first step of the procedure, one needs to select variables intended to

be used in the discrimination. The larger the number of the input variables, the more optimized multivariate likelihood function can be developed selecting different subsets of the variables. The most optimized multivariate likelihood function results in the highest signal to background separation.

For each selected variable, reference histograms have to be produced. Each histogram includes  $n_i$  bins with the value of each bin  $f_{ijk}$ , where the index  $i$  stands for the variable,  $j$  for the bin, and  $k$  for the type of events. In the current analysis the types of events are the charm signal and several possible single-muon background candidates. The total number of event types, including the charm signal and background candidates, is  $M$ . Separate histograms are created for signal and background samples. The histograms must be normalized to unit area:  $\sum_{j=1}^{n_i} f_{ijk} = 1$ .

Based on the reference histograms, the likelihood function is calculated for every event type by determining in which bin  $j$  a particular event is found in the distribution of variable  $i$ :

$$p_{ik} = \frac{f_{ijk}}{\sum_{k=1}^M f_{ijk}}. \quad (89)$$

Finally, the multivariate likelihood function,  $L$ , for the signal can be determined as:

$$L_{signal} = \frac{\prod_{i=1}^{n_{var}} p_{i,signal}}{\sum_{k=1}^M \prod_{i=1}^{n_{var}} p_{ik}}. \quad (90)$$

The likelihood function provides the probability of observing the signal or background. The values, at which the likelihood is maximum, refer to the most probable match to the true signal content of the data. If one produces a histogram

for the likelihood function distribution, the likelihood function with good signal-to-background separation appears to have the signal distribution peak close to one (the last bin) and the background peak close to zero (the first bin), meaning that the last bin is the most sensitive area to the signal. The ratio of the signal to the background in the last bin demonstrates the likelihood function effectiveness of differentiating the signal from the background.

The advantages of the multivariate likelihood function are small amount of time needed for the calculations and relatively simple procedure to implement in the analysis and to be programmed. Thus the various combinations of the input variables can be examined relatively easy and fast.

## 8 CONCLUSION AND OUTLOOK

The proton spin deficit phenomenon still remains one of the most exciting unresolved puzzles in physics. With longitudinally-polarized proton-proton collisions, the high-energy experiments at RHIC proceed with measurements of the gluon contribution to the proton spin using strongly-interacting probes in hard-scattering processes described by perturbative Quantum Chromodynamics. Since heavy-flavor production at RHIC energies is dominated by gluon-gluon processes, the production of  $c\bar{c}$  pairs in polarized  $p-p$  collisions directly probes the polarized gluon distribution  $\Delta g(x)$  and hence the gluon polarization  $\Delta G$ . Therefore, the production of single muons from charm decay in polarized  $p-p$  collisions is sensitive to the polarized gluon distribution in the proton.

With the Muon Arms in the PHENIX detector covering the pseudorapidity ranges of  $-2.25 \leq \eta \leq -1.15$  and  $1.15 \leq \eta \leq 2.44$ , single-muon data have been successfully collected in polarized proton-proton collisions at  $\sqrt{s} = 200$  GeV.  $\Delta G$  can be extracted from the experimentally measured double-helicity asymmetry. We measured the single-muon  $A_{LL}$  for inclusive muons from longitudinally-polarized  $p-p$  collisions from PHENIX 2003 data. Measurements were performed in the  $p_T$  range up to 8 GeV/ $c$  in 8  $p_T$  bins. The PHENIX 2003 inclusive single-muon  $A_{LL}$  results and  $A_{LL}$  predictions for PHENIX 2006 single-muon data demonstrate that large statistical uncertainties preclude constraining the gluon polarization with the current limited statistics available for the  $A_{LL}$  measurements.

There are several sources of inclusive muon candidates in addition to the open-charm single muons. In order to develop discriminants and selection cuts for enriching the charm content of a sample of single-muon events, a multistage Monte Carlo simulation (including the PHENIX detector response) has been conducted to investigate correlations between muon tracks in the Muon Arms at forward rapidity and charged hadron/lepton tracks in the Central Arms of the PHENIX detector at mid rapidity. Two separate simulation outputs have been produced and compared: for charm ( $c\bar{c}$ ) events and for minimum-bias events. Azimuthal-angle correlations of the maximum- $p_T$  Central-Arm and Muon-Arm tracks have been studied as a function of Muon-Arm track  $p_T$  and have been compared for  $c\bar{c}$  events and minimum-bias events. The simulation indicated somewhat increased tendency for charm events to have the maximum- $p_T$  Central-Arm and Muon-Arm tracks emitted back-to-back in azimuthal angle  $\phi$ , but only for low muon  $p_T$ . We also studied correlations between the  $p_T$  of the Muon-Arm track and the  $p_T$  of the particles detected in the Central Arms, including combinations of the variables. No kinematical  $p_T$  regions, where contributions from the open-charm sample were significantly larger than contributions from the minimum-bias sample, were observed in the transverse-momentum correlations.

The simulation demonstrates that it is not possible to use  $\phi$  and  $p_T$  correlations by themselves to develop selection criteria to differentiate the open-charm muons from other inclusive muon candidates. But it is possible to do this in combination with other variables proceeding with additional studies. The ultimate goal of the

correlation studies is to develop multivariate selection criteria which can significantly enhance the charm content of a sample of single-muon events, by studying and comparing different kinematic quantities of the Muon-Arm tracks at forward rapidity and the Central-Arm tracks at mid-rapidity. The further studies should involve likelihood calculations assigning probability or level of confidence for every muon to originate in charm decays.

The multivariate track correlation studies can be complementary to the future measurements intended with the silicon vertex detectors in PHENIX, including the VTX covering the central rapidity and the FVTX covering the forward rapidity, which are under construction. These silicon vertex detectors will give new opportunity to study heavy-quark (charm and bottom quark) production by measuring the displaced decay vertex and will significantly improve the PHENIX capability for proton-spin studies.

## REFERENCES

- [1] M. Gell-Mann, Phys. Lett. **8**, 214 (1964).
- [2] G. Zweig, CERN Report No. TH-401, 1964 (unpublished); CERN Report No. TH-412, 1964 (unpublished).
- [3] C. Amsler *et al.* (Particle Data Group), Phys. Lett. B **667**, 1 (2008).
- [4] J. I. Friedman, in *Les Prix Nobel 1990: Nobel Prizes, Presentations, Biographies and Lectures* (Almqvist & Wiksell, Stockholm/Uppsala, 1991); J. I. Friedman, Rev. Mod. Phys. **63**, 615 (1991).
- [5] F. E. Close, *An Introduction to Quarks and Partons* (Academic, London, 1979).
- [6] B. W. Filippone and X. Ji, Adv. Nucl. Phys. **26**, 1 (2001).
- [7] D. H. Perkins, in *Proceedings of the XVI International Conference on High Energy Physics, Chicago-Batavia, Ill., 1972*, edited by J. D. Jackson and A. Roberts (N. A. L. Batavia, Ill., 1973), Vol. 4, p. 189.
- [8] D. H. Perkins, *Introduction to High Energy Physics* (Addison-Wesley, Reading, MA, 1987).
- [9] T. Sloan, Phil. Trans. R. Soc. Lond. A **359**, 379 (2001).
- [10] J. D. Bjorken, Phys. Rep. **148**, 1467 (1966).
- [11] J. D. Bjorken, Phys. Rev. D **1**, 1376 (1970).
- [12] J. Ellis and R. L. Jaffe, Phys. Rev. D **9**, 1444 (1974).
- [13] J. Ellis and R. L. Jaffe, Phys. Rev. D **10**, 1669 (1974).
- [14] J. Ashman *et al.* (EMCollaboration), Phys. Lett. B **202**, 603 (1988).
- [15] J. J. Aubert *et al.* (EMCollaboration), Phys. Lett. B **123**, 275 (1983).
- [16] P. L. Anthony *et al.* (SLAC E142 Collaboration), Phys. Rev. Lett. **71**, 959 (1993).
- [17] K. Abe *et al.* (SLAC E154 Collaboration), Phys. Rev. Lett. **79**, 26 (1997).
- [18] K. Ackerstaff *et al.* (HERMES Collaboration), Phys. Lett. B **404**, 383 (1997).
- [19] B. Adeva *et al.* (SMC Collaboration), Phys. Rev. D **58**, 112001 (1998).
- [20] K. Abe *et al.* (SLAC E143 Collaboration), Phys. Rev. D **58**, 112003 (1998).
- [21] A. Airapetian *et al.* (HERMES Collaboration), Phys. Lett. B **442**, 484 (1998).

- [22] P. L. Anthony *et al.* (SLAC E155 Collaboration), Phys. Lett. B **463**, 339 (1999).
- [23] A. Airapetian *et al.* (HERMES Collaboration), Phys. Rev. Lett. **84**, 2584 (2000).
- [24] G. Bunce, N. Saito, J. Soffer, and W. Vogelsang, Annu. Rev. Nucl. Part. Sci. **50**, 525 (2000).
- [25] R. L. Jaffe and X. Ji, Phys. Rev. Lett. **67**, 552 (1991).
- [26] R. L. Jaffe and X. Ji, Nucl. Phys. **B375**, 527 (1992).
- [27] X. Ji, Phys. Rev. D **49**, 114 (1994).
- [28] G. P. Ramsey, J. Qiu, D. Richards, and D. Sivers, Phys. Rev. D **39**, 361 (1989).
- [29] S. V. Bashinsky and R. L. Jaffe, Nucl. Phys. **B536**, 303 (1998).
- [30] A. Harindranath and R. Kundu, Phys. Rev. D **59**, 116013 (1999).
- [31] N. S. Craigie, K. Hidaka, M. Jacob, and F. M. Renard, Phys. Rep. **99**, 69 (1983).
- [32] J. P. Ralston and D. E. Soper, Nucl. Phys. **B152**, 109 (1979).
- [33] X. Ji, Phys. Lett. B **289**, 137 (1992).
- [34] C. Bourrely, J. Soffer, F.M. Renard, and P. Taxil, Phys. Rep. **177**, 319 (1989).
- [35] S. Frixione, Phys. Lett. B **429**, 369 (1998).
- [36] M. Glück, E. Reya, M. Stratmann, and W. Vogelsang, Phys. Rev. D **53**, 4775 (1996).
- [37] T. Gehrmann and W. J. Stirling, Phys. Rev. D **53**, 6100 (1996).
- [38] D. de Florian, O. A. Sampayo, and R. Sassot, Phys. Rev. D **57**, 5803 (1998).
- [39] D. de Florian, S. Frixione, A. Signer, and W. Vogelsang, Nucl. Phys. **B539**, 455 (1999).
- [40] M. Stratmann and W. Vogelsang, J. Phys. Conf. Ser. **69**, 012035 (2007), and references therein.
- [41] S. S. Adler *et al.* (PHENIX Collaboration), Phys. Rev. Lett. **91**, 241803 (2003).
- [42] J. Adams *et al.* (STAR Collaboration), Phys. Rev. Lett. **97**, 152302 (2006).
- [43] B. I. Abelev *et al.* (STAR Collaboration), Phys. Rev. Lett. **97**, 252001 (2006).

- [44] S. S. Adler *et al.* (PHENIX Collaboration), Phys. Rev. Lett. **98**, 012002 (2007).
- [45] S. Kretzer, Phys. Rev. D **62**, 054001 (2000).
- [46] B. Kniehl, G. Kramer, and B. Pötter, Nucl. Phys. **B582**, 514 (2000).
- [47] B. Kniehl, G. Kramer, and B. Pötter, Nucl. Phys. **B597**, 337 (2001).
- [48] L. Bourhis, M. Fontannaz, J. P. Guillet, and M. Werlen, Eur. Phys. J. C **19**, 89 (2001).
- [49] J. Pumplin *et al.* (CTEQ Collaboration), JHEP **0207**, 012 (2002).
- [50] B. Jäger, A. Schäfer, M. Stratmann, and W. Vogelsang, Phys. Rev. D **67**, 054005 (2003).
- [51] B. Jäger, M. Stratmann, and W. Vogelsang, Phys. Rev. D **70**, 034010 (2004).
- [52] D. de Florian, Phys. Rev. D **67**, 054004 (2003).
- [53] F. Aversa, P. Chiappetta, M. Greco, and J. P. Guillet, Nucl. Phys. **B327**, 105 (1989).
- [54] L. E. Gordon and W. Vogelsang, Phys. Rev. D **48**, 3136 (1993).
- [55] L. E. Gordon and W. Vogelsang, Phys. Rev. D **50**, 1901 (1994).
- [56] P. Aurenche *et al.*, Nucl. Phys. **B297**, 661 (1988).
- [57] H. Baer *et al.*, Phys. Rev. D **42**, 61 (1990); Phys. Lett. B **234**, 127 (1990).
- [58] S. S. Adler *et al.* (PHENIX Collaboration), Phys. Rev. Lett. **93**, 202002 (2004).
- [59] S. S. Adler *et al.* (PHENIX Collaboration), Phys. Rev. D **73**, 091102 (2006).
- [60] A. Adare *et al.* (PHENIX Collaboration), Phys. Rev. D **76**, 051106 (2007).
- [61] K. Boyle, *2007 RHIC & AGS Users' Meeting, BNL, June, 2007.*
- [62] M. Sarsour, *2007 APS DNP Meeting, Newport News, Virginia, Oct., 2007.*
- [63] M. Glück, E. Reya, M. Stratmann, and W. Vogelsang, Phys. Rev. D **63**, 094005 (2001).
- [64] D. de Florian, R. Sassot, M. Stratmann, and W. Vogelsang, hep-ph/0804.0422.
- [65] D. de Florian, G. A. Navarro, and R. Sassot, Phys. Rev. D **71**, 094018 (2005).
- [66] P. Liebing, AIP Conf. Proc. **915**, 331 (2007).

- [67] E. S. Ageev *et al.* (COMPASS Collaboration), Phys. Lett. B **633**, 25 (2006).
- [68] B. Adeva *et al.* (SMC Collaboration), Phys. Rev. D **70**, 012002 (2004).
- [69] M. Alekseev *et al.* (COMPASS Collaboration), arXiv:0802.3023v1.
- [70] A. P. Contogouris, S. Papadopoulos, and B. Kamal, Phys. Lett. B **246**, 523 (1990).
- [71] M. Karliner and R. W. Robinett, Phys. Lett. B **324**, 209 (1994).
- [72] T. Sjöstrand, Comput. Phys. Commun. **82**, 74 (1994).
- [73] T. Sjöstrand *et al.*, Comput. Phys. Commun. **135**, 238 (2001).
- [74] T. Sjöstrand, L. Lönnblad, and S. Mrenna, hep-ph/0108264.
- [75] S. Dawson, R. K. Ellis, and P. Nason, Nucl. Phys. **B303**, 607 (1988).
- [76] S. Dawson, R. K. Ellis, and P. Nason, Nucl. Phys. **B327**, 49 (1989); **B335**, 260(E) (1990).
- [77] W. Beenakker, H. Kuijf, J. Smith, and W. L. van Neerven, Phys. Rev. D **40**, 54 (1989).
- [78] W. Beenakker, R. Meng, G. A. Schuler, J. Smith, and W. L. van Neerven, Nucl. Phys. **B351**, 507 (1991).
- [79] I. Bojak and M. Stratmann, Phys. Rev. D **67**, 034010 (2003).
- [80] M. Cacciari, P. Nason, and R. Vogt, Phys. Rev. Lett. **95**, 122001 (2005).
- [81] R. Vogt, arXiv:0709.2531v1.
- [82] E. Norrbin and T. Sjöstrand, Eur. Phys. J. C **17**, 137 (2000).
- [83] B. Andersson, G. Gustafson, G. Ingelman, and T. Sjöstrand, Phys. Rep. **97**, 31 (1983).
- [84] S. S. Adler *et al.* (PHENIX Collaboration), Phys. Rev. Lett. **96**, 032001 (2006).
- [85] A. Adare *et al.* (PHENIX Collaboration), Phys. Rev. Lett. **97**, 252002 (2006).
- [86] M. Cacciari, hep-ph/0407187.
- [87] D. Acosta *et al.* (CDF II Collaboration), Phys. Rev. Lett. **91**, 241804 (2003).
- [88] S. S. Adler *et al.* (PHENIX Collaboration), Phys. Rev. Lett. **96**, 032301 (2006).
- [89] K. Adcox *et al.* (PHENIX Collaboration), Phys. Rev. Lett. **88**, 192303 (2002).

- [90] S. S. Adler *et al.* (PHENIX Collaboration), Phys. Rev. Lett. **94**, 082301 (2005).
- [91] M. L. Mangano, P. Nason, and G. Ridolfi, Nucl. Phys. **B405**, 507 (1993).
- [92] H. L. Lai *et al.*, Eur. Phys. J. C **12**, 375 (2000).
- [93] A. Adare *et al.* (PHENIX Collaboration), Phys. Lett. B **670**, 313 (2009).
- [94] S. S. Adler *et al.* (PHENIX Collaboration), Phys. Rev. D **76**, 092002 (2007).
- [95] W. Fischer, Nucl. Instrum. Methods Phys. Res., Sect. B **241**, 281 (2005).
- [96] <http://www.bnl.gov/RHIC/>.
- [97] J. W. Harris *et al.* (STAR Collaboration), Nucl. Phys. **A566**, 277c (1994).
- [98] F. Videbaek *et al.* (BRAHMS Collaboration), Nucl. Phys. **A566**, 299c (1994).
- [99] B. B. Back *et al.* (PHOBOS Collaboration), Nucl. Instrum. Methods Phys. Res., Sect. A **499**, 603 (2003).
- [100] S. Bültmann *et al.* (pp2pp Collaboration), Nucl. Instrum. Methods Phys. Res., Sect. A **535**, 415 (2004).
- [101] S. Bültmann *et al.* (pp2pp Collaboration), Phys. Lett. B **647**, 98 (2007).
- [102] C. Aidala *et al.*, <http://spin.riken.bnl.gov/rsc/report/masterspin.pdf>.
- [103] V. I. Ptitsin, Yu. M. Shatunov, and S. Peggs, in *Proceedings of the Particle Accelerator Conference, Dallas, TX, 1995* (IEEE, New York, 1995), Vol. 5, p. 3331.
- [104] K. Adcox *et al.* (PHENIX Collaboration), Nucl. Instrum. Methods Phys. Res., Sect. A **499**, 469 (2003).
- [105] H. Satz, Nucl. Phys. (Proc. Suppl.) **B94**, 204 (2001).
- [106] M. Allen *et al.* (PHENIX Collaboration), Nucl. Instrum. Methods Phys. Res., Sect. A **499**, 549 (2003).
- [107] K. Adcox *et al.* (PHENIX Collaboration), Nucl. Instrum. Methods Phys. Res., Sect. A **499**, 489 (2003).
- [108] M. Aizawa *et al.* (PHENIX Collaboration), Nucl. Instrum. Methods Phys. Res., Sect. A **499**, 508 (2003).
- [109] L. Aphecetche *et al.* (PHENIX Collaboration), Nucl. Instrum. Methods Phys. Res., Sect. A **499**, 521 (2003).

- [110] H. Akikawa *et al.* (PHENIX Collaboration), Nucl. Instrum. Methods Phys. Res., Sect. A **499**, 537 (2003).
- [111] H. D. Sato, Ph.D. thesis, Kyoto University, Kyoto, Japan, 2003.
- [112] S. H. Aronson *et al.* (PHENIX Collaboration), Nucl. Instrum. Methods Phys. Res., Sect. A **499**, 480 (2003).
- [113] S. S. Adler *et al.* (PHENIX Collaboration), Nucl. Instrum. Methods Phys. Res., Sect. A **499**, 560 (2003).
- [114] S. S. Adler *et al.* (PHENIX Collaboration), Nucl. Instrum. Methods Phys. Res., Sect. A **499**, 593 (2003).
- [115] J. Murata *et al.*, Nucl. Instrum. Methods Phys. Res., Sect. A **500**, 309 (2003).
- [116] [http://www.phenix.bnl.gov/WWW/publish/villatte/shielding\\_study/bbc\\_muid\\_30148.eps](http://www.phenix.bnl.gov/WWW/publish/villatte/shielding_study/bbc_muid_30148.eps).
- [117] M. Brooks *et al.*, PHENIX Analysis Note No. 255, 2004 (unpublished).
- [118] V. Riabov and Yu. Riabov, PHENIX Analysis Note No. 366, 2005 (unpublished).
- [119] <http://root.cern.ch/drupal/>.
- [120] <https://www.phenix.bnl.gov/WWW/p/draft/tanida/spinpwg/rellumi/preliminary/rellumi-run/>.
- [121] <http://www4.rcf.bnl.gov/~cnipol/>.
- [122] X. Wang, *The 18th International Symposium on Spin Physics, University of Virginia, Charlottesville, Virginia, Oct., 2008*.
- [123] H. Liu *et al.*, PHENIX Analysis Note No. 636, 2007 (unpublished).
- [124] A. Datta, PHENIX Analysis Note No. 689, 2008 (unpublished).
- [125] <https://www.phenix.bnl.gov/WWW/offline/wikioffline/index.php/PHPythia>.
- [126] T. Sjöstrand, S. Mrenna, and P. Skands, hep-ph/0603175.
- [127] <https://www.phenix.bnl.gov/WWW/offline/wikioffline/index.php/Simulations>.
- [128] <http://www.fluka.org>.
- [129] <http://wwwasdoc.web.cern.ch/wwwasdoc/geant/geantall.html>.
- [130] <https://www.phenix.bnl.gov/phenix/WWW/simulation/primer4/seq-primer.html>.

- [131] K. Goulianos, arXiv:hep-ph/0203141v2.
- [132] M. L. Brooks and J. M. Moss, PHENIX Technical Note No. 361, 1997 (unpublished).
- [133] S. R. Budd, Ph.D. thesis, University of Illinois at Urbana-Champaign, 2008, available at <http://lss.fnal.gov/archive/thesis/fermilab-thesis-2008-41.pdf>.